Simulation and characterization of multi-layered surface acoustic wave devices for filtering and sensing applications

Hugo Chambon

Par **Hugo CHAMBON**

Simulation and characterization of multi-layered surface acoustic wave devices for filtering and sensing applications

Thèse présentée pour l'obtention du grade de Docteur de l'UTC

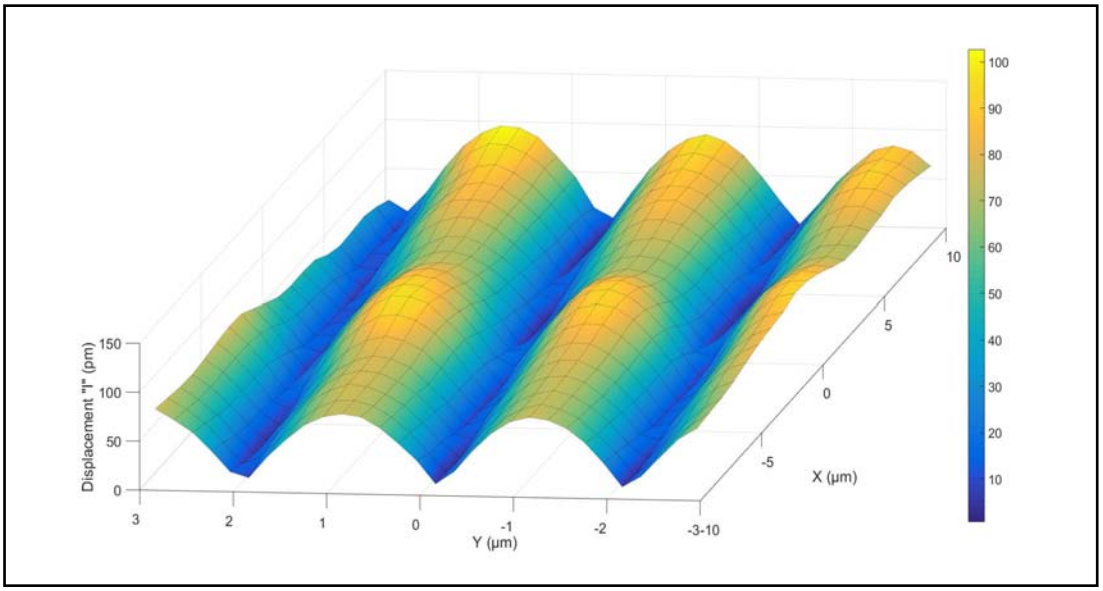

Soutenue le 10 octobre 2019
Spécialité : Acoustique et Vibrations : Unité de recherche en Mécanique - Laboratoire Roberval (FRE UTC - CNRS 2012)
D2512

Thèse de Doctorat

de

L'université de Technologie de Compiègne

Spécialité : Acoustique et Vibrations

Présentée par

Hugo CHAMBON

Simulation and characterization of multi-layered surface acoustic wave devices for filtering and sensing applications

Soutenue le 10 Octobre 2019 devant le jury composé de :

Frédéric SARRY	Professeur des Universités, Université de Lorraine, Nancy, France	(Examinateur)
Catherine POTEL	Professeur des Universités, Le Mans Université, Le Mans, France	(Examinateur)
Fréderic LAMARQUE	Professeur des Universités, UTC, Compiègne, France	(Examinateur)
Thierry AUBERT	Enseignant Chercheur (HDR), CentraleSupélec, Metz, France	(Rapporteur)
Thérèse LEBLOIS	Professeur des Universités, Université de Franche-Comté, Besançon, France	(Rapporteur)
Mohamed-Ali HAMDI	Professeur Émérite, UTC, Compiègne, France	(Directeur de thèse)
Ayech BENJEDDOU	Professeur des Universités, Supméca, Paris, France/ UTC, Compiègne, France	(Directeur de thèse)
Pascal NICOLAY	Professeur (HDR), Carinthia University of Applied Sciences, Villach, Autriche	(Directeur de thèse)

Abstract

This thesis deals with the design and characterization of multilayer acoustic wave micro-devices.

The fifth generation of communication (5G) requires more efficient acoustic resonators (frequencies > 3GHz, wider bandwidth). In this context, we have designed and optimized using FEM simulation, the geometry of Lamb wave resonator based on AlScN. The final device, consisting of a layer composed of 30% Sc and deposited on a Bragg W/SiO_2 mirror, shows excellent performance (coupling coefficient of 5% and quality factor of 768) as well as a good agreement with the simulation. To characterize the surface of BAW and SAW over the 5G frequency range, we also designed and developed a heterodyne interferometer. The latter has been used successfully to characterize surface vibrations with amplitudes between 1 and 10 pm at 5.95 GHz.

Furthermore, thanks to their robustness and ability to be wirelessly interrogated, SAW sensors are used in harsh environments and are of great interest for medical applications and structural health monitoring. Recently, the introduction of multi-material stacks offers new development opportunities. We thus studied a pressure sensor composed of two complementary layers, as well as a so-called package-less sensor using different acoustic impedance layers. To design these new sensors, we have developed a simulation tool based on the extraction of mode coupling parameters and taking into account the effects of temperature, stresses and strains to estimate their sensitivity.

Keywords: Surface acoustic wave, filter, sensor, finite element, simulation, Lamb wave, Bragg mirror, heterodyne interferometry.

Résumé

Cette thèse porte sur la conception et la caractérisation de micro-dispositifs à ondes acoustiques multicouches.

La cinquième génération de communication (5G) nécessite des résonateurs acoustiques plus performants (fréquences > 3GHz, bande passante plus large). Dans ce contexte, nous avons conçu et optimisé par simulation FEM la géométrie de résonateurs à ondes de Lamb à base d'AlScN. Le dispositif final, constitué d'une couche composée de 30% de Sc et déposée sur un miroir de Bragg W/SiO_2, montre d'excellentes performances (coefficient de couplage de 5% et facteur de qualité de 768) et un bon accord avec la simulation. Pour caractériser la surface de BAW et SAW sur la gamme de fréquence 5G, nous avons également conçu et développé un interféromètre hétérodyne. Ce dernier a été utilisé avec succès pour caractériser des vibrations de surface d'une amplitude comprise entre 1 et 10 pm à 5,95 GHz.

Par ailleurs, grâce à leur robustesse et leur capacité à être interrogé sans-fil, les capteurs SAW sont utilisés dans des environnements difficiles et suscitent un grand intérêt pour les applications médicales et de contrôle de santé intégré. Récemment, l'introduction d'empilements multi-matériaux offre de nouvelles opportunités de développements. Nous avons ainsi étudié un capteur de pression composé de deux couches complémentaires, ainsi qu'un capteur dit package-less utilisant des couches d'impédances acoustiques différentes. Pour concevoir ces nouveaux capteurs, nous avons développé un outil de simulation reposant sur l'extraction de paramètres de couplage de modes et tenant compte des effets de la température, des contraintes et des déformations pour estimer leur sensibilité.

Mots-clés : Onde acoustique (élastique) de surface, filtre, capteur, éléments finis, simulation, onde de Lamb, miroir de Bragg, interférométrie hétérodyne.

Acknowledgment

Throughout the writing of this dissertation I have received a great support and assistance. I would first like to express my sincere gratitude to Dr. Werner Scherf, CEO of the Carinthian Tech Research AG* who enabled me to join the CTR* and complete my PhD work there.

I would like to thank my advisors, Pr. Ayech Benjeddou, Pr. Mohamed-Ali Hamdi and Dr. Pascal Nicolay for their continuous support to my PhD study and related research. They provided me with valuable guidance to successfully complete my dissertation. I would like in particular to thank Pascal who was always available whenever I ran into a trouble spot or had a question about my research or writing. He consistently steered me in the right direction whenever he thought I needed it.

I would also like to acknowledge my thesis reviewers: Dr. Thérèse Leblois of the MN2S department at Femto-st and Dr. Thierry Aubert from CentraleSupélec. I am deeply grateful for their very valuable comments on this thesis.

I would like to thank all the partners at RF360, EPFL and IMTEK, especially Ulrike Roesler, Maximilian Schiek, Fazel Parsapour and Nicolas Kurz, for their excellent cooperation

My sincere thanks also go to my colleagues at the CTR for their collaboration. They supported me greatly and were always willing to help me. I would particularly like to thank Gudrun Bruckner, Thomas Moldaschl, Andreas Tortschanoff, Markus Zauner, Jaka Pribošek and Sarah Risquez. I would also like to thank the students, Claude Humbert, Aoun Amin Awan, and Quentin Chapelier who were involved in the experimental development of this research project. Without their dedicated participation and input, the experimental work could not have been conducted.

Finally, I express my very sincere gratitude to my family and friends for providing me with their support and continuous encouragement throughout my years of study and through the process of researching and writing this thesis. This accomplishment would not have been possible without them.

Thank you.

Funding support: This project was performed within the COMET Centre ASSIC Austrian Smart Systems Integration Research Center, which is funded by BMVIT, BMDW, and the Austrian provinces of Carinthia and Styria, within the framework of COMET - Competence Centers for Excellent Technologies. The COMET programme is run by FFG.

*The Carinthian Tech Research AG has merged on the 11th of July 2019 with Silicon Austria Labs GmbH

Content

List of figures

List of Tables

Résumé substantiel

Les dispositifs à ondes élastiques de surface (abrégé SAW pour *Surface Acoustic Wave*) sont des microsystèmes électromécaniques constitués d'un substrat piézoélectrique sur lequel sont déposés des transducteurs en forme de peignes interdigités (abrégé IDT pour *Inter-Digital Transducer*) permettant de convertir des signaux électriques en ondes mécaniques et inversement. Les IDTs permettent de générer de manière spécifique des ondes de surface ayant pour longueur d'onde, le double de la distance séparant deux doigts au sein du peigne. Deux structures principales sont utilisées pour les dispositifs SAW: le résonateur et la ligne à retard (voir Figure i). Dans sa forme la plus simple, le résonateur possède un unique IDT encadré par des réflecteurs (doigts non connectés). L'ensemble forme une cavité résonante dont la caractéristique électrique présente une résonance de faible impédance électrique et une antirésonance de haute impédance. La ligne à retard est quant à elle constituée de deux IDTs. Un premier transducteur génère des ondes qui se propagent à la surface du substrat, puis qui sont converties en un signal électrique par le second IDT. L'apodisation des IDTs (modification de la forme des peignes) d'entrée et de sortie permet de synthétiser des filtres sur mesure.

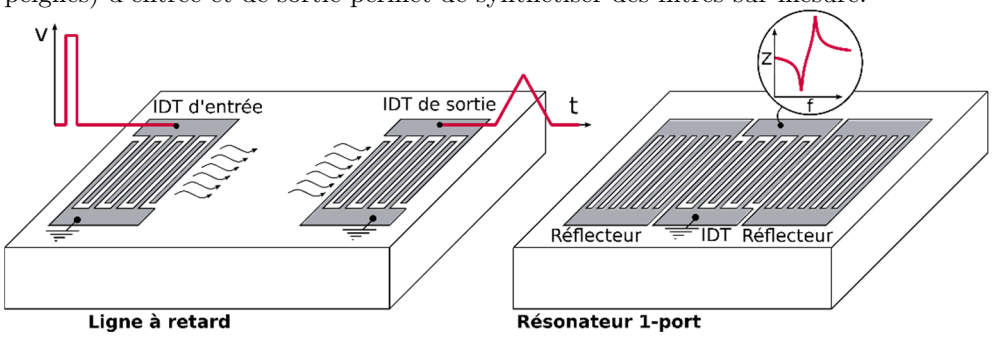

Figure i Ligne à retard et résonateur SAW.

Les dispositifs SAW sont principalement utilisés pour les applications de filtrage passif et plus marginalement comme capteurs. Pour les applications de filtrage, les résonateurs SAW sont connectés en échelle afin d'obtenir des filtres passe-bande à hautes performances. Les lignes à retard exploitent quant à elles au mieux les possibilités de conception dans le plan (apodization) pour la réalisation des fonctions de filtrages complexes. Lorsqu'ils sont utilisés comme capteurs, les dispositifs SAW exploitent la modification de la vitesse de l'onde de surface par la grandeur physique à observer, qu'il s'agisse de température, de contrainte ou de masse déposée à leurs surfaces. En utilisant un capteur SAW basé sur une structure de résonateur, ce changement de vitesse peut être quantifié via le décalage de sa fréquence de résonnance. De son côté, un capteur SAW de type ligne à retard convertit le changement de vitesse en changement de temps de réponse.

Dans le chapitre 1, après une brève introduction du principe de fonctionnement et des applications des dispositifs SAW, nous discutons de la méthode de couplage

de modes (abrégée COM pour *Coupling Of Modes*). Cette méthode est utilisée dans ce manuscrit pour simuler des dispositifs SAW complets à l'aide de la méthode des éléments finis (abrégée FE pour *Finite Elements*). Le modèle COM permet un gain de temps considérable comparé à un modèle FE complet qui doit traiter d'importantes disparités géométriques au sein de la structure du dispositif SAW. Le modèle COM exploite de la grande périodicité des dispositifs SAW et permet d'extraire quatre paramètres phénoménologiques d'une structure infinie périodique représentative d'une section du dispositif (voir Figure ii). Les paramètres COM sont ensuite assemblés à l'aide d'une méthode de matrices en cascade pour obtenir la réponse électrique du dispositif. Dans le chapitre 1, nous détaillons la méthode d'extraction des paramètres COM à partir de la simulation FE. Ces quatre paramètres COM peuvent être extraits d'un modèle dit de cellule élémentaire qui représente un réseau périodique infini utilisant uniquement une paire de doigts et des conditions aux limites périodiques (voir Figure ii).

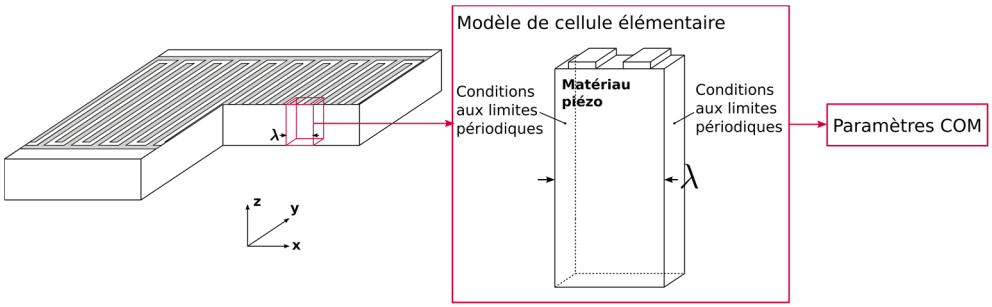

Figure ii Cellule élémentaire utilisée pour calculer les paramètres COM.

Les dispositifs SAW sont construits à partir d'un substrat piézoélectrique monocristallin sur lequel les IDTs sont déposés en une seule étape de lithographie. En raison de cette simplicité intrinsèque, les capteurs SAW sont robustes et nécessitent peu de maintenance. En outre, ils peuvent être interrogés sans fil et de manière passive (sans alimentation et électroniques embarquées) sur de courtes distances (environ 1 m). Par conséquent, ils sont considérés comme de très bons candidats pour les environnements difficiles. Cependant, contrairement à leurs concurrents tels que les capteurs CMOS, il n'existe pas de capteurs SAW disponibles sur catalogue. Ainsi, la partie sensible du capteur et ses attributs périphériques (packaging, antenne interne et antenne d'interrogation) sont spécifiquement conçus pour chaque application. Pour cette raison, et ce malgré le faible coût des matières premières, le coût d'un capteur SAW est relativement élevé comparé aux solutions technologiques concurrentes. Afin de réduire le temps nécessaire pour le développement d'un nouveau capteur et donc son coût, nous avons développé un modèle FE basé sur le concept de cellule élémentaire utilisé pour extraire les paramètres COM. Le modèle développé, expliqué dans le chapitre 2, permet de calculer la variation de la vitesse des ondes de surface due à une perturbation externe dans un dispositif multicouche. Pour ce faire, le modèle prend en compte la sensibilité du matériau à la température et aux déformations à travers des coefficients des maté-

riaux et la contrainte initiale. Le modèle développé a été comparé à un modèle de référence et à des résultats expérimentaux obtenus par le CTR (*Carinthian Tech Research AG*, Villach, Carinthie, Autriche). Confortée par le bon accord entre les simulations et ces références, la procédure de simulation proposée a été appliquée à un capteur de pression innovant constitué d'une membrane mince de Niobate de Lithium sur un substrat de Silicium (voir Figure iii). Ce capteur, conçu pour détecter les faibles variations de la pression intracrânienne, présentait expérimentalement des dysfonctionnements. D'une part, l'effet de la température n'était pas parfaitement compensé, et d'autre part, sa réponse thermique indiquait de façon inattendue un problème dans la gamme de température d'intérêt. En utilisant le modèle FE, nous avons démontré que la sensibilité résiduelle à la température provient d'un mauvais positionnement des réflecteurs le long de la ligne à retard. De plus, le problème dans la réponse thermique a pu être identifié comme étant dû au flambement de la membrane. En outre, le modèle FE est capable de prédire avec précision la température de flambement et la réponse du capteur après le flambement. Enfin, le modèle FE a été utilisé pour concevoir un prototype innovant de capteur prometteur sans packaging (voir Figure iii). Le packaging est souvent très contraignant dans la conception du capteur et son abandon permet de réduire davantage le temps nécessaire à son développement. Afin d'éviter toute contamination de surface susceptible de perturber les mesures, le capteur sans packaging utilise un empilement de couches piézoélectriques pour guider l'onde sous la surface. En utilisant le modèle FE, il a été possible d'optimiser l'épaisseur de l'empilement afin d'augmenter le couplage électromécanique du dispositif. La sensibilité à la température du concept et la réponse temporelle attendue ont pu ensuite être évaluées. L'étude a également mis en évidence certaines limites de la conception des capteurs, principalement liées à la défaillance du capteur à haute température.

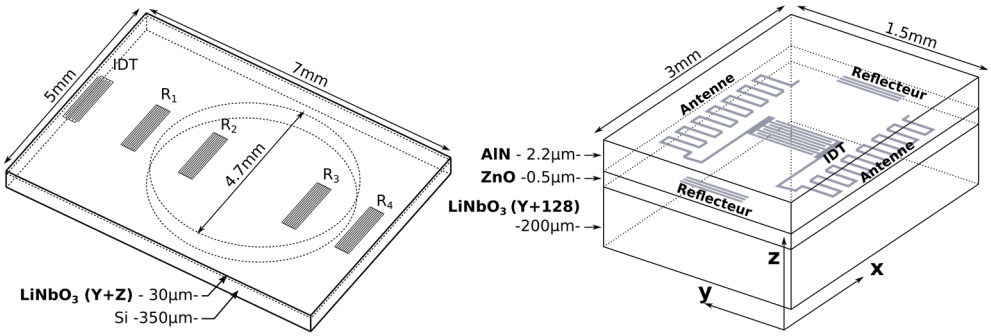

Figure iii Capteurs de pression intracrânienne et sans packaging.

La recherche sur les filtres micro-acoustiques pour la télécommunication est motivée par deux technologies en cours de développement, l'internet des objets (abrégé IoT pour *Internet of Things*) et la cinquième génération de télécommunication (5G). D'une part l'IoT a pour conséquence une augmentation du nombre d'objets connectés capables de communiquer les uns avec les autres ce qui aug-

mente la demande en filtres micro-acoustiques haute performance et plus économiques. D'autre part, la 5G fait appel à des nouveaux filtres ayant une bande passante plus large et travaillant à des fréquences plus élevées. Une idée prometteuse pour répondre à ces besoins consiste à utiliser des ondes de Lamb combinant les avantages des dispositifs sur couche mince piézoélectrique (technologie FBAR pour *Film Bulk Acoustic Wave Resonator*) et les avantages de la technologie SAW. La technologie sur couche mince permet d'utiliser des substrats de silicium de grande taille facilitant les économies d'échelle et d'augmenter la fréquence. De son côté, la technologie SAW permet de bénéficier de la souplesse de conception offerte par l'apodisation. Cependant, le Nitrure d'Aluminium (AlN), utilisé dans les applications FBAR, présente un faible coefficient de couplage piézoélectrique, ce qui aboutit à des filtres ayant une faible bande passante. Pour faire face à ce problème, il est possible de doper l'AlN avec une concentration élevée en Scandium afin d'améliorer ses propriétés piézoélectriques. Dans le chapitre 3, nous décrivons la conception de résonateurs à ondes de Lamb et de filtres en AlScN avec des concentrations de Scandium de 15% et 30%. Deux partenaires ont participé à ce projet ambitieux, l'Institut für Mikrosystemtechnik (IMTEK, Université de Fribourg, Allemagne) était responsable de la détermination des nouveaux paramètres de matériau et l'École Polytechnique Fédérale de Lausanne (EPFL, Suisse) était chargée de la fabrication des dispositifs. Les premiers prototypes de résonateurs à ondes de Lamb étaient des structures de type membranes suspendues, construites en AlScN avec une teneur en Scandium de 15%. La conception des prototypes a été fortement influencée par les contraintes de fabrication. Néanmoins, les simulations ont montré que les meilleures performances étaient obtenues avec des dispositifs dotés d'une électrode inférieure flottante en Platine d'épaisseur 50 nm, sur laquelle est déposé 1 µm d'AlScN. Les IDTs en Aluminium, permettant d'exciter les ondes, ont pour épaisseur 80 nm et pour longueurs d'ondes 6 µm et 8 µm. Ces résonateurs suspendus à ondes de Lamb présentaient un bon coefficient de couplage ($K^2 \approx 2{,}5\%$), supérieur aux valeurs rapportées dans la littérature. Cela montre que la réponse piézoélectrique de l'AlN est renforcée par le dopage au Scandium. Cependant, les facteurs de qualité obtenus pour ces structures sont relativement faibles (Q=300), ce qui résulte en un faible facteur de mérite ($FoM = K^2 \times Q = 7{,}5$). Sur la base des connaissances acquises avec ces premiers démonstrateurs, nous avons conçu une deuxième série de démonstrateurs pour des résonateurs à ondes de Lamb ayant une teneur en Scandium de 30%. Ces dispositifs ont été fabriqués sur des miroirs de Bragg qui permettent de maintenir l'énergie acoustique dans la couche piézoélectrique active (voir Figure iv). Deux miroirs différents ont été étudiés et fabriqués. Le premier miroir est en Tungstène (W) et en Oxyde de Silicium (SiO_2). Ces deux matériaux ont un rapport d'impédance acoustique élevée qui se traduit par une réflectivité élevée du miroir. Malheureusement, la couche de Tungstène étant conductrice, celle-ci doit être structurée afin d'éviter que les dispositifs soient couplés par couplage capacitif. Le second miroir composé d'AlN et de SiO_2 a un rapport d'impédances plus faible, mais plus facile à fabriquer car il n'implique pas de struc-

turation. Nous avons conçu deux prototypes de résonateurs ayant le même type de couche piézoélectrique et les mêmes types d'électrodes, mais des miroirs de Bragg différents. Les épaisseurs des couches composant le miroir de Bragg ont été optimisées dans les deux cas pour améliorer la réflectivité du miroir et ainsi augmenter le facteur de qualité. Le dispositif réalisé sur le miroir SiO_2/W présente un coefficient de couplage K^2=5,2% et un facteur de qualité Q=768 donnant un facteur de mérite FoM=38.6 (voir Figure iv), alors que le dispositif sur le miroir SiO_2/AlN présente un coefficient de couplage K^2=4,6% et un facteur de qualité Q=862, résultant en un facteur de mérite FoM=38.7. À notre connaissance, ces FoM sont les plus élevés de l'état de l'art. De plus, un bon accord a été trouvé entre la simulation et les résultats expérimentaux, ce qui confirme la bonne précision des paramètres matériaux utilisés.

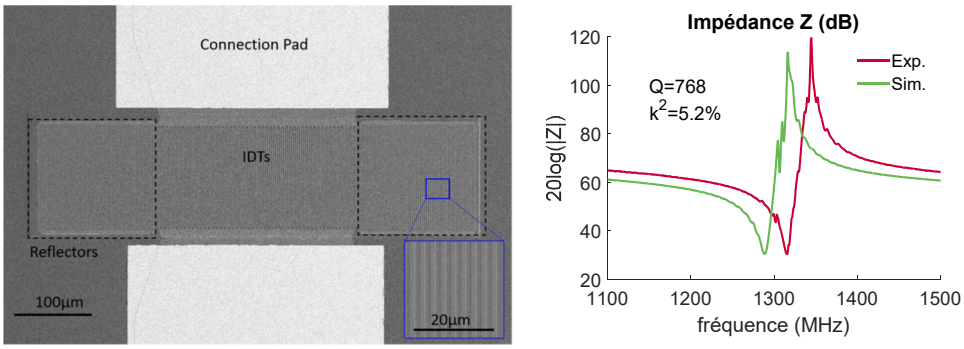

Figure iv Image SEM d'un résonateur sur miroir de Bragg. Impédances expérimentale et simulée du résonateur sur miroir de Bragg W/SiO_2

La caractérisation des dispositifs micro-acoustiques se fait généralement par mesure électrique (paramètres S_{ij}). Bien que cette méthode soit précise, elle n'offre aucune compréhension de leur comportement acoustique. Pour cette raison, les concepteurs des dispositifs micro-acoustiques utilisent, de manière complémentaire, des techniques optiques pour visualiser les déplacements de surface. Cependant, la future génération de filtres pour les applications 5G fonctionnera à des fréquences très élevées. À ces hautes fréquences, aucun dispositif n'est disponible dans le commerce pour visualiser les ondes acoustiques. Dans le chapitre 4, nous décrivons la conception et la mise en œuvre d'un dispositif de caractérisation ayant pour but de détecter des vibrations de hautes fréquences et de faibles amplitudes à la surface des dispositifs micro-acoustiques. La configuration optique choisie est un interféromètre hétérodyne. Ce dernier est constitué d'un faisceau de mesure réfléchit par le dispositif mesuré, et un faisceau de référence préservé de toute modification. L'interféromètre hétérodyne diffère de l'interféromètre de Michelson du fait du décalage en fréquence du faisceau de mesure par un modulateur acousto-optique (abrégé AOM pour *Acousto-Optic Modulator*). Par ailleurs, dans l´interféromètre hétérodyne, la surface vibrante module la phase du faisceau de mesure. Le signal d'interférence généré par la recombinaison des deux faisceaux est composé d'une modulation de battement oscillant à la fréquence de décalage et deux signaux ayant

la fréquence de la vibration plus ou moins la fréquence du décalage (voir Figure v). De plus, la différence d'amplitudes entre ces signaux est directement proportionnelle à l'amplitude de la vibration mécanique observée. Lors de la mise en œuvre optique, un soin particulier a été apporté au diamètre du spot laser reflété par la surface vibrante. En effet, ce dernier définit la résolution du dispositif dans le plan. Idéalement, le diamètre du spot doit être deux fois inférieur à la longueur d'onde acoustique que nous souhaitons détecter. Dans la configuration actuelle, un spot de diamètre de 1.4 µm a été obtenu, ce qui était suffisant pour observer une longueur d'onde de 2 µm. Par ailleurs, différentes sources d'instabilités ont été supprimées du montage optique ; la première table optique a été remplacée par une table amortie activement afin de réduire les perturbations de basses fréquences générées par l'environnement, et le laser initialement prévu a été remplacé par un laser stabilisé. Pour détecter les signaux interférométriques à hautes fréquences, une électronique sur mesure a été construite. Celle-ci est basée sur une démodulation I/Q qui génère un signal de fréquence intermédiaire en mélangeant le signal interférométrique avec une onde sinusoïdale pure provenant d'un oscillateur local. Le signal basse fréquence obtenu est ensuite échantillonné par un convertisseur analogique-numérique. L'amplitude de ce signal correspond à l'amplitude de la vibration observée. Afin de réduire le bruit de phase, les générateurs de fréquence présents dans le montage (oscillateur local, signal d'excitation du dispositif acoustique, AOM) partagent la même horloge de référence qui est le générateur de l'AOM. Avec la configuration actuelle, nous avons caractérisé des dispositifs FBAR et SAW ayant des fréquences de plus en plus élevées, avec une résolution en amplitude de l'ordre du picomètre (voir Figure v). En particulier, nous avons caractérisé un dispositif FBAR ayant une fréquence de résonance proche de 6 GHz. À notre connaissance, il s'agit de la fréquence de résonance la plus élevée caractérisée optiquement sur un dispositif micro-acoustique.

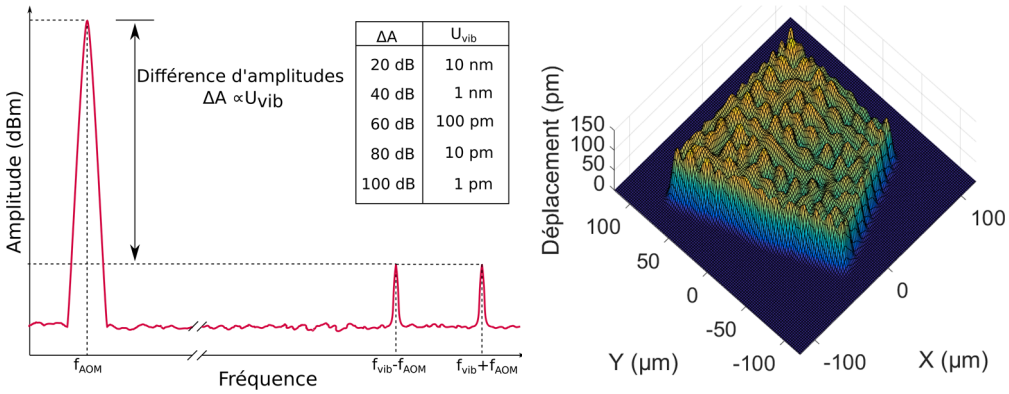

Figure v Interférences optiques observées dans le domaine fréquentiel. Exemple de caractérisation d'un FBAR à 1993MHz.

List of publications

Journal Articles (Articles à Comité de Lecture – ACL): 4

4. ACL published in 2019
Journal: Applied Physic Letters, vol. 114, art. n° 223103 (4 pages), 2019. DOI: 10.1063/1.5088892
Title: Free Standing and Solidly Mounted Lamb Wave Resonators based on $Al_{0.85}Sc_{0.15}N$ thin film
Authors: F. Parsapour, V. Pashchenko, **H. Chambon**, P. Nicolay, I. Bleyl, U. Roesler, and P. Muralt

3. ACL published in 2019:
Journal: Mechanics of Advanced Materials and Structures. DOI: 10.1080/15376494.2019.1579397.
Title: Package-less SAW RFID sensors for structural health monitoring applications. A concept study.
Authors: **H. Chambon**, P. Nicolay, C. Floer, A. Benjeddou

2. ACL published in 2018:
Journal: MDPI Sensors, vol. 18, p. 3482, 2018 (13 pages). DOI: 10.3390/s18103482 (Open Access)
Title: AlN/Si-based surface acoustic wave pressure sensor
Authors: P. Nicolay, **H. Chambon**, G. Bruckner, C. Gruber, S. Ballandras, E. Courjon, F. Bassignot, M. Stadler

1. ACL published in 2017:
Journal: International Journal of Smart and Nano Materials, vol. 8, n° 2-3, pp. 95-109, 2017
Title: Analysis of the sensitivity to pressure and temperature of a membrane-based SAW sensor.
Authors: **H. Chambon**, P. Nicolay, G. Bruckner and A. Benjeddou.

Proceedings Articles (Articles de Conférences Internationales avec Actes – ACTI): 6

6. ACTI
Conference: Conference IFCS-EFTF 2019
Place and date: 18-19 Avril 2019, Orlando, USA
Title: SAW RFID devices using connected IDTs as an alternative to conventional reflectors
Authors: C. Floer, S. Hage-Ali, O. Elmazria, P. Nicolay, **H. Chambon**, S. Zhgoon, A. Shvetsov

5. ACTI
Conference: 2018 IEEE International Ultrasonics Symposium
Place and date: 22-25 October 2018, Kobe (Japan)
Title: Glue-less and robust assembly method for SAW strain sensors
Authors: P. Nicolay, J. Bardong, **H. Chambon**, P. Dufilié

4. ACTI (Oral presentation in 2018):
Conference: 7th International Symposium on Aircraft Materials (ACMA 2018)
Place and date: 24-26 April 2018, Compiègne (France)
Title: Package-less SAW RFID sensors for structural health monitoring applications. A concept study.
Authors: **H. Chambon**, P. Nicolay, C. Floer, A. Benjeddou

3. ACTI:
Conference: 7th International Symposium on Aircraft Materials (ACMA 2018)
Place and date: 24-26 April 2018, Compiègne (France)
Title: SAW RFID sensors and devices for industrial applications, a short review.
Authors: P. Nicolay, **H. Chambon**, G. Bruckner

2. ACTI:
Conference: VIII ECCOMAS Thematic Conference on Smart Structures and Materials (SMART 2017)
Place and date: 5-8 juin 2017, Madrid (Spain)

Title: Simulation of the properties and behaviour of an implantable passive and wireless surface acoustic wave RFID tag, for structural health monitoring applications.
Authors: P. Nicolay, **H. Chambon**, G. Bruckner

1. ACTI:
Conference: VIII ECCOMAS Thematic Conference on Smart Structures and Materials (SMART 2017)
Place and date: 5-8 June 2017, Madrid (Spain)
Title: Finite element simulation of lithium niobate based surface acoustic delay line sensor for pressure and temperature sensing.
Authors: **H. Chambon**, P. Nicolay, G. Bruckner, A. Benjeddou

POSTERS: 4

4. POSTER, presented by posting and discussion in 2018:
Conference: 2018 IEEE International Ultrasonics Symposium
Place and date: 22-25 October2018, Kobe (Japan)
Title: High frequency optical probe for BAW/SAW devices
Authors: **H. Chambon**, P. Nicolay, T. Moldaschl, C. Humbert, A. A. Awan, M. Schiek, T. Metzger, A. Benjeddou

3. POSTER:
Conference: 2018 IEEE International Ultrasonics Symposium
Place and date: 22-25 October 2018, Kobe (Japan)
Title: Towards an AlScN-based packageless acoustic wave sensor with RFID capabilities, for applications above 350°C.
Authors: P. Nicolay, N. Naumenko, T. Aubert, **H. Chambon**

2. POSTER:
Conference: EUROSENSORS 2018
Place and date: 9-12 September 2018, Graz (Austria)
Title: Multilayered, package-less SAW Sensors: latest developments.
Authors: P. Nicolay, **H. Chambon**, G. Bruckner

1. POSTER, presented by posting and discussion in 2016:
Conference: SAW Symposium
Place and date: October 2016, Dresden (Germany)
Title: Investigation of a SAW temperature sensor with low longitudinal strain sensitivity.
Authors: **H. Chambon**, P. Nicolay, A. Binder, K. Shaposhnikov and M. Kaltenbacher

Oral Communications (COM): 1

1. COM (Oral presentation in 2018)
Conference: COMSOL day
Place and date: 27 June 2018, Graz (Austria)
Title: Modeling and simulation of Surface Acoustic Wave (SAW) strain sensors.
Authors: **H. Chambon**, P. Nicolay, T. Moldaschl

List of abbreviations and acronyms

(R)DL	(Reflective) Delay-Line
(T)FBAR	(Thin) Film Bulk Acoustic Resonator
5G	Fifth Generation of telecommunication
AGC	Automatic Gain Controller
AOM	Acousto-Optic Modulator
BAW	Bulk Acoustic Wave
BAW-SMR	Bulk Acoustic Wave Solidly Mounted Resonator
BEM	Boundary Element Method
CMOS	Complementary Metal Oxide Semiconductor
CMR	Contour Mode Resonator
COM	Coupling Of Modes
CTR	Carinthian Tech Research A.G.
DFT	Density Functional Theory
DoF	Degrees of Freedom
DUT	Device Under Test
EPFL	École Polytechnique Fédérale de Lausanne
FE(M)	Finite Element (Method)
FoM	Figure of Merit ($k^2 \times Q$)
FPD	Fast PhotoDiode
GPS	Global Positioning System
GSM	Global System for Mobile Communications
HF	High Frequency
ICP	IntraCranial Pressure
IDT	Inter Digital Transducer
IEF	Impedance Element Filter
IF	Intermediate Frequency
IMTEK	Institut für Mikrosystemtechnik
IoT	Internet of Things
ISM	Industrial, Scientific, Medical
LNA	Low Noise Amplifier
LO	Local Oscillator
LTE	Long Term Evolution
LWR	Lamb Wave Resonator
SM-LWR	Solidly Mounted Lamb Wave Resonator
NA	Numerical Aperture
PBS	Polarized Beam Splitter
PML	Perfectly Matched Layer
RF	Radio Frequency
RFID	Radio Frequency IDentification
SAW	Surface Acoustic Wave
SEM	Scanning Electron Microscope
SHM	Structural Health Monitoring
SMR	Solidly Mounted Resonator
SNR	Signal to Noise Ratio
TCD	Temperature Coefficient Delay
TCF	Temperature Coefficient Frequency
TEC	Thermal Expansion Coefficient
UMTS	Universal Mobile Telecommunications System
VIA	Vertical Interconnect Access
VNA	Vector Network Analyser
WORM	Write Once Read Many
FFT	Fast Fourier Transform

Chapter 1 Introduction

In this chapter, we introduce the Surface Acoustic Wave (SAW) device technology. First, we detail the constitutive elements of a SAW device, then we present the two major applications of SAW devices: filters and sensors. In the last part of the chapter, we explain the numerical method used in this manuscript to simulate the devices.

1.1 Principle of SAW device/generation of SAW

In 1885, Lord Rayleigh discovered the solution for Surface Acoustic Waves (SAW) [1]. A wave is a propagative perturbation within medium in equilibrium. When shifted from its equilibrium, the medium reacts to reach it again. An elastic (acoustic) perturbation travels through the medium with a determined velocity, defined by the material properties (stiffness and density). Acoustic waves can either propagate in the bulk of the medium (Bulk Acoustic Wave* -BAW-) or with their energy focused at the surface of it. The displacement associated to the perturbation can be longitudinal (same direction as the propagation), transverse (perpendicular to the propagation direction) or a combination of both which is the case for a Rayleigh type SAW, see Figure 1.1.

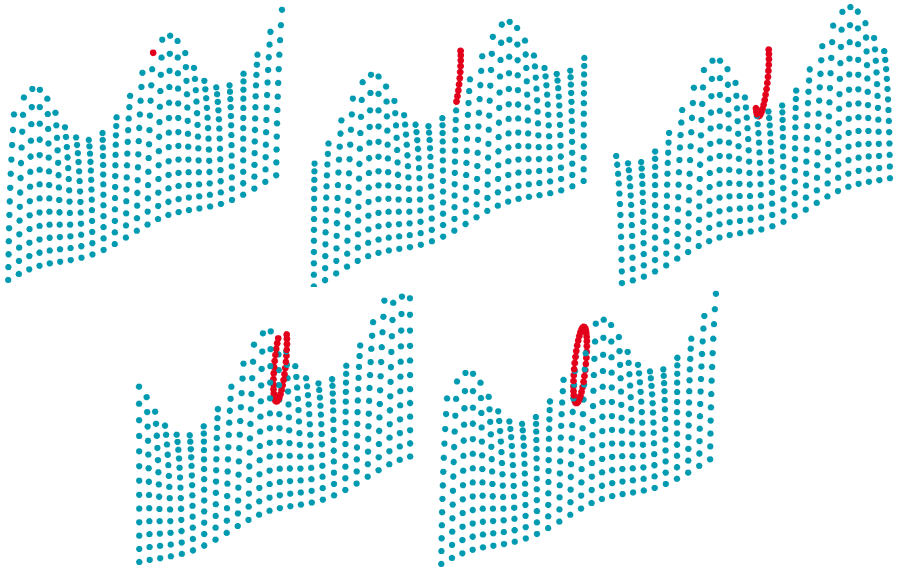

Figure 1.1 Animation of a Rayleigh acoustic mode. The wave has both longitudinal and transverse motions resulting in an elliptic movement when observing a single particle (red dots). The amplitude of the wave decreases exponentially in the depth of the medium. The properties of the medium determine the velocity of the wave.

* The bulk acoustic wave devices are out of the scope of this introduction to SAW. Nevertheless, some explanations about these devices can be found in Appendix A

The general complex displacement vector of a particle is given by the following equation (1.1):

$$\vec{u} = \overrightarrow{U_0}\, e^{-\alpha z/\lambda} e^{j2\pi f\left(t-\frac{x}{v}\right)} \quad 1.1$$

Where, x is the direction of the propagation, z is perpendicular to the substrate surface, α is the decay coefficient in the depth of the substrate, v is the wave propagation velocity, f is the frequency and λ its wavelength. In Table 1.1, we give the SAW velocities for some often-used substrates.

Substrate material	Crystal orientation	Velocity (m/s)	TCF (ppm/°C)	K^2 (%)
$LiNbO_3$	Y+128° X	3992	75	5.3
$LiNbO_3$	Y Z	3488	94	4.8
Quartz	ST-X	3158	0*	0.16
AlN	C-axis	5760		0.47
$LiTaO_3$	Y-Z	3230	38	0.9

Table 1.1 Velocity, temperature sensitivity and electromechanical coupling coefficient for common piezoelectric materials used in SAW. The values are extracted from [2], the AlN velocity and coupling coefficient are from [3]. (*At room temperature)

In 1880, Pierre and Jacques Curie discovered the piezoelectric effect [4]. A material with piezoelectric properties creates an electrical field when it is deformed (that is called the direct piezoelectric effect). Inversely, the material is deformed by applying an electrical field (that is the inverse piezoelectric effect), see Figure 1.2. This means that a piezoelectric material can be used as an electromechanical transducer in order to both generate and detect acoustic waves. SAW devices may be produced from piezoelectric materials such as Quartz (SiO_2), Lithium Niobate ($LiNbO_3$), Zinc Oxide (ZnO) and Lithium Tantalate ($LiTaO_3$) that are available in single crystal wafer form. However, the wafer size for such material is limited to 6-inch. Aluminium Nitride (AlN) is another piezoelectric material used to fabricate SAW. This material is not present in a wafer form but can be deposited using thin film technologies. An epitaxial layer of AlN can be grown on a substrate by sputtering of Aluminium in a Nitrogen plasma. A more complete list of materials used in SAW devices and their characteristics can be found in [5].

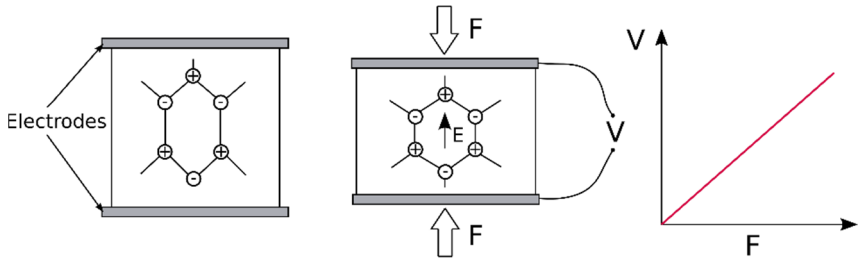

Figure 1.2 Principle of the piezoelectric effect. The application of a force on the medium generates strain and stress fields in the material which result in an electric field (direct piezoelectric effect) that creates a potential difference between the two electrodes.

In 1965, White and Voltmer introduced the Inter Digital Transducer (IDT) [6]. They designed comb-shaped electrodes that make possible to specifically generate

and pick-up SAWs at the surface of a piezoelectric medium, see Figure 1.3. These transducers are composed of fingers (also called digits) periodically spaced and connected to bus bars. The overlap between the two combs of the IDT is called the aperture. The bus bars are connected to an electrical radio-frequency source in order to generate waves or to a receiver to detect the waves. The IDT selectively generates SAW with a wavelength corresponding to the spacing between fingers. The generated acoustic energy is sent in two directions (±x). The velocity of the generated waves depends on the substrate material and the kind of waves generated. The velocity is derived from the material properties. Its computation is tedious due to the piezoelectric and anisotropic nature of the material used. In particular two specific velocities can be computed: v_{free} is the so-called "free-velocity" which corresponds to the velocity of the wave computed on a surface electrically free of charge and v_{metal} is the so-called "metalized-velocity", which is the velocity of the wave obtained on an electrically shorted (grounded) surface by an ideally thin metallic layer. These two velocities enable to define the electromechanical coupling coefficient (K^2), see equation (1.2).

$$K^2 = 2\frac{v_{free} - v_{metal}}{v_{free}} \qquad 1.2$$

The free-velocity and the electromechanical coupling coefficient are characteristic parameters that are often reported in the literature [7]. The typical SAW free-velocity is around 4000m/s for the piezoelectric material considered to generate SAW. In Table 1.1, we give the velocities and electromechanical coupling coefficients for some often-used substrates. The frequency of the wave changes with the pitch of the IDT electrodes.

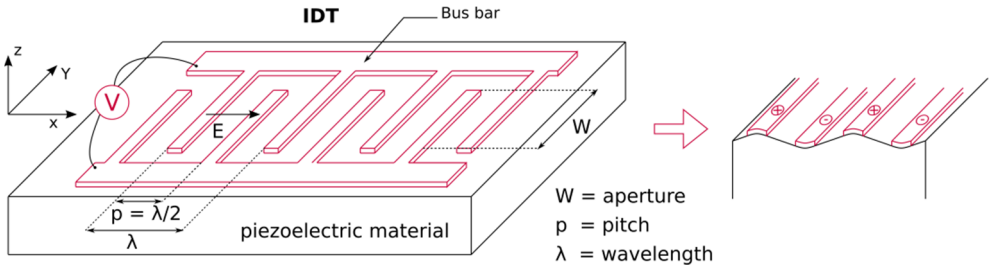

Figure 1.3 Schematic of an IDT. The spacing periodicity between the fingers defines the wavelength. By applying a potential difference between the two electrodes, an electric field is created within the piezoelectric material. The latter will generate a deformation that will propagate on the substrate.

The IDTs are often made from thin metal layers of Aluminium, Platinum, Copper or Molybdenum. The constitutive material of the IDT affects the behaviour of the wave depending on its density and stiffness. Today, these IDTs are manufactured at low cost and in great number using photolithographic processes similar to those employed in the microelectronics industry. The metallic thin film is deposited by sputtering on a piezoelectric substrate and the IDTs are structured through lift-off or etching processes. The photolithographic process limits the maximum reachable frequency. Indeed, the current ultraviolet-technology, used to pattern the IDT,

limits the finger width to approximately 300 nm, thus limiting the wavelength to 1.2 µm and therefore the frequency to 2.5 GHz. IDT based SAW devices are now widely used; they are well known for their low cost, small size and reliability.

1.2 SAW devices applications

Surface acoustic wave devices come in two different layouts: the delay-line and the resonator, see Figure 1.4. The delay-line takes advantage of the slow velocity (in comparison to the velocity of light) of the SAW to generate large delays within a compact design. The simplest layout consists of two IDTs facing one another. The gap between the two IDTs defines the time delay generated by the line. Two acoustic absorbers are deposited at both ends of the acoustic path. On the left side the acoustic absorber damps the waves emitted by the input IDT towards the left, while on the right, the absorber avoids the reflection of the waves on the edge of the substrate. Those delay-lines found their first applications in Radar systems [8].

The one-port resonator is the simplest resonator layout. It consists of an IDT accompanied by two Bragg reflectors on each side. In order to reflect waves with a wavelength λ, the reflectors have a large number of fingers with a pitch of $\lambda/2$, all set at the same electric potential. These reflectors reflect the acoustic waves toward the input IDT. The reflected acoustic waves interact constructively or destructively with the wave emitted by the IDT depending on the frequency.

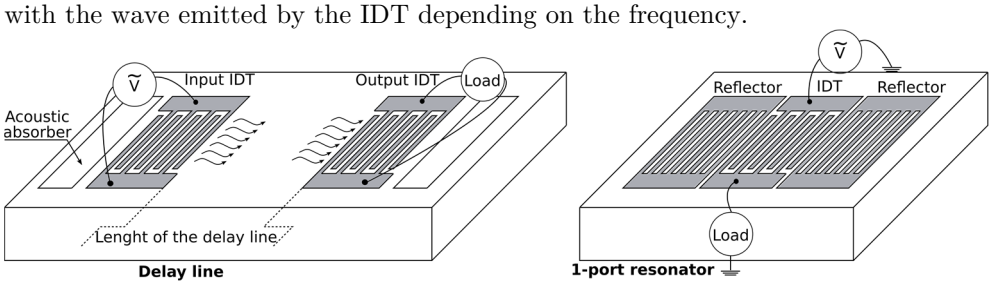

Figure 1.4 Schematic of a delay-line (Left) and a resonator(Right).

1.2.1 SAW Filters

In general, a filter must receive and transmit an electromagnetic signal located within a certain bandwidth spread around a given centre frequency and rejects the other signals.

Delay-line filter:

Based on the SAW delay-line principle, it is possible to create complex filter functions. Indeed, the frequency characteristic of the filter can be designed at convenience by playing with the overlap between fingers within the IDTs that is called apodization. This concept is easier to understand when considering the impulse response of a delay-line as pictured in Figure 1.5, adapted from [9].

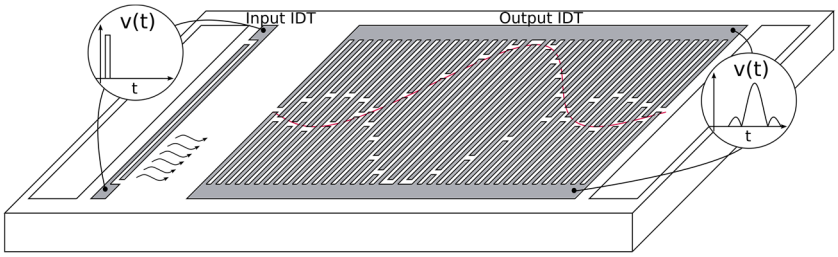

Figure 1.5 Delay-line with an apodized output IDT. The overlap between the fingers within the output IDT has the form of a sinc function symmetrized along the propagation direction. Hence the impulse response of the delay-line is an absolute value of this sinc function.

We assume that the number of fingers in the input IDT on the left side is small enough so that, in response to an electrical pulse, it will generate a corresponding SAW pulse. When travelling across the output IDT, this SAW pulse will generate a voltage proportional to the overlap between the fingers. By using the corresponding apodization, it is theoretically possible to obtain any impulse response at the output. While the impulse response in time domain corresponds to the absolute value of the apodized IDT, the filter function in frequency domain is its Fourier transform function. In the example in Figure 1.5, the output IDT apodization has the form of a cardinal sine function. Therefore, the time response of the delay-line is a sinc function. In the frequency domain, this means that the delay-line is equivalent to a rectangle or bandpass filter, see Figure 1.6.

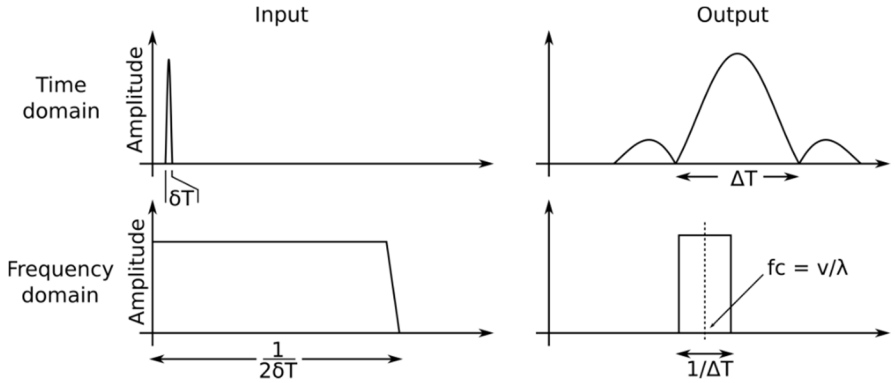

Figure 1.6 Frequency response of the apodized delay-line. The function represented here is an idealized bandpass (rectangle) function. In practice, the response will be affected by the finite length of the sinc apodization of the output IDT and the number of fingers in the input IDT.

Resonators-based filter:

The SAW resonators are the building blocks of Impedance Element Filter (IEF). A simple 1-port resonator has the electrical response of an RLC circuit with an added capacitance in parallel. This model, presented in Figure 1.7, is called the Butterworth-van Dyke equivalent circuit. In this model, the capacitance C_m and inductance L_m are called motional components. They are related to the acoustic behaviour of the SAW. The parallel capacitance C_0 is related to the transducer

capacitance and the resistor R materializes the losses in the resonator. The electrical characteristic of the resonator exhibits a resonance having a low impedance value and an anti-resonance frequency having a high impedance, see the frequency characteristic in Figure 1.7. By mounting two resonators in a ladder layout [10], where the resonance of the serial resonator (red) matches the anti-resonance of the parallel one (blue), it is possible to achieve a bandpass filter centred on the resonance frequency of the series resonator. The scattering parameter* curve of the resulting filter (Figure 1.8) shows a passband having high S_{12} values. At the centre of the passband, the series resonator is at its lowest impedance, whereas, the parallel resonator is at its highest impedance. Therefore, the input electrical signal passes through the filter without being short-circuited by the parallel resonator. The width of the passband is directly related to the distance between resonance and anti-resonance frequencies. The filter depicted in Figure 1.8, for the sake of comprehension, would be considered as badly designed. A well-designed filter would have better defined passband edges and a larger and flatter passband. Based on the same principle, more complex filters having a substantial number of resonators are designed.

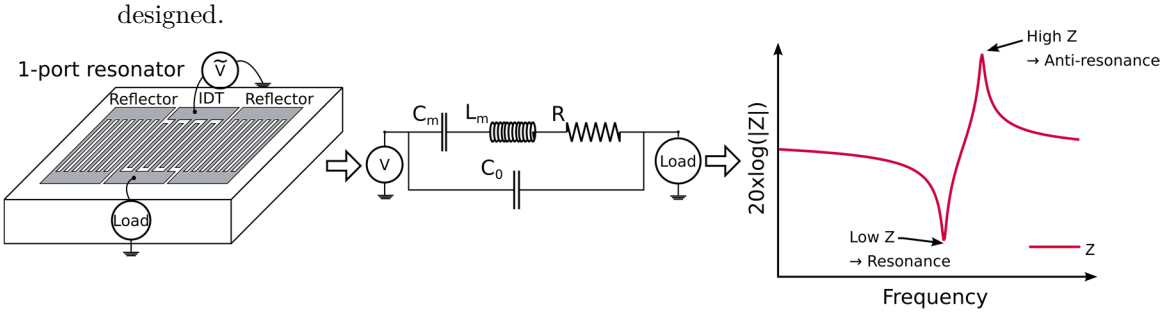

Figure 1.7 A 1-port resonator, its equivalent electric model, and impedance characteristic . The simulation of the equivalent circuit gives the impedance characteristics of the individual filters. By slightly changing the motional components in the model, it is possible to have two resonators with corresponding resonance and anti-resonance frequencies. We obtained the impedance curve from the modified Butterworth-van Dyke model in [11].

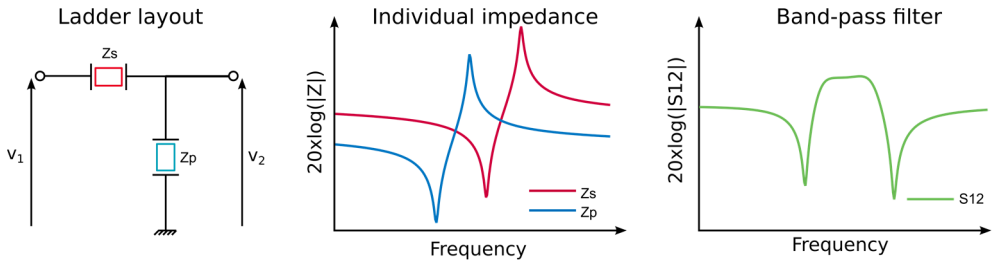

Figure 1.8 Working principle of a simple ladder-type filter.(Left) Schematic of a 2-resonator ladder filter. (Middle) Impedance characteristics of the individual resonators. (Right) Scattering parameter (S12) of the resulting filter. The latter exhibits small ripples in the passband that attest an imperfect matching between the resonance and anti-resonance of the resonators.

* The scattering parameter (S_{ij}) describes the electrical behaviour of a linear electrical network between the ports i and j in terms of reflected power (i=j) or transmitted power (i≠j).

When considering SAW resonators, the electromechanical coupling coefficient K^2 is related to the distance between the resonance and anti-resonance frequencies and, therefore, to the achievable filter bandwidth. The quality factor of the resonator corresponds to the sharpness of the admittance resonance peak. One of the definitions considers the quality factor as being the 3 dB bandwidth of the resonance peak over the resonance frequency:

$$Q = \frac{\Delta f_{3dB}}{f_r} \quad 1.3$$

The electromechanical coupling coefficient and the quality factor are among the most important parameters that define a resonator. Consequently, a Figure of Merit (FoM) is often used to describe the performance of a resonator:

$$FoM = Q \times K^2 \quad 1.4$$

Filter electrical frequency characteristic:

A generic SAW bandpass filter characteristic is given in Figure 1.9. The filter is characterized using the scattering parameter S_{12} obtained experimentally from a Vector Network Analyser (VNA) for instance. The requirements and tolerances are often specified using a mask made from rectangle areas delimiting the filter frequency response which should stay within the white area. Typically, an ideal bandpass filter should have low insertion losses within the passband, steep slopes for the passband skirts, high stopband attenuation and low ripples. The filters requirements show rather large tolerances, because the frequency characteristics are likely to shift with temperature changes. Indeed, for most of the piezoelectric materials and their crystal orientations (referred as "cuts"), the SAW velocities and hence the filter responses are temperature dependent. An increase in temperature tends to decrease the substrate velocity and, therefore, shifts the filter characteristic towards the lower frequencies. This feature, while regarded as a drawback in the filter industry, is used advantageously to develop SAW based temperature sensors. The Temperature Coefficient of Frequency (TCF) is a measure of the resonant frequency shift due to temperature. It is often given in part-per-million per degree Celsius (ppm/°C). Typical TCF of piezoelectric materials are presented in Table 1.1.

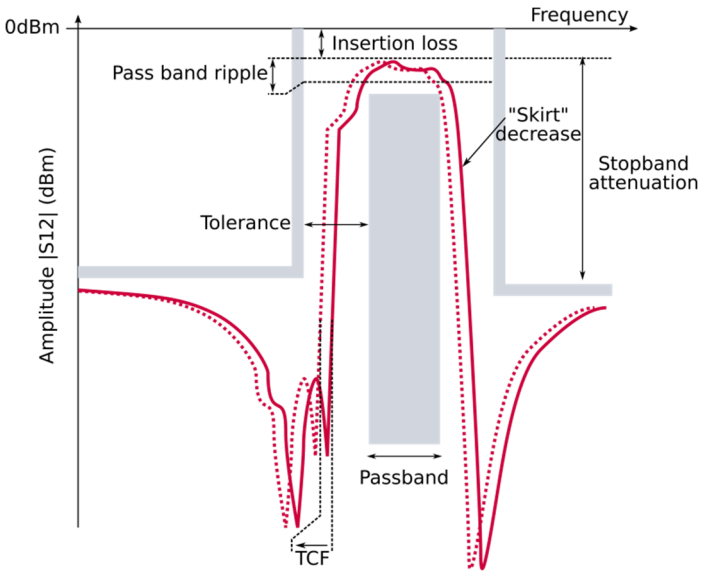

Figure 1.9 Frequency characterization of a SAW bandpass filter. The dashed line represents the characteristic of the filter after an increase in temperature.

Filtering applications:

The main application field of SAW devices is the production of high frequency filters [12]. These filters are used in mobile, military and automotive industries. They are extensively used in cellular phones where they benefit from their small size and low cost. The phone market alone represents today more than 7 billions of active units and it [12]. One of the essential components of a phone is the RF front-end that filters the many electromagnetic signals needed to its operation. It is built using tens of micro-acoustic filters, duplexers or multiplexers based on BAW and SAW technologies. Together, these technologies can cover frequencies ranging from 500 MHz to 3 GHz.

As an example, Figure 1.10 illustrates a simplified receiver-transmitter circuitry required after the main phone antenna to detect one of the GSM bands (the detailed architecture of a receiver is out of scope). The principle of the receiver is to convert down the incoming signal by mixing it with a high frequency signal provided by a phase-locked loop frequency synthesizer. The product of the mixing is a low frequency signal called Intermediate Frequency (IF) carrying the original information. On the other hand, the transmitter modulates an IF signal with a synthesizer and sends the latter to the antenna. In this circuitry, SAW devices are present in the form of a duplexer (R1+T2). The latter is a three-port device of which one port is connected to the antenna, while the two others are connected to a receiver and a transmitter. The duplexer enables simultaneous sending and receiving of signals through a unique antenna. For this purpose, the filter R1 must have low insertion loss to transmit signals with low amplitudes, while, the filter T2 must sustain high-power input. Additional SAW filters are present in the form of bandpass filters (R2, R3 and T1). In a modern mobile phone, such circuits are used for telecommunication purposes (GSM, UMTS, LTE) and for data transfer (Blue-

tooth, Wi-Fi). Additional receivers are also present to detect GPS signals. An extensive review of receiver architecture can be found in [13].

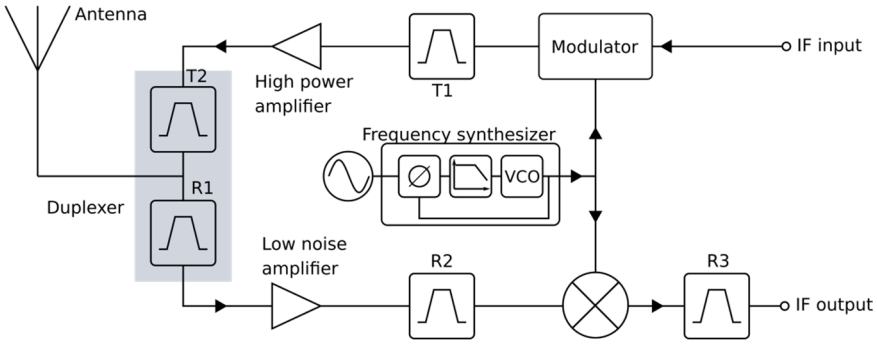

Figure 1.10 Simplified circuit of the receiver/transmitter in a mobile phone for GSM signal (adapted from [7]).

These mature existing technologies need constant innovation to meet the increasingly demanding requirements of the customers. For example, recently the 4G standard has evolved towards the LTE (Long Term Evolution) one in order to offer increased network capacity and speed to the end users. Furthermore, lower insertion loss, wider passband, smaller footprint and height, more reliable and more cost-efficient devices are always required. To answer these challenges, the manufacturers recently developed and improved innovative technologies. For instance, temperature compensated SAW resonators were developed to improve the selectivity of the duplexers without degrading the electromechanical coupling coefficient [14]–[16]. In parallel, advanced manufacturing methods using high resolution lithography and innovative packaging solutions helped to meet these continuously more demanding requirements.

Upcoming filters:

Now, two new challenges are coming and motivate the research in micro-acoustic technologies. On one hand, the fifth generation of telecommunication (5G) is arriving for which higher frequencies (in the range between 3.5 GHz and 6 GHz) are required in order to reach higher data rates. Acoustic devices could play a significant role in the 5G if they meet these specifications. On the other hand, with the emergence of the Internet of Things (IoT), the number of connected devices capable of communication will increase significantly, which will increase the demand for more cost efficient and reliable acoustic filters.

Unfortunately, the current SAW technology has limitations with respect to high frequency applications. As explained, the SAW frequency is proportional to the substrate velocity and inversely proportional to the wavelength defined by the pitch between fingers within the IDT. The ultraviolet-lithographic process used today to produce the IDTs limits the minimum pitch and so, the maximum SAW frequency to less than 2.5 GHz. Improving the lithographic process to pattern IDTs with a smaller pitch is a tedious task that leads to manufacture expensive devices.

Furthermore, reducing the size of the devices also generates an increase in the acoustic energy density per unit area. This higher energy density, when not properly dissipated, increases the temperature of the devices which then behaves non-linearly. (Note that, $LiNbO_3$ and $LiTaO_3$, which are preferred materials to develop SAW devices, have a poor thermal conductivity which limits their capability to dissipate heat). Consequently, the most promising way is to develop substrates with higher acoustic velocity that may reduce the constraints on the lithography. In addition to this, $LiNbO_3$ and $LiTaO_3$ substrates are limited in size (Ø<150 mm) which inevitably limits the maximum number of devices that can be produced on a single wafer. It is therefore helpful to have a technology which allows using larger substrates. To overcome some of these limitations, diamond-based SAW structures were introduced [17]. Indeed, diamond has a high wave velocity (≈11000 m/s) enabling to design high frequency filters. It also has the advantage of having a high thermal conduction coefficient for efficient heat dissipation. However, diamond is not a piezoelectric material, so the substrate is made active by the deposition of an AlN layer. Unfortunately, the resulting stack exhibits a poor electromechanical coupling coefficient and the price of the resulting devices might be an obstacle to their transfer to the market.

On the other hand, Film Bulk Acoustic Resonator (FBAR, see Appendix A) are devices consisting of a piezoelectric material such as AlN sandwiched between electrodes that generates BAW. The device is generally built on a Silicon substrate from which it must be acoustically isolated. FBAR technology has several advantages compared to SAW technology. First, the Silicon substrates have a high thermal conductivity, and are therefore, suitable for high power applications. In addition, AlN can be deposited on Silicon wafers as large as 300 mm in diameter, which allows a significant economy. Finally, the high acoustic velocity of BAW in AlN enables to reach frequencies up to 6 GHz. Today, FBAR technology is more suitable for high frequency applications than SAW. However, in order to acoustically isolate FBARs, it is necessary to manufacture complex free-standing membrane, or multi-layered substrates. In addition, FBAR does not offer flexible design capability such as the lateral design offered by SAW*. Furthermore, AlN has also a low electromechanical coupling coefficient compared to that of the materials used in SAW devices (see Table 1.1) thus limiting the maximum bandwidth.

To summarize, the design of resonators and filters for the 5G would be preferably done using devices offering apodization capability like that offered by the IDT of SAW devices, but exploiting substrates having advanced material properties (high velocity, high coupling, high thermal conduction, low TCF). In **Chapter 3**, we investigate a solution to answer this challenge. We propose to combine the thin film technology (similar to FBAR) and the SAW technology. We use a thin piezoelectric film made of Scandium doped AlN within which we generate Lamb waves using IDT-like electrodes. The piezoelectric film is acoustically isolated from the

* SAW filters benefit from advanced apodization capabilities.

Silicon substrate by means of a multi-layered structure. The active material is doped to enhance the weak piezoelectric coupling of AlN. The latter may be deposited on large wafers. The high velocity of the Lamb waves within this material enables to achieve an equivalent SAW resonant frequency with an increased pitch within the IDT. Therefore, we ease the constraint on the lithographic process. In order to design this new multi-layered structure, advanced simulation tools are required. We detail hereafter in section 1.3.2 of **Chapter 1,** the simulation method that we use**.**

Moreover, high-frequency devices need dedicated characterization tools to visualize the surface waves. While tools are commercially available, none of them is suitable for the high-frequency range imposed by the 5G. Therefore, in **Chapter 4**, we report on the development of an optical tool based on heterodyne interferometry to characterise micro-acoustic devices operating at very high frequencies.

1.2.2 SAW Sensors

SAW sensors use the mechanical waves they generate to sense a quantity (called the measurand) in their environment [18]. The measurand is observed as a change in phase, amplitude or frequency of the signal generated by the sensor. Whatever the nature of this change, it must be compared to a reference signal to have an absolute measure of the measurand.

SAW sensors are sensitive to quantities that affect the wave velocity. The sensitivity changes with the substrate material and the crystal orientation used to design the sensor. The most predominant effects are those of temperature, mass, strain or stress and voltage. As we have already seen, when the temperature of the SAW device increases, the propagation velocity of the wave shifts. An increase of the temperature tends to soften the material constants of the piezoelectric substrate and, thus, the wave velocity. A mass load on the surface will also reduce the wave velocity. A strain field has different effects; on one hand, it changes the material constants, and on the other hand, it generates a stress field that also affects the velocity. Finally, a voltage affects the velocity by generating strain and stress at the surface of the material through the piezoelectric effect. The order of magnitude for the different measurands are reported in Table 1.2. We find that temperature and mass changes have predominant effects. Their detection is therefore easier. On the other hand, their effect will have to be compensated if one wishes to measure another quantity.

Measurand	Sensitivity
Temperature	100 ppm/K
Mass	30 ppm/g.cm^2
Strain	1 ppm/micro-strain
Voltage	1 ppm/V

Table 1.2 Sensitivity of SAW to different physical phenomena, from [19] (see also [20]).

As their filter counterparts, SAW sensors are small; they are manufactured using the same fabrication processes and they are reliable/robust devices, since they

are simply made of a piezoelectric substrate with a thin metallic layer on the top. In addition, a great advantage of the SAW sensors is their ability to be interrogated wirelessly and passively. To do so, an electromagnetic interrogation signal is sent towards the sensor antenna from a short distance (in the order of few meters). The SAW device converts this signal via an IDT into mechanical waves that are, first, affected by their environment, and then sent back via an antenna. This operation is performed without the need for power supply or embedded electronics at the sensor element. The robustness and wireless capability of SAW sensors make them suitable for harsh environment conditions. They are also nonprogrammable WORM (Write Once Read Many) devices. However, this feature can be seen as an advantage for security but also as a drawback for the versatility of these devices.

To take advantage of the wave velocity sensitivity, SAW sensors use the same two layouts as the filters to take advantage of the sensitivity of the wave velocity. For the sake of understanding, the interrogation techniques for the resonator and delay-line sensor mentioned below are simplified and the inner functioning of the interrogation hardware (referred as "reader") is not detailed. A review of the SAW sensors interrogation techniques and associated reader architecture can be found in [21].

Resonator-based sensors

The resonant frequency of a resonator-based sensor changes due to a change in the measurand. The interrogation of a resonator sensor is typically done by first sending a continuous wave excitation signal with a frequency close to the theoretical resonant frequency in order to charge the resonator. Then, the electrical signal is converted into mechanical energy taking the form of standing waves. Next, the excitation signal is quickly switched off, and the stored mechanical energy is converted back into an electrical signal and sent via the antenna. The reader acquires the ring-down of the resonator and detects the change in the frequency, which is proportional to the effect of the measurand. See Figure 1.11.

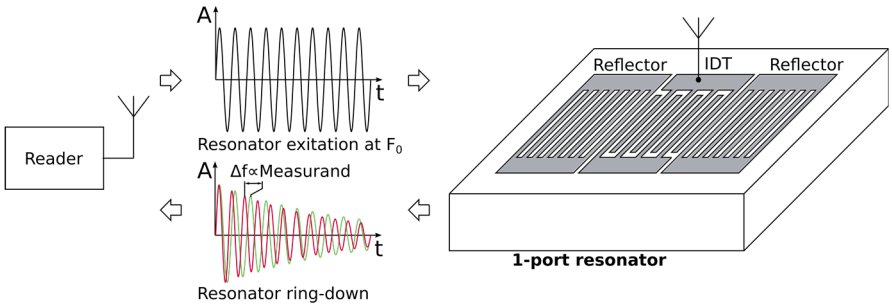

Figure 1.11 Interrogation of a 1-port resonator-based SAW sensor. The red curve corresponds to the ring-down observed when the measurand is zero. The green curve corresponds to a signal detected when a measurand influences the response.

A resonator-based SAW sensor has a high-quality factor that results in sharp peaks in the frequency domain. The reader needs a high resolution in frequency, which determines the resolution of the sensing. The sensor can be very small and

allows point-like measurements. However, this sensor layout has also some drawbacks. For instance, multiple resonators (a least two sensors) must be installed in order to realize a differential measurement. Additionally, too large temperature changes may shift the sensor frequency out of the available frequency band.

Delay-line based sensors

A Delay-Line (DL) based sensor shows a change in phase due to a change of the measurand. It can be interrogated using radar-like interrogation principles, see Figure 1.12. Typically, the reader sends a pulse to the sensor antenna, then the input IDT converts the latter into a mechanical wave. Next, the wave travels along the acoustic path of the device towards the output IDT. Here, the wave is converted back into an electrical signal and sent via the antenna. The time required by the sensor to send a response peak ($t_1 - t_0$) is the sensor delay. The latter will change ($\Delta t = t_2 - t_1$) due to a measurand affecting the wave velocity. The sensitivity of such a sensor (*i.e.*, the amount of delay it produces for a given measurand change) is directly proportional to the length of the DL. However, the acoustic losses and the electromechanical coupling coefficient of the substrate material limit the length and size of the DL.

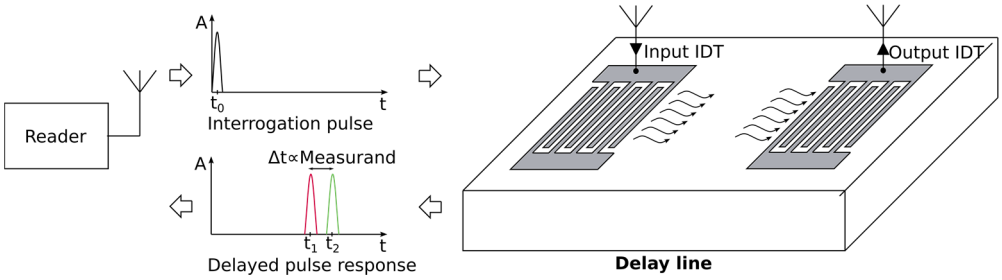

Figure 1.12 Interrogation of a delay-line based SAW sensor. The red peak is observed when the measurand is zero. The green peak is delayed due to a change of the measurand.

Reflective Delay-Lines (RDL) are often used in place of delay-lines, see Figure 1.13. A RDL has the advantage of having a single antenna and IDT that are responsible for receiving and transmitting the signals. Acoustic reflectors are used to send back part of the mechanical energy towards the IDT. By changing the position and number of reflectors, it is possible to obtain a series of peaks which is unique to the sensor. Consequently, it is possible to have an identification of the sensors. This is called pulse position encoding in time domain.

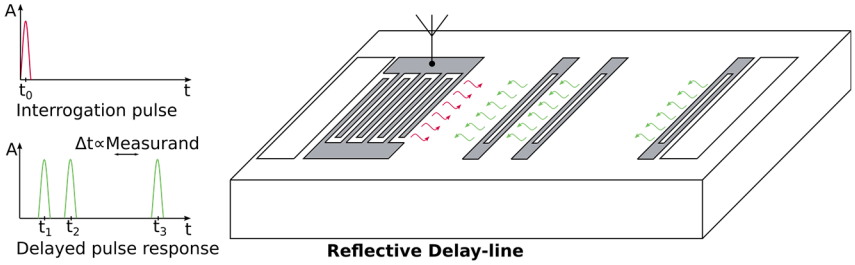

Figure 1.13 Interrogation of a reflective delay-line based SAW sensor.

A delay-line based sensor is a wide frequency band device which has sharp peaks in the time domain. It is possible to make differential measurements on a single sensor by splitting the acoustic path in several sections with reflectors. The effect of temperature on the frequency response is small compared to the total bandwidth; consequently, it is possible to measure high temperature changes while having a large number of sensors to interrogate. However, SAW delay-lines are relatively long (>4 mm) compared to resonators and they cannot be considered as point-like measurements. Finally, sophisticated phase tracking readings are required to have high resolution measurements.

In Figure 1.14, we present picture of the interrogation reader as well as sensors developed by the CTR.

Figure 1.14 Pictures of the sensors developed at CTR. From left to right are presented, a reader, a packaged SAW sensor with its antenna, the same sensor with its package opened and a sensor chip. The reader was developed at CTR; it is meant to interrogate SAW delay-lines working in the ISM band at 2.45GHz. The interrogation principle is based on the Frequency Sweep of Continuous Waves (FSCW).

Wireless interrogation and identification

When interrogating a sensor wirelessly, the frequency should lay in one of the Industrial, Scientific, Medical (ISM) bands. These radio bands have a relatively narrow band and are limited in power which makes interrogation from far distances more difficult. The limitation of the power of the enquiring signal implies that the electromechanical coupling coefficient of the piezoelectric medium is of tremendous importance when considering wireless interrogation. Furthermore, the SAW sensor must be connected to an antenna. Generally, the size of the antenna shrinks with the frequency, contrary to the antenna gain and reading distance which increase with the antenna size. As a general example, when working in the ISM band centred at 2.45 GHz, the available bandwidth is 80 MHz, the allowed maximum power that can be sent is 10 mW and the sensor monopole antenna is generally 3 cm long.

During a wireless interrogation of SAW, all the sensors inside the domain covered by the interrogation antenna are answering simultaneously. Consequently, it is possible to have overlaps between the sensor responses. These overlaps are manageable when the number of sensors is low but become difficult to address when more sensors are involved. Consequently, attention must be paid to the reader antenna directivity when having a great number of wireless devices in a confined space.

The identification of sensors based on a resonator layout is possible by having different central frequencies for each resonator. In this case, the working frequen-

cies should stay in the considered ISM bandwidth but should not overlap one another when a change of the measurand is happening. This limits the maximum number of identified sensors to a relatively low number (typically less than ten).

The number of identification codes generated by the pulse encoding method limits the number of sensors that is possible to identify. The maximum number of reflectors that one can place on the acoustic path of a RDL depends on the length of the delay-line and the width of the generated peaks that should not overlap in the time domain. To ensure a high enough reflected signal, the number of reflectors is limited to 20. If we consider that two reflectors are used to detect a measurand, the number of reflectors dedicated to identification is reduced to 18. Considering all possible code combinations, the number of identifications is higher than 10^{10} [22]. Therefore, SAW reflective delay-lines are often used for identification and referred as ID-tags [23].

Temperature sensing

As shown by Table 1.2, the sensitivity of SAW devices to temperature is greater than the other effects. Consequently, temperature is the simplest effect to measure using SAW sensors. Nevertheless, this sensitivity is highly dependent on the piezoelectric substrate and crystal orientation selected, see Table 1.1. Therefore, the crystal should be selected carefully to ensure a maximal sensitivity to temperature.

Thanks to their robustness and wireless communication capability, SAW sensors are particularly suitable for high temperature applications. For instance, Binder *et al.* [24] used a SAW RDL sensor for temperature measurement up to 250 °C of a high speed, high voltage induction motor. In [25], Bernauer *et al.* developed a SAW temperature sensor for the surveillance of overhead power lines. The sensors could be read wirelessly from a distance of 15 m with a resolution of 0.02 K.

The maximum operating temperature of SAW sensors depends on their constitutive materials. For instance, Aluminium electrodes can be used for temperatures up to 300 °C. For higher temperatures, other materials should be considered such as Platinum (Pt) or Iridium (Ir). However, the latter are heavy and tend to reduce the SAW velocity which makes more difficult the realization of sensors operating in the ISM band that is centred at 2.45 GHz. Indeed, at these high frequencies, it becomes more difficult to reduce the wavelength in order to compensate for the loss in velocity. In addition, the linear approximation of the TCF does not hold anymore at high temperatures, rendering the detection more difficult [26]. $LiNbO_3$ and $LiTaO_3$ are the materials that hold the linear approximation at the highest temperature and have a relatively high TCF, that is why they are the preferred material to design temperature sensors.

Stress and strain sensing

When considering stress measurement, it is important to take the temperature into account. Because of the high sensitivity of SAWs to temperature compared to the other effects, temperature can be a major parasitic effect. A conventional solution

to suppress the latter unwanted effect is to use two sensors, where one is dedicated to temperature measurements and the other is devoted to the desired phenomenon. The readings from the temperature sensor are then used to compensate the result from the actual sensor. The method was employed by Buff *et al.* [27] to develop a wireless pressure and temperature sensor based on two SAW resonators. The sensor is a quartz membrane that integrates the SAW resonators which is deformed under pressure (up to 10 bar). Similarly, Binder *et al.* [28] developed a pressure sensor based on differential measurement using a single RDL chip with identification and temperature compensation integrated. Here, the pressure (tested up to 7 bar) causes a stainless-steel membrane to deflect and a ball transfers the load to the sensitive chip.

The parasitic effect of cross sensitivities may also be suppressed using a crystal cut insensitive to the considered unwanted effect. A typical example is to use the Quartz ST-X cut which is not sensitive to small temperature variation around the room temperature [29]. Therefore, it is often used to develop strain sensitive sensors [30].

Because of their strain sensitivity, SAW sensors could be of interest for Structural Health Monitoring (SHM) applications where a grid of sensors is used to detect damages in engineering structures. For this purpose, the high-integration, identification and sensing capabilities of SAW devices might be very useful. An embedded SAW sensor could be able to follow a tagged product over its entire life cycle and deliver on-demand, real-time RFID and sensing information. Wilson *et al.* [31]–[33] have already highlighted the benefits of using SAW sensors for aeronautics and space SHM applications. The wireless operation of SAW sensors avoids the use of wires thus providing a lightweight sensing solution. Their battery-less capability guaranties maintenance-free operations of the sensor and, consequently, their implementation in location difficult to reach for an operator. For example, in [33], an orthogonal frequency coded SAW sensor was used to track the failure of individual bolts used to attach stiffeners on aeronautic panels. Also, in [34], Perry *et al.* used SAW resonators to monitor the growth of cracks in a concrete beam. Finally, it is believed, that the low cost of SAW sensors as well as their wireless data transmission capacity are great advantages for civil engineering applications.

Gas sensing (mass loading)

Since the acoustic energy is focused at the surface of the device, the SAW sensors are intrinsically very sensitive to the surface state. Especially, if the sensor uses a Rayleigh wave that has a shear component perpendicular to the plane. This high surface sensitivity makes possible to sense a very small mass change at the surface of the device. This property was advantageously used to develop gas sensors [35]. To do so, a sensitive layer is deposited on the sensor. When the sensitive coating absorbs the gas molecule, it becomes heavier and changes the velocity of the wave traveling underneath. However, for this application, the effect of temperature should be compensated. To do so, a second naked SAW device can be used as a

reference such as in Figure 1.15. For small temperature variation, another solution is to take advantage of a crystal cut insensitive to small temperature changes around room temperature [36].

However, with a Rayleigh wave, the detection of particles or molecules in a liquid medium is impossible since the liquid tends to damp the waves. To bypass this problem, Du *et al.* [37] proposed to use Love waves that have a pure in-plane shear polarization and, therefore, no elastic interaction with an ideal liquid (*i.e.* non-viscous). These kinds of sensors are of great interest for biological and chemical applications in liquids. Nevertheless, the viscosity of a real liquid tends to interfere with the sensor response by increasing the insertion losses. Consequently, the viscosity should be taken into account [38].

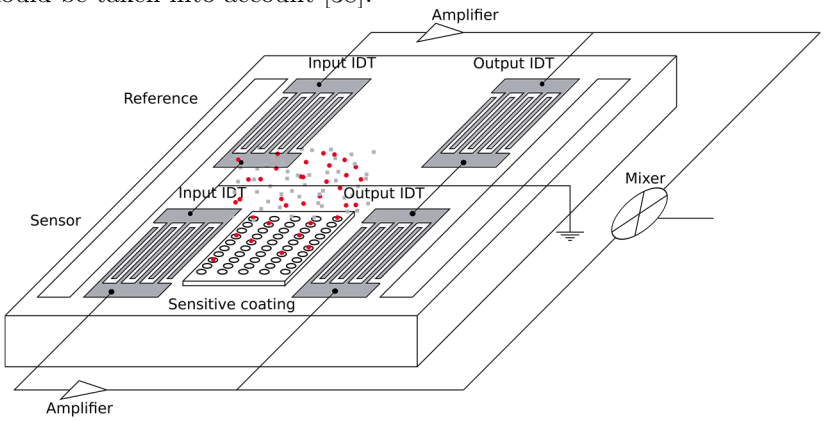

Figure 1.15 Practical implementation of a SAW gas sensor. A second SAW sensor without coating is added, the latter acts as a reference to compensate the temperature effect. The difference in frequency (at the output of the mixer) between the two devices depends only on the amount of absorbed gas. Adapted from [39].

To increase the selectivity of the sensor, additional devices coated with different selective layers can be used. Each coating is more or less sensitive to a certain gas and a numerical data processing improves the overall sensitivity. The main limitation of these sensors come from the sensitive layer. The latter should be highly selective and reversible. The absorption and release velocity should be high. Additionally, the material should be deposited in a uniform and reproducible manner.

Packaging

The high sensitivity to the surface state also means that, for applications which do not require the surface to be accessible (applications such as temperature or strain measuring), the sensor must be packaged in a closed housing to avoid any surface degradation. When referring to the packaging of a sensor, the antenna is included.

Challenges for the SAW sensors

SAW sensors are intrinsically simple devices comprising a piezoelectric substrate with a thin metal deposition. This simplicity means that the device is robust, reliable and cheap to manufacture. In addition, SAW sensors are versatile, which means

that they can detect different phenomena such as temperature, stress and mass, beside their identification capability. They can be passively and remotely interrogated using an electromagnetic signal having a frequency located in one of the ISM bands. The term passive implies that they do not embed any battery or electronics. Consequently, they do not require any maintenance. The measurement is directly read from the sensor electrical response in real time. All these characteristics make them candidates of choice for sensing or identification applications in harsh environments.

Despite all these advantages, SAW sensing is still a niche field (especially when compared to the SAW filters). Indeed, SAW sensors suffer from competitors with similar characteristics such as IC-sensors which have the advantage of being inexpensive and available on-the-shelf [40]. Nevertheless, SAW sensors can address specific application needs such as high temperature, corrosive environment, where IC-sensors fail [41]. In order to fulfil the requirement for these harsh environment conditions, SAW sensors are often built from ground up for each application, therefore:

- A new sensitive element (the SAW chip) is designed, the piezoelectric material, the electrode material and the layout are selected according to the needs of the application;
- A package and an antenna are specifically built around the sensitive element. They should withstand the potentially hostile environment conditions. The package may be functionalized to ensure transmission of temperature or stress. The antenna should have enough range to receive the interrogation signal;
- A customized interrogation antenna is sometimes built to answer the needs of the application. Its directivity is designed to send a given interrogation signal level and such that no more than two sensors can answer simultaneously; otherwise, it would be difficult to identify the origin of the signal.

Moreover, the development of a SAW sensor requires a lot of experience from its designers and, ultimately, several prototypes and tests are necessary to ensure that the sensor fulfils the application requirements.

The material cost of a SAW sensor is low. Indeed, the sensitive part of the sensor is small, and it can be manufactured in batches (thousands of sensors can be produced in a single production run). Therefore, the principal cost of a sensor comes from its development and its assembly in the package.

In **Chapter 2**, we present a FE simulation tool that we developed to model the electroacoustic behaviour of multi-layered sensors and their sensitivity (shift in frequency, phase and velocity) to a measurand. The purpose of this tool is to ease and shorten the development time required to develop a new sensor. In the last part of the chapter, we investigate the possibility to further reduce the development time by removing the sensor package using a multi-layered structure.

1.2.3 SAW Actuators

A promising application of SAW devices is found in lab-on-chip devices. The latter devices are microfluidic devices that integrate laboratory functions that are used for biological or chemical applications. They are manufactured using process inherited from microelectronics, and they deal with small quantity of biochemical material to reduce the cost of operation. Since the SAW device and lab-on-chip share the similar micro-manufacturing method, their common integration is easier. In addition, the generated SAWs have the proper wavelength to interact with the fluid and particles. When interacting with a fluid, part of the SAW acoustic energy leaks into the fluid. It has been demonstrated in the past that SAW can be used to control fluids or manipulate droplets within the fluid [42]. This application will not be further discussed, since it is out of the scope of this document.

1.3 Numerical simulation of SAW filters and sensors

1.3.1 3D and 2D models limits

In order to illustrate the limits of the 3D and 2D models, the following simulations have been performed.

3D model

The first simulation is a 3D model of a delay-line with apodized IDT similar to that presented in Figure 1.5. The substrate material is $LiNbO_3$ Y-128. The wavelength of the device is 4 µm. The input IDT is made of a single pair of fingers; one finger is grounded and the other receives the input voltage (V_{in}), which is a Gaussian pulse of short duration. The output IDT is apodized. The lengths of the fingers follow the amplitude of a cardinal sine function between $-\pi/2$ and $\pi/2$. One comb of the IDT is grounded, the other one is set as floating potential and it is used to get the output voltage. The electrode heights of both IDTs are infinitely thin. In order to reduce the size of the domain and avoid reflections, the outer boundaries are made of low reflecting surfaces. The displacements on three corners are set to zero to prevent the entire geometry to move. The mesh is made of hexahedrons (see Figure 1.16); it was initiated on the top surface and then extended in the thickness of the substrate using a geometric distribution. The fingers have 4 elements in width and 60 in the length. The total geometry consists of 2.7×10^6 elements using a linear interpolation. A time dependent study is carried out, for which the time step is set to $\lambda/80v_{SAW}$ =0.25 ps. The simulation time is about 10 hours on a computer having an Intel Xeon E5 V3 as processor and 64 GB of RAM.

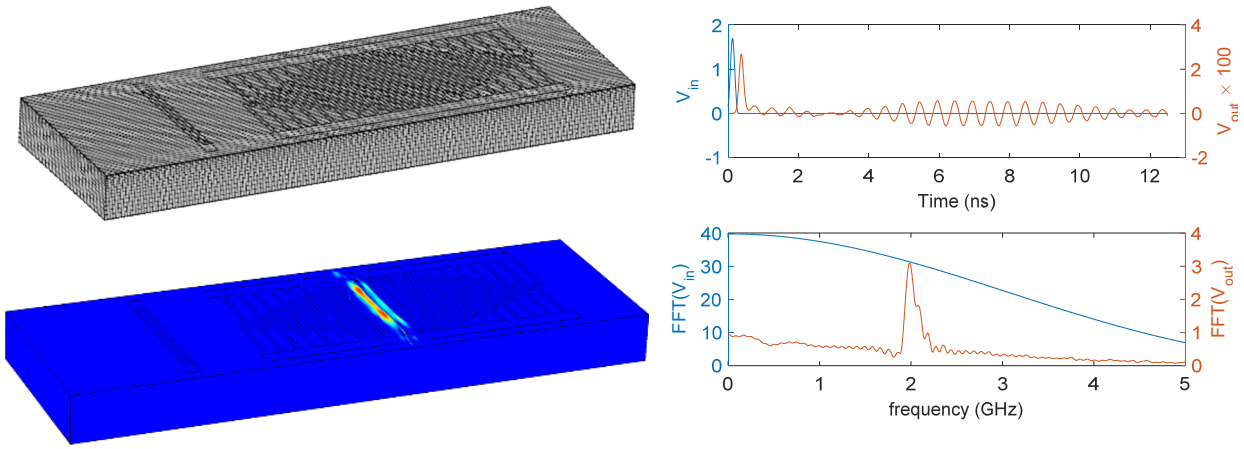

Figure 1.16 3D simulation of an entire apodized delay-line. (Top left) Picture of the mesh that was used for the simulation. In the picture, the input IDT is visible on the left and the apodized output IDT on the right. The elements are made coarser for the sake of representation. (Bottom left) Picture representing the stresses (von Mises) at t = 6 ns. (Right) Input and Output voltages in the time and frequency domain.

The temporal signals and their Fourier Transforms are presented in Figure 1.16. As explained in the introduction, the output voltage is proportional to the overlap between the fingers (*i.e.* the aperture). The first peak in the response corresponds to the capacitive coupling. In the frequency domain, the response of the sensor presents a passband centred around 2 GHz. The Fourier Transform of the excitation signal informs us that the Gaussian peak should be shorter in duration in order to excite the device more consistently over the frequencies of interest.

2D model

A 2D model of an entire 1-port resonator has also been simulated. The latter consists of a 30-finger IDT surrounded by two 70-finger reflectors. The pitch of the device is p=2 µm with a 50% metallization ratio. The electrodes are made from p/15 µm thick Aluminium. The substrate material is $LiNbO_3$ having a Y-Z cut. Its height is limited to 7λ and the displacements on the bottom edge of the substrate are set to zero. One comb of the IDT is using a terminal from which we apply a voltage and observe the charge generated. The second comb of the IDT and the reflectors are grounded. We defined areas close to the edge as Perfectly Matched Layers (PML) in order to avoid the reflection of the waves on the outer edges. The mesh uses quadrilateral elements with second order interpolation functions. There are 32 elements per wavelength in the propagation direction and 35 in the substrate height resulting in a total number of degrees of freedom of 5.7×10^5 and study time of 15 hours. We performed a frequency domain study from 750 MHz to 950 MHz with frequency steps of 0.25 MHz.

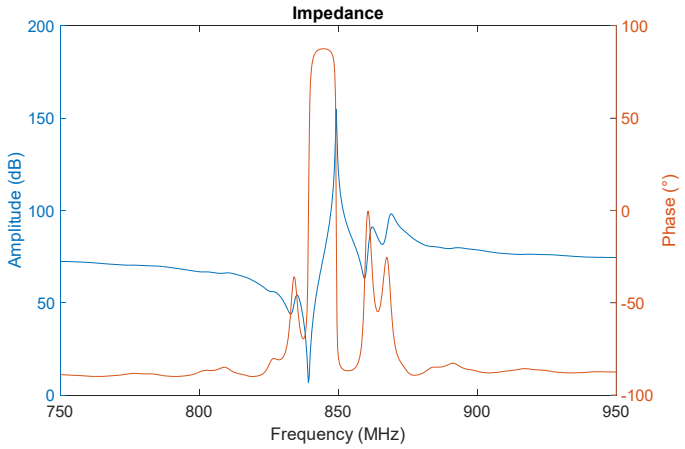

Figure 1.17 Frequency response of an entire resonator simulated in 2D.

The frequency response of the resonator (Figure 1.17) clearly shows the resonance and anti-resonance frequencies. In addition, ripples are present in the response. For evident reason of computation time, we cannot simulate the device using a 2D full model. A much faster method is then needed for design optimization purposes.

1.3.2 COM model (Method used in this document)

As demonstrated in the previous section, the simulation of an entire SAW device is theoretically possible using the FE method but it is time consuming due to the high aspect ratio between the overall geometry, and the wavelength of the SAW (see Figure 1.18). Consequently, other models have been developed to simulate SAW devices. These models can be divided in two categories (a review of the different existing models is available in [43]).

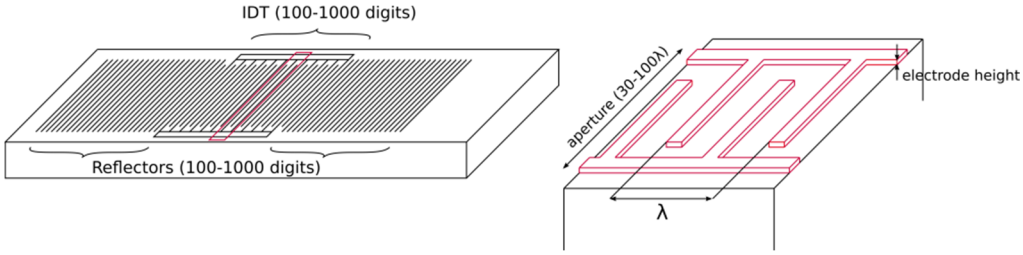

Figure 1.18 Illustration of the different aspect ratios in a SAW device. λ is the wavelength (in the µm range), IDT length ≈ $10^2 \times \lambda$, acoustic path ≈ $10^3 \times \lambda$, electrode height ≈ $10^{-2} \times \lambda$, aperture ≈ $10^2 \times \lambda$. There is 5 to 6 orders of magnitude between the smallest and the biggest structure, which makes the meshing of the entire device difficult.

The first category of models is called "lumped elements model" because it uses discrete elements such as resistors, capacitances and inductances. Among them, the Delta function model is the earliest. However, it does not include internal reflections, which can have a huge influence on the device behaviour. The equivalent circuit model overcomes this weakness; it is derived from the cross-field model,

where the transducer is modelled as an array of bulk transducers and the electric field is assumed to be either in line or in cross field.

The second category and the more recent ones are based on black box models, where a section of the device is modelled as a black box. One of them is the so-called P-matrix model (see Figure 1.19). The latter describes any section of a SAW with a 3×3 matrix, see equation (1.5). The acoustic and electric ports are related by a linear equation. In (1.5) a_1 and a_2 are the amplitudes of the incident wave at the ports 1 and 2. b_1 and b_1 are the amplitudes of the wave leaving the transducer. i and u are, respectively, the transducer current ant voltage. See details in [9].

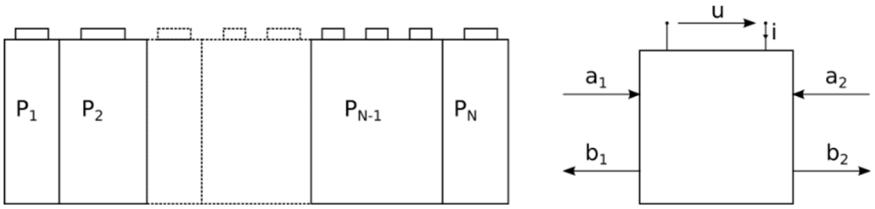

Figure 1.19 Schematic principle of the P-matrix method. Each section of the acoustic path is described by a P-matrix. The matrices are cascaded to determine the behaviour of the whole acoustic path.

$$\begin{Bmatrix} b_1 \\ b_2 \\ i \end{Bmatrix} = \begin{bmatrix} p_{11} & p_{12} & p_{13} \\ p_{12} & p_{22} & p_{23} \\ -4p_{13} & -4p_{23} & p_{33} \end{bmatrix} \begin{Bmatrix} a_1 \\ a_2 \\ u \end{Bmatrix} \quad 1.5$$

Another model is the so-called Coupling Of Mode (COM) model; it is also described using a 3×3 matrix with ports related by differential linear equations. This is the method chosen for this document. It will be discussed in the following sections, as well as the determination of the matrix parameters.

Coupling Of Modes (COM)

The COM model allows to simulate SAW devices in an efficient way. Nevertheless, the accuracy of the model depends on its parameters (the so-called COM parameters). The COM parameters can be experimentally determined using dedicated test structures (long resonators). When doing so, the COM parameters have the advantage of reflecting the manufacturing process. However, the method is tedious and time consuming since each slight change of the geometry or material requires to build new test structures for which the COM parameters will be extracted.

For this reason, it is advantageous to extract them from a numerical model. Since the COM theory considers the propagation of waves in an infinite periodic grating, COM parameters can also be extracted from the simulation of a transducer section in an infinite periodic grating. The main parameters of such a grating are illustrated in Figure 1.20. To simulate this model, two methods are available, the FEM/BEM (BEM stands for Boundary Element Method) and the full FEM. In the FEM/BEM, the behaviour of the wave in the substrate is computed analytically using Green's functions and the influence of the electrodes is considered using FEM. Boundary elements are used to account for the mass loading effect of the electrode on the waves. The FEM/BEM has the advantage of a shorter computa-

tion time, but it deals badly with multi-layered structures [44]. The full FEM hasn't this problem, and it is now very fast thanks to the advances in computer technology. The FEM is the preferred simulation method in this work since it enables to easily simulate the properties of multi-layered infinite periodic grating. However, the FEM software does not directly yield the values of the COM parameters. Therefore, the next section is dedicated to the extraction of the COM parameters using FEM simulations.

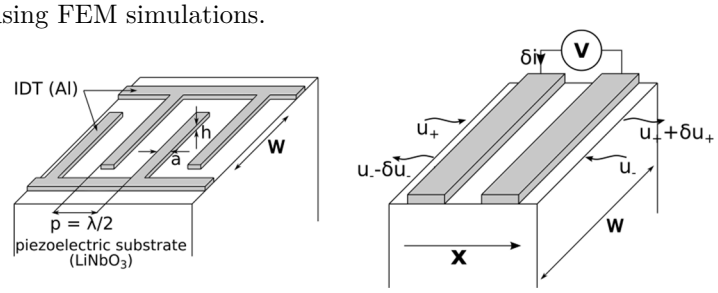

Figure 1.20 Schematic of an IDT (left) and model (right) used to extract COM parameters. p is the pitch, W is the aperture, h and a are the electrode thickness and width.

The COM theory considers two mechanical waves u_+ and u_- propagating in the positive and negative directions. When traveling through the grating, these waves can be reflected and contribute to the wave propagating in the opposite direction. The COM model considers only the reflection of the first harmonic. It also assumes that the amplitudes may decrease due to the attenuation and that there is a linear transduction coefficient due to the piezoelectricity. This leads to the following equations [45], [46]:

$$\frac{du(x)_+}{dx} = -j\left(\frac{\omega}{v_{SAW}} - j\gamma\right)u_+(x) - j\kappa_{12}u_-(x)e^{-j2\pi x/p} + j\zeta V e^{-j\pi x/p} \quad 1.6$$

$$\frac{du(x)_-}{dx} = j\overline{\kappa_{12}}u_+(x)e^{j2\pi x/p} + j\left(\frac{\omega}{v_{SAW}} - j\gamma\right)u_-(x) - j\bar{\zeta}Ve^{j\pi x/p} \quad 1.7$$

$$\frac{dI(x)}{dx} = -2j\bar{\zeta}u_+(x)e^{j\pi x/p} - 2j\zeta u_-(x)e^{-j\pi x/p} + j\omega CV \quad 1.8$$

Where, v_{SAW} (m/s) is the SAW velocity, γ (m^{-1}) is the attenuation, κ_{12} $(\%/m)$ is the reflection coefficient, ζ $(\Omega^{-1/2})$ is the transduction coefficient and C $(F/period)$ is the capacitance.

Assuming that the waves are $2p$-periodic:

$$u_+(x) = R(x)e^{-j\pi x/p} \quad 1.9$$

$$u_-(x) = S(x)e^{j\pi x/p} \quad 1.10$$

This yields, after substitution in (1.6), the COM equation:

$$\begin{Bmatrix} \frac{dR(x)}{dx} \\ \frac{dS(x)}{dx} \\ \frac{dI(x)}{dx} \end{Bmatrix} = \begin{bmatrix} -j\theta_u & -j\kappa_{12} & j\zeta \\ j\overline{\kappa_{12}} & j\theta_u & -j\bar{\zeta} \\ -2j\bar{\zeta} & -2j\zeta & j\omega C \end{bmatrix} \begin{Bmatrix} R(x) \\ S(x) \\ V(x) \end{Bmatrix} \quad 1.11$$

Where, $\theta_u = \frac{\omega}{v_{SAW}} - \frac{\pi}{p} - j\gamma$ (rad/m) is the detuning factor. The behaviour of the system can be fully described using the five COM parameters (v_{SAW}, κ_{12}, ζ, C, γ). These parameters are determined from the simulation of an infinite periodic grating, using different electrical boundary conditions, as detailed in [45], [46].

Short circuit behaviour

When considering no attenuation ($\gamma = 0$), the equations system (1.11) under short-circuit (superscripted SC) conditions (*i.e.*, $V = 0$) corresponds to a homogeneous system, and the grating behaves like if there was no electric field and transduction ($\zeta = 0$):

$$\begin{Bmatrix} \frac{dR(x)}{dx} \\ \frac{dS(x)}{dx} \end{Bmatrix} = \begin{bmatrix} -j\theta_u & -j\kappa_{12} \\ j\overline{\kappa_{12}} & j\theta_u \end{bmatrix} \begin{Bmatrix} R(x) \\ S(x) \end{Bmatrix} \tag{1.12}$$

We look for solutions of the form:

$$\begin{Bmatrix} R(x) \\ S(x) \end{Bmatrix} = \begin{Bmatrix} R_0 \\ S_0 \end{Bmatrix} e^{jqx} \tag{1.13}$$

Thus, substituting this solution in (1.12), we get the system:

$$\begin{bmatrix} -j\theta_u - jq & -j\kappa_{12} \\ j\overline{\kappa_{12}} & j\theta_u - jq \end{bmatrix} \begin{Bmatrix} R_0 \\ S_0 \end{Bmatrix} = \{0\} \tag{1.14}$$

which has non-zero solutions only if the matrix determinant is zero:

$$\theta_u{}^2 - q^2 - |\kappa_{12}|^2 = 0 \tag{1.15}$$

The general solutions then are:

$$\begin{Bmatrix} R^{SC}(x) \\ S^{SC}(x) \end{Bmatrix} = A \begin{Bmatrix} 1 \\ \frac{jq - \theta_u}{\kappa_{12}} \end{Bmatrix} e^{-jqx} + B \begin{Bmatrix} \frac{jq - \theta_u}{\overline{\kappa_{12}}} \\ 1 \end{Bmatrix} e^{jqx} \tag{1.16}$$

Where, A and B are constants to be determined by the boundary conditions and q is the wave number of the existing mode, given by:

$$q = \begin{cases} \pm\sqrt{\theta_u{}^2 - |\kappa_{12}|^2} & if\ \ \theta_u{}^2 > |\kappa_{12}|^2 \\ \pm j\sqrt{|\kappa_{12}|^2 - \theta_u{}^2} & if\ \ \theta_u{}^2 < |\kappa_{12}|^2 \end{cases} \tag{1.17}$$

Substituting the detuning factor (θ_u) in the dispersion relation (1.17), we find a quadratic polynomial equation in terms of the frequency. The two solutions of this polynomial are the two frequencies that define the stop band edges of the dispersion relation for the short circuit condition:

$$f_{SC}^{\pm} = \frac{v_{SAW}}{\lambda}\left(1 \pm \frac{\lambda|\kappa_{12}|}{2\pi}\right) \tag{1.18}$$

The average of these two frequencies and their difference give the SAW velocity and the reflection coefficient:

$$v_{SAW} = \lambda\frac{f_{SC}^{+} + f_{SC}^{-}}{2}\ ,\ |\kappa_{12}| = \frac{\pi}{v_{SAW}}(f_{SC}^{+} - f_{SC}^{-}) \tag{1.19}$$

Open grating behaviour

In open grating (superscripted OG) condition, the current is zero. Thus, the third line in 1.11 gives this expression of the voltage [45], [46]:

$$V = \frac{2}{C\omega}\left(\bar{\zeta}R(x) + \zeta S(x)\right) \tag{1.20}$$

Substituting this relation in the first two lines of 1.11 yields:

$$\begin{Bmatrix} \frac{dR(x)}{dx} \\ \frac{dS(x)}{dx} \end{Bmatrix} = \begin{bmatrix} -j\left(\theta_u - \frac{2\zeta^2}{C\omega}\right) & -j\left(\kappa_{12} - \frac{2\zeta^2}{C\omega}\right) \\ j\left(\overline{\kappa_{12}} - \frac{2\zeta^2}{C\omega}\right) & j\left(\theta_u - \frac{2\zeta^2}{C\omega}\right) \end{bmatrix} \begin{Bmatrix} R(x) \\ S(x) \end{Bmatrix} \tag{1.21}$$

A non-trivial solution exists if the matrix determinant is zero:

$$\left(\frac{2\pi f}{v_{SAW}} - \frac{\pi}{p} - \frac{2|\zeta|^2}{C\omega}\right)^2 - \left|\kappa_{12} - \frac{2\,\zeta}{C\,\omega}\right|^2 = 0 \tag{1.22}$$

This gives the two following solutions:

$$f_{OG}^{\pm} = \frac{v_{SAW}}{2\pi}\left(\frac{\pi}{p} + \frac{2|\zeta|^2}{C\omega} \pm \left|\kappa_{12} - \frac{2|\zeta|^2}{C\omega}\right|\right) \tag{1.23}$$

which define the stop band edges in open grating condition. In addition, we can assume that the coupling and transduction coefficients are real [46]. Then, adding the two stop band frequencies for the open grating condition yields:

$$f_{OG}^{+} + f_{OG}^{-} = \frac{v_{SAW}}{\pi}\left(\frac{\pi}{p} + \frac{2|\zeta|^2}{C\omega}\right) \tag{1.24}$$

Therefore, from the latter and the first of 1.19, we get the relation between ζ and C:

$$\frac{2|\zeta|^2}{\pi C\omega} = \frac{(f_{OG}^{+} + f_{OG}^{-}) - (f_{SC}^{+} + f_{SC}^{-})}{v_{SAW}} \tag{1.25}$$

We need another relation between ζ and C to determine them. This can be obtained from the harmonic admittance of the IDT.

Harmonic admittance

To determine the harmonic admittance in the case of no attenuation ($\gamma = 0$), we apply a harmonic driving voltage [45], [46]. Since the potential on the electrode fingers does not depend on the position x, a particular solution of the mechanical equations (first two lines) in 1.11 has the form:

$$\begin{Bmatrix} \tilde{R}(x) \\ \tilde{S}(x) \end{Bmatrix} = \begin{Bmatrix} A_+ \\ A_- \end{Bmatrix} V \tag{1.26}$$

Substituting this in the first two lines of 1.11 provides:

$$\frac{dA_+V}{dx} = -j\theta_u A_+ V - j\kappa_{12} A_- V + j\zeta V \tag{1.27}$$

$$\frac{dA_-V}{dx} = j\overline{\kappa_{12}} A_+ V + j\theta_u A_- V - j\bar{\zeta} V \tag{1.28}$$

Since $\frac{dV}{dx} = 0$ and after simplification by V we get:

$$\begin{bmatrix} -j\theta_u & -j\kappa_{12} \\ j\overline{\kappa_{12}} & j\theta_u \end{bmatrix} \begin{Bmatrix} A_+ \\ A_- \end{Bmatrix} = \begin{Bmatrix} -j\zeta \\ j\bar{\zeta} \end{Bmatrix} \quad 1.29$$

Inverting this system, yields $\{A_+, A_-\}$. Thus, the solutions in (1.26) become:

$$\begin{Bmatrix} \tilde{R}(x) \\ \tilde{S}(x) \end{Bmatrix} = \frac{1}{{\theta_u}^2 - |\kappa_{12}|^2} \begin{Bmatrix} \theta_u\zeta - \kappa_{12}\bar{\zeta} \\ \theta_u\bar{\zeta} - \overline{\kappa_{12}} \end{Bmatrix} V \quad 1.30$$

Substituting further this solution in the third line of 1.10 yields the harmonic admittance:

$$Y(f) = \frac{dI/dx}{V} = -2j\frac{2\theta_u|\zeta|^2 - 2Re(\overline{\kappa_{12}}\zeta^2)}{\theta_u^2 - |\kappa_{12}|^2} + j2\pi fC \quad 1.31$$

which shows a resonance and an anti-resonance at two different frequencies. After substituting the already known COM parameters (v_{SAW}, κ_{12}, $\zeta(C)$), it becomes possible to extract the capacitance (C) by fitting the simulated harmonic admittance using equation (1.31).

COM parameters extraction using FEM

The simulation of the infinite periodic grating can be done using COMSOL Multiphysics 5.3a. The model is implemented in 3D. From this model, we extract the COM parameters using specific boundary conditions that reproduce the three configurations (short circuit, open grating, harmonic admittance), described in the previous section.

It is possible to reduce the model geometry to a pair of fingers by using periodic boundary conditions on potential and displacement. In addition, as the aperture of the device is considered infinite, it can be (in the model) reduced to a fraction of the wavelength by using periodic boundary conditions. The substrate thickness is also reduced to a few wavelengths, using a PML that is placed at the bottom of the substrate [47]. This avoids reflections of acoustics modes at the bottom of the substrate.

An air layer is also taken into account above the substrate. Nevertheless, $LiNbO_3$ has a high permittivity. Thus, air is expected to have a relatively weak influence on the results. The resulting model is often referred as a unit-cell model. It is shown in Figure 1.21.

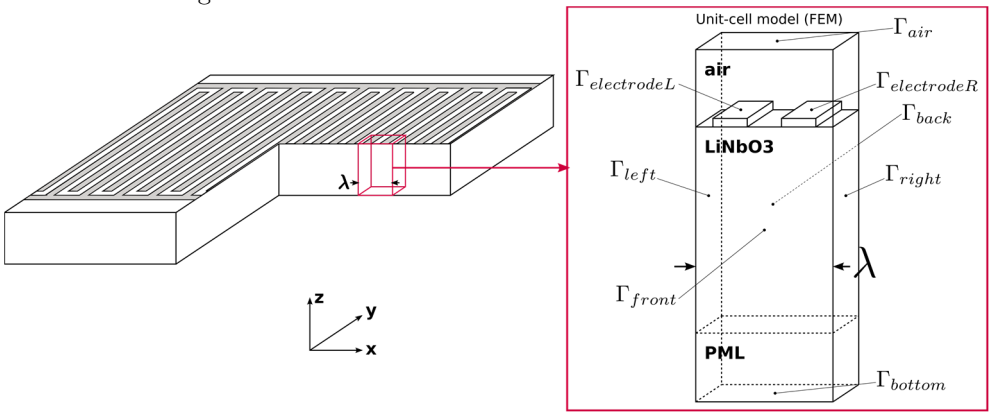

Figure 1.21 COMSOL unit-cell model of an infinite periodic grating.

Governing equations

As the metallic electrodes have a high conductivity compared to the piezoelectric substrate or the air layer, their conductivity is assumed to be infinite. Consequently, the electrodes are not simulated from an electrostatic point of view. Also, the air layer is supposed to have no stiffness or mass. As a result, the mechanical equation is not solved in the air layer.

The electromechanical behaviour of the piezoelectric material is described by the following constitutive equations that couple the stress σ and strain S to the electrical field E and electric displacement field D:

$$\begin{aligned} \sigma_{ij} &= c^E_{ijkl} S_{kl} - e_{kij} E_k \quad i,j,k,l = 1,2,3 \\ D_i &= e_{ikl} S_{kl} + \epsilon^S_{ik} E_k \end{aligned} \tag{1.32}$$

Where, c^E is the short circuit stiffness matrix, e is the stress piezoelectric matrix, and ϵ^S is the blocked permittivity matrix. In addition, assuming small displacements, the strains are $S_{kl} = \frac{1}{2}\left(u_{k,l} + u_{l,k}\right)$, and $E_k = -V_{,k}$. Thus, the mechanical and electrostatic equations are (in the absence of body and surface charges and body force):

$$\rho \ddot{u}_j = \sigma_{ij,i} \ or \ \rho \ddot{u}_j = c^E_{ijkl} u_{k,li} + e_{kij} V_{,ki} \tag{1.33}$$

$$0 = D_{i,i} \ or \ 0 = e_{ikl} u_{k,li} - \epsilon^S_{ik} V_{,ki} \tag{1.34}$$

The electrostatic and mechanical boundary conditions used for the electrostatic and mechanical equations are detailed in Table 1.3.

	Electrostatic			
Boundary	Short circuit	Open grating	Harmonic admittance	Mechanical
$\Gamma_{left}, \Gamma_{right}$	$V_{\Gamma_{left}} = V_{\Gamma_{right}}$			$u_{i_{\Gamma_{left}}} = u_{i_{\Gamma_{right}}}$
$\Gamma_{front}, \Gamma_{back}$	$V_{\Gamma_{front}} = V_{\Gamma_{back}}$			$u_{i_{\Gamma_{front}}} = u_{i_{\Gamma_{back}}}$
Γ_{air}	*free*			*N.A.*
Γ_{bottom}	$V = 0$			$u_i = 0$
$\Gamma_{electrodeR}$	$V = 0$	$\int D_i . n_i dS = 0$	$V = cos(\omega t)$	$\sigma_{ij} . n_i = 0$
$\Gamma_{electrodeL}$	$V = 0$	$\int D_i . n_i dS = 0$	$V = 0$	$\sigma_{ij} . n_i = 0$

Table 1.3 Electrostatic and mechanical boundary conditions for the COM parameters extraction using the unit-cell model.

Comparison with literature reference

The method described above was evaluated using [45] as a reference, where the COM parameters are given for a specific structure that was reproduced. As specified in the COM theory, the COM parameters are extracted from a single IDT in an infinite periodic grating, modelled in COMSOL as in Figure 1.22.

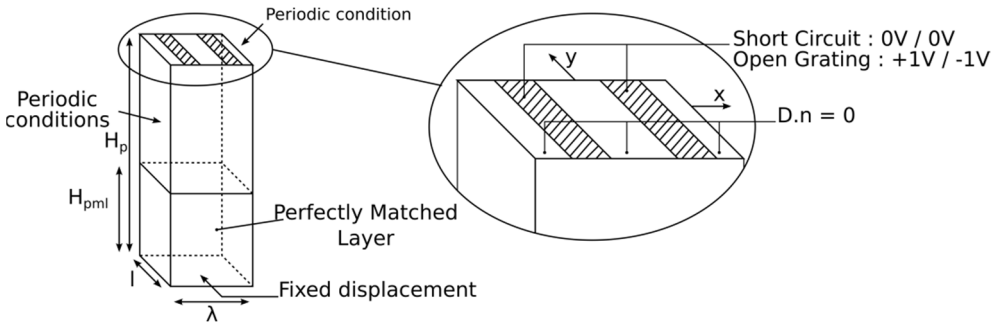

Figure 1.22 Schematic of the model used to extract COM parameters

The 3-D COMSOL model has the following geometrical parameters:

- h_{met} (metallization height): $\emptyset$;
- λ (wave length): $4\,\mu m$;
- l (aperture of the modelled device): $\lambda/800$;
- W (aperture of real device): λ;
- H_p (substrate height): $4\,\lambda$;
- H_{pml} (Perfectly Matched Layer height): λ;
- a/p (metallization ratio): 0.5.

It should be noted that, to save computation time, the real aperture of the device is not modelled but only a fraction of it. Therefore, a correction factor (W/l) must be applied to the computed real charge: $(Q = Q_{Comsol} \times \frac{W}{l})$.

In order to compare the results with [45], the material data are taken from [48] (recalled in Appendix B.1). In addition, the waves should propagate in the Z direction of the crystal. In COMSOL, to properly orientate the crystal, a local coordinate system using Euler angles may be defined. In our case the material tensors are rotated using the following Euler angles: $(\phi, \theta, \psi) = (90,90,0)$ corresponding to the Y-Z cut.

The mesh used for the simulation consists in prismatic triangular elements with quadratic interpolation functions, as shown in Figure 1.23. The mesh uses smaller elements near the electrode edges since the variation of the electric displacement is higher in these regions (see [46]). The convergence study (see Figure 1.23) yields to choose a mesh with 2×10^5 degrees of freedom.

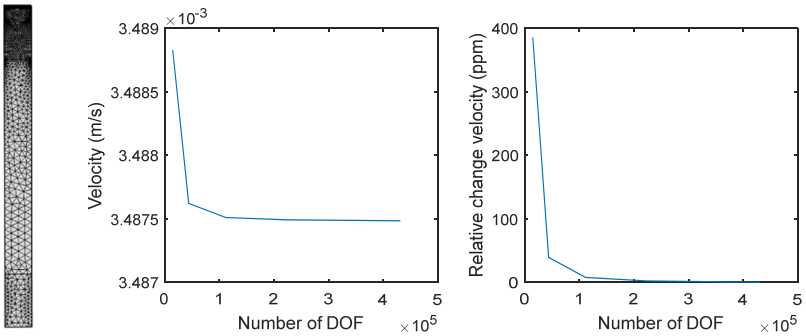

Figure 1.23 Illustration of the mesh used for the simulation and result of the convergence study. For the latter, we observe that the change in velocity and the relative change in velocity depend on the number of degrees of freedom (DOF).

The SAW velocity and reflection coefficient are determined from the stop band analysis in short and open-circuit. As mentioned in section 1.3.2, two eigenvalue analyses must be performed successively. The first eigenvalue analysis, with short circuit conditions, yields two frequencies denoted f_{SC}^{+} and f_{SC}^{-}; one corresponds to the resonant frequency f_r, the other one is f_c (the common stop band edge). The second eigenvalue analysis, with open grating conditions, gives two frequencies denoted f_{OG}^{+} and f_{OG}^{-}; One is the anti-resonant frequency f_a and the other one is the common stop band edge f_c.

When performing an eigenvalue analysis, the solver outputs a large number of frequencies, among which, only two are of interest. To discriminate the relevant ones, we use the imaginary parts of the eigenfrequencies which must be low for the Rayleigh mode that propagates near the surface and, thus, is not damped in the PML.

The short circuit simulation yields $f_{SC}^{-} = f_R$=853.60 MHz and $f_{SC}^{+} = f_C$=862.62 MHz. Consequently, the centre frequency f_0 and the velocity of the SAW wave, v_{SAW}, are:

$$f_0 = \frac{f_{SC}^{+}+f_{SC}^{-}}{2} = \frac{f_r+f_c}{2} = 858.12\ MHz,\ v_{SAW} = \lambda f_0 = 3432.46\ m/s$$

The open grating simulation yields f_{OG}^{-}=862.62 MHz and $f_{OG}^{+} = f_A$=871.42 MHz. The identification of the common stop band edge $f_c = f_{SC}^{+} = f_{OG}^{-}$=862.62 MHz enables to calculate the reflection coefficient as (see equation 1.19):

$$\kappa_{12} = \frac{2\pi}{\lambda}\frac{f_c-f_r}{f_c+f_r},\ \kappa_p = \lambda\kappa_{12} = 3.30\%$$

The capacity and transduction coefficient are determined from the harmonic impedance. For this purpose, we select f=840 MHz as the point-fitted frequency since it must be far from the resonance and anti-resonance frequencies, and we get:

$$C = 3.9789\times10^{-2}pF/period \rightarrow C_n = C\lambda/W = 39.789\times10^{-5}pF/\mu m/period$$

and:

$$\zeta_p = \lambda\zeta = 0.0026657\Omega^{-1/2} \rightarrow \zeta_n = \zeta_p/\sqrt{W/\lambda}\ = 53.398\times10^{-5}\Omega^{-1/2}$$

The comparison between the obtained results and those of the reference [45] is given in Table 1.4.

Parameter	[45]	COMSOL (present)
$f_r\ (MHz)$		853.60
$f_a\ (MHz)$		871.42
$f_c\ (MHz)$		862.62
$f_0\ (MHz)$	858	858.12
$v_{SAW}\ (m/s)$	3432	3432.46
$\kappa_p\ (\%)$	3.23	3.30
$\zeta_n\ (\times 10^{-5}\Omega^{-1/2})$	53.5	53.398
$C_n\ (10^{-5}pF/\mu m/period)$	40.9	39.789

Table 1.4 Computed COM parameters

In [45] the authors used a Green's function model to model the SAW propagation and extract the COM parameters. The COM parameters we computed using the finite element model are close to the one found in [45]. The remaining discrepancies might be due to the non-perfect convergence of the FEM model and/or to difference in the working point used to compute the capacitance and transduction coefficient.

Chapter 2 Simulation of multi-layered sensors

Accurate simulations of SAW sensors are extremely important to reduce their development time and improve their sensitivity. However, the entire simulation of a sensor is highly time consuming. The problem being that the overall size of the sensor is in the centimetre range, while the acoustic phenomenon occurs at the micrometre scale. Therefore, it is a challenging task to simulate the entire sensor in a single simulation, including the effect of the measurand on the packaging and on the electroacoustic behaviour. To overcome this issue, these two aspects of the simulation must be computed separately.

- First, one must simulate the static effect of the measurand (temperature, pressure…) on the entire sensor and in particular on the piezoelectric chip. At this stage, some simplifications may be introduced to ease the simulation (*i.e.* omission of the IDT, and reflector that have little influence on the static simulation).

- Then, one computes the electro-acoustic behaviour. Here, a dynamic simulation is needed that must include the effect of the measurand computed in the first step. The computation yields the sensitivity of the wave to the measurand.

The FEM is generally preferred to address the first step, because it can simulate the complex geometry of the sensor. The second step may be covered by several methods that enable to determine the electro-acoustic responses of SAW devices. For instance, in [49] and [50], Wang *et al.* first used the FEM to study the static bending of their pressure sensor. Then, they considered the electro-acoustic behaviour of the sensor through a lumped element model. Nevertheless, the simulation of SAW sensors, based on lumped element model, is not sufficient in this context. Indeed, our goal is to simulate multi-layered SAW sensors from scratch, starting from the material constants. To do so, the FEM is a well-established method that, in combination with the COM method, is an effective approach to determine the electro-acoustic behaviour of the sensors. FEM has been used thoroughly to determine resonators or delay-lines responses for sensor applications. As a general example, Zhang *et al.* [51] developed a temperature sensor based on $LiNbO_3$. A COM model was used to predict the SAW response but not the sensitivity, saying that the shift in frequency due to temperature was not considered. However, in the context of sensor development, it would be interesting to have in addition to the COM parameters, the shift in SAW velocity due to a measurand (incl. mass and electrical load, temperature, strain and stress fields).

In the FE simulation of the acoustic behaviour, the effect of a mass load is the simplest to consider, since it only requires adding a layer of a given mass and stiffness to the unit-cell model. Therefore, the COM model can be conveniently used to

compute the effect of mass loading. For instance, in [52], Hao *et al.* computed, using the FEM, the change in COM parameters and optimized the electrical response of a resonator sensitive to mass. Actually, a model of a gas sensor (a kind of mass sensor) is already available in the COMSOL library [53]. Just as well, the computation of the sensor sensitivity to an electrical load is easy because it is considered directly in the COM equations as done by Fu *et al.* [54], for an impedance-loaded SAW delay-line.

Considering the effect of strain and stress or temperature is a more tedious task, since these fields affect the material constants and geometry of the sensor. The Temperature Coefficients of Frequency (TCF) are reported for the most common piezoelectric crystals and may suffice in certain applications (*i.e.* single layer structure) but are not adapted to multi-layered structures. For instance, Zhang *et al.* [55] used the COM model to simulate the electrical response of a quartz delay-line. Their model used a simple linear relation to consider the effect of the pressure and temperature on the time delay generated by the sensor. Also, Zhang *et al.* [56] studied a pressure sensor based on SAW resonators. They used the COM method to compute the electrical response and thermal shift in frequency was taken into account through a predetermined TCF.

Furthermore, the effects of strain- or temperature-biased fields were studied in the past through a perturbation model. For example, Sinha and Tiersten [57] developed a model with which they computed the change in free velocity due to an initial strain field. In particular they applied the method to a Quartz resonator, which centre frequency changes with acceleration [58]. Also, Hauden *et al.* [59] developed a perturbation model for both strain and temperature. They also confronted it to experimental results.

Here, we propose to improve the unit-cell model introduced previously, and use it for the extraction of the phenomenological COM parameters in SAW devices submitted to strain and temperature changes, and consequently compute the effect of strain and temperature on these parameters. It becomes therefore possible to compute the sensitivity of a full SAW sensor to strain and temperature, from the computed strain/stress and temperature fields (step 1) and from the computed sensitivities of the COM parameters (step 2). The full electrical response of the sensor as well as its sensitivity to the measurand can be computed in a third step (step 3), using P-Matrix algorithms [45].

In this chapter, we describe in detail these two computation steps, before applying the method for the computation, analysis and optimization of the properties of different SAW sensors. We notably investigate two implantable sensors, based on innovative multi-layered structures. The first one is meant for medical applications, while the second one is a concept study of a package-less temperature sensor based on an innovative stack of materials.

2.1 Simulation of the sensitivity of the sensor

The sensitivity to the measurand is the most critical characteristic when designing a SAW sensor. It may be determined using a three steps simulation process that is possible under three assumptions:

- Firstly, the measurand variation should be slow compared to the wave propagation phenomenon so that the measurand can be computed using a static study. It should also be noticed that the interrogation rate of a SAW sensor is typically from 100 Hz to 1000 Hz which is very low compared to the frequency of the waves.
- Secondly, the load generated by the measurand should be small. For instance, large strain fields could introduce non-modelled wave guiding effects [60]. It is however not an issue with brittle piezoelectric materials and thus limited to small deformations.
- Thirdly, the bias load generated by the measurand is assumed to be homogeneous. The computation of the change in velocity due to the measurand is done using the unit-cell model in which the strain and stress fields are considered homogeneous.

In the following sub-sections, we are only interested in loads that generate temperature, stress and strain changes of the acoustic response, since they are the most difficult to compute using the FEM tool.

2.1.1 Three steps simulation process

A three steps simulation process is used to simulate an entire SAW device, including the effect of a measurand (see Figure 2.1).

In a first step, the effect of the measurand (in terms of temperature, strain and stress fields) is computed along the propagation path of the sensor. At this stage, it is possible to take the influence of the sensor housing into account. In a second step, the so-called COM parameters are extracted from the simulation of a simplified infinite grating of electrodes (an improved unit-cell model). These phenomenological parameters are computed for all the surface states present in the acoustic path (*i.e.* IDT, reflector gratings, free surface...). They can already be used to compute the sensitivity of the sensor with respect to temperature, strain and stress. Finally, in a third step, the frequency response of the whole device can be computed using the obtained sets of COM parameters and the device geometry (position and number of electrodes, aperture...). The obtained complete set of COM parameters allows a fine tuning of the RF response of the sensor.

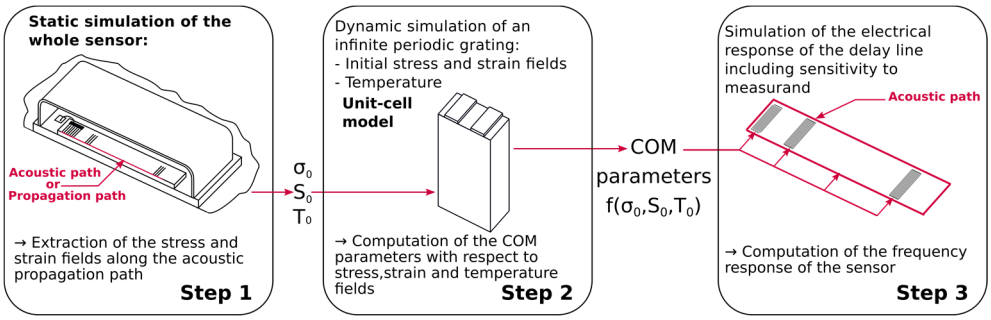

Figure 2.1 Illustration of the 3 steps process used to simulate entire sensors. The outcomes of the first step are the static strain (S_0), stress (σ_0) and temperature (T_0) along the propagation path. They are averaged before being used in the unit-cell model. From the second step, we obtain strain, stress and temperature dependent COM parameters from which it is possible to compute the electrical response of the sensor (in step 3).

In most situations, the computation of the free surface wave velocity is sufficient to calculate the sensor sensitivity. However, for some of the applications studied below, the whole set of COM parameters is computed to illustrate the general computation procedure, as described above.

2.1.2 Acoustic sensitivity to temperature and strain/stress

For an initially pre-stressed structure, under the assumption that the displacement causing the waves is small compared to the initial displacement responsible for the pre-stress field (σ^0), the mechanical equation (1.33) becomes [61]:

$$\rho\ddot{u}_j = c^E_{ijkl}u_{k,li} + e_{kij}V_{,ki} + \sigma^0_{ik}u_{j,ki}\ ; i,j,k,l = 1,2,3 \qquad 2.1$$

In addition, to consider the effect of the initial strain (S^0) on the material stiffness and density, the stiffness tensor and the density must be modified according to their respective sensitivity to the applied strain [62]. This is discussed hereafter. The effect of initial strain on the stiffness constants is described as follows (linear dependency) [62].

$$\tilde{c}^E_{pq} = c^E_{pq} + c_{pqr}S_r \quad p,q,r = 1,\dots,6 \qquad 2.2$$

The constants c_{pqr} are called third-order stiffness coefficients. They are determined experimentally [63] and generally presented in a 6×6×6 matrix. However, due to crystal symmetries, only few coefficients are needed to depict the entire matrix. For instance, in the case of $LiNbO_3$, 14 coefficients are sufficient (see Appendix B.1). Besides, the strain field affects the density, which changes proportionally to the change in volume [62]:

$$\frac{\Delta\rho}{\rho_0} = \frac{\rho_-\rho_0}{\rho_0} = -\frac{V - V_0}{V} \approx -\left(S^0_{xx} + S^0_{yy} + S^0_{zz}\right) \qquad 2.3$$

The effect of a temperature elevation (ΔT) is easier to consider since it only affects material parameters. Assuming that the material properties are linearly dependent on the temperature variation (ΔT), we get:

$$\begin{aligned} \widetilde{c_{pq}^{E}} &= c_{pq}^{E}\left(1 + TC\left(c_{pq}^{E}\right) \times \Delta T\right) \\ \widetilde{e_{ip}} &= e_{ip}\left(1 + TC\left(e_{ip}\right) \times \Delta T\right) \\ \widetilde{\epsilon_{ij}^{S}} &= \epsilon_{ij}^{S}\left(1 + TC\left(\epsilon_{ij}^{S}\right) \times \Delta T\right) \end{aligned} \qquad 2.4$$

The temperature dependent coefficients (TC) are determined experimentally and are well known for $LiNbO_3$ [64]. All the constants used to carry out the analysis are reported in Appendix B.

In practice, the effect of the temperature is taken into account using MATLAB. The set of equations (2.4) is entered in a script that returns the modified material constants. The biased strain field ($S^0 = S^{mecha} + S^{therm}$) is already computed in the coordinate system oriented according to the piezoelectric crystal orientation. The elastic part of the strain tensor (S^{mecha}) which results from mechanical deformation is used to modify the stiffness of the material. While the total deformation (S^0) is used to modify the material density. The biased stress field is considered directly in the FEM unit-cell model. Figure 2.2 illustrates the approach.

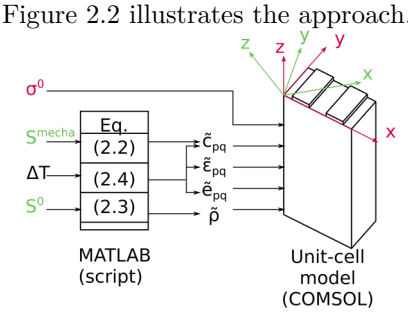

Figure 2.2 Illustration of the approach to consider the initial strain, stress and temperature in the unit-cell model.

2.1.3 Comparison with the literature, Nalamwar experiment

The approach we developed was confronted to an existing study made by Nalamwar *et al.* [62]. In this study, they investigated the effect of pure flexural strain on the SAW velocity at a fixed temperature. In their computation, they differentiated the effects of the strain and stress fields. The studied structure is a pure $LiNbO_3$ cantilever which length is along the Zc crystal axis. The IDTs are directly deposited on the surface of the cantilever that is bent by a defined force, see Figure 2.3.

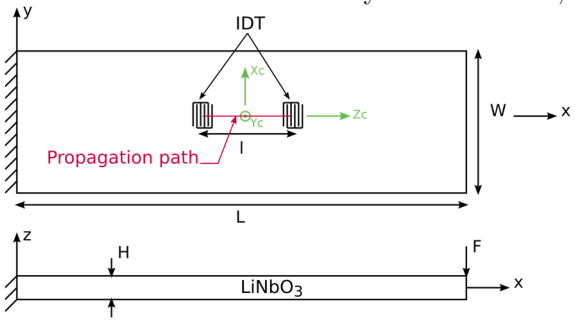

Figure 2.3 Schematic of the structure studied by Nalamwar *et al.* [62]. (X, Y, Z) is the coordinate system of the geometry, (Xc, Yc, Zc) is the crystal orientation coordinate system ; L is the length of the beam (33 mm); W is the width of the beam (5 mm); H is the thickness of the beam (1.97 mm); l is the length between the IDTs (5.08 mm); F is the bending force (1, 5, 10, 50 N).

To reproduce Nalamwar *et al.* [62]_study, we built a FEM model of the $LiNbO_3$ cantilever, from which we computed the average stress and strain fields generated for different forces along the propagation path. Note that the average strain field is computed in the local coordinate system of the crystal (Xc, Yc, Zc) (shown in green in Figure 2.3), while the stress field is computed in the coordinate system of the geometry (X, Y, Z) (in black in Figure 2.3). This makes their inclusion in the improved unit-cell model more convenient. Then we included these fields in the improved unit-cell model in order to compute their influence on the SAW velocity. Similarly to what was reported by Nalamwar *et al.* [62], we proceeded in several steps:

- firstly, we considered only the effect of the strain field on the material constants,
- secondly, we considered only the effect of the initial stress,
- thirdly, we considered only the effect of the strain on the density,
- finally, all these effects were combined (giving us the real velocity).

The obtained sensitivities at each step are shown in Figure 2.4 (left), where they are compared to those reported by Nalamwar *et al.* [62]. The fractional change in phase has also been computed (only for the combined effect) using the formula:

$$\frac{\Delta\phi}{\phi} = S^0 - \frac{\Delta v}{v_0}, \Delta\phi = \phi_{load} - \phi_0, \Delta v = v - v_0 \qquad 2.5$$

Where ϕ_0 and v_0 are the initial phase and SAW velocity in the section (when no load is applied), $S^0$and v are respectively the strain in the propagation direction and velocity in the loaded section. The obtained relative phase difference is shown in Figure 2.4 (right).

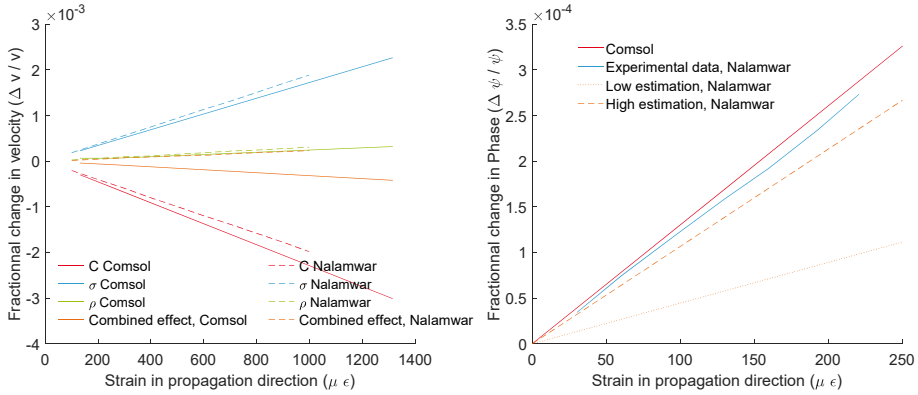

Figure 2.4 Computed sensitivities vs. Nalamwar *et al.* [62]. (Left) Relative change in velocity versus strain applied in the propagation direction. "C" denotes a simulation in which only the effect of the strain on the material stiffness is considered. "σ" denotes a simulation in which only the stress is considered. "ρ" denotes a simulation in which only the change in density is considered. (Right) Comparison of the computed combined sensitivity vs. literature results, by Nalamwar *et al.* [62].

In Figure 2.4 (left), we notice that the effect of the stress, the change in density and the change in material stiffness tend to compensate each other. Therefore, the

combined effect of all these phenomena on the velocity is small. We also notice, that Nalamwar *et al.* computed a positive shift in velocity vs. strain, whereas we computed a negative shift. Regarding the phase difference (Figure 2.4 right), the two numerical estimations they reported are lower than the experimental data, while the sensitivity we computed fits the experimental observations better.

2.2 Application 1: A simple sensor

In this first application, we studied a SAW temperature sensor submitted to a strain load. SAW sensors are promising solutions for high temperature applications (T>300 °C). For such applications, hard ceramic adhesives are often used to mount the SAW chip in its package. These glues might transfer unintended strain from the environment to the sensor. As SAW devices are also sensitive to strain, this might significantly disturb the temperature measurements. A possible solution is to use strain-insensitive crystal orientations for temperature sensor fabrication. However, orientations that also fulfil the other design requirements are hard to find. A second solution might be to take advantage of the anisotropic strain sensitivity of already optimized SAW devices and mount them in a way that the different strain effects compensate each other.

In this context, a first experiment was performed at CTR, in 2010. Researchers investigated different mounting angles for a SAW sensor glued on a steel blade submitted to a pure longitudinal stress field. The sensor was based on $LiNbO_3$ Y-Z, which is sensitive to strain and temperature. The objective was to find a mounting angle at which the sensitivity of the sensor to stress is close to zero.

Experiment description

Maier carried the experimental work [65] at CTR. In his experiment, a pure longitudinal stress deforms a steel blade. The stress on the blade is applied by imposing the displacement at both ends with the help of a custom-made jig. On the blade, two sensors are mounted:

- A $LiNbO_3$ Y-Z SAW sensor: it is a 2.45 GHz delay-line with 6 reflectors. This sensor is glued on the blade, at an angle α.
- A strain gauge (10×9 mm): it is glued on the opposite face of the blade and used as a reference deformation gauge.

The parameters of the experiments are shown Figure 2.5.

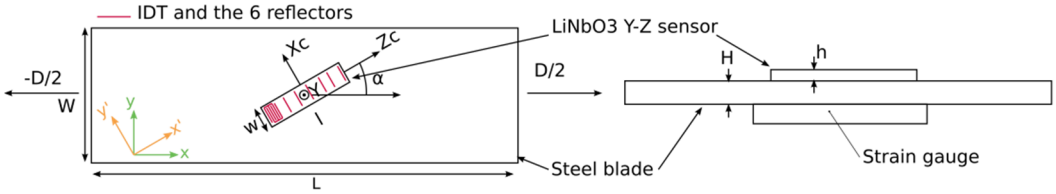

Figure 2.5 Illustration of SAW sensor on the steel blade. L is the length of the blade (140 mm); W is the width of the blade (15 mm); H is the height of the blade (1 mm); l is the length of the sensor (8 mm); w is the width of the sensor (1.6 mm); h is the height of the sensor (0.5 mm); α is the mounting angle of the SAW sensor ([0°,90°]).

Pictures of the sensors used for the experiment are presented in Figure 2.6. For the study of the sensitivity, we considered only the path between the first and sixth reflector which offers the largest length (denoted ΔL_{1-6}) and thus the largest sensitivity. ΔL_{1-6} is 3.4 mm long.

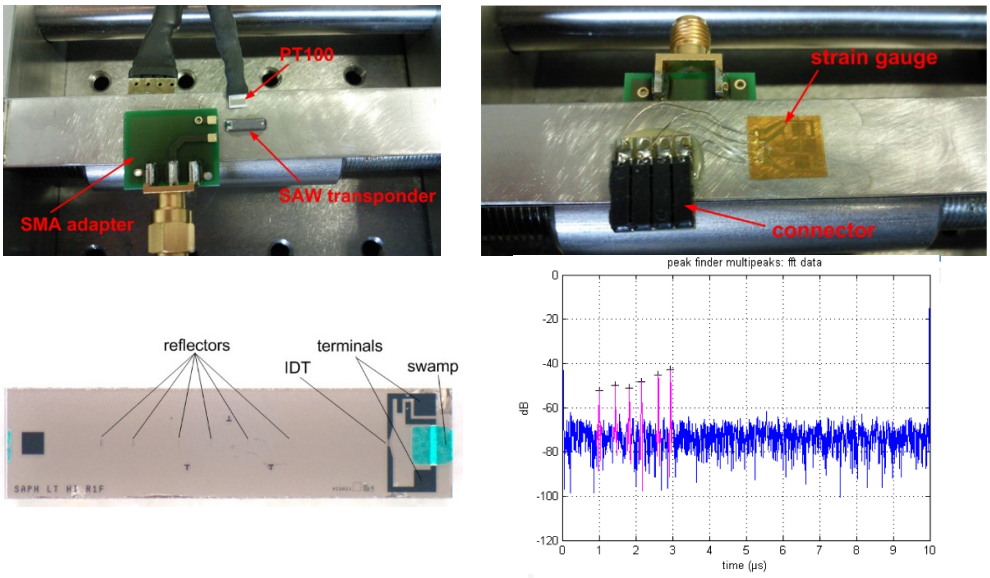

Figure 2.6 Picture of the experimental setup. (Top left) Picture of the SAW sensor on the blade. (Top right) Picture of the strain gage on the opposite side. (Bottom left) Detailed view of the sensor where we see the six reflectors, the IDT that generates the wave and the contacting pads. (Bottom right) Time response of the sensor.

As mentioned already, the objective of this experiment was to find, in this specific stress field, a mounting angle that results in a minimal sensitivity of the sensor to the environmental strain. The principle is to benefit from the anisotropic sensitivity of $LiNbO_3$ to strain which is much larger in the direction of the wave propagation. Consequently, if the sensor is mounted with its propagation direction along a minimal strain axis, the effect of this strain should be minimized.

For such a simple beam submitted to a pure longitudinal stress, the generated strain field is well known. It is given in the green axis system as pictured in Figure 2.5.

$$S = \begin{bmatrix} S_{xx} & 0 & 0 \\ 0 & S_{yy} & 0 \\ 0 & 0 & S_{zz} \end{bmatrix}_{x,y,z} = \begin{bmatrix} S_{xx} & 0 & 0 \\ 0 & -\nu S_{xx} & 0 \\ 0 & 0 & -\nu S_{xx} \end{bmatrix}_{x,y,z} \qquad 2.6$$

This strain field can be expressed in the rotated axis system using a simple rotation of the angle α around the z-axis (see details in Appendix C.1)

$$S' = \begin{bmatrix} S_{xx}\cos(\alpha)^2 - \nu S_{xx}\sin(\alpha)^2 & (S_{xx} - S_{yy})\cos(\alpha)\sin(\alpha) & 0 \\ (S_{xx} - S_{yy})\cos(\alpha)\sin(\alpha) & S_{xx}\sin(\alpha)^2 - \nu S_{xx}\cos(\alpha)^2 & 0 \\ 0 & 0 & S_{zz} \end{bmatrix}_{x',y',z'} \qquad 2.7$$

Since we want to find the angle α that minimises the strain in the propagation direction (Ox'), we have the equation:

$$\alpha = min\,(S_{xx}\,cos(\alpha)^2 - \nu S_{xx}\,sin(\alpha)^2) \qquad 2.8$$

The minimum of this function is actually a zero which occurs at α=61.3° for a Poisson's ratio ν=0.3. Four different angles (0°,60°,70°,90°) were investigated experimentally. The experimental results are reported at the end of this section, in Figure 2.8, where they are compared to the simulation results described below.

Step1: Static simulation of the strain and stress fields over the propagation path

A static simulation of the complete system comprising the blade and the SAW sensor is performed in COMSOL. The displacement amplitude at the ends of the blade is pre-defined (i.e. imposed), to apply a constant stress on the blade. To simplify the model, the glue used to mount the SAW sensor on the metallic blade is not considered. In addition, the very thin IDTs and reflectors at the surface of the piezoelectric substrate are not part of the model. The stress and strain fields on the surface of the sensor are computed, for α=0° to 90° (with 5° steps). An example of the (von Mises) stress and deformed shape of the blade is presented in Figure 2.7 (left). From these simulations, we extract the strain and stress distributions along the acoustic path of the sensor. The resulting strain components are shown in Figure 2.7 (right). On this graph, the two blue lines denote the position of reflectors 1 and 6. The stress and strain fields vary along the acoustic path. Their averaged value arethen used to compute the velocity change.

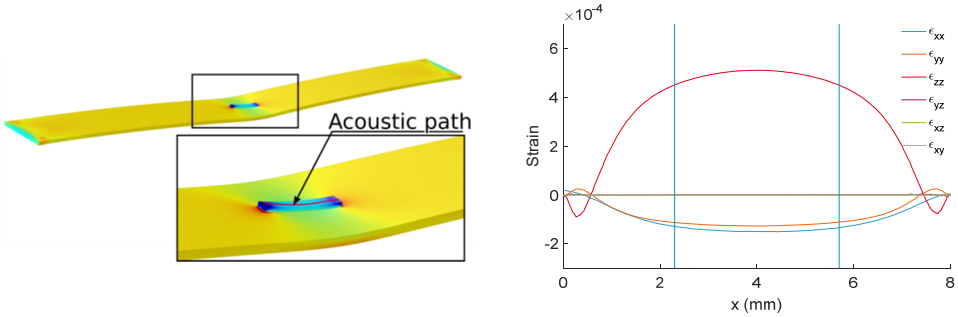

Figure 2.7 Stress and strain fields in the structure. (Left) von Mises stress field in the entire structure at an angle α=0°. (Right) strain components along the acoustic path of the sensor, at the same angle.

Step 2: Simulation of the acoustic behaviour

For this first application case, we didn't need to compute the complete set of COM parameters. It was sufficient to determine the change in the SAW free velocity. Indeed, the sensor is a delay-line; consequently, most of the wave propagation takes place on a substrate free of electrodes. The free velocity of the SAW is computed with a COMSOL eigenvalue analysis using the improved unit-cell model without top electrodes. To determine the free velocity, the top surface of the unit-cell model

must be free of charge. With this condition, the eigenvalue analysis of the unit-cell model yields a single frequency for the Rayleigh mode which corresponds to the free velocity. We can then determine the change in free velocity due to stress and strain fields computed beforehand. From the change in velocity, we compute the change in phase using formula (2.5). The computed sensitivities at the different angles are shown in Figure 2.8 (left). Figure 2.8 (right) shows the phase shift for the four different mounting angles depending on the longitudinal strain measured on the opposite side of the blade (*i.e.* using the reference strain gauge). The computed results are compared to the experimental results obtained previously by CTR.

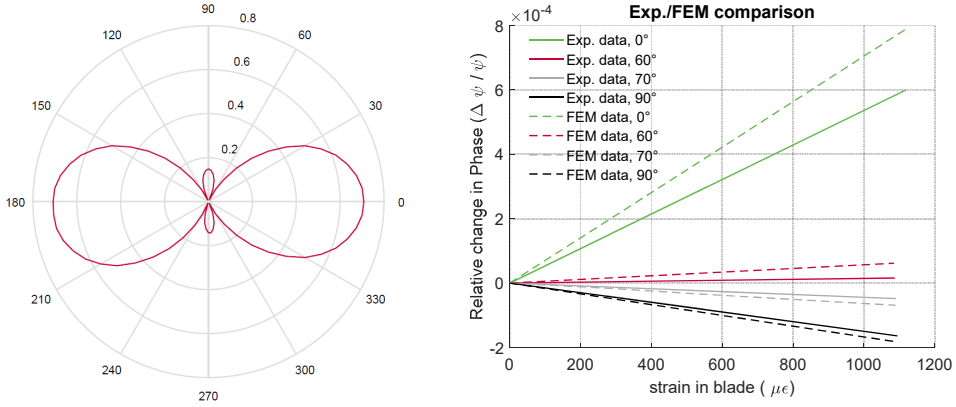

Figure 2.8 Sensitivity of the sensor to strain at different orientations. (left) Polar representation of the computed sensitivity. (Right) Comparison of the sensitivities computed using the unit-cell model and the experimental data.

A specific mounting angle is obtained, at which the sensitivity to a pure longitudinal stress is close to zero. Experimental and numerical results are in accordance. They both give a similar value (about 60 degrees) for this angle. Discrepancies between the experimental and simulation results could be explained by the fact that the simulation does not take into account the glue. There are also substantial uncertainties on the material constants.

This study validated the concept that an appropriate orientation might be used (at least in specific cases) to strongly reduce the strain effect on a SAW temperature sensor.

2.3 Application 2: Brain Pressure sensor using a bilayer structure

In this section, we investigate a more complex sensor based on a bilayer structure with the combined effects of temperature and strain. The sensor we studied was designed to detect small changes in Intra Cranial Pressure (ICP). Monitoring of the ICP is vital in some applications since an elevated ICP can lead to serious brain damages and death. In this context, SAW pressure sensors are ideal candidates, which benefit from their small size and passive (*i.e.* without embedded electronics) wireless operation. Therefore, they require less maintenance operations and are less prone to failure. The SAW sensor can be implanted after surgery, directly on the skull, where it detects pressure through a hole, drilled in the skull bone. It needs to be connected to an antenna implanted between the bone and the scalp. It becomes therefore possible to interrogate the sensor wirelessly, through the scalp. The first prototype of an implantable SAW ICP sensor developed by CTR was introduced in 2013 [66]. The demonstrator was based on a 2.45 GHz SAW Reflective Delay-Line (RDL) deposited on Y-Z Lithium Niobate. It uses a single delay-line which reflectors have been positioned to ensure maximum pressure sensitivity while allowing a thermal compensation (see explanations in section 2.3.1 below and [67]). However, the sensor exhibits flaws, which need to be understood in order to further improve it. For instance, there is a non-linearity in the temperature sensitivity that prevents the sensor from being used above 45 °C.

Using the model we developed, the sensitivity of the sensor to pressure could be computed and compared to experimental results. The origin of the residual sensitivity to temperature and the non-linearity in the thermal response of the sensor could be identified.

2.3.1 Design of the sensor

The sensor is made of a thin piezoelectric layer of $LiNbO_3$, (wafer-)bonded to a Silicon substrate using a thin Au/Cr bonding layer. A cavity is etched in the Silicon substrate (over the whole Si thickness, up to the $LiNbO_3$ layer, see Figure 2.9). The $LiNbO_3$ above the cavity then constitutes a membrane that is deformed under pressure. A reflective SAW delay-line is patterned on the surface, over the whole structure (incl. the membrane). When a pressure difference is applied between the cavity (reference pressure) and the outside, the stress and strain generated on top of the membrane affects the SAW velocity.

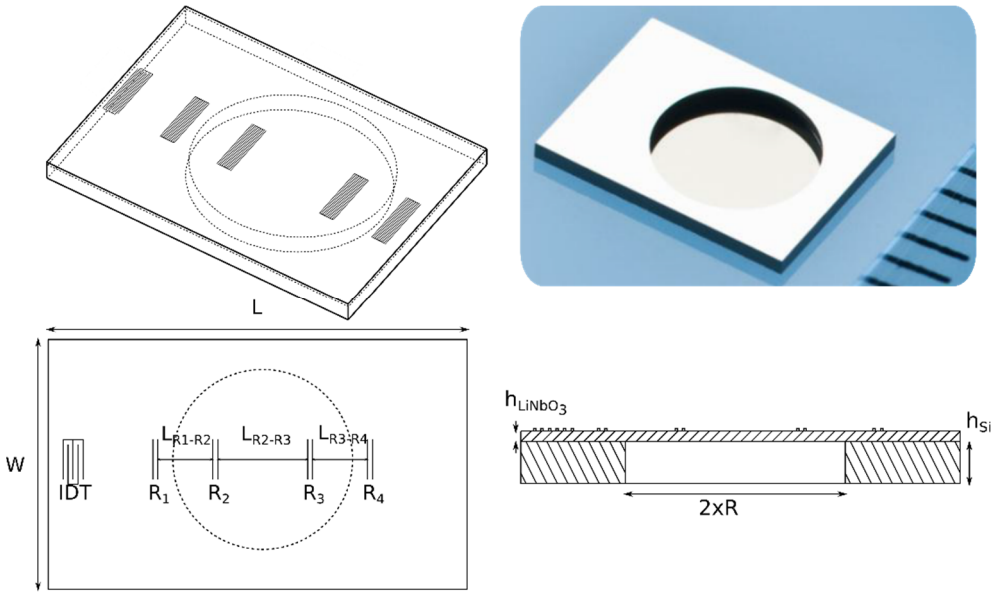

Figure 2.9 Illustration and picture of the ICP sensor. The picture of the bottom-side of the sensor shows the cavity underneath the membrane. The schematics show the dimensions of the sensor in which:

- L **is the sensor length (7 mm);**
- W **is the sensor width (5 mm);**
- R **is the membrane radius (2.35 mm);**
- h_{LiNbO_3} **is the height of the $LiNbO_3$ layer (30 µm);**
- h_{Si} **is the height of the Silicon substrate (500 µm);**
- L_{R1-R2} **is the length between reflector 1 and 2 (1360 µm);**
- L_{R2-R3} **is the length between reflector 2 and 3 (2720 µm);**
- L_{R3-R4} **is the length between reflector 3 and 4 (1360 µm).**

The propagation path of the acoustic waves is divided into three sections that are designed to optimize the sensor sensitivity to pressure (see Figure 2.9). The first section L_{R1-R2} and third section L_{R3-R4} have equal lengths and generate the respective delays τ_1 and τ_3. The second section L_{R2-R3} is twice longer and generates a delay τ_2. Each section corresponds to different pressure and temperature sensors. They are designed to work in a so-called dual mode. They are identically sensitive to temperature variations but are subjected to strain fields of opposite signs. The sensor sensitivity is obtained by computing the quantity $S = \tau_2 - (\tau_1 + \tau_3)$ which makes it possible to minimize the temperature sensitivity, while increasing the pressure sensitivity.

The positions of the reflectors R2 and R3 were determined using an analytical model of the membrane to ensure that section L_{R1-R2} and L_{R3-R4} are submitted to longitudinal strains of opposite signs compared to that in the middle section L_{R2-R3}. As a consequence, τ_2 and $\{\tau_1, \tau_3\}$ have opposite signs and the quantity S is maximum.

The position of the reflectors is determined considering only the longitudinal strain, which has the biggest influence on the SAW velocity. The longitudinal

strain in a homogeneous membrane under pressure is computed from the following expression (see Appendix C.2):

$$\epsilon_{rr} = \frac{Pz}{16D}(R^2 - 3r^2) \qquad 2.9$$

It is shown in Figure 2.10. On this graph, the vertical lines represent the positions of the reflectors. Reflectors R2 and R3 are positioned on the zeros of the longitudinal strain ϵ_{rr}.

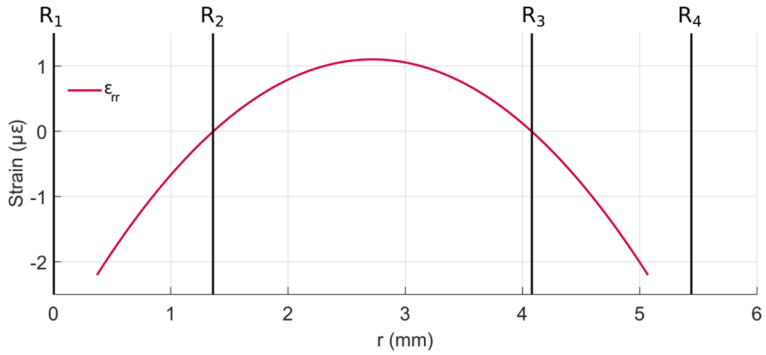

Figure 2.10 Longitudinal strain in the ICP sensor for a pressure P=1000 Pa. The black vertical lines represent the positions of the reflectors on the acoustic path.

In such configuration, the temperature sensitivity is directly proportional to the propagation length. Therefore, the combined sections L_{R1-R2} and L_{R3-R4} generate the same delay as section L_{R2-R3}, which is twice longer. Consequently, the quantity $S = \tau_2 - (\tau_1 + \tau_3)$ should be temperature independent.

2.3.2 Simulation of the SAW sensor sensitivity to pressure

To determine the SAW sensor sensitivity to pressure only, the simulation is carried out at the reference temperature T_0 (in our case, T_0=20 °C).

Step 1: Static simulation of the pressure effect

As a first step, we built a static model of the whole sensor, in which we did not consider the acoustic phenomena. Taking advantage of symmetries in material, geometry and load, we modelled only a quarter of the SAW sensor. In our configuration, the acoustic path of the sensor lays along the Z crystallographic axis of $LiNbO_3$ (i.e. the material tensors must be rotated accordingly, using the following Euler angles: 0,90,90). The substrate is made of a single Silicon crystal. The material parameters used for this study are given in Appendix B. The boundary conditions are illustrated in Figure 2.11. The displacements of the sensor are prescribed at the bottom of the substrate. Pressure is applied inside the cavity, with respect to the outside pressure. The mesh is based on prismatic element (for the entire geometry). It was refined near the edges of the membrane, where we expect some concentration of stress.

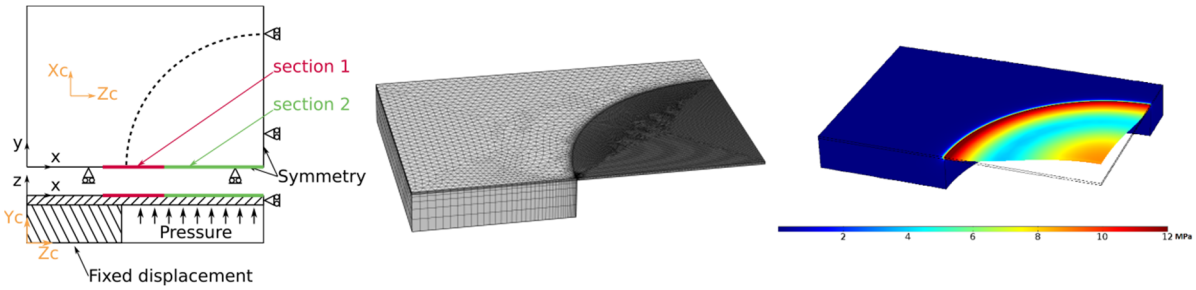

Figure 2.11 Numerical static model of the ICP sensor. (Left) Model for the static simulation of the entire sensor. (Middle) Representation of the mesh. (Right) Representation of the von Mises stress (MPa) over the structure, for a 3000 Pa applied pressure.

The model yields the stress and strain fields along the SAW propagation path. The results are presented in Figure 2.12, where they are compared to the results obtained analytically. Because only a quarter of the entire geometry is modelled, we do not have the result on the entire SAW propagation path. Nevertheless, we can extrapolate the stress and strain fields on the second half of the section L_{R2-R3} and on the section L_{R3-R4} using the symmetry conditions.

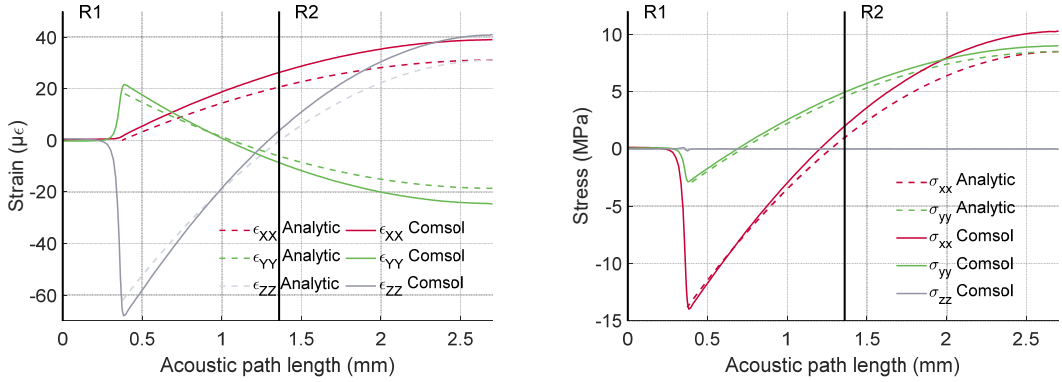

Figure 2.12 Analytical and numerical stress and strain fields, at P=3000 Pa. The vertical lines R1 and R2 denote the positions of the first and second reflectors. Note that the strain fields are given in the crystal axis orientation (Xc, Yc, Zc) and the stresses are given in the geometry directions (X, Y, Z).

These strain and stress fields are then included in the improved unit-cell model, where they are used to compute the change in SAW velocity due to pressure (see Step 2, hereafter). However, only their averaged values over the section length are included in the model, which is still a good approximation as we consider only the linear effect of strain and stress on the material properties in the improved unit-cell model.

Step 2: Dynamic simulation: determination of the change in wave velocity due to pressure

The effect of strain on the material parameters was taken into account first, using the third order coefficients of $LiNbO_3$ from [63], see Appendix B.1. Using an eigenfrequency analysis with free boundary condition at the top surface, we then

computed the change in free velocity due to the presence of the strain and stress fields. We then computed the relative phase shift using equation (2.5). It was then possible to compute the actual phase shift, from the section lengths. The numerical sensitivity is compared to the experimental results, in Figure 2.13. The computed sensitivity is 0.0879 rad/mbar, which is in almost perfect agreement with the experimental one. Note that the sensitivity is strongly influenced by the thickness (Figure 2.13, right). This hints towards a future potential problem, as it is difficult to obtain reproducible membrane thicknesses over the whole wafer, using standard fabrication processes (polishing).

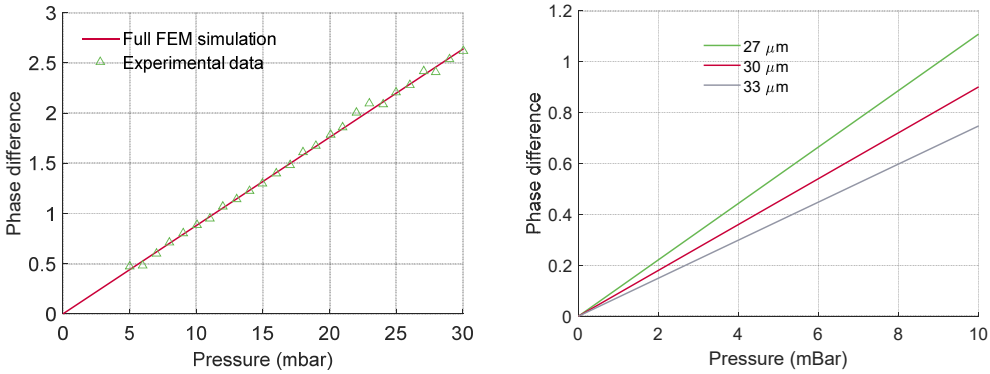

Figure 2.13 Sensitivity of the ICP sensor to pressure. (left) Computed sensitivity compared to the experimental results. (Right) Sensitivity computed for different membrane thicknesses.

In our case, the computation of the free-surface wave velocity is enough to calculate the sensor sensitivity. However, the whole set of COM parameters was computed to illustrate the general computation procedure.

We summarize in Table 2.1 the obtained COM parameters, for the two different sections, when a pressure of 3000 Pa is applied on the membrane. For comparison purposes, we also computed the COM parameters in the initial state, where no pressure is applied. One notices from these results that the first three COM parameters of "loaded section 1" are bounded from below by the values of "loaded section 2" and from above by those of the "unloaded section 1". The opposite bounding happens for the fourth COM parameters. It can be explained by the fact that the COM parameters are more influenced in section 2 compared to section 1, although section 1 is locally subjected to a higher level of stress (notably near the edges). This is because the strain and stress fields are first averaged over the whole section before computing the COM parameters. As "section 1" extends over the substrate where there is almost no stress/strain, this leads to "section 1" COM parameters being less affected in averaged than "section 2" COM parameters, although "section 1" comprises the point of maximum stress/strain.

Normalized parameter	Initial state unloaded	Section 1 loaded	Section 2 loaded	Unit
v_{SAW}	3432.907	3432.435	3432.230	m/s
$\kappa_p(=\lambda\kappa_{12})$	3.271	3.227	3.226	%
$\zeta_n\left(=\zeta\lambda^{\frac{3}{2}}/W^{\frac{1}{2}}\right)$	53.713	53.625	53.528	$10^{-5}\times\Omega^{-\frac{1}{2}}$
$C_n(=C\,\lambda/W)$	40.959	41.031	41.109	$10^{-11}\times F/\mu m/period$

Table 2.1 COM parameters in initial state and under 3000 Pa load. The initial state values are identical for sections 1 and 2.

2.3.3 Simulation of the SAW sensor residual sensitivity to temperature

The sensitivity to temperature is computed without any pressure applied. As the sensor is made of two different materials, strain and stress fields are generated when the sensor is heated up (bimorph effect). This affects the wave propagation conditions, in addition to the pure temperature effect itself.

Step 1: Static simulation of the thermal effect

A static thermomechanical study was carried out to determine the initial stress and strain fields due to the bimorph effect. We used the same model (static) as previously and applied a homogeneous temperature field. The material constants necessary to this study are reported in Appendix B. The resulting strain and stress fields generated by temperature elevation are significant. They are of the same order of magnitude as those computed when applying pressure only (see Figure 2.14). These fields have an influence on the surface acoustic wave behaviour and they should be considered in the computation of the wave velocity.

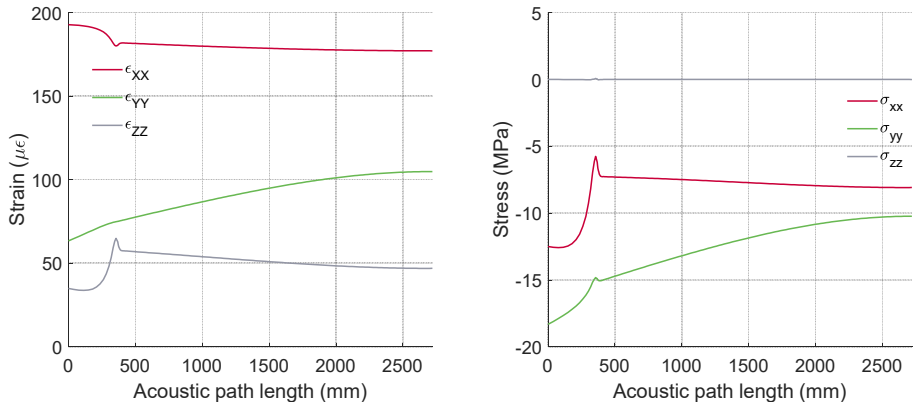

Figure 2.14 Stress and strain fields in the principal directions, along the acoustic path, generated by a temperature increase of 10 °C ($\sigma_{zz}=0$).

Step 2: Dynamic simulation, determination of change in wave velocity due to temperature

The acoustic behaviour under thermal load is obtained using the improved unit-cell model, which now also includes the temperature as well as the stress and strain fields computed in Step 1. The COM parameters were extracted at T_1=30 °C. The parameters are given in Table 2.2 where they are compared to the COM parame-

ters obtained for pure $LiNb0_3$ (used as a reference), at the same temperature (T_1). The comparison of the expected velocities in the "pure $LiNb0_3$" and "actual configuration" cases demonstrates the significant additional effect of the bimorph-related stress and strain fields.

Normalized parameter	Initial state at T_0	Section 1 at T_1	Section 2 at T_1	Pure $LiNbO_3$ at T_1	Unit
v_{SAW}	3432.907	3429.736	3429.765	3429.467	m/s
$\kappa_p(=\lambda\kappa_{12})$	3.271	3.219	3.219	3.218	%
$\zeta_n(=\zeta\lambda^{3/2}/W^{1/2})$	53.713	53.762	53.767	53.638	$10^{-5}\times\Omega^{-1/2}$
$C_n(=C\lambda/W)$	40.959	41.196	41.191	41.294	$10^{-11}\times F/\mu m/period$

Table 2.2 COM parameters, at T_0 and T_1=T_0+10 °C.

These parameters (Table 2.2) allow to compute the sensor sensitivity to pressure and temperature, taking the bimorph effect (thermal stress) into account (see Figure 2.15). The results show that taking the thermal stress into account definitely improves the accuracy of the simulation. The remaining discrepancy between experimental and numerical results could be due to the unknown pre-stressed state of the membrane (residual stress due to manufacturing) or to the inaccuracy of the third order material coefficients.

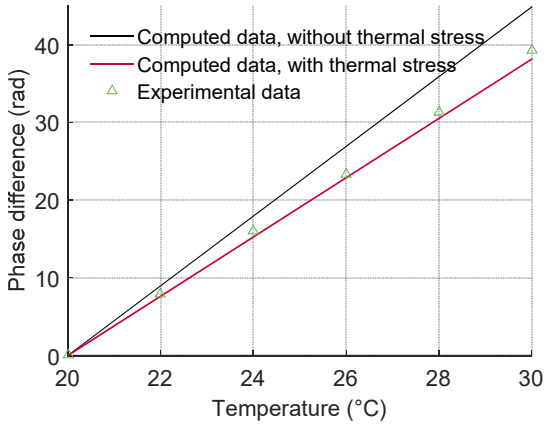

Figure 2.15 Sensitivity of the ICP sensor to temperature, computed between reflectors 1 and 4.

The discrepancy may also be due to the "incomplete" change of the elastic constants in the strained material (2.2). Indeed, differently from [62] and [63] where expanded internal energy and thus thermodynamic tension was used, it was shown in [57], [68] and [69] using proper (rotationally invariant) nonlinear electro-elastic equations and a special thermodynamic functional that the effective nonlinear elastic constants present two additional terms that are proportional to the displacement gradients. Nevertheless, the latter are not direct outputs of commercial finite element codes. Thus, they need heavy numerical (compared to the expected gained accuracy versus experimental results) and non-accurate (due to the required numerical differentiations) post-treatments. For these reasons, it was pre-

ferred here to use the simpler relation (2.2). This practice is admitted by the ANS/IEEE standard on piezoelectricity [70] (see page 42 therein).

It is worthy to mention that, although pressure and temperature variations were considered here individually, the present analysis can be used for their simultaneous variations. In this case, the strain S in (2.9) should be replaced by $S_{tot} = S + S_{th}$, where S_{th} is the thermally induced strain while S is due to the pressure variation.

2.3.4 Buckling effect

The thermally induced stress and strain fields can also result in a more dramatic change in the device behaviour, as they can lead to the buckling of the membrane above a given temperature threshold. We presumed that buckling explains the discontinuity observed at ~43 °C, in the phase versus temperature curves of peaks R4, obtained for one test device (see Figure 2.16). This discontinuity is a major issue, as 43 °C is still located in the operating range of the ICP sensor.

To confirm the root-cause of the observed discontinuity, we developed first an analytical model to compute the theoretical critical buckling temperature of a homogenous membrane (see model description in Appendix C.3). This model yields a critical temperature of ΔT_C=15.3 °C (see equation C.25), which is close to the observed experimental value (~23°C). The buckling generates a displacement of the membrane, which was analytically computed to be close to 50 µm, for an extra temperature elevation of 20 °C, above the critical temperature (see [71]).

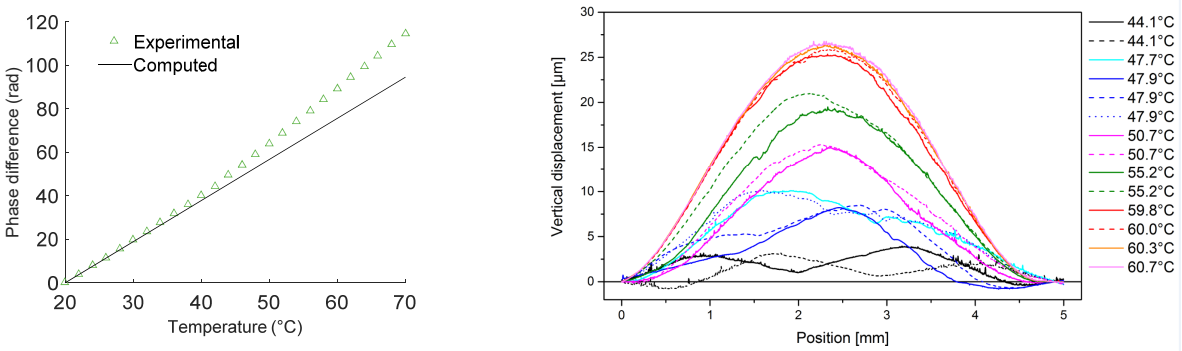

Figure 2.16 Experimental behaviour of the sensor in response to temperature increase. (Left) Phase difference between reflectors 1 and 4, versus temperature. (Right) Evolution of the shape of the membrane versus temperature, in the absence of applied pressure (*i.e.* deformation due to temperature changes only). The measurements were done using a profilometer (Dektak XT-A Surface Profil) and a custom-made hot plate, to heat up the device.

The membrane displacement was then measured experimentally, versus temperature (see Figure 2.16). The measurements were performed at zero pressure (*i.e.* the pressure stayed constant and equal to the atmospheric pressure, on both sides of the membrane, during the whole experiment). The temperature was set using a custom-made hot plate. The deformation clearly increases with temperature, and a sudden change of the shape is observed, between 44 °C and 50 °C. The measure-

ments also show that the membrane was already in a deformed state, at room temperature. This is due to the residual stress that is generated in the $LiNbO_3$/Si structure after wafer bonding and concentrates in the membrane after the Si is etched away. Interestingly, the shape becomes more regular at higher temperature, when the thermally-induced deformation gets larger. At a temperature of 60 °C, we observed a displacement of approximately 25 µm.

Possible solutions to the buckling issue include thermal annealing (to reduce residual stress and shift the buckling point outside the temperature operating range of the sensor), and the pre-stressing of the membrane, to operate beyond the buckling point of the membrane, in a buckling-free deformation range. Another solution would be to modify the membrane shape in order to benefit from the anisotropic behaviour of the $LiNbO_3$ and shift the buckling point beyond 45 °C. However, such improvements will require more advanced simulations to be performed first, using (ideally) a dedicated FEM model.

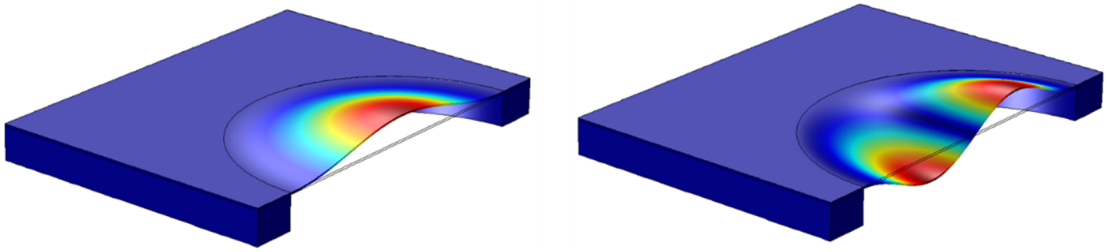

Figure 2.17 Deformed shape of the two first buckling modes of the ICP sensor. (Left) deformation at 44.5°C. (Right) deformation at 63.5°C.

We built such a 3D model using COMSOL Multiphysics. The model was used to perform thermomechanical studies of the membrane. It takes advantage of the symmetries of the geometry, material and loads, which make it possible to represent one fourth of the entire structure only. This simplification is acceptable, as the first buckling mode also has that symmetry. This was verified by making a first model of the entire geometry and solving the eigenvalue problem to determine the critical temperature and corresponding deformed shape (see Figure 2.17). Further simplification of the model is achieved, by not taking into account the IDT, reflectors and Au/Cr bonding layer. In the model, the thickness of the membrane is exactly 30 µm. The boundary conditions include fixed displacements at the bottom of the substrate. The temperature is considered homogeneous, in the entire structure. No residual stress is considered, in the model. Therefore, the membrane is perfectly flat, at the initial temperature T_0.

An eigenvalue analysis allowed to compute the buckling temperature as well as the deformed shape of the membrane, after buckling. The computations yield a buckling temperature of 44.5 °C, which constitutes a bifurcation point. The membrane can then deform (buckle) in one of the two possible directions, up or down. As both directions are equivalent, a solution must be found to impose the deformation in one chosen direction, numerically. This is achieved in COMSOL by

fixing beforehand a level of deformation on the membrane (by applying a pressure or a force on it), and by letting the FEM software search for the temperature that will correspond to this deformation, in the buckled state (see Figure 2.18). The results show a maximum displacement of 35 µm at 60 °C. This is 40% larger than the experimentally observed displacement (see Figure 2.18). The stress and strain fields along the acoustic path of the sensor were also computed. Therefore, it becomes possible to compute the additional (unwanted) sensor sensitivity to temperature in the buckled state. The effect of this extra temperature sensitivity generated by the buckling of the membrane on the sensor phase response is shown in Figure 2.18. The sensitivity S of the sensor is compared to the experimental curve for the whole temperature range. Before the buckling, the sensitivity S is negative due to a non-optimal positioning of the reflectors. After the Buckling, the model overestimates the temperature sensitivity S, but it gives the right tendency.

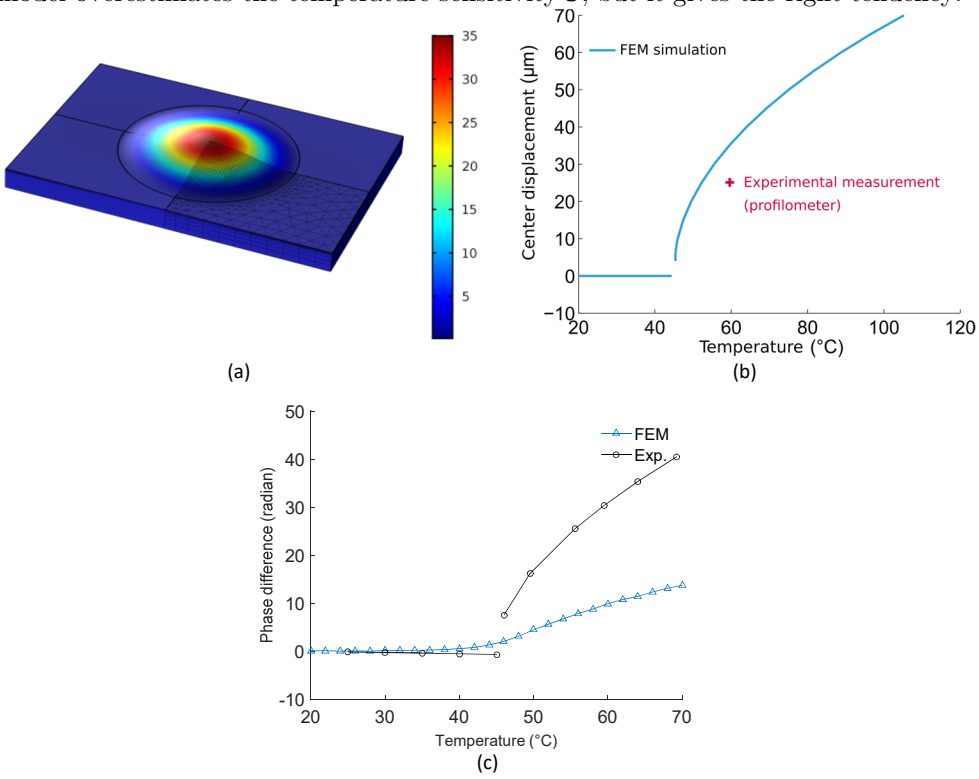

Figure 2.18 Post-buckling behaviour of the ICP sensor. (a) Deformed shape of the membrane after buckling, at a temperature of 60°C. Only one fourth of the model was actually used to perform the computations, following the symmetry of the system. (b) Displacement vs. temperature, at the centre of the membrane. (c) Phase response of the sensor (sensitivity S) vs. temperature, in the complete operating temperature range, including buckling effect.

2.4 Application 3: Innovative multi-layered sensor

As discussed before, SAW devices are sensitive to their surface-states (adsorption, pollution, degradation etc.), and they must be connected to an antenna. Therefore, they must be packaged. However, the housing can fail in many ways and consti-

tutes one of the main weak points of a SAW sensor. That is why a new kind of SAW devices was recently proposed [72], [73]. In the latter, multi-layered structures are used to guide and protect the wave below the surface. Housings are thus no longer needed. These package-less structures have the potential to strongly increase the reliability and ease-of-integration of SAW sensors, while reducing their development time and cost.

In this application, we propose and study a concept of package-less SAW sensor for Structural Health Monitoring (SHM) applications, based on a promising multi-layered structure. For this purpose, the section below is dedicated to a detailed description of this innovative concept. The following section gives an overview of some of the expected properties of the sensor in terms of temperature sensitivity and time response. The obtained results, limitations and expected technical challenges are discussed as a closure.

2.4.1 Description of the concept

The proposed concept of package-less sensor for SHM applications is shown in Figure 2.19. The sensor is based on a RDL made of an IDT and two reflectors. The waves are generated by the IDT and travel along the acoustic path of the device (*i.e.* along the X axis, in our case) within the ZnO layer. The pitch of the IDT (*i.e.* the distance between the centres of two successive fingers) must be chosen so that the working frequency of the device lies in one of the Industrial, Scientific and Medical (ISM) radio bands, thus allowing for the wireless interrogation of the sensor. In the presented concept, we found that a pitch of 859 nm is required to have the sensor operate in the 2.45 GHz ISM band. In this frequency range, it can be wirelessly interrogated using one of CTR developed Frequency Stepped Continuous Wave (FSCW) or Frequency Modulated Continuous Wave (FMCW) readers.

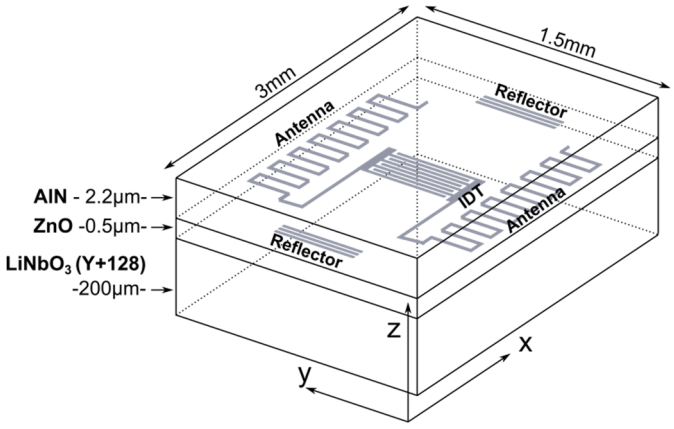

Figure 2.19 Concept of a package-less SAW sensor, based on an RDL design. A dipole antenna is connected to the bus-bars of the IDT. It is also buried in the multi-layered structure.

In this concept, the antenna required to interrogate wirelessly the sensor, is implemented directly in the structure, on the same physical level as the IDT and

reflectors. The patterning of the IDT, reflectors and antenna would therefore be performed in one unique photolithography step, which would help simplifying the fabrication process. Here, the sensor is based on a three-layer stack structure, namely AlN/ZnO/$LiNbO_3$ Y+128. This structure has recently been experimentally tested [73]. It uses a low acoustic-velocity ZnO layer stacked between two faster layers. The wave is guided in the low-velocity layer. We optimized the thicknesses of the layers iteratively using a modified version of the SAW unit-cell model, to ensure proper guidance of the wave at 2.45 GHz and a high-enough electromechanical coupling coefficient for wireless interrogation. The unit-cell model is presented in Figure 2.20; it uses a 3D geometry to account for the possible out of plane behaviour of the wave. The model enables fast computations of the phenomenological COM parameters. Later, they are used to compute the real electroacoustic response of a given RDL.

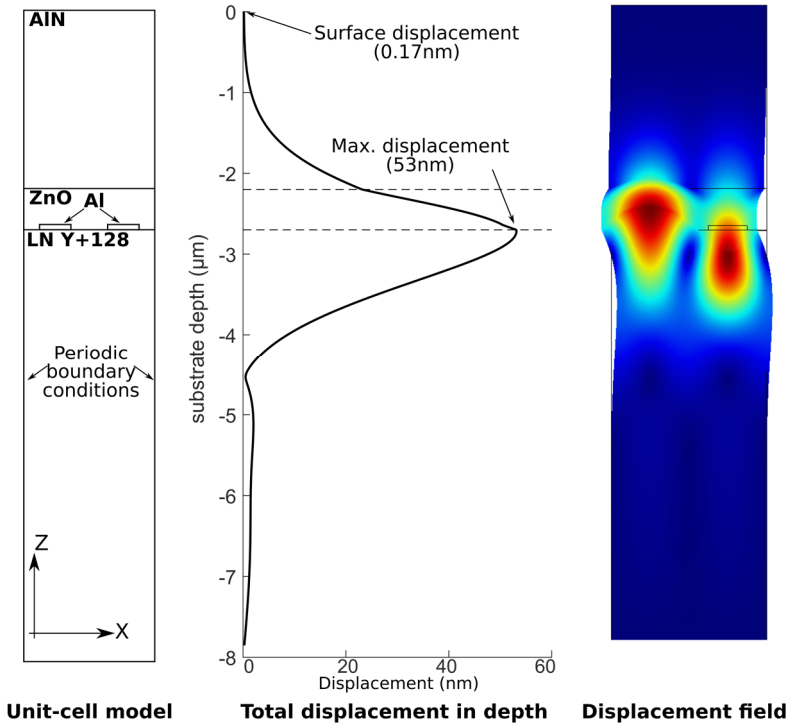

Figure 2.20 Unit-cell model and displacement field in the package-less sensor. (Left) representation of the unit-cell model, from which the COM parameters are computed using the electrostatic boundary conditions detailed in Table 1.3. (Right) 1D and 2D plots of the total displacement at the resonance frequency. Good guidance of the waves is considered achieved once the ratio between the surface displacement (0.17 nm) and maximum displacement (53 nm) is lower than 1%.

2.4.2 Temperature sensitivity and time signature

In this section, we evaluate the concept using the numerical tool we developed. In particular, we estimate the expected sensitivity of the wave velocity to temperature (TCD) so that the position of the reflectors can be later defined to achieve a given temperature sensitivity. The COM parameters of the structure are also extracted, allowing the computation of the signature (in time domain) of one possible sensor design. A diagram illustrating the simulation procedure we used to determine the expected sensitivity and time response of the sensor is presented in Figure 2.21.

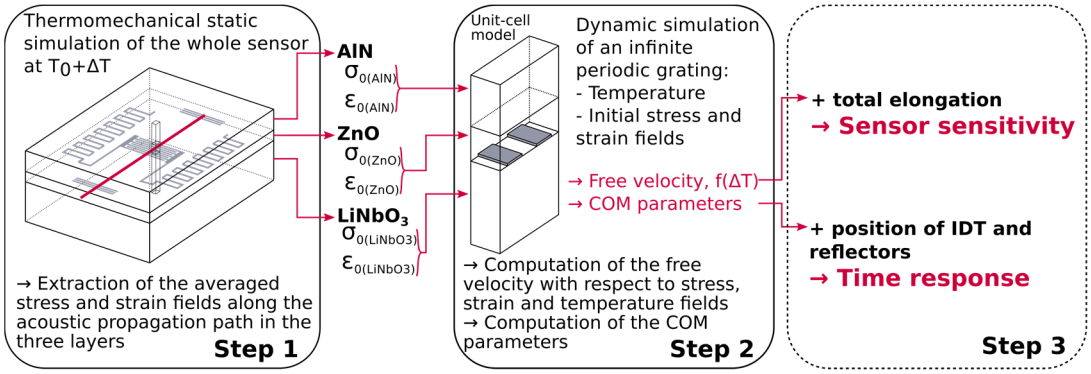

Figure 2.21 3-step simulation procedure used to determine the temperature sensitivity and time response of the package-less SAW sensor.

Step 1: Analysis of the static thermomechanical behaviour

In a first step, we simulate the entire sensor using a static thermomechanical FE analysis. The model neglects the thin and small metallic components of the device (IDT, reflectors, antenna). The resulting structure and the associated boundary conditions are shown in Figure 2.22. The latter also shows the FE mesh that was built using brick elements with a quadratic interpolation for the two considered "physics" (electrostatics and mechanics). We refined the mesh by increasing the number of elements in the layers and along the acoustic path. The materials data that we used for the simulation are given in Appendix B.

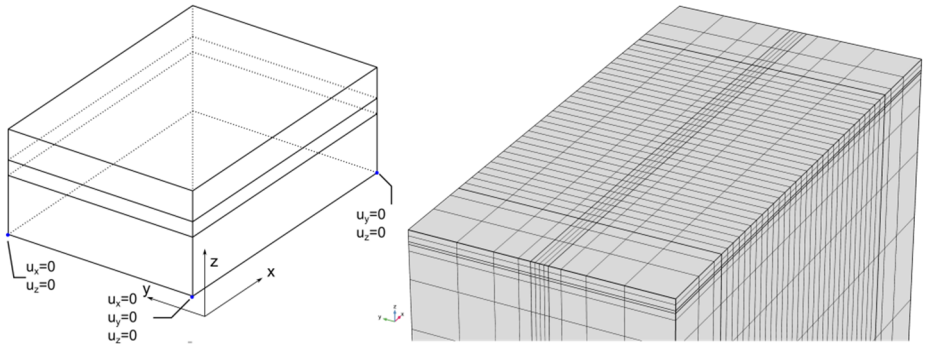

Figure 2.22 Numerical model used for the static study of the package-less sensor. (Left) model used for the static thermomechanical analysis. (Right) illustration of the used FE mesh (with 1.6×10^5 Degrees Of Freedom or DOFs). The aspect ratio along the z axis has been refined to have a better rendering of the thin layers.

Because the top layers are very thin compared to the substrate, it could lead to computation problems. Consequently, we carried out a convergence study of the FE model by monitoring the von Mises stress in the region of the acoustic path for the three different layers. The corresponding results are presented in Figure 2.23.

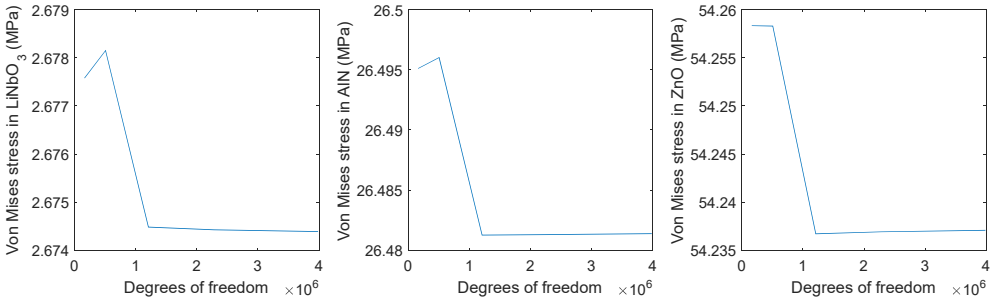

Figure 2.23 Convergence study of the static model of the package-less sensor. Curves representing the evolution of the maximum von Mises stress in the three layers versus the total number of DOFs. The retained mesh in the thickness consists of 3 FEs in ZnO layer, 6 FEs in AlN and 30 FEs in $LiNbO_3$, for a total of 4×10^6 DOFs.

In the present multi-layered structure, the strains are generated by temperature changes (through thermal expansion). Indeed, due to the fact that the layers have different Thermal Expansion Coefficients (TEC), strains are thermally generated. Therefore, the total strain is the sum of the thermal and elastic strains.

The simulation results presented in Figure 2.24 show that, due to TEC mismatches, a temperature increase generates discontinuities in the stress and strain fields at the interfaces. Nevertheless, in a given layer (except on the edges), the elastic and total strain fields (as well as the corresponding stress fields) are relatively homogeneous in the XY plane. The average value of a given field component over the whole surface can therefore be used as a good estimate of the field component at each location. Single 3×3 tensors are subsequently computed for each field, leading to three tensors per layer: elastic strain, total strain and stress. We therefore considered 9 tensors in the further computations.

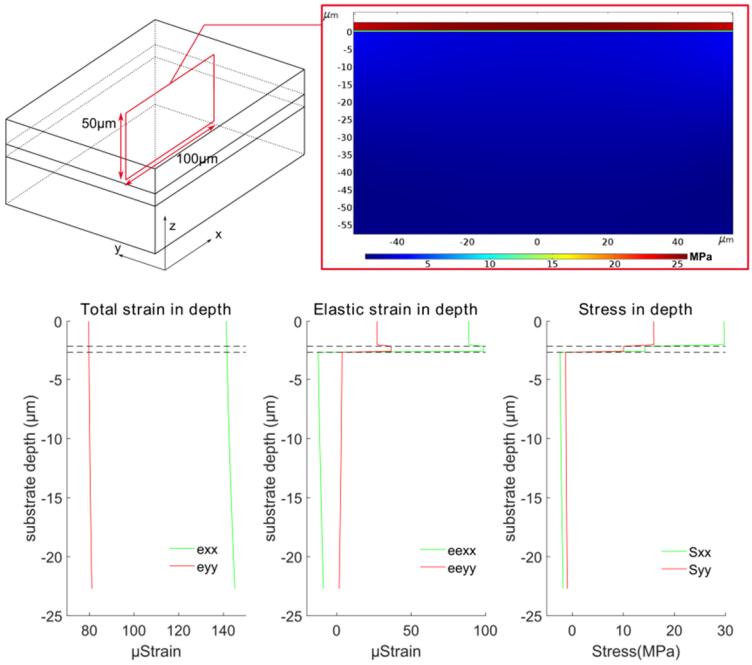

Figure 2.24 Strain and stress fields in the package-less sensor. (Top) Cross-section of the stress field generated in the multi-layered structure for a temperature increase of (only) 10 K. (Bottom) amplitude of the elastic strain and stress fields versus depth. Strong discontinuities appear at the interfaces. However, the fields are homogenous in the bulks, between the interfaces.

We evaluated the thermomechanical behaviour of the multi-layered structure for temperatures up to 150 °C. In particular, we computed the von Mises stress in the different layers. The results are shown in Figure 2.25. It appears from the latter that the stresses rise significantly in the two top layers (AlN and ZnO) with temperature, while those in the $LiNbO_3$ substrate remain low. Besides, we compared the von Mises stresses to their respective maximum tensile stresses which are reported in [74] and [75] to be $\sigma_{ZnO}^{Tenstress}$=412 MPa and $\sigma_{AlN}^{Tenstress}$=300 MPa, respectively. We noticed that the von Mises stress in the AlN layer exceeds the maximum tensile stress for a temperature elevation around 110 °C, thus limiting the operation of the sensor to temperatures below 130 °C. In addition, the strong discontinuities in the strain and stress fields, which are expected to appear at the interfaces when the temperature increases, might lead to delamination and failure at even lower temperatures.

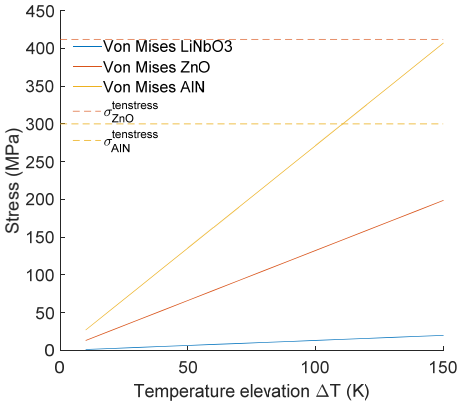

Figure 2.25 Von Mises stress in the 3 layers vs. temperature elevation. The horizontal dotted lines denote the maximum tensile stresses in AlN and ZnO.

Step 2: Analysis of the dynamic electromechanical behaviour

This time, we used an improved unit-cell model which FE mesh is presented in Figure 2.26.

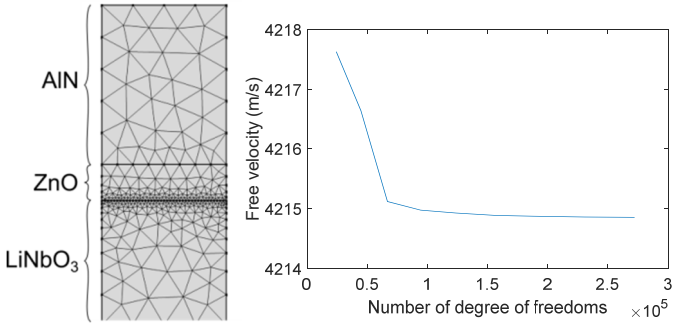

Figure 2.26 Convergence study, for the unit-cell model used to compute the properties of the package-less sensor. (Left) The FE mesh used for the convergence study. The pictured mesh has a low number of elements (18252 DOFs) for the sake of representation. (Right) Convergence of the free velocity vs. number of degrees of freedom.

The model does not consider the electrodes, as the free surface velocity is the only parameter of importance, in this study. The mesh consists of prismatic triangular elements with quadratic interpolations of the mechanical displacement and electric potential fields. We studied the convergence of the FE mesh by tracking the free velocity while increasing the number of DoFs (see Figure 2.26). We finally selected a FE mesh with 1.8×10^5 DoFs. The materials data used for the simulation are given in Appendix B. The so-called second-order coefficients were used to compute the material sensitivity to temperature, whereas third-order coefficients were used to compute the material sensitivity to strain. Stress effects were obtained using standard computation procedures, in pre-stressed state.

Unfortunately, as the third-order coefficients are not known for AlN and ZnO thin layers, we could compute the effect of stress and temperature in these two layers but not the effect of strain. Note that in addition to the change in wave velocity (Δv), the total deformation in the propagation direction ($\varepsilon_{xxtotal}$) is also

required to compute the TCD, according to the following relation: $TCD = \varepsilon_{xxtotal} - \Delta v/v$. The TCD values, obtained from the computations of the free-surface velocities at different temperatures, are given for the multi-layered structure in Table 2.3, where they are also compared to those of the reference $LiNbO_3$ Y+128 (LNY+128) orientation.

$\Delta T\ (K)$	Structure		v (m/s)	TCD ($10^{-6}/K$)
0	AlN/ZnO/LNY+128	Free surface	4215.08	35.0
10			4214.19	
50			4210.68	
100			4206.27	
0	LNY+128	Free surface	3981.93	71.4
10			3979.70	
50			3970.80	
100			3959.64	

Table 2.3 TCD values of the multi-layered and reference structures.

The obtained TCD can be used to set the position of the reflectors in order to reach a given temperature sensitivity. Indeed, the sensitivity $d\tau/dT$ of an RDL (where τ is the delay time of the echo and dT is the change in temperature) is directly proportional to $L \times TCD$, where L is the distance between the IDT and the corresponding reflector. Besides, it can be noticed from Table 2.3 that the obtained TCD is two times lower than that of a typical $LiNbO_3$-based SAW RDL sensor. This means that a sensor based on the newly described multi-layered structure should be twice longer (*i.e.* >10 mm-long) than a standard SAW RDL sensor in order to achieve the same absolute sensitivity.

We also computed the COM parameters at room temperature, for the multi-layered structure. We considered in the simulation Aluminium electrodes, with a metallization ratio η=0.5, a pitch of 859 nm and a thickness of 59 nm. The obtained COM parameters are presented in Table 2.4. The resulting approximated harmonic admittance is shown in Figure 2.27. These COM parameters are enough to compute the electroacoustic behaviour of the IDT and reflectors. The behaviour of the waves in the gaps between the IDT and the reflectors is simply described using the computed free-surface velocities. Note that the actual TCD of the real structure also depends on the material used to fabricate the IDT and the reflectors [76]. However, in the case of a long RDL that is essentially made of free space, this effect is negligible.

$v\ (m/s)$	4170.42
$\kappa_n(\%)$	-0.36
$\zeta_n\left(10^{-5}\Omega^{-\frac{1}{2}}\right)$	66.37
$C_n\ (10^{-11}\ F/\mu m/period)$	53.47

Table 2.4 COM parameters of the AlN/ZnO/LNY+128 structure with 59 nm-thick Aluminium electrodes deposited on the LNY+128 substrate and buried in ZnO. The metallization ratio is η=0.5. The propagation losses were not computed.

Table 2.3 and Table 2.4 therefore contain all the information that is required to compute the full electrical response of a given RDL design, based on 59 nm-thick Aluminium electrodes with η=0.5, as well as its thermal behaviour around room temperature.

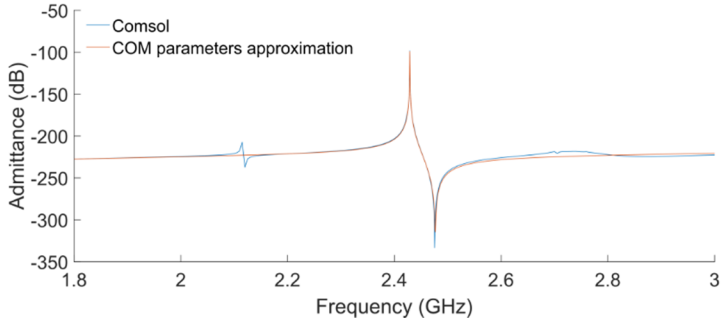

Figure 2.27 Harmonic admittance curves of the package-less sensor (blue: directly computed using full-FEM simulations; red: re-constructed using the computed COM parameters). Since the COM method is only a local approximation of the electroacoustic behaviour for a given mode, the first mode simulated in COMSOL at 2.1 GHz does not appear in the COM approximation.

Step 3: Response of the sensor, in time-domain

As mentioned above, the obtained COM parameters can be used to compute the actual electrical response of a sensor, in time domain, starting from the complete set of geometrical parameters of the acoustic path (*i.e.* number of fingers in the IDT and reflectors, aperture, respective position of the IDT and reflectors, electrical boundary conditions of the reflectors, etc.). The computation method is described in detail in [77]. We simulated a design similar to that presented in Figure 2.19. The IDT is made of 40 fingers (20λ, with λ=1.72 µm), with an aperture of 20λ. The short-circuited reflectors are made of 30 fingers, each. The gaps between the reflectors and the IDT are 1 mm (left Reflector-IDT) and 1.28 mm (IDT-Right Reflector), respectively. Note that the propagation losses (in ZnO and AlN) are not taken into account, here. Demonstrators are required to determine the losses experimentally. The expected signature of the sensor in time domain is shown in Figure 2.28. It is the inverse Fourier Transform of the frequency response of the device, computed in the 2.2-2.8 GHz band (12001 points). The two first peaks (at 0.5 µs and 0.62 µs) correspond to the direct echoes, from the two reflectors (single transit echoes). The other peaks correspond to multiple-transit echoes, between the reflectors and the IDT. Peaks three and five correspond to echoes that travelled two times between the IDT and the reflectors (double transit echoes). In peak four, two signals overlap. They were reflected by one reflector towards the other one (through the IDT), before getting reflected back towards the IDT (single + double transit echoes). For practical applications, only single transit echoes are usually used.

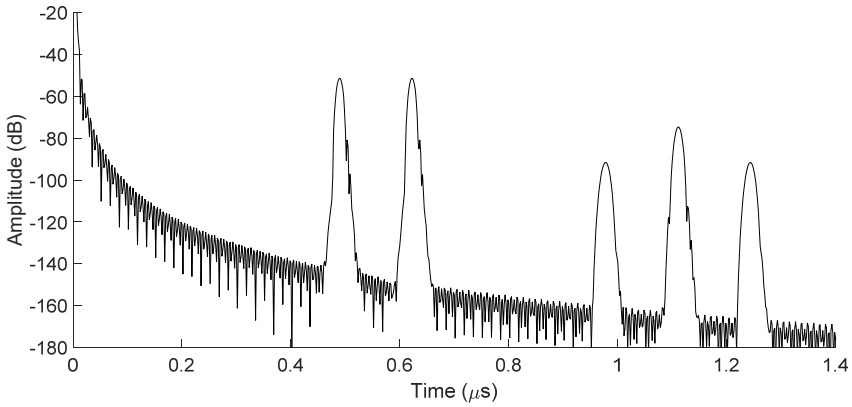

Figure 2.28 Time response of the 2-reflector RDL package-less sensor. (*i.e.* Reflection coefficient S11 in time domain without considering propagation losses in ZnO and AlN).

2.4.3 Summary, conclusions and perspectives

In the present section 2.4, we proposed an innovative package-less SAW delay-line structure that integrates an antenna. This device enables to fully remove the housing around the SAW sensor thus making it a simpler device that is easier to integrate in a SHM context. The SAW package-less structure is based on a multi-layered piezoelectric substrate comprised of AlN, ZnO and LNY+128. The stack thicknesses were designed so that the acoustic energy is guided underneath the surface, in the ZnO layer, making the sensor immune to surface perturbation. Additionally, the pitch of the interdigital transducer has been selected so that the sensor can be wirelessly and passively interrogated at 2.45 GHz using one of CTR readers. Using numerical tools, the shift in velocity due to temperature was estimated. Thus, the delay-line length was designed to achieve an expected sensitivity of 0.33 rad/°C. The reader planned for this application has a minimum resolution of 0.04 rad, when it receives a powerful signal from the sensor and considering averaging over few measurements. Therefore, the sensor resolution is estimated to be 0.12 °C. The time response of the sensor was computed and optimized using the COM method.

Although the presented concept is promising, the study highlighted several issues. Indeed, the sensor has relatively low TCD (in comparison to that of a standard RDL SAW sensor). In addition, because of the thermal stress generated in the multi-layer, the structure is expected to fail for temperature ~130 °C, nevertheless this might be sufficient for many SHM applications. Besides, a quite long antenna would be needed to interrogate the sensor at 2.45 GHz (>30 mm for a quarter-wave dipole antenna), resulting in a large sensor. Moreover, strong propagation losses are expected, which might cause a whole range of issues. First demonstrators and thorough experimental tests are now required to test the concept, assess the issues and propose corresponding solutions.

Chapter 3 Multi-layered filters for high frequency applications

The market for analog telecommunication filters is dominated by electro-acoustic technologies, essentially based on surface acoustic wave (SAW) and bulk acoustic wave (BAW) devices. There are two upcoming challenges for these technologies:

- The production of low-cost and high-quality filters for the Internet of Things (IoT) applications,
- The development of very-high frequency filters (up to 6GHz) to answer the 5G requirements.

To address these challenges, the BAW and SAW technologies are in competition. The pros and cons of both technologies are briefly summarized in the following paragraphs.

The main advantage of the SAW technology lies in its lateral-design capability (incl. apodization). However, the SAW technology suffers from several limitations. The SAW velocities on conventional piezoelectric substrates are low (<4000 m/s), which makes them more suitable for the lower frequency range (<2.5 GHz). To produce higher frequency filters, it is therefore necessary to drastically reduce the pitch and size of the IDT, which is a highly challenging task. Furthermore, the small size of the IDT generates power-handling issues (as the same power is applied on a much smaller surface) as well as impedance matching issues (due to the reduction of the static capacitance of the device). Besides, thin fingers are highly resistive, therefore they generate additional power-dissipation issues that might result in an unwanted increase of the device temperature. Moreover, the piezoelectric wafers used to produce SAW devices are limited in size (≤6-inch), which reduces the opportunities for cost reduction through the manufacturing of large batches. Finally, the SAW fabrication processes are not CMOS-compatible* which constitutes an issue for further integration of the devices.

The Thin Film Bulk Acoustic wave Resonator (TFBAR) technology is based on Aluminium Nitride (AlN) thin films vibrating between two metallic electrodes. These simple structures form resonators that may be used as building blocks for filtering applications (see Appendix A). Since AlN can be deposited on large Silicon wafers (up to 8-inch), TFBAR devices can be produced at lower cost, using CMOS-compatible processes. Additionally, the acoustic velocity of AlN is high, which makes this material more suitable for high frequency devices. Because of the diffi-

*CMOS (or IC -Integrated Circuit-) compatibility refers to the ability of a device to be integrated on a conventional CMOS chip, which imposes constraints on the production processes.

culty to grow high-quality thick layers, the resonance frequency of a TFBAR, which is inversely proportional to its thickness, is however limited to the high-frequency range (>1 GHz). The TFBAR devices are also more difficult to manufacture, and present lower coupling coefficients than their SAW counterparts. They also lack the lateral design capability of the SAW devices.

To face the mentioned upcoming challenges, a new class of devices must be developed to combine the best of the two technologies, *i.e.* lateral design capabilities and fast, highly coupled guided waves propagating in CMOS compatible thin films.

A new promising solution to achieve such devices was suggested by Bjürstrom *et al.* in 2005 [78] and has since been studied by numerous authors. It is based on high velocity and high-coupling plate modes (Lamb waves), usually guided in thin AlN piezoelectric layers and generated using IDT-like structures, or "electrodes". Such devices are called Lamb Wave Resonators (LWR). They make it possible to combine the best of the SAW and BAW technologies, as both lateral-design and guided bulk waves in thin films are used. Two configurations are used to trap the acoustic energy within the resonator, see Figure 3.1. In the first configuration, reflector gratings are used to reflect the waves towards the centre IDT, and therefore build a resonance cavity around it. In the second one, the free-edges of the suspended structure are directly used to reflect the waves, which makes it possible to reduce the size of the device. This last configuration is often referred to as Contour-Mode-Resonator (CMR).

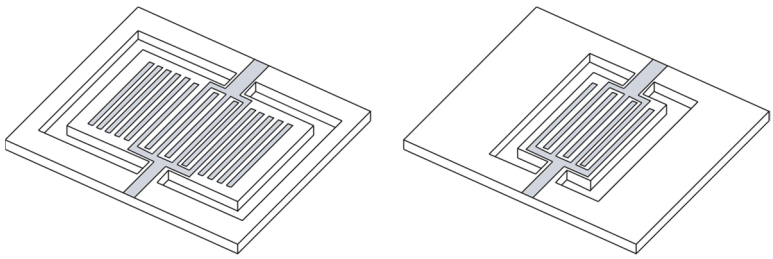

Figure 3.1 The two configurations used to trap the acoustic energy within the LWR. (Left) LWR using conventional finger reflectors to contain the acoustic energy within the IDT. (Right) LWR using the contour edges to reflect the wave towards the IDT. This device has a reduced footprint.

The generation of the Lamb waves is possible through different IDT-like or electrode configurations, which are detailed in Figure 3.2. The figure illustrates the electric fields generated in the four possible configurations. Each configuration excites the piezoelectric material in a specific way, which results in different coupling coefficients.

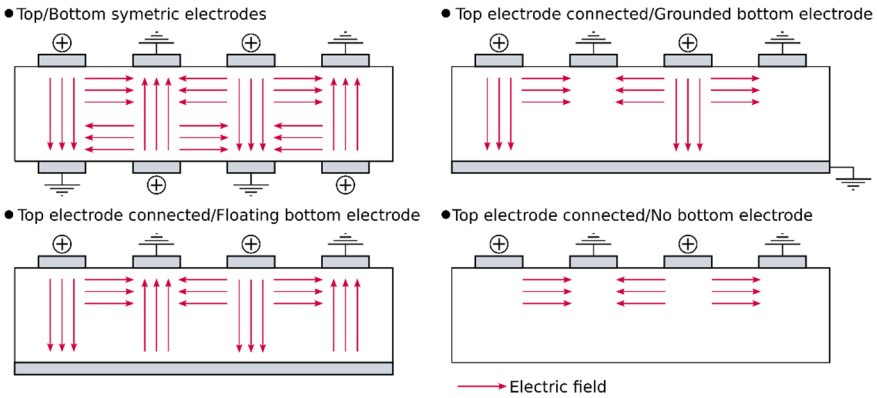

Figure 3.2 The four electrode configurations used to excite Lamb waves in piezoelectric films. The red arrows represent the main component of the electric field within the piezoelectric layer.

Bjürstrom *et al.* [78] [79] first produced a free-standing LWR made of c-axis oriented AlN. Using the first symmetric Lamb mode (S_0), they reached a resonant frequency of 570 MHz. However, the coupling coefficient of the obtained structure remained relatively low. In the following years, several authors published results based on improved designs [80]–[85]. The main results are summarized in table 3.1. Among these publications, Stephanou and Pisano [84] investigated two kinds of electrode configurations (double side electrodes and single side electrodes). They showed that, as expected, the double side electrodes generate a higher coupling. In [81], [82], Lin *et al.* investigated different configurations for the bottom electrode ("ground", "floating" and "open"). They could demonstrate that a higher coupling is obtained in the "floating" configuration. In [80], Lin *et al.* investigated a CMR with convex edges. The quality factor was significantly improved ($\times 2.6$), at the expense of a degraded coupling coefficient. In [86], Zuo *et al.* demonstrated a ladder type bandpass filter based on 1-port LWRs. Their best filter operated at 270 MHz and achieved a bandwidth of 0.34% at -3 dB. Similarly, Piazza *et al.* [87] developed a bandpass filter based on 2-port LWRs. The filters operated at 225 MHz and achieved a bandwidth of 0.22%. A review of the thin film LWR technology can be found in [88].

Following the example of the BAW technology, where BAW resonators are either free-standing (FBAR) or mounted on a reflective acoustic Bragg mirror (BAW-SMR, see Appendix A), Kone *et al.* [89]–[91] proposed and studied in 2010, a LWR solidly mounted on an acoustic Bragg mirror. They used a 1.7 µm thick AlN layer with Molybdenum electrodes on both sides. The top electrode was an IDT, and the bottom electrode was a floating metallic plane. They used the edges of the piezoelectric material as reflectors, in a CMR fashion. The Bragg mirror was made of six alternated layers of Silicon Oxicarbide (SiOC) and Silicon Nitride (SiN). In this configuration, SiOC and SiN are respectively the low and high acoustic impedance layers. The thickness of each layer was determined using the scattering matrix method, to reflect the longitudinal and shear polarizations of the S_0 mode. With this structure, they achieved a resonator operating at 1830 MHz,

with a coupling coefficient of 2% and a quality factor of 160. They could also demonstrate the co-integration of BAW and LWR on the same wafer. However, the low coupling coefficient and FoM of these devices blocked them from being further developed and commercialized.

Year, Author [ref.]	Type	Config.	Mode	F (MHz)	K (%)	T (nm)	λ (µm)	Q	FoM (K.Q)
2005-2006 Björstrom[78] [79]	Fingers reflectors	Top elec.	S_0	885	0.4	2000	12	250	1
		Sym. IDT		570	0.8	2000	18	880	7.04
2005 Volatier [85]	CMR	Floating bottom	S_0	92	0.8	550		2000	**16**
2006 Stephanou [84]	CMR	Sym. IDT	S_0	1283	0.415	1500	5.2	1420	**5.9**
				1180	0.49	1500	5.2	390	**1.9**
2006-2007 Yantchev [92]	Fingers reflectors	AlN on Diamond	S_0	890	0.34	n.a	12	2000	**6.8**
2010 Rinaldi [83]	CMR	Floating bottom	S_0	3040	1.5	250	4.8	520	**7.8**
				3460	1.85	250	4	500	**9.25**
				4540	1.3	250	2.8	360	**4.68**
2011-2014 Lin [82] [81]	CMR	Grounded	S_0	850.5	0.78	1500		800	6.2
		Floating		850.3	1.05	1500		850	8.9
		Open		948.1	0.18	1500		3033	4.6
2011 Lin [80]	CMR	Straight	S_0	492.8	0.18	1500		3280	**5.9**
		Convex		517.9	0.35	1500		1255	**4.4**
2010 Kone [91]	CMR SMR	Floating	S_0	1830	2	1700	8.4	160	**3.2**
2013 Konno [93]	Fingers reflectors	No bottom electrode	S_0	2630	7.39	1000	2	117	7.71

Table 3.1 Review of the LWRs found in the literature. The FoMs (in bold) are derived (see equation 1.4) from the other values.

Only recently, potential solutions to this issue have been proposed. They rely on doped-AlN layers with improved piezoelectric properties. These dopants partially replace (substitute) the Aluminium atoms in the AlN lattice. Several dopants were investigated in the past; Chromium (Cr) was investigated by Luo *et al.* [94], Erbium (Er) was investigated by Kabulski *et al.* [95] and Tantalum (Ta) was studied by Liu *et al.* [96]. However, the most promising dopant is Scandium (Sc). Akiyama *et al.* [97], [98] first studied this material. They reported a piezoelectric response up to four times larger than that of AlN, for sputter deposited AlScN layers. Matloub *et al.* studied TFBAR structures made of $Al_{0.88}Sc_{0.12}N$* [99]. They could observe a 40% increase in the d_{33} piezoelectric coefficient. In [100], these authors also studied the transverse piezoelectric coefficient e_{31}. The latter was found to be 50% larger in comparison to that of AlN. In 2013, Konno *et al.* reported a free-standing LWR based on AlScN [93]. They achieved a Scandium concentration close to 40%. They reported a coupling coefficient up to 7.39% and a quality factor of 117 resulting in a FoM of 7.71 at 2.63 GHz. In parallel to these

* The designation $Al_{(1-x)}Sc_xN$ will be used in the manuscript when necessary to denote a specific concentration of Scandium. The value of x stands for the atomic Scandium concentration in percentage.

experimental developments, Density Functional Theory (DFT) calculations were performed by Caro *et al.* [101] and Tasnadi *et al.* [102] to determine the expected properties of AlScN at high Sc concentration.

As Solidly Mounted Lamb Wave Resonators (SM-LWR) are more robust and easier to fabricate than their free-standing counterparts, SM-LWR devices based on highly-doped AlScN layers look the most promising solution to combine the best of the SAW and BAW technologies, and meet the specifications of the next generation of RF Filters for IoT and 5G.

In this chapter, we describe the results we have obtained over the last three and a half years, in the frame of a scientific and industrial project dedicated to the development of such devices. Three main partners were involved in the project: RF360 (Munich, Germany), the École Polytechnique Fédérale de Lausanne (EPFL, Switzerland) and the IMTEK (Institut für Mikrosystemtechnik, Freiburg, Germany). The three main components of this project were:

- The fabrication of high-quality, highly-doped AlScN thin layers, up to %Sc=30%, at the EPFL (see PhD Thesis, F. Parsapour, 2019 [103]).

- The determination of accurate sets of material parameters (stiffness, piezoelectric, dielectric and density) for different Scandium concentrations, up to %Sc=50%, at the IMTEK. These parameters were determined using a combination of literature studies, experimental measurements (using specific test structures) and DFT computations. The test structures included free-standing LWRs (see PhD Thesis, N. Kurz, 2019 [104]).

- The modelling, analysis and design of the LWR test devices and SM-LWR prototype 1-port resonators and ladder-type filters. This third component was performed at CTR in the frame of the present PhD Thesis, and is detailed in the present chapter.

A free-standing LWR demonstrator (D0) with a low Sc concentration (~15%) was modelled, designed and fabricated first. The goals were to test the fabrication processes and to check the accuracy of the models and first sets of constants. The modelling and design procedure and characterization results of this first demonstrator are reported in section 3.1. In a second step, a SM-LWR prototype (D1) was modelled, designed and fabricated. Prototype D1 was based on a highly doped AlScN layer, with %Sc=30%. The modelling and design procedure and characterization results of demonstrator D1 are reported in section 3.2. In this section, we also present the characterization results of the prototype 2-port Ladder-Type filter (P1) that was realized at the end of the project. This prototype was made of two (%Sc=30%) SM-LWR, connected in parallel.

3.1 Free standing resonator (Demonstrator D0)

After a quick reminder of the nature of Lamb modes, we discuss here the modelling and design of LWRs, which strongly depend on fabrication constraints.

3.1.1 Lamb Waves

Lamb waves (also called plate waves) propagate in a plate which thickness (t) is comparable to the wavelength of the wave λ ($0.1 \leq \lambda/t \leq 10$). The plate modes are classified according to their particle motion. They are divided in two main families: the antisymmetric (A_n) and symmetric (S_n) modes (see Figure 3.3).

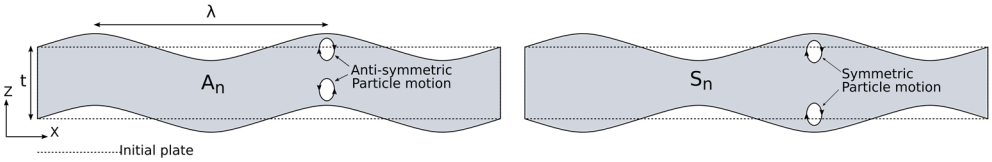

Figure 3.3 (Left) Schematic of the anti-symmetric mode and (Right) of the symmetric mode.

In BAW devices, the wavelength is equal to twice the thickness of the active layer (when operating at the first harmonic frequency), while the wavelength in a SAW device is equal to twice the IDT pitch. It is therefore quite easy to select the geometrical parameters of the chosen device to achieve a given operating frequency. It is more complicated in the case of a LWR, where the velocity of the Lamb modes depends both on the thickness and on the IDT pitch. Consequently, the layer thickness and the IDT pitch must be determined together, to achieve a given operating frequency. To do this, dispersion curves are needed.

The dispersion curve of a wave relates its wavelength or velocity to its frequency. For BAW and SAW, the wave velocity is constant, which gives a direct relationship between the wavelength and frequency (λ=v/f). In the case of a LWR, the dispersion curves can be obtained from different models. The method proposed by Viktorov [105] gives the analytical dispersion relation, for homogeneous isotropic materials. Campbell and Jones [106] devised another semi-analytical method, to compute the velocities of SAW propagating on piezoelectric substrates. We used a slightly modified version of their algorithm, to compute the dispersion curves of Lamb modes, in thin piezoelectric films, in the absence of electrodes. We used these results to confirm the more advanced COMSOL FE models (see Figure 3.4). We used a 2D model, with plane strain assumptions. We limited the width (W) of the plate to one wavelength (W=1×λ) and applied periodic boundary conditions on both sides.

In the below example, we took λ=4 µm and performed a parameter-sweep study, where the thickness changes from t=λ/20 to t=λ. On Figure 3.5, we can see the computed dispersion curves, obtained for the first five modes in a pure AlN plate, considering electrically free top and bottom surfaces.

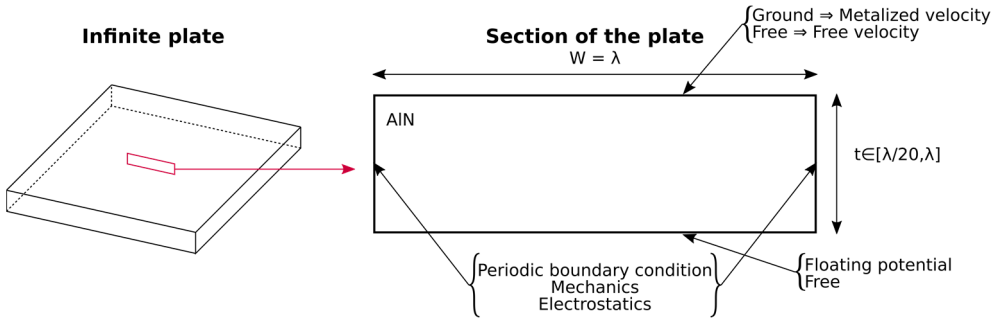

Figure 3.4 Plane strain 2D model used to compute the dispersion relations in a pure AlN plate. We simulated only one section of the infinite plate having a width equal to the wavelength of interest. Periodic boundary conditions were used to account for the periodicity of the section.

The obtained dispersion relations are given in terms of velocity versus normalized thickness $2\pi t/\lambda$. One notices that the Lamb modes velocities converge towards the SAW velocity when the thickness increases.

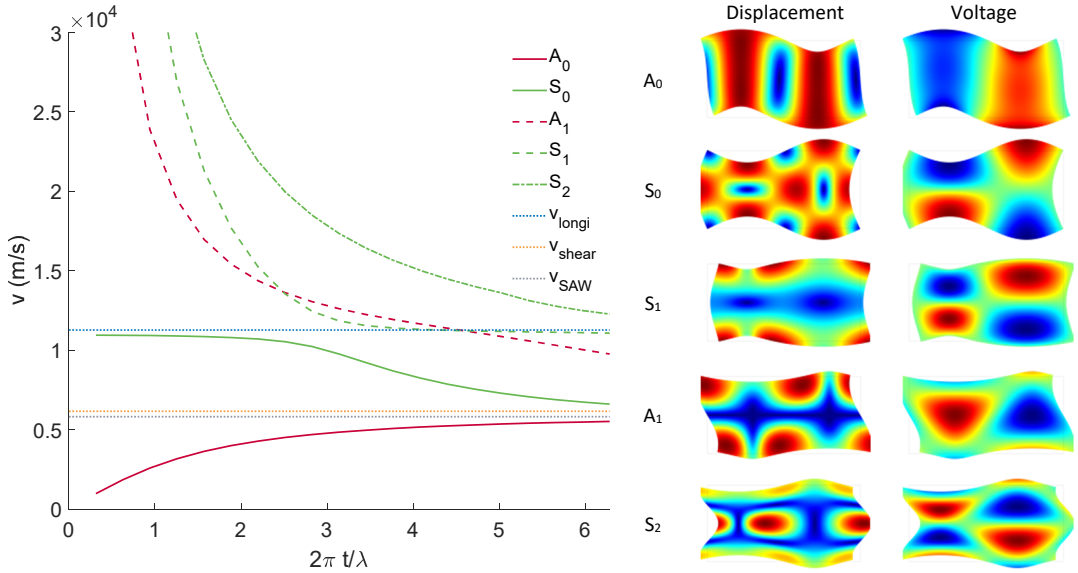

Figure 3.5 Dispersion curves of the first five Lamb modes. The graph also shows the velocity of the bulk longitudinal and shear modes as well as the SAW velocity in pure AlN. (Right) Displacement and voltage fields of the different modes, for a thickness $2\pi t/\lambda$=3.14.

From these dispersion curves, we can make several conclusions. Higher order Lamb modes present higher velocities that may have an interest for very high frequency applications. The velocity of the A_0 mode is slower than the SAW velocity. On the contrary, the velocity of the S_0 mode lies between the SAW and BAW velocities.

In Table 3.2, we compare FEM and semi-analytical results (velocities and coupling coefficients), see Appendix D. The coupling coefficients were computed using equation 1.2. In the FE model, the "metalized" velocity is obtained when the top

surface is grounded. The "free" velocity is obtained when the top surface is left electrically free of charges. The comparison confirms the validity of the FE model.

	$2\pi t/\lambda = 1.5$		$2\pi t/\lambda = 2$	
	[106]	COMSOL	[106]	COMSOL
V_{free}	9460	9458	9270	9268
V_{metal}	9345	9345	9160	9158
K^2	2.394%	2.396%	2.384%	2.335%

Table 3.2 Comparison between the Campbell and Jones and the numerical FE model (COMSOL). For this comparison we used a wavelength of λ=2.28 µm, and two different $2\pi t/\lambda$ values. The results obtained with COMSOL showed a good agreement with those obtained using [106].

3.1.2 Free standing LWR design

An upgraded version of the FEM model presented in the previous section was developed to compute and investigate the properties of free-standing LWRs, with IDTs. The Figure 3.6 introduces the model and its associated mesh. This model considers different electrode thicknesses (including infinitely thin electrodes) and electrical configurations. It is based on the model described in detail in Chapter 1.

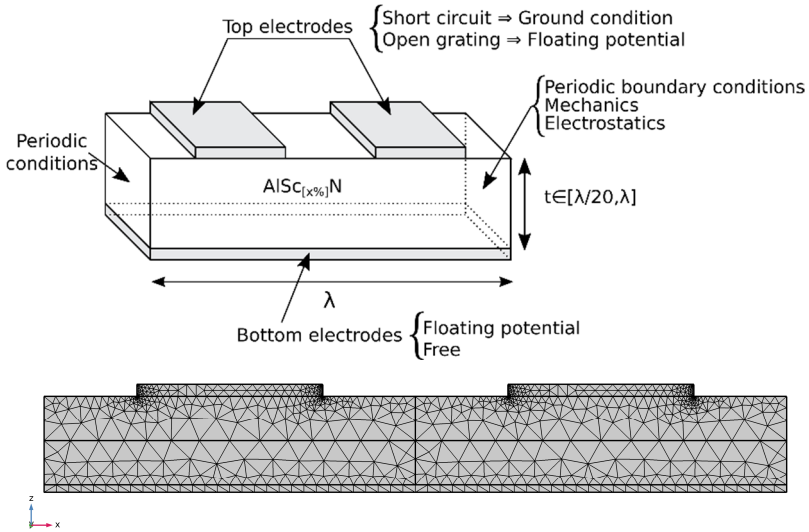

Figure 3.6 Unit-cell model used to extract the velocity and coupling coefficient of free-standing LWRs.

In the following study, the full set of COM parameters was not always required. Instead, we performed a simplified analysis based only on the frequency and coupling coefficient. To do so, we computed the open-grating and short-circuit behaviours first, as explained in section 1.3.2. From these two simulations, the resonance and anti-resonance frequencies as well as the wave velocity and the coupling coefficient are extracted. The coupling coefficient is approximated using equation 3.1 (see below). This information is enough, to assess the level of performances of a given free-standing LWR configuration (at least in a first approximation).

$$K^2 = 2 \times \frac{f_a - f_r}{f_a} \quad 3.1$$

Note that different sets of material constants were used throughout the study, as the existing sets were continuously improved by our partners, over the years of the project duration. As the main purpose of Chapter 3 is to describe the models and procedures used to design free-standing LWR and SM-LWR demonstrator and prototypes, we will not discuss here the different sets of materials parameters. More information about the used sets can be found in the PhD Thesis and related publications by our IMTEK partners, N. Kurz *et al.* [104] [107]. As they were published already [108] and for information and comparison purposes, the material parameters for %Sc=15% are reported in this document (see Appendix B).

Selection of the best suited Lamb mode and IDT configuration

The dispersion curves presented in Figure 3.5 show that the higher order modes are more sensitive to thickness variations. To use them would generate numerous issues, as they would be highly sensitive to fabrication tolerances. For this reason, only the lower order A_0 and S_0 modes are considered in the following study.

Despite the potentially higher coupling, the double side IDT configuration was eliminated because of the complexity of its implementation. Indeed, in this configuration, Vertical Interconnect Accesses (VIA) through the AlScN, are required to connect the top and bottom electrodes. Furthermore, the need for a very accurate alignment between top and bottom electrodes strongly increases the complexity of the fabrication process. Therefore, only the configurations with either a floating or an electrically free (normal electric displacements are zero) bottom electrode were considered.

Using the FEM model presented in Figure 3.6, we computed the velocity and coupling coefficient of the remaining possible configurations, to select the best possible one. The study was performed assuming infinitely thin top and bottom electrodes. A sweep of the normalized wavelength was performed by changing the thickness (t) while keeping the wavelength constant (λ=4 µm). The obtained curves are shown in Figure 3.7.

As mentioned before, high quality thick Aluminium Nitride layers are difficult to grow. Consequently, in the frame of this project, we restricted ourselves to thicknesses below 1 µm. Additionally, to ease the constraints on the lithography process, we limited ourselves to wavelengths larger than 4 µm. These two fabrication constraints confine the normalized thickness to low values ($2\pi t/\lambda<1.57$). In this region, the dispersion curves show that it is more advantageous to consider LWR based on the symmetric S_0 mode, as the velocity of this mode is significantly larger than that of the A_0 mode. In addition, the coupling coefficient of the S_0 mode is better in the floating bottom electrode configuration.

Therefore, we selected this configuration *i.e.* S_0 with floating bottom electrode. This choice is consistent with the state-of-the-art, as all the publications mentioned in Table 3.1 used the S_0 mode.

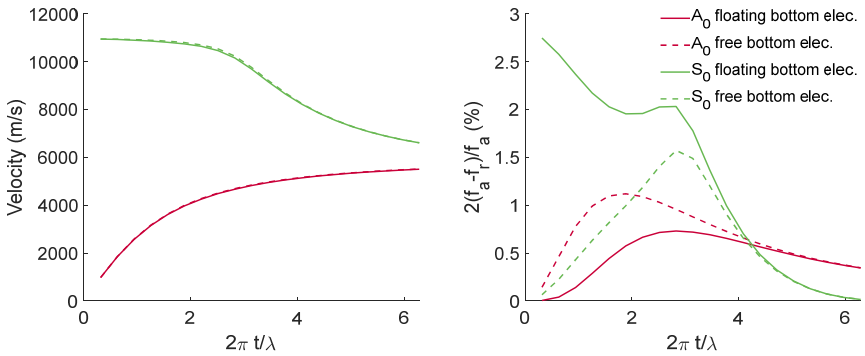

Figure 3.7 Comparison of the velocity (Left) and electromechanical coupling coefficient (Right) of the A_0 and S_0 modes in a pure AlN plate, with free or floating bottom electrode.

Due to an important lattice mismatch between AlN and Silicon, the growth of high-quality c-oriented AlN is achieved using well-selected seed layers [109]. The same applies to the growth of AlScN. In our case, Platinum (Pt) was selected, as it was already reported to be a particularly good seed-layer for AlScN growth [110]. The Platinum layer is deposited on a Si(100) substrate. As a bottom electrode is needed to improve the electromechanical coupling coefficient, the Pt seed layer is preserved (*i.e.* not etched away) at the end of the fabrication process and is subsequently used as bottom electrode.

As it was also necessary to confirm that the properties of the selected mode and configuration would further improve and keep being the best possible ones at higher Sc concentrations, we performed a complementary study. In this study, we computed the influence of the Scandium content (%Sc=15, 30, 40%) on the velocity and coupling coefficient of the A_0 and S_0 modes in a free-standing LWR. The results are presented in Figure 3.8. Note that these computations were performed using the best set of material parameters (not provided for confidentiality reason) obtained within the project.

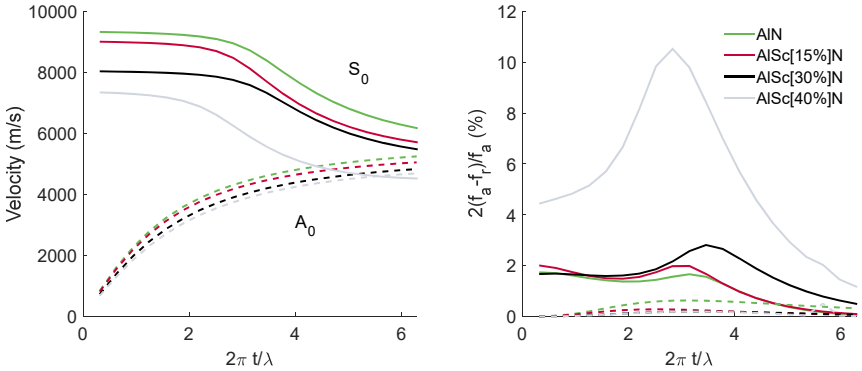

Figure 3.8 (Left) Velocity and (right) coupling coefficient of the S_0 and A_0 modes for different Scandium concentration.

The increase in Scandium concentration tends to soften the material, which results in lower velocities at higher Sc concentration, for both A_0 and S_0 modes. This effect is larger for the S_0 mode. However, the increase in Sc is more favourable to

the symmetric mode S_0, in terms of electromechanical coupling coefficient. This constituted one more argument in favour of the S_0 mode, in the floating bottom electrode configuration.

In figure 3.9, we show the results of a complementary study, where we compare the dispersion curves of the S_0 mode of free-standing LWR structures, computed using different sets of material parameters. The first set was essentially based on existing literature data (DFT: [101], [102], [111], experimental: [99], [112], [113]). The second one was determined by our partners (EPFL and IMTEK), in the frame of the present work [104]. The obtained curves differ significantly, demonstrating the need for very accurate set of constants, to optimize the design of LWR structures. For instance, the first set of material parameters yield overestimated coupling coefficients, at lower normalized wavelengths.

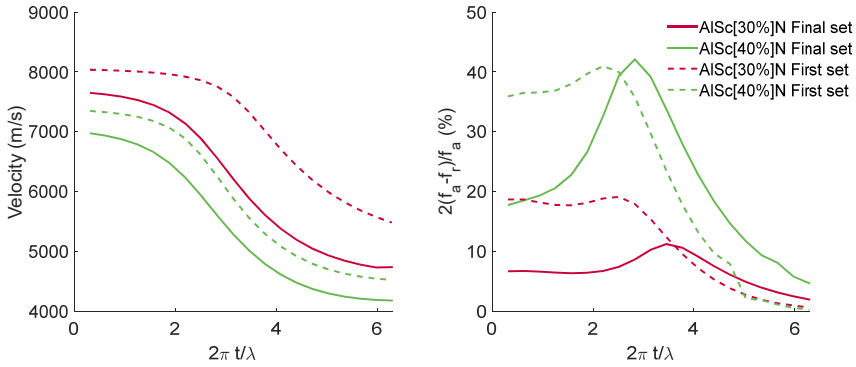

Figure 3.9 Velocity and electromechanical coupling coefficient obtained using two different sets of material parameters. The two sets were obtained at different project stages.

Bottom electrode thickness

The next step was to define the thickness of the Pt bottom electrode. We investigated several thicknesses using the $Al_{0.85}Sc_{0.15}N$ unit-cell model with λ=4 µm. The results of this study are presented in Figure 3.10. The thickness of the Pt bottom electrode strongly influences the S_0 Lamb mode velocity. It slows it down, because of its low acoustic velocity.

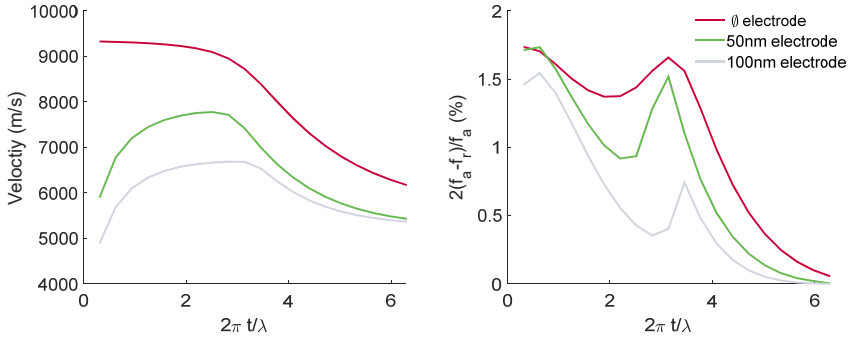

Figure 3.10 Influence of the bottom electrode thickness on the velocity and electromechanical coupling coefficient. As mentioned earlier, the electrode bottom material is Pt because of manufacturing constraints; hence, only the effect of its thickness was investigated.

The dispersion curves (Figure 3.10, left) also show that the velocity sharply decreases in the low normalized thickness region, where we plan to operate the device. It is therefore recommended to use the thinnest possible Pt layer, to maximize the velocity. However, the quality of the AlScN layer highly depends on the quality of the Pt seed layer, which degrades at lower thicknesses (<50 nm). Subsequently, a thickness of 50 nm was selected.

Then, we investigated the influence of the wavelength on the properties of the device, while keeping the thickness of the Platinum electrode constant (50 nm). As we fixed the thickness of the bottom electrode, it was not sufficient anymore to study the evolution of the device properties (velocity and electromechanical coupling coefficient) versus the normalized wavelength only. Indeed, it is possible to get the same normalized thickness value by combining two different wavelengths with two different thicknesses. However, due to the fixed (*i.e.* "non-normalized") bottom electrode thickness, the two configurations will yield two different velocities and electromechanical coupling coefficients. This phenomenon is illustrated in Figure 3.11 which shows that large variations in the electromechanical coupling coefficient and velocity are expected, for a given normalized thickness value, when λ changes from 4 to 8 µm with a step of 2 µm.

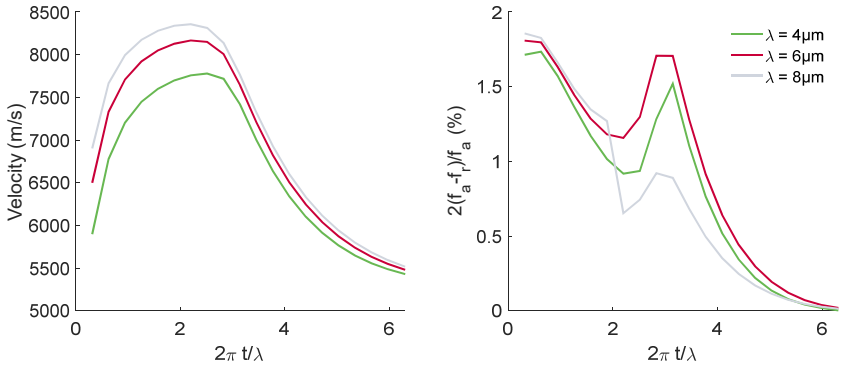

Figure 3.11 Influence of the device wavelength on the frequency and electromechanical coupling coefficient of the S_0 mode.

Top electrode material and thickness

Three materials were studied for the top electrode: Al and Cu, which are the most often used for SAW IDTs, and Pt which utilisation would have simplified the manufacturing process by limiting the number of materials employed. Using the $Al_{0.85}Sc_{0.15}N$ unit-cell model with a λ=4 µm and a 50 nm-thick Pt bottom electrode, we studied the influence on the S_0 mode of a 50 nm-thick top electrode made of each of these three materials. The final results (Figure 3.12) show that the Pt top-electrode might provide a boost in the coupling coefficient around a normalized thickness of $2\pi t/\lambda$=3. Unfortunately, it was not possible to check this prediction numerically and experimentally, due to several reasons (incl. non-accurate material data at the design stage, and the need for thicker AlScN layers). We recommend investigating further this promising operating point, which might result in devices with strongly improved coupling coefficients.

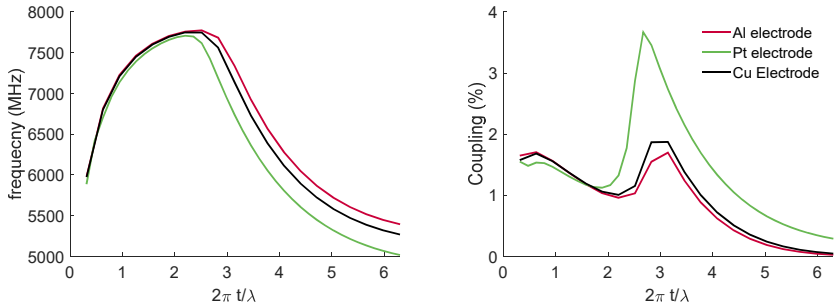

Figure 3.12 Influence of the top electrode material on the resonant frequency and electromechanical coupling coefficient of the S_0 mode.

In the selected normalized wavelength range ($2\pi t/\lambda < 1.57$, see above and Figure 3.12), there is almost no difference in velocity and electromechanical coupling coefficients, due to the electrode material. We therefore selected Al, which is the most common material, for SAW IDTs.

Then, we investigated the effect of Al thickness variations. The results are presented in Figure 3.13 . The graph shows that the electrode thickness has little influence on the velocity and electromechanical coupling coefficient at low normalized thickness values. Finally, the Aluminium thickness was selected to be 80 nm in order to ensure a sufficient electrical conductivity.

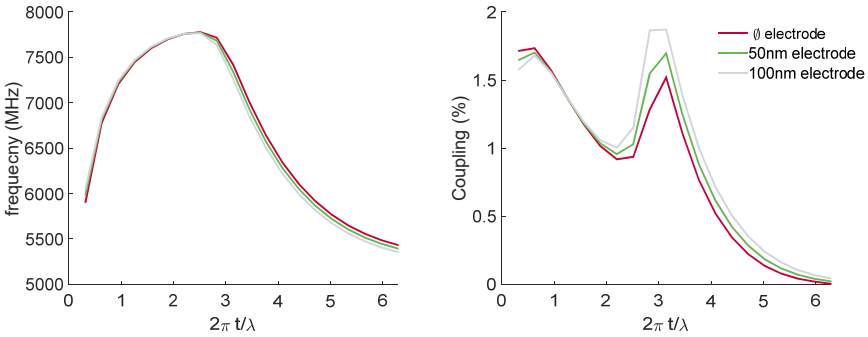

Figure 3.13 Influence of the Aluminium top electrode thickness on the frequency and electromechanical coupling coefficient of the S_0 mode.

Final thicknesses and device layout

To summarize, we decided to build free-standing S_0-mode LWRs made of %Sc=15% AlScN, with a normalized thickness below 1.57. The $Al_{0.85}Sc_{0.15}N$ was to be grown on a 50 nm thick Platinum bottom electrode, which thickness was selected to achieve excellent quality AlScN layers without degrading the velocity. As top electrode and reflectors, we decided to use 80 nm thick Aluminium gratings. To reflect the waves, we decided to use reflectors instead of device boundaries (*i.e.* CMR configuration), as this configuration was closest to the final LWR design, implemented on Bragg mirrors without AlScN etching steps. The last parameters to be determined were the thickness of the AlScN layer and the wavelength. As mentioned earlier, these two parameters must be studied separately, as the thicknesses of the bottom and top electrodes are fixed. The results of this study are

presented in Figure 3.14. On the latter, we superimposed the limits fixed by manufacturing constraints (*i.e.* λ>4 µm, t_{AlScN}>0.5 µm). Finally, for the fabrication, we selected a thickness of 1 µm for the AlScN Layer, as this thickness lies in the desirable range, and because of earlier practical experience at the EPFL. For the wavelength, we selected three distinct values, namely λ=5 µm, 6 µm and 8 µm (corresponding to the normalized thicknesses of $2\pi t/\lambda$=1.26, 1.05 and 0.78). The LWR were made of large IDTs (150λ) and reflectors (40fingers), to improve the resonance characteristics. They had an aperture of 30λ.

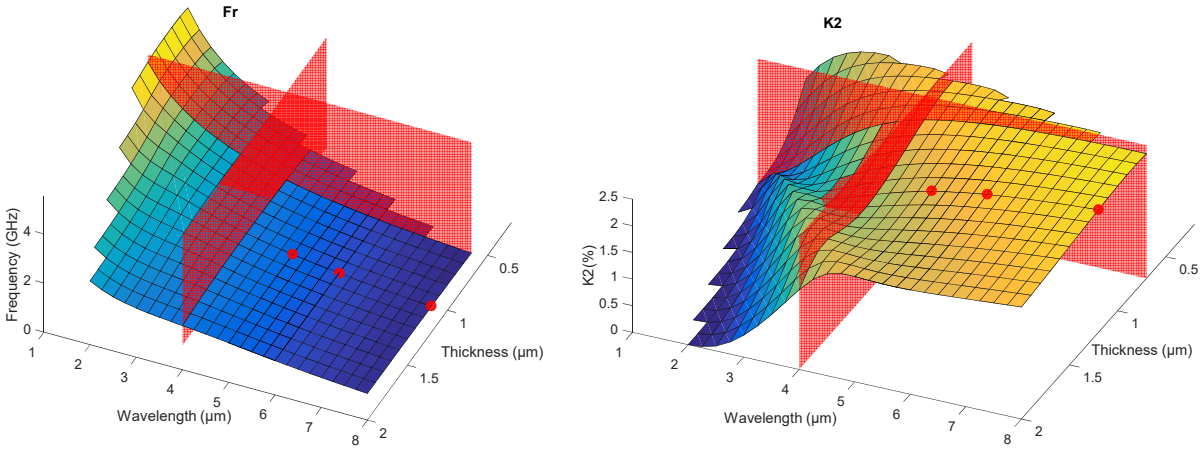

Figure 3.14 Dispersion and electromechanical coupling coefficient surfaces vs. wavelength and AlScN thickness. Note that these results were obtained with an earlier set of material parameters (not provided for confidentiality reason). The fabrication constraints are materialized on the figure, using red planes.

3.1.3 Micro-fabrication

The fabrication of the prototypes was performed at the EPFL, by our partners. The devices were fabricated on 100 mm diameter wafers using a five-mask and CMOS compatible process. The process steps are as follows (more details about the process steps and layer structure can be found in [114]): first, a 200 nm thick Silicon Oxide layer (SiO_2) is grown on the Silicon (Si) substrate by wet oxidation. A 200 nm Silicon Nitride (Si_3N_4) is then deposited on top of it, by chemical vapour deposition. Then, the 50 nm-thick Platinum bottom electrode is sputter-deposited and patterned using ion beam etching and a protective resin mask. A 1 µm-thick $Al_{0.85}Sc_{0.15}N$ layer is then deposited using the process described in [114]. Subsequently, the Aluminium IDT and the reflectors are sputtered and patterned using dry etching and a protective resin mask. Following this step, the device is released from the substrate. First, the AlScN/Si_3N_4/SiO_2 stack is etched using ion beam etching. This step defines the edges of the device. Finally, the Silicon substrate, SiO_2 and Si_3N_4 layers are dry-etched from below, to fully liberate the structure (see process steps in Figure 3.15). In Figure 3.15 (4), the anchors that hold the device suspended and ensure the electrical connection are visible. The actual thicknesses of the devices were determined by SEM measurements. They are reported in Table 3.3.

		Demonstrator D0	
		Theoretical	Real
Layers	Al/Cu (nm)	80	90
	AlScN (nm)	1000	1000
	Pt (nm)	50	60

Table 3.3 Actual thicknesses of the layers in the demonstrator D0

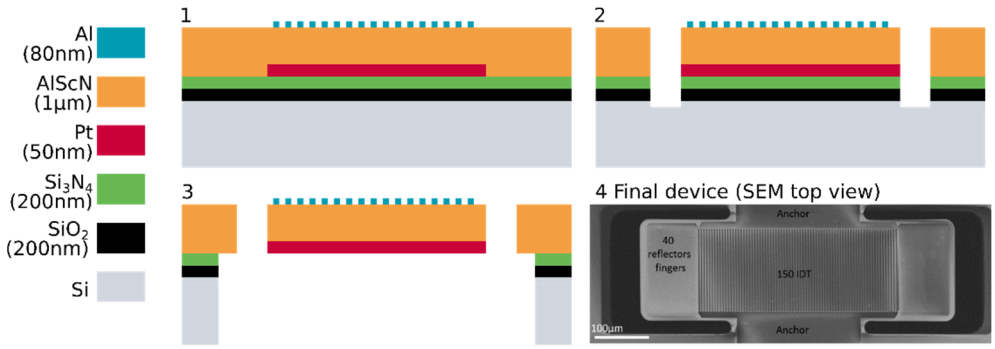

Figure 3.15 Microfabrication process of the free-standing LWR. (1) Device after deposition and patterning of the bottom and top electrodes. (2) device after front side liberation. (3) Device after back side liberation. (4) SEM picture of the free-standing LWR after release, made at the EPFL.

3.1.4 Results

In this section, we report the experimental results for λ=6 µm and 8 µm and compare them to our simulation results. Although the devices with λ=5 µm did not work well enough to provide usable data, we still computed some of their main expected properties (COM), for future use.

To simulate the experimental response of the devices, we computed their COM parameters, using the measured thicknesses and best sets of material coefficients (not provided for confidentiality reason). The results are summarized in Table 3.4. We then used these COM parameters to compute the electrical response of the devices, using the well-known P-Matrix method [9].

	K^2 (%)	f_c (MHz)	f_r (MHz)	f_a (MHz)	v (m/s)	κ (%)	ζ $(10^{-5}\Omega^{-\frac{1}{2}})$	C $(10^{-11}\ F\ /\mu m/period)$
λ = 5 µm	3.53	1586.45	1595.34	1618.89	7954.48	-1.755	12.102	12.385
λ = 6 µm	**4.02**	**1341.50**	**1351.21**	**1373.98**	**8078.13**	**-2.264**	**13.454**	**13.152**
λ = 8 µm	**3.77**	**1021.21**	**1029.90**	**1049.70**	**8204.45**	**-2.664**	**15.504**	**15.023**

Table 3.4 COM parameters for the actual (*i.e.* fabricated) demonstrators D0

To take into account the parasitic effects of the bottom electrode (capacitive coupling of the input and output ports, through the connection pads) and fingers (ohmic losses), lumped elements were added to the simulated circuit (see figure

3.16). The values of the added capacitance and resistance were tuned manually, to match the experimental data seen on the Smith chart*.

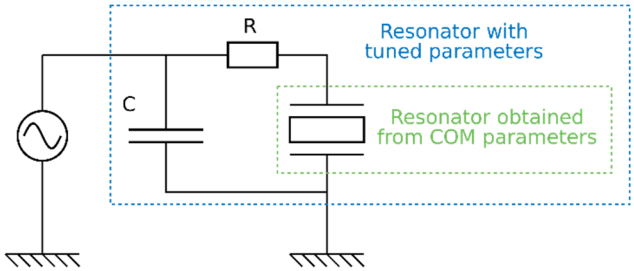

Figure 3.16 Schematic of the modified electric circuit to account for possible parasitic effects. A resistor R is added in series and a capacitance C is added in parallel.

In Figure 3.17 we compare the simulated and experimental impedances of the λ=6 µm resonator. An 8 Ω series resistor and a 6 pF parallel capacitor are used, as lumped-elements.

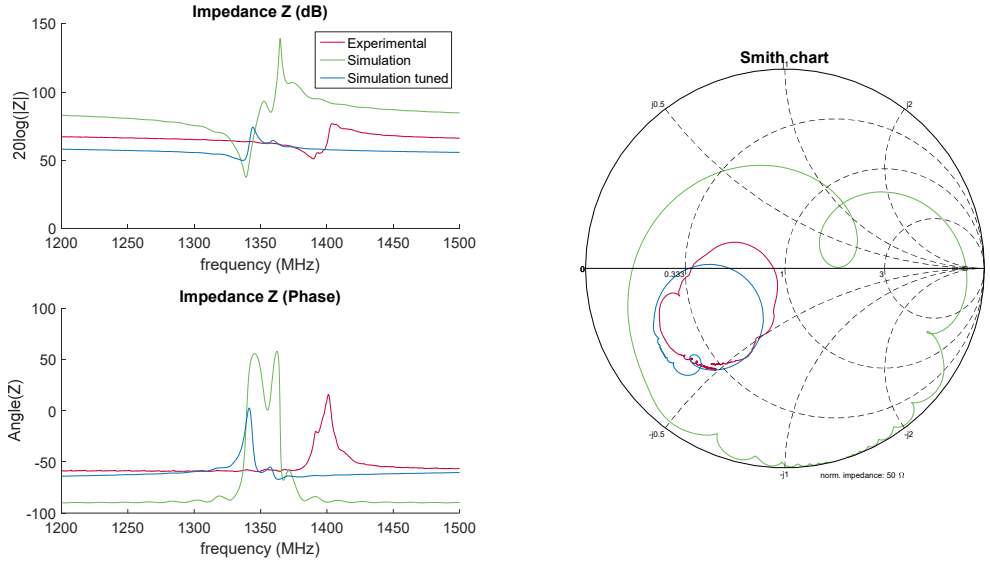

Figure 3.17 Comparison between experimental characterisation and simulated data, for the free-standing structure (λ=6 µm). Red: experimental. Green: simulation without additional lumped-elements. Blue: simulation, with additional lumped-elements.

In Figure 3.18 we compare the simulated and experimental impedance of the λ=8 µm resonator. A 10 Ω series resistor and a 15 pF parallel capacitor were used, as lumped-elements.

* The Smith chart is a graphical representation of the real and imaginary part of the reflexion factor $\Gamma = \frac{Z-Z_0}{Z+Z_0}$, where Z is the impedance of the load and Z_0 is the reference impedance (usually 50 Ω).

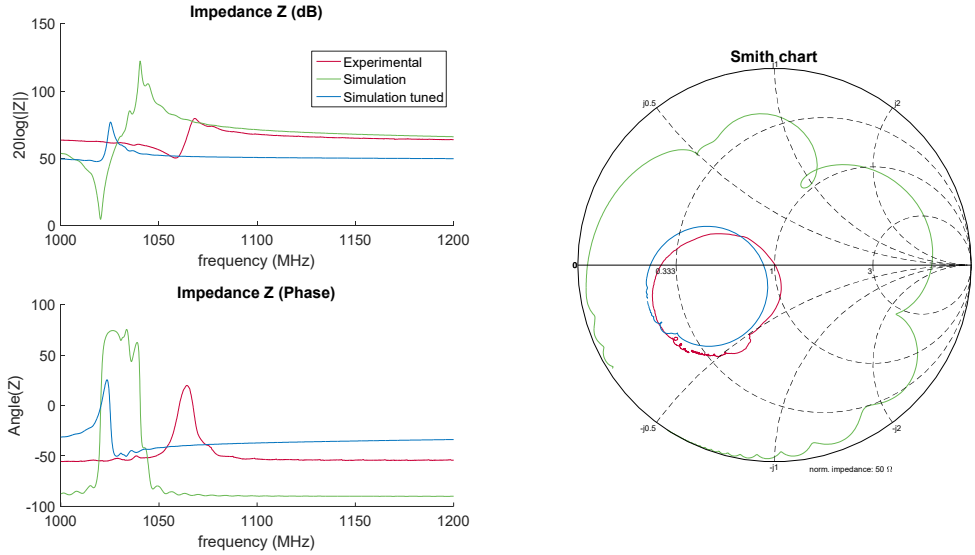

Figure 3.18 Comparison between experimental characterisation and simulated data, for the free-standing structure (λ=8 µm). Red: experimental. Green: simulations, without additional lumped-elements. Blue: simulation, with additional lumped-elements.

Table 3.5 summarizes the frequencies and electromechanical coupling coefficients* [115] determined experimentally and numerically. The quality factors were computed by our EPFL partner, through fitting of a Butterworth-van Dyke model. We see that the simulations could approximate reasonably the resonance frequencies of both devices but were unable to grasp the electromechanical coupling coefficient without a manual tuning of the electrical characteristics. The experimental coupling is almost twice lower than the simulated one (without lumped element). It is however close to that obtained with lumped-elements. The presence of a parasitic capacitance on the real device might therefore explain the observed degradation of the coupling coefficients.

	$K^{2*}(\%)$	$f_r(MHz)$	$f_a(MHz)$	Q
λ = 6µm, Sim.	4.78	1338	1365	
λ = 6µm, Sim. tuned	2.18	1333	1345	
λ = 6µm, Exp.	2.78	1389	1405	121
λ = 8µm, Sim.	4.89	1020	1041	
λ = 8µm, Sim. tuned	2.14	1017	1026	
λ = 8µm, Exp.	2.29	1059	1069	105

Table 3.5 Summary of the frequency and electromechanical coupling coefficients* [115] determined experimentally and numerically for the free-standing LWR.

* The coupling coefficients were computed using the following formula for an easier comparison with the results from our partners:

$$K^2 = \frac{\pi f_r}{2 f_a} \cot\left(\frac{\pi f_r}{2 f_a}\right)$$

The resonators having a λ=6 µm and λ=8 µm showed respective electromechanical coupling coefficients K^2=2.78% and K^2=2.29%, which are approximately two times better than the values reported in the literature for pure AlN (see Table 3.1). This highlights the benefit of using Scandium doped AlN. However, these devices also exhibited poor quality factors (Q=121 and Q=105 respectively), which result in low figure-of-merits (FoM=3.36 and FoM=2.40 respectively) that are comparable to the FoM found in the literature for LWR.

These results came late in the project timeline; therefore, more time is required to have an exhaustive comprehension of the latter. However, we can make two remarks. The quality factors found for these two configurations are low compared to the values reported in the literature for similar configurations (see Table 3.1). The relatively high losses of our devices may be explained by the anchors used as it is well-known that the anchors losses are the dominant losses in LWR device [116]. In addition, some spurious modes are observed in the electrical response of our resonators; this is a known drawback of the free-standing LWR [117], [118].

3.2 Solidly Mounted LWR (Demonstrator D1)

In this part, we discuss the design of the second generation of demonstrators (D1), based on the S_0 Lamb mode. D1 has two key features: it is solidly mounted on a substrate and it has a high concentration of Scandium (%Sc=30%).

The Solidly Mounted Resonator (SMR) offers several advantages compared to its free-standing counterpart. SMRs are easier to manufacture since the tedious task of releasing the devices from their substrates is not needed. They are inherently more robust and dissipate heat more efficiently. However, SMRs usually have lower quality factors due to leakage of the acoustic energy in the substrate.

The design of the demonstrator D1 was conducted in two steps, see Figure 3.19. First, we defined a free-standing structure made of an $Al_{0.70}Sc_{0.30}N$ layer. Secondly, we designed an appropriate acoustic Bragg mirror. These two steps are discussed below.

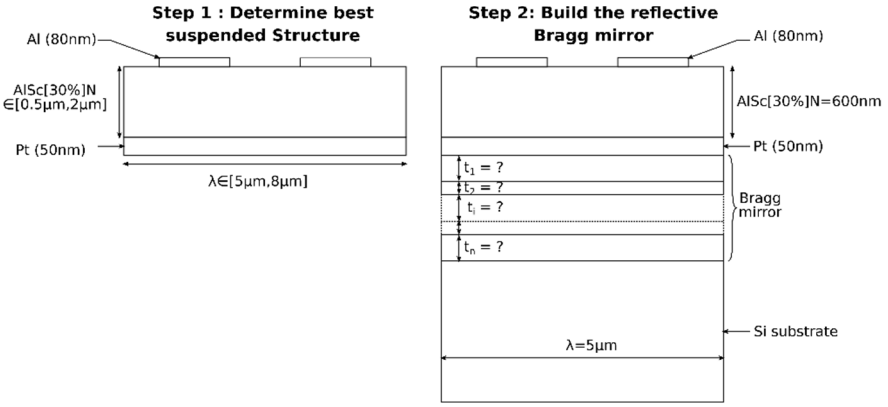

Figure 3.19 Illustration of the process used to find the best SM-LWR. (Left) Schematic of the suspended structure used to find the best configuration regarding the wavelength and thickness. (Right) Selected suspended structure on top of the to-be-defined Bragg mirror.

3.2.1 Free-standing structure

Based on the previous study, we decided to grow the $Al_{0.70}Sc_{0.30}N$ layer on a 50 nm thick floating Pt bottom electrode. On top of the AlScN layer, we decided to have an 80 nm thick Al IDT and reflectors.

To select the appropriate wavelength and the thickness of the $Al_{0.70}Sc_{0.30}N$ layer, we simulated the possible configurations using the unit-cell model presented in Figure 3.6. The wavelength was varied from 5 µm to 8 µm. The lower limit (5 µm) was fixed by the capability of the available lithography tool, while the upper limit (8 µm) was arbitrary fixed, to guarantee a high-enough operating frequency (>1 GHz). Based on the knowledge acquired during the fabrication of the D0 demonstrators, the thickness of the AlScN layer was limited to the range 0.6 µm≤ h ≤2 µm. The results of the parametric study are presented in Figure 3.20.

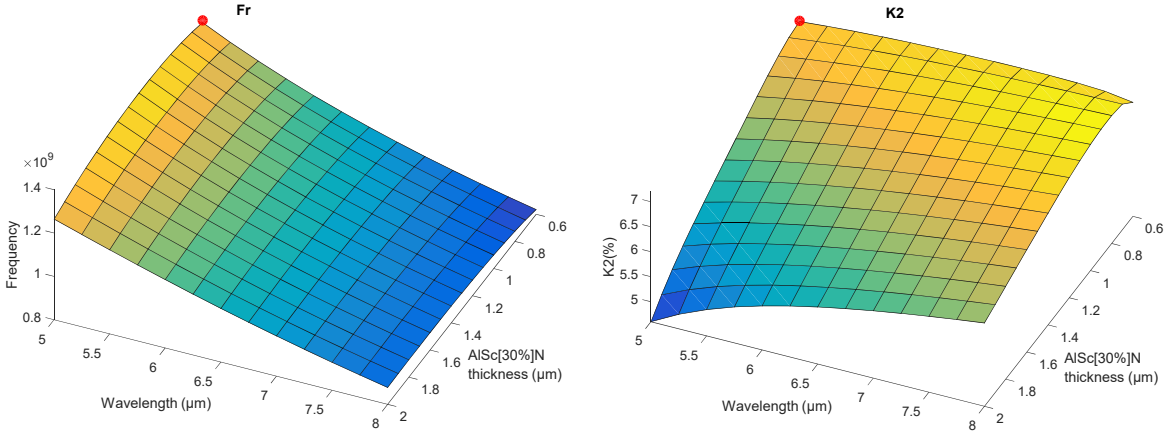

Figure 3.20 Visualisation of the device resonant frequency and electromechanical coupling coefficient as a function of the $Al_{0.70}Sc_{0.30}N$ thickness and device wavelength. The red dot shows the selected configuration. Note that the results were obtained using an earlier version of the material parameters (not provided for confidentiality reason), as the final and best ones were not available yet.

Within these boundaries, we selected first the configuration offering the highest resonant frequency (λ=5 µm), as a high frequency also makes it possible to reduce the thickness of the layers in the Bragg mirror, which constitutes an advantage from the fabrication point of view. We then selected the thickness offering the highest electromechanical coupling coefficient (t=0.6 µm). Such a design should operate at 1291 MHz, with a coupling coefficient of K^2=6.8%. The Bragg mirror was then designed, to confine the S_0 mode in this LWR.

3.2.2 Solidly mounted structure

The Bragg mirror uses a stack of alternate layers of low and high acoustic impedances to reflect the waves. For a device using only one kind of wave (longitudinal or shear) at frequency f, the optimum mirror reflectivity is obtained in the "quarter-wave" configuration [119], meaning that the thickness of the low acoustic impedance layers is:

$$t_{low} = \frac{\lambda_{low}}{4} = \frac{v_{low}}{4f} \quad 3.2$$

And the thickness of the high acoustic impedance layers is:

$$t_{high} = \frac{\lambda_{high}}{4} = \frac{v_{high}}{4f} \quad 3.3$$

In these equations, v_{low} and v_{high} are the velocities of the mode to be reflected, in the high and low impedance layers.

There are several aspects to consider when designing a Bragg mirror. First, the efficiency of the Bragg mirror to reflect a chosen mode depends greatly on the impedance difference (or impedance ratio) between the high and low-impedance layers. If the difference is small, the mirror will require more layers to efficiently reflect the waves. As shear and longitudinal modes have different acoustic velocities, the layer thicknesses in the mirror will also depend on the nature of the mode to be reflected. Since the S_0 Lamb mode comprises both longitudinal and shear modes, a compromise must be found to reflect it efficiently.

We introduced a weight factor $R \in [0,1]$ that balances the ability of the mirror to reflect the two modes. The thicknesses of the Bragg mirror constitutive layers now read:

$$t_{low} = R\frac{\lambda_{L(low)}}{4} + (1-R)\frac{\lambda_{S(low)}}{4} = R\frac{v_{L(low)}}{4f} + (1-R)\frac{v_{S(low)}}{4f} \quad 3.4$$

$$t_{high} = R\frac{\lambda_{L(high)}}{4} + (1-R)\frac{\lambda_{S(high)}}{4} = R\frac{v_{L(high)}}{4f} + (1-R)\frac{v_{S(high)}}{4f} \quad 3.5$$

A ratio $R = 1$ corresponds to a mirror optimized to reflect a pure longitudinal wave. A ratio $R = 0$ corresponds to a mirror optimized to reflect a pure shear wave. This parameter (R) can now be used to perform parameter sweep studies and optimize the mirror performances. For instance, we can look for the maximum reflectivity versus R (see the following sections, SiO2/W mirror: and SiO2/AlN mirror:).

We also investigated two different kinds of Bragg mirrors: the first one uses Tungsten (W) as high acoustic impedance material and Silicon Oxide (SiO_2) as low acoustic impedance material. This pair of materials has a relatively high impedance ratio (Z_W/Z_{SiO2}=7.8), meaning that few layers are enough to build an effective mirror. However, the manufacturing of a SiO_2/W Bragg mirror comes with some fabrication constraints. As the first layer above the Silicon substrate and the last layer below the Platinum bottom electrode must both be SiO_2, only odd numbers of layers are possible. The main drawback of this pair of materials comes however from the high electrical conductivity of W. Indeed, the W layers can generate capacitive coupling issues. They must therefore be structured so that they lie only below the acoustic tracks, and not below the connection pads. The patterning of the W layers implies additional photolithography and etching steps and generates height differences that might result in cracks (see Figure 3.21). These added steps make the W/SiO_2 mirror more expensive to produce.

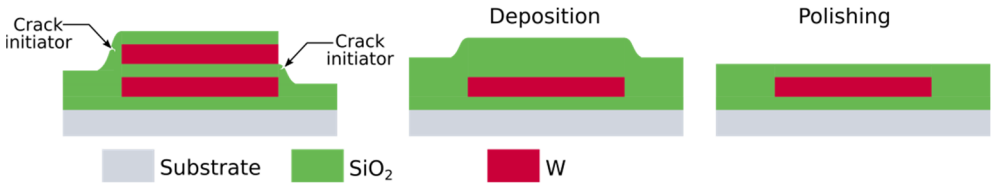

Figure 3.21 (Left) Illustration of the formation of cracks due to height difference. (Right) Illustration of the process required to avoid the crack initiation, consisting in , first, the deposition of a thick layer of SiO_2, then a polishing to achieve a flat surface at the correct height.

A second mirror made of AlN and SiO_2 was studied as an alternative. Unlike W, AlN is a dielectric. Consequently, it cannot generate capacitive coupling, and it is not necessary to structure the layers anymore. However, AlN has lower acoustic impedance than W, and the resulting Bragg mirror impedance ratio Z_{AlN}/Z_{SiO2} is only 2.8. This mirror must also start and end with a SiO_2 layer, meaning that the total number of layers is odd.

SiO_2/W mirror:

This section is dedicated to the study of the influence of the weight ratio (R) on the performance of a SiO_2/W Bragg mirror. We investigated 3-layer and 5-layer alternatives. The numerical study was conducted using the unit-cell model presented in Figure 3.22. The model comprises the $Al_{0.70}Sc_{0.30}N$ piezoelectric layer with top and bottom electrodes and the Bragg mirror stack. The W metallic layers in the Bragg mirror are modelled as perfectly conductive material. Therefore, only the mechanical equation is solved in W. The SiO_2 layers and Si substrate are modelled as dielectric materials meaning that both mechanical and electrostatic equations are solved in these layers. The mesh associated to this model is also presented in Figure 3.22. To evaluate the performances of the SiO_2/W Bragg mirrors at different R values, eigenvalue problems were solved using short-circuit and open-grating electric boundary conditions. The resonance frequency and electromechanical coupling coefficient were extracted from these values, following the method presented in Chapter 1.

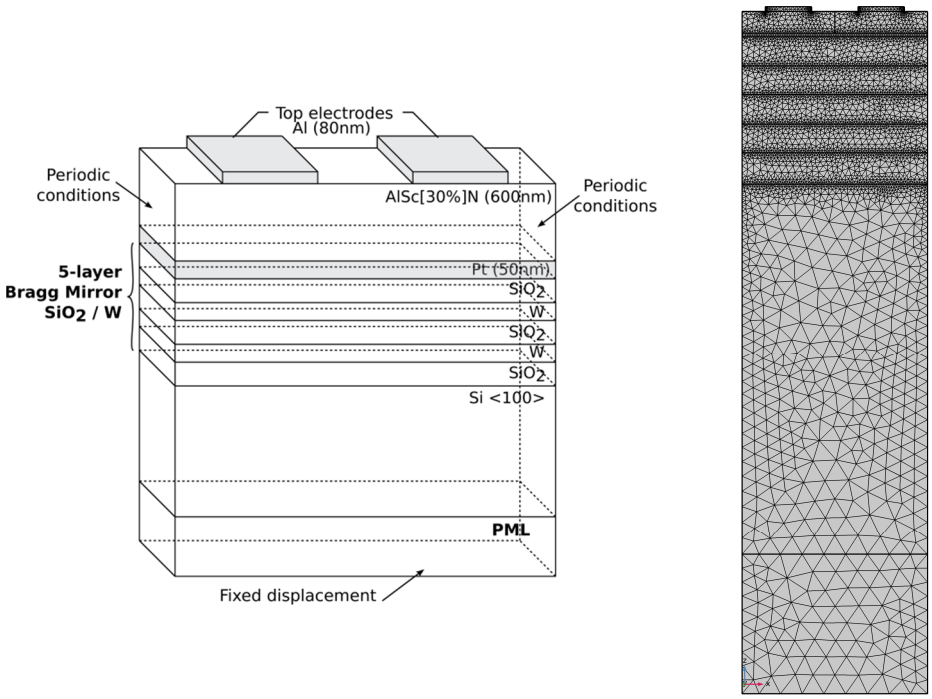

Figure 3.22 Unit-cell model of a SM-LWR.

The thicknesses of the layers in the Bragg mirror must be tuned, to isolate the S_0 mode propagating in the AlScN layer, at 1291 MHz (*i.e.* at the resonance frequency of the suspended device). As the frequency and wave velocities (see Appendix B) in the layers are now fixed, the thicknesses depend only on the ratio R (see equations 3.4 and 3.5). We performed a parameter sweep study, changing the value of R from 0 to 1, and tracking the evolution of the resonant frequency, the electromechanical coupling coefficient and the damping at the resonant frequency. The results are presented in Figure 3.23. As shown in Figure 3.22, a PML is placed below the Bragg mirror, to account for the acoustic influence of a semi-infinite silicon substrate. In the model, the PML is the only layer that generates losses, which result in a non-zero imaginary part of the resonance frequency. When acoustic waves are not completely reflected by the Bragg mirror, they reach the PML where they are damped and thus generate losses. Therefore, the imaginary part of the resonnant frequency increases with the amount of acoustic energy that is going through the Bragg mirror. It can therefore be used as an indicator of the mirror capability to reflect the S_0 mode. In Figure 3.23, only the results for the 5-layer mirror stack are reported since the 3-layer alternative showed poor performances.

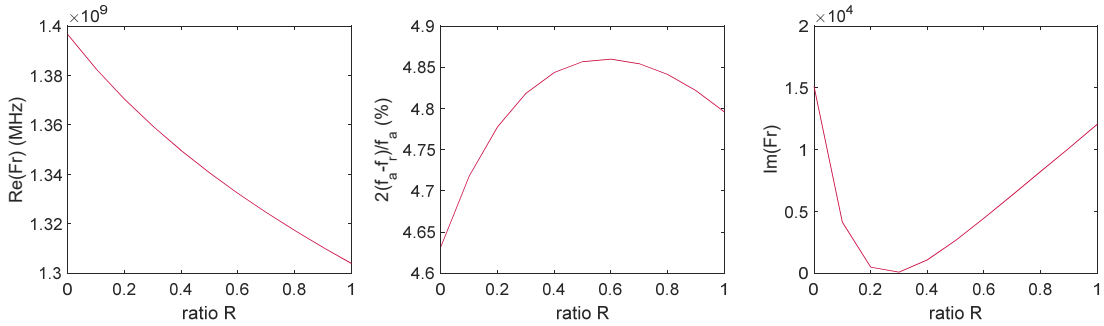

Figure 3.23 Performance of the W/SiO_2 Bragg mirror as function of the weight ratio R. (left) Real part of the resonance frequency, (middle) electromechanical coupling coefficient and (right) imaginary part of the resonance frequency.

Figure 3.23 shows that the overall effect of the Bragg mirror is to increase the resonant frequency and decrease the electromechanical coupling coefficient (when compared to the equivalent suspended structures). The curve of the latter shows a maximum for a weight ratio R=0.6 while the minimal losses are achieved at R=0.3. The displacement fields for R=0.3 and R=0.6 were computed and compared to the displacements obtained with a 3-layer stack (R=0.3). The results are presented in Figure 3.24. The displacement fields obtained for the 3-layer stack show that a significant portion of the waves is leaking into the substrate (i.e. there is still a high displacement amplitude, below the third layer). For the 5-layer Bragg mirror, the difference between the ratio R=0.3 and R=0.6 is hardly distinguishable.

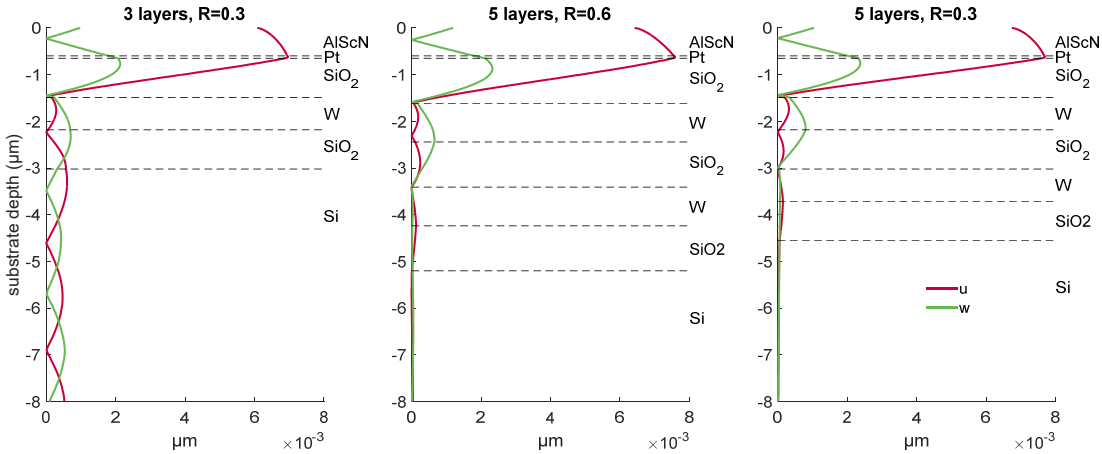

Figure 3.24 Displacement fields at the resonance frequency in the W/SiO_2 Bragg mirror, in propagation direction (u, in red) and perpendicular to the propagation direction (w, in green). (left) 3 layers BM; (middle) 5 layers BM with a weight ratio R=0.6; (right) 5 layers BM with a weight ratio R=0.3. The two different weight ratios lead to different layers thicknesses within the stack. For comparison purposes, the scales of the axis are all the same. The dashed lines materialize the layers interfaces.

SiO_2/AlN mirror:

This section is dedicated to the study of the influence of the weight ratio (R) on the performance of a SiO_2/AlN Bragg mirror. We investigated 5-layer and 7-layer

alternatives. In the numerical model, W was simply replaced by AlN. The computation procedure (i.e. parameter sweep study) was identical to that used before, in the SiO_2/W case. The results are presented in Figure 3.25. The graphs show that the AlN/SiO_2 Bragg mirrors tend to increase the frequency and decrease the electromechanical coupling coefficient, compared to the free-standing structure. There is no significant difference between the 5-layer and 7-layer alternatives regarding the resonant frequency and electromechanical coupling coefficient. Nevertheless, the 7-layer Bragg mirror shows a better reflectivity than the 5-layer alternative.

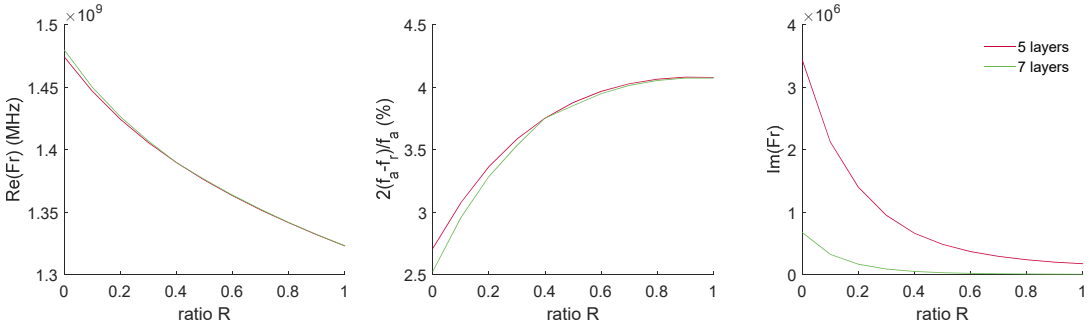

Figure 3.25 Performance of the 5 and 7-layer AlN/SiO_2 Bragg mirrors as function of the weight ratio R. (left) Real part of the resonance frequency, (middle) electromechanical coupling coefficient and (right) imaginary part of the resonance frequency.

The displacement fields at the resonance frequency were computed for the two mirrors. The results are presented in Figure 3.26. From the latter, we can see that the 5-layer Bragg mirror is less efficient than the 7-layer Bragg mirror, to reflect the incoming waves.

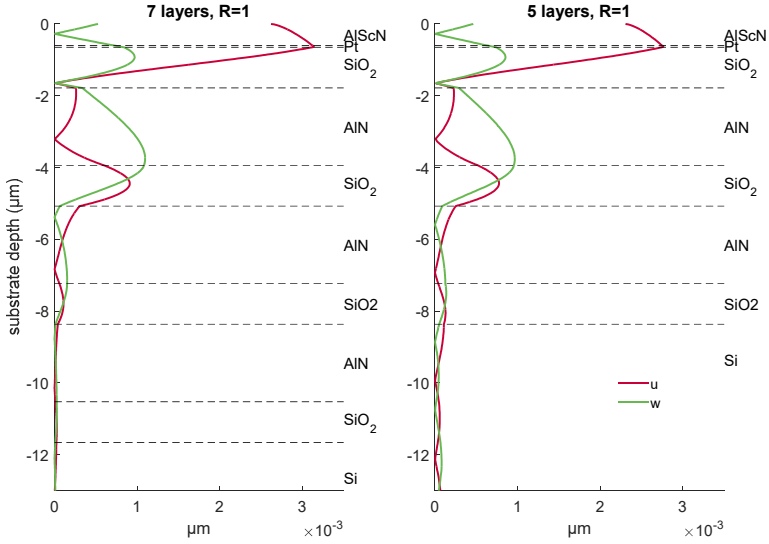

Figure 3.26 Displacement fields at the resonance frequency, in the 7 and 5-layer AlN/SiO_2 Bragg mirrors.

Comparison SiO_2/AlN and SiO_2/W mirrors

The quality factors of the most promising structures were evaluated. The results are reported in Figure 3.27. To compute quality factors, propagation losses in the Bragg mirror layers must be taken into account. We did not need losses in the previous models, as the goal of the previous studies was to evaluate the reflectivity properties of the mirrors, only. To compute losses, isotropic damping coefficients* were introduced for each layer in the unit-cell model. They are reported in Appendix B. The quality factor was extracted from the real part of the harmonic admittance, using a Lorentz fitting function (equation 3.6, [120]) and formula 3.7. See results in Figure 3.27 (left).

$$f(x) = \frac{I\gamma^2}{(x - x_0)^2 + \gamma^2} \qquad 3.6$$

$$Q = \frac{x_0}{2\gamma} \qquad 3.7$$

Where, x_0 is the centre of the Lorentz distribution, I is a scaling parameter and γ represents the half-width at half-maximum.

The study shows that the 5-layer SiO_2/W Bragg mirrors have higher quality factors than the other configurations. There is, however, no significant difference between R=0.3 and R=0.6, for this 5-layer SiO_2/W configuration.

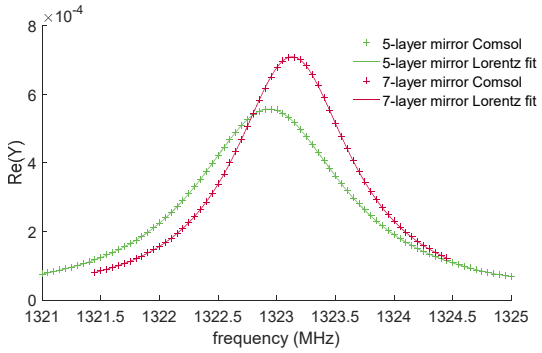

Bragg mirror stack	Quality factor
SiO_2/W (3x) R=0.3	477
SiO_2/W (5x) R=0.3	1476
SiO_2/W (5x) R=0.6	1463
SiO_2/AlN (5x) R=1	861
SiO_2/AlN (7x) R=1	1098

Figure 3.27 Quality factor of the most promising mirrors. (Left) real part of the harmonic admittance and Lorentz fit, at the resonance, for the AlN/SiO_2 Bragg mirrors made of 5 and 7 layers. (Right) Quality factors of the unit-cell model computed for the most promising configurations. The quality factor of the "lossy" 3-layers SiO_2/W Bragg mirror is added for comparison.

3.2.3 Microfabrication

Using the results obtained in the previous section, we fabricated two versions of demonstrator D1. The first version was built on a 5-layer SiO_2/W Bragg mirror with the weight ratio offering the best quality factor (R=0.3). The second version was built on a 7-layer AlN/SiO_2 Bragg mirror, with R=1. The theoretical and measured thicknesses of these two mirrors are reported in Table 3.6 and Table 3.7.

*When considering a so-called isotropic damping, the stiffness matrix is replaced by the following expression: $C \to (1 + i \cdot \eta)C$. Where, η is the isotropic damping coefficient.

Demonstrator D1 5 layers SiO2/W Bragg mirror				
Layers		Theo.	Real	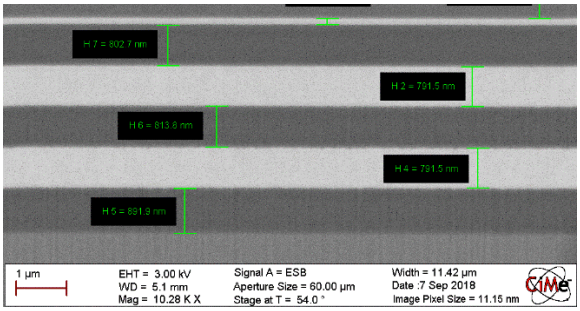
	Al (nm)	80.00	130	
	$Al_{0.70}Sc_{0.30}N$ (nm)	600.00	600	
	Pt (nm)	50.00	100	
	SiO_2 (nm)	839.52	802	
	W (nm)	693.13	791	
	SiO_2 (nm)	839.52	814	
	W (nm)	693.13	791	
	SiO_2 (nm)	839.52	891	
	Si (µm)	385	385	

Table 3.6 Theoretical and measured thicknesses in the SiO_2/W Bragg mirror. The right picture is a SEM cross section of the Bragg mirror, from which the thicknesses were determined. The picture was made at the EPFL.

Demonstrator D1 7 layers SiO_2/AlN Bragg mirror				
Layers		Theo.	Real	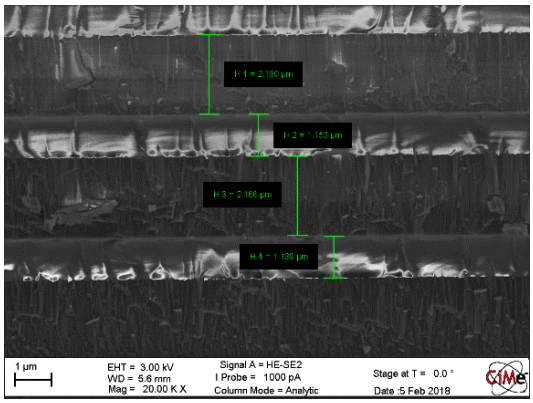
	Al (nm)	80.00	130	
	$Al_{0.70}Sc_{0.30}N$ (nm)	600.00	600	
	Pt (nm)	50.00	100	
	SiO_2 (nm)	1132.46	1153	
	AlN (nm)	2158.48	2180	
	SiO_2 (nm)	1132.46	1153	
	AlN (nm)	2158.48	2166	
	SiO_2 (nm)	1132.46	1139	
	AlN (nm)	2158.48	2158	
	SiO_2 (nm)	1132.46	1132	
	Si (µm)	385	385	

Table 3.7 Theoretical and measured thicknesses in the SiO_2/AlN Bragg mirror. The right picture is a SEM cross section of the Bragg mirror, from which the thicknesses were determined. The picture was made at the EPFL.

The fabricated resonators consisted of 100, 200 or 300 finger-IDT, surrounded by two shorted 60 finger-reflectors. The wavelength was 5 µm. The aperture was 30λ. Figure 3.28 shows a SEM picture of one of the fabricated devices (200 finger-IDT resonator).

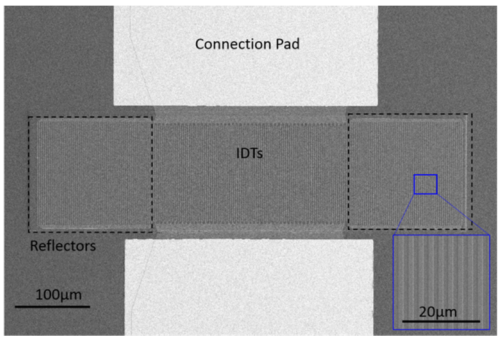

Figure 3.28 SEM picture of a Lamb wave resonator deposited on a Bragg mirror, made at the EPFL.

3.2.4 Results

Using the unit-cell model, the measured geometric parameters and the latest (i.e. best!) set of material parameters for $Al_{0.70}Sc_{0.30}N$ (not provided for confidentiality reason), we computed the COM parameters for the fabricated structures (see Table 3.8). Using these COM parameters and a P-Matrix algorithm, we computed their expected frequency characteristics. We present here the results obtained for the longest resonators (i.e. 300 finger-IDT), which performed best.

	K^2 (%)	f_c (GHz)	f_r (GHz)	f_a (GHz)	v (m/s)	κ (%)	ζ $(10^{-5}\,\Omega^{-\frac{1}{2}})$	C $(10^{-11}F/\mu m\,/period)$
SiO_2/W λ = 5 µm	**5.05**	**1289.56**	**1304.27**	**1332.14**	**6484.6121**	**-3.5636**	**60.735**	**26.117**
SiO_2/AlN λ = 5 µm	**4.06**	**1271.53**	**1281.43**	**1303.24**	**6382.4136**	**-2.4355**	**52.698**	**25.268**
SiO_2/AlN λ=5.125 µm	**4.04**	**1247.20**	**1257.66**	**1278.96**	**6418.7368**	**-2.6229**	**53.364**	**25.878**

Table 3.8 COM parameters, computed for the fabricated demonstrators D1

The computed and experimental frequency characteristics of the resonator fabricated on a W/SiO_2 Bragg mirror are presented in Figure 3.29. An additional 4 Ω series resistor was used, to account for extra Ohmic losses, and better match the experimental results in the Smith chart. There is a good agreement between the simulated and experimental data, see Table 3.9 hereafter.

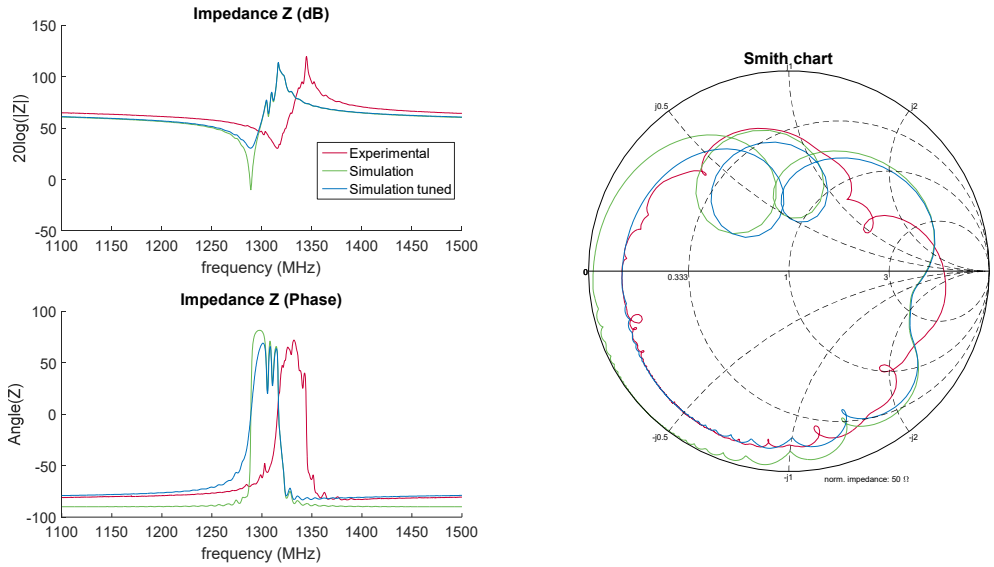

Figure 3.29 Electrical characteristics of the SM-LWR on a W/SiO_2 mirror. (Top left) Absolute part of the impedance. (Bottom left) Phase of the impedance. (Right) Smith Chart.

The results obtained for the resonator deposited on the AlN/SiO_2 Bragg mirror are presented in Figure 3.30. No extra lumped-element was used in this case, to better fit the experimental data. The experimental resonant frequency is lower than

the simulated one, whereas the experimental electromechanical coupling coefficient is higher. The differences are respectively -0.2% and +4.7%, see Table 3.9 hereafter.

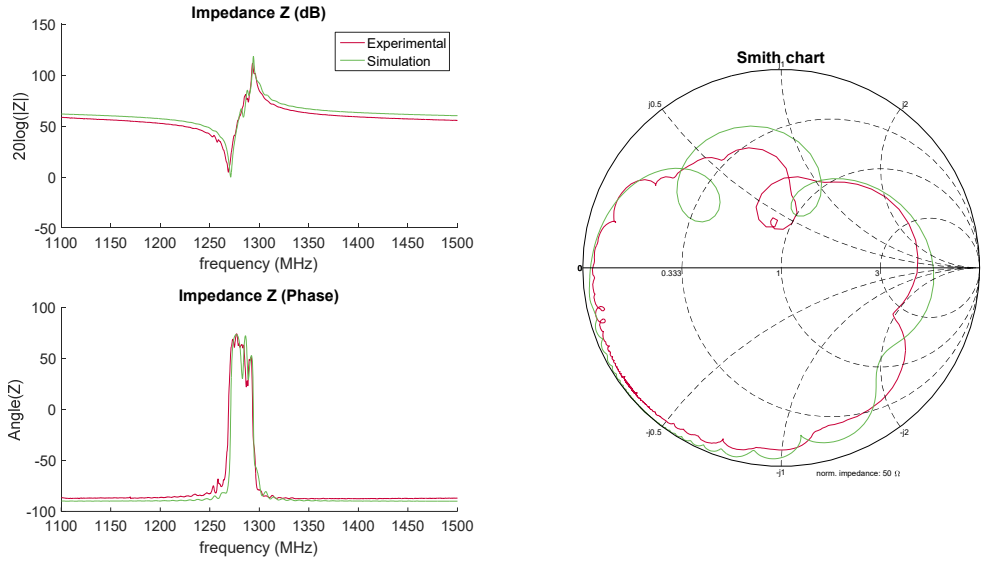

Figure 3.30 Electrical characteristics of the SM-LWR on a AlN/SiO_2 mirror. (Top left) Absolute part of the impedance. (Bottom left) Phase of the impedance. (Right) Smith Chart.

The experimental frequencies, coupling coefficients and quality factors are summarized in Table 3.9. The latter shows a relatively good agreement between numerical predictions and experimental results. The quality factor of the AlN/SiO_2 mirror is slightly lower than that of the W/SiO_2 mirror, and the quality factors are close to 700 in both cases. The fabricated resonator built on the SiO_2/W Bragg mirror had a coupling coefficient K^2=5.03% and a quality factor of Q=768 resulting in a FoM=38.6. The resonator built on the SiO_2/AlN Bragg mirror had K^2=4.50%, Q=862 and FoM=38.7. To our knowledge, these FoMs are the highest reported in the literature for LWRs and they open new perspectives for future applications.

The whole set of results (Figure 3.17 & Figure 3.18 for the free-standing LWR configuration, and Figure 3.29 & Figure 3.30 for the SM-LWR configuration) show that the solidly mounted resonators might perform even better than their free-standing counterparts, which is a very encouraging result. The higher quality factor of the SM-LWR may be explained by the absence of anchors and borders, and also by the absence of electro-mechanical coupling to the large number of resonant structural modes which arise in free-standing plate.

	$K^{2*}(\%)$	$f_r(MHz)$	$f_a(MHz)$	Q	FoM
W/SiO_2, Sim.	5.13	1289	1317	871	44.6
W/SiO_2, Sim. tuned	5.13	1289	1317	673	34.5
W/SiO_2, Exp.	5.03	1317	1345	768	38.6
AlN/SiO_2, Sim.	4.30	1271	1294	770	33.1
AlN/SiO_2, Exp.	4.50	1269	1293	862	38.7

Table 3.9 Frequencies, electromechanical coupling coefficients* [115] and quality factors determined numerically and experimentally, for the SM-LWRs.

On the same wafer, ladder-type bandpass filter demonstrators were fabricated. They are made of two resonators having 180 fingers in their IDT, 50 fingers in the reflectors and an aperture of 25λ. In our design, the series and parallel resonators have a wavelength of 5 µm and 5.125 µm respectively, which results in a slightly lower resonance frequency for the parallel resonator. We computed the COM parameters for each resonator. They are reported in Table 3.8. Using our P-Matrix algorithm, we computed the electrical characteristics of the bandpass filters. They are compared to the experimental data, in Figure 3.31. There is a relatively good agreement between numerical predictions and experimental data, which constitutes an important and promising result. It was indeed the final goal of the whole project to demonstrate the feasibility of a SM-LWR Ladder-Type filter, based on 30%Sc-doped AlN thin layers.

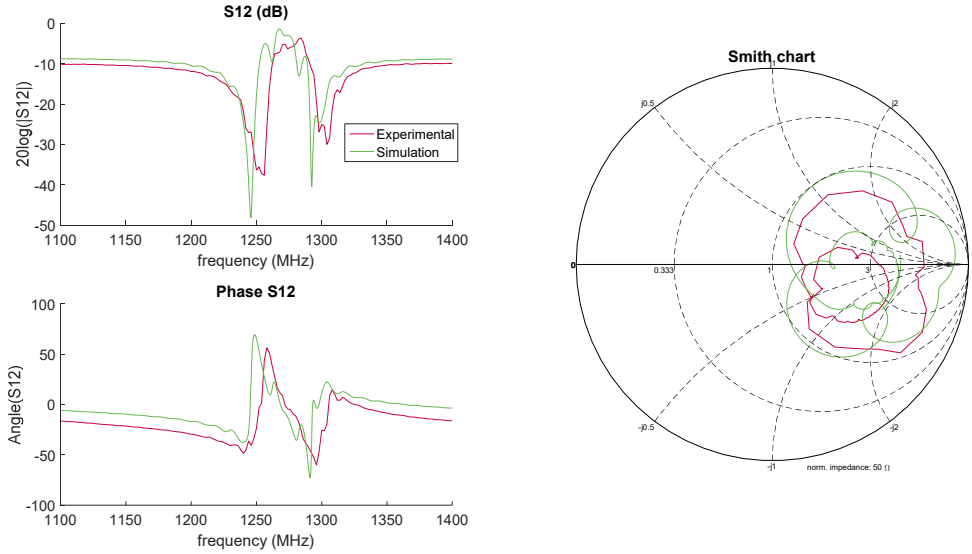

Figure 3.31 Electrical characteristics of a ladder-type filter made of two LWRs deposited on an AlN/SiO_2 Bragg mirror.

* The electromechanical coupling coefficients were computed using the following relation for an easier comparison with the results of our partners: $k^2 = \frac{\pi f_r}{2 f_a} \cot\left(\frac{\pi f_r}{2 f_a}\right)$

3.3 Conclusion

In this chapter, we investigated the potential of AlScN-based LWRs for filtering applications. Free-standing and SMR demonstrators were fabricated using C-MOS compatible processes. Both configurations showed higher velocities than that of the equivalent SAW, which demonstrates that high velocity Lamb wave modes may be used to ease the constraints on the lithography. The demonstrators also exhibited high electromechanical coupling coefficients (in comparison to AlN) that highlight the benefit of using Scandium doped AlN. The best performing resonators were achieved thanks to the SM-LWR configuration which has also proven to be the easiest to manufacture.

It is important to notice that although the fabricated SM-LWRs achieved good performances, we may consider some improvements of the latter. In the short run, the thicknesses of the layers within the Bragg mirrors could be computed by considering the resonant frequency of the SM-LWR as the frequency to isolate (instead of the resonant frequency of the equivalent free-standing LWR). The structure might also benefit from an overall optimization of the individual thicknesses in the stack.

Chapter 4 Characterization of high frequency multi-layered devices

The development of a new SAW or BAW device is typically done using a three-step process consisting in 1) a design phase using advanced simulations, 2) prototyping and 3) electrical characterization. The electrical response of the device can be quickly determined using a Vector Network Analyser (VNA), which yields the definitive characteristics. Nevertheless, the VNA provides only indirect information about the electroacoustic behaviour. Therefore, in addition to the electrical characterization, direct visualization tools of the waves provide useful information about the acoustic behaviour of the device. They are especially suited to directly detect unforeseen effects and elucidate loss mechanisms.

In this chapter we report on the development of a tool designed to visualize the out-of-plane displacement at the surface of micro-acoustic devices. The out-of-plane displacement generated by a mechanical wave at a given point on the surface ($z = 0$ in equation 1.1), is described by the following equation:

$$U_z = U_{vib} cos(2\pi f_{vib} t + \phi_{vib}) \quad 4.1$$

We developed this visualisation tool with the objective of characterizing the micro-acoustic devices for the next generation of telecommunication (5G). The latter calls for new high frequency, low loss SAW and BAW filters that are expected to operate at frequencies up to 5 GHz. A short list of the requirement is given below:

- Frequency range, f_{vib} from 3.5 to 5 GHz,
- Lateral resolution/spot size, less than 1 µm,
- Detection of the RMS amplitude U_{vib} and phase ϕ_{vib},
- Minimum detectable displacement amplitude, 10 pm,
- Minimum incremental motion, 300 nm step size,
- Field of view, 300×300 µm,
- Scanning time, less than one day (~1 pt/s),
- Frequency scan capability.

A wide variety of techniques were developed in the past to obtain the topology of the displacements on micro-acoustic devices. Some authors proposed to probe SAW using a Scanning Electron Microscope (SEM), which features stroboscopic effect capability [121]–[124]. However, a SEM is an expensive tool and the implementation of the stroboscopic functionality is a tedious task. For these reasons the method is not part of this study. Methods using an Atomic Force Microscope (AFM) are also worth mentioning since they have been used to detect SAW propagation [125] and interaction between SAW and a phononic structure [126]. Nevertheless, AFM methods can be considered as invasive techniques since the cantilever is in contact with the surface and therefore, it can influence the mechan-

ical behaviour of the waves [127]. Finally, other more singular techniques have been used. In [128], Kolomenskii *et al.* used laser generated SAWs to shake micron-sized Alumina particles. In [129], Tan *et al.* used SAWs to move smoke particles. In both cases, the particles, depending on their size and density compared to the ambient fluid, are gathered in the nodal regions. The results are Chladni figures showing the propagation of the waves. Nevertheless, these techniques are invasive since the measuring method interacts with the waves and may potentially affect the Device Under Test (DUT). Therefore, these techniques are not part of the study. In the following sections, we consider only optical characterization techniques.

4.1 Optical characterization of vibrations

A mechanical vibration can be optically detected using three different principles. The first principle uses the variation in intensity of a refracted beam covering several acoustic wavelengths. In this case, the acoustics waves act as a diffraction grating. We do not describe this technique since it does not enable single point detection of the wave amplitude. The second method is based on modulation of the reflection angle by the acoustic wave; this is explained in section 4.1.1. The third principle takes advantage of the phase modulation of the light generated by the acoustic vibration. However, photodiodes are not sensitive to the phase information carried by light beam but only to its intensity; thus, the phase modulation produced by a vibration should be converted to a change in intensity. This is achieved by creating interferences between a reference light and the modulated light beam. The methods based on interferometric principle are detailed in sections 4.1.2, 4.1.3 and 4.1.4. The general equation giving the light intensity of the interferences between two beams is given in Appendix E.2. Reviews of the possible different optical detection methods can be found in [130]–[133].

4.1.1 Knife-edge and deflection principle

The purpose of this method is to determine the amplitude U_{vib} of the wave from the sinusoidal variation of the illuminance caused by the change of the beam direction after reflection on the wave. Figure 4.1 shows the principle of the knife-edge method. The laser beam, focused using a first lens (L1), is reflected by the surface of the DUT. The mechanical vibrations on the DUT result in modulation of the reflection angle of the beam.

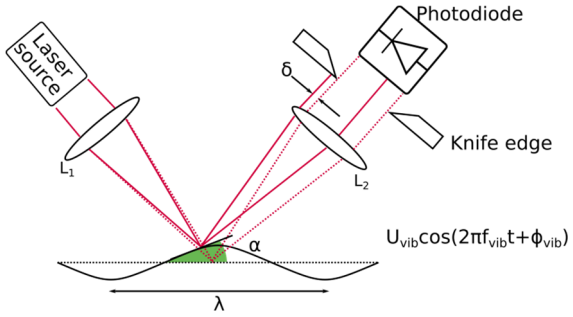

Figure 4.1 Illustration of the knife-edge principle. The dashed lines represent the beam when reflected by a flat surface. In this case the photodiode collects all the light. When the surface is tilted (solid lines), the reflection angle changes and causes the incident beam to be shifted by a distance δ. Part of this reflected light is blocked by the knife-edge causing a change of illuminance. Practically, the edges of the photodiode are used as knife-edges.

The light intensity on the photodiode is modulated in frequency by the vibration frequency (f_{vib}) and in amplitude by the reflection angle which is proportional to the vibration amplitude. If the latter is small compared to the observed wavelength, then the displacement of the beam δ is (see the development in Appendix E.1):

$$\delta = 2f_2\alpha = f_2\frac{dU_Z}{dx} = -\frac{2\pi U_{vib}}{\lambda}sin\left(2\pi f_{vib}t + \frac{2\pi}{\lambda}x\right) \qquad 4.2$$

Where, f_2 is the focal length of the second lens (L2) and λ is the wavelength of the observed vibration. The formula shows that the method is sensitive to the first derivative of the vibration. This technique has the inconvenient of requiring a good surface quality [130]. It has been used in [134] to develop a fast scanning SAW probe. Kamizuma *et al.* [134] used a single objective lens to focus the laser on the surface of the DUT and to collect the reflected light. They also used a continuous scanning method which enables to capture a large number of points per second.

4.1.2 Homodyne Interferometry and stroboscopic effect:

In a homodyne interferometer (see Figure 4.2), a laser beam (having an optical wavelength Λ) is split into two beams of different polarizations using a Polarized Beam Splitter (PBS). I_1 and I_2 are the respective light intensities of the two beams. One of these beams is used as a reference, and its path length is δ_{ref}. The second beam is reflected by the DUT, and its path length δ_{DUT} is modulated by the amplitude and frequency of the vibration $U_{vib}cos(2\pi f_{vib}t)$. The two beams are then recombined to create interferences. The photodiode produces a current proportional to the following equation (see development in Appendix E.3):

$$I_{12} = I_1 + I_2 + 2\sqrt{I_1 I_2}cos\left(2\pi\frac{\delta_{ref} - \delta_{DUT}}{\Lambda} - 2\pi\frac{U_{vib}}{\Lambda}cos(2\pi f_{vib}t)\right) \qquad 4.3$$

The interference signal consists of a continuous part and an alternative part carrying the information of the DUT vibration. The SAW/BAW vibration amplitudes are much smaller than the wavelength of the laser ($U_{vib}/\Lambda \ll 1$). Consequently, the current resulting from the interference oscillates around the co-

sine of the path difference $(\delta_{ref} - \delta_{DUT})$ (see Figure 4.2 right). The optimal sensitivity is therefore located at the working point verifying $2\pi(\delta_{ref} - \delta_{DUT})/\Lambda = (n + 1/4)(n \in N)$, see the detailed calculation in Appendix E.3. A movable reference mirror ensures that the interferometer is stabilized around a working point located at a quarter wavelength (see Figure 4.2). The position of the reference mirror (or the DUT itself) must be monitored so that the low frequency external perturbation (temperature and vibrations) on the path difference $(\delta_{ref} - \delta_{DUT})$ remains small compared to the vibration we want to observe. A homodyne interferometer operating in the quarter wavelength conditions produces interferences with the following intensity:

$$I_{12} = I_1 + I_2 + 4\pi\sqrt{I_1 I_2}\frac{U_{vib}}{\Lambda}cos(2\pi f_{vib}t) \qquad 4.4$$

The interferometer pictured in Figure 4.2, has polarization elements to avoid optical losses and back reflection in the laser cavity. It features two quarter-wave plates placed before the reference mirror and the DUT. After two passes in the quarter-wave plate, the polarity of the beams is shifted by $\pi/2$. This ensures that the beams are going towards the photodiode after the reflection.

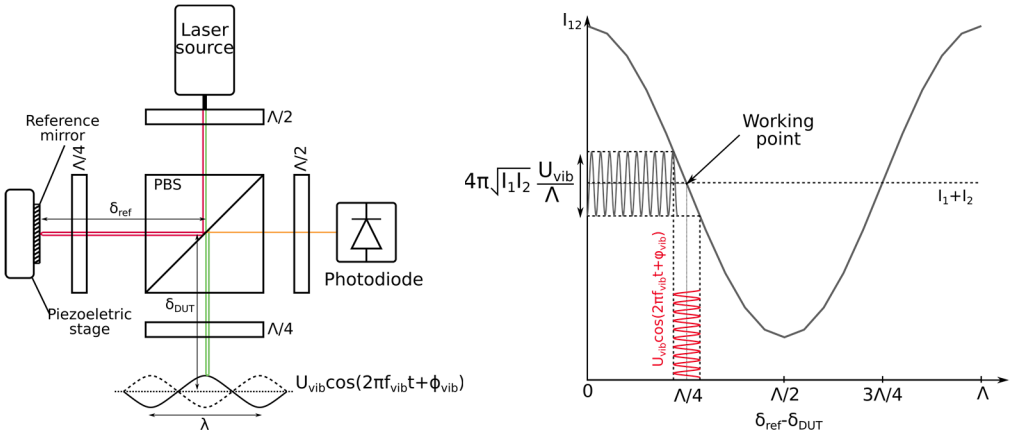

Figure 4.2 Schematic of the homodyne interferometer. (Right) Graph showing the interference intensity I_{12} versus the path difference between the measurement and reference arm. To ensure a maximum sensitivity, the homodyne interferometer is stabilized around a working point such that the path difference is $\Lambda/4$.

A Michelson stabilized interferometer was developed by Knuuttila *et al.* [135], [136] to observe vibration on the surface of a SAW for frequencies up to 950 MHz. The homodyne interferometer is also the core principle of the stroboscopic interferometer. In a stroboscopic homodyne interferometer, such as that developed by Lipiainen *et al.* [137] (or the more complex white light interferometer [138]), a pulsed light source is used to freeze the waves in a given mechanical phase state. In other terms, a pulsed light, having the same frequency as the vibration (or a fraction of the latter), is used to create a stationary image of the surface. Consequently, a slow photodiode can be used to detect the interference intensity. Practically, a CCD camera can replace the photodiode and this technique is used

to generate full-field images of the acoustic device. The technique was proved to be sensitive enough to detect SAW and BAW in a fast manner. Nevertheless, the pulse duration of the stroboscopic source limits the maximum detectable frequency.

4.1.3 Heterodyne interferometry and holography:

In a heterodyne interferometer (see Figure 4.3), an Acousto-Optic Modulator (AOM) splits a single laser beam into two beams of intensity I_1 and I_2. The zero-order beam remains at the frequency of the laser f_{laser} while the first order beam sees its frequency shifted by the frequency of the AOM resulting in an optical frequency $f_{laser} + f_{AOM}$. One of these beams is headed towards the DUT where it is reflected and modulated by the vibration. The two beams are then recombined to produce interferences. The resulting interference signal, as observed by a photodiode, is given by (see the demonstration in E.4):

$$I_{12} = I_1 + I_2 + 2\sqrt{I_1 I_2}\left(cos\left(2\pi f_{AOM}t + \frac{2\pi}{\Lambda}(\delta_{ref} - \delta_{DUT})\right)\right.$$
$$+ \frac{2\pi U_{vib}}{\Lambda}\left(sin\left(2\pi(f_{vib} + f_{AOM})t + \phi_{vib} + \frac{2\pi}{\lambda}(\delta_{ref} - \delta_{DUT})\right)\right. \quad 4.5$$
$$\left.\left. + sin\left(2\pi(f_{vib} - f_{AOM})t + \phi_{vib} - \frac{2\pi}{\lambda}(\delta_{ref} - \delta_{DUT})\right)\right)\right)$$

From this equation, we see that the resulting interference signal is composed of two parts. One is the so-called reference-signal which frequency is that of the AOM and which amplitude depends on the quality of the alignment as well as the surface reflectivity of the DUT. The second part of the interference intensity consists of two sinusoidal signals that characterize the mechanical vibration. Their amplitudes are proportional to the observed vibration amplitude and their frequency is $f_{vib} \mp f_{AOM}$. Figure 4.3 (Right) shows a representation of this signal in the frequency domain.

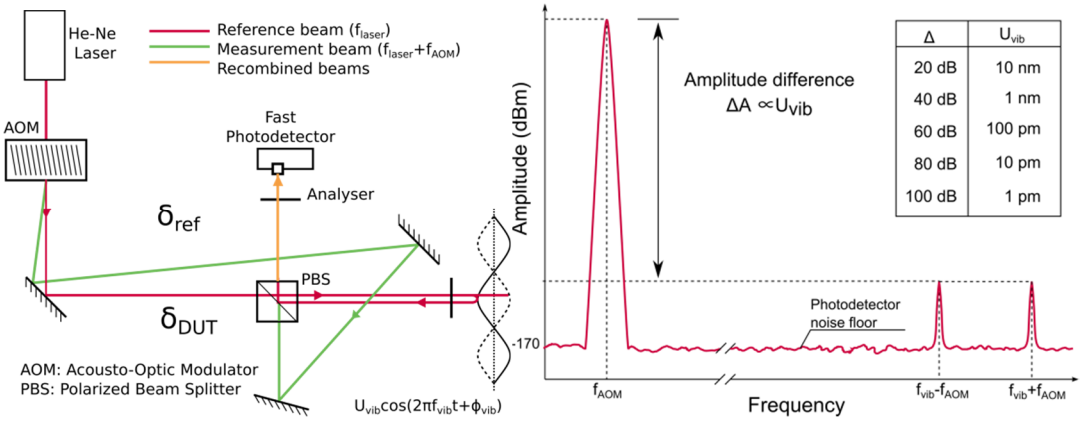

Figure 4.3 Schematic of a heterodyne interferometer. (Right) Expected interference signal coming out of the fast photodiode as observed on a spectrum analyser. As described by equation (4.10), the difference in amplitudes between the reference peak and signal peaks is proportional to the vibration amplitude. The table in inset shows the equivalence between the amplitude difference and the vibration amplitude.

The great advantage of the heterodyne interferometer is the generation of two oscillating signals which amplitude ratio is directly proportional to the amplitude of the observed mechanical vibration. In the frequency domain, the amplitude of the reference peak is:

$$A_{ref} = 2\sqrt{I_1 I_2} \tag{4.6}$$

The amplitude of the secondary signals is:

$$A_{secondary} = 2\sqrt{I_1 I_2} \times \frac{2\pi U_{vib}}{\Lambda} \tag{4.7}$$

And,

$$\frac{A_{secondary}}{A_{ref}} = \frac{2\pi U_{vib}}{\Lambda} \tag{4.8}$$

The equation in the decibel scale gives:

$$dB(A_{secondary}) - dB(A_{ref}) = dB(\tfrac{2\pi U_{vib}}{\Lambda}) \tag{4.9}$$

Or:

$$U_{vib} = \frac{\Lambda}{2\pi} 10^{(dB(A_{secondary}) - dB(A_{ref}))} \tag{4.10}$$

In addition, a change in the relative path difference $\delta_{ref} - \delta_{DUT}$ affects the two signals in the same way. It is therefore possible to fully remove these effects with a coherent detection (see [130]). Nevertheless, the latter is not appropriate in our case since we target high frequency vibration detection, and yet these perturbing variations are slow enough to not disturb the measurement.

Several heterodyne interferometers have already been built in the past with different variations. Royer *et al.* [139] proposed a very compact interferometer design, while Kokkonen *et al.* [140], [141] implemented a classical heterodyne setup able to detect vibration in the gigahertz range. Also, Teyssieux *et al.* [142] proposed a double-pass interferometer.

Based on the heterodyne interferometer, Telschow *et al.* [143], [144],[145] developed a full-field interferometer capable of acquiring a great number of points per second. Instead of an Acousto-Optic Modulator (AOM), they used an electro-optic modulator, which can change the phase of an optic beam at high frequency (up to several GHz). The electro-optic modulator is used to produce interferences with a beat frequency of only some Hertz. These interferences are used to locally modify the refractive index in a photorefractive crystal. The crystal is then illuminated to create a hologram that is observed using a conventional CCD camera.

4.1.4 Sagnac effect and time differential interferometry:

In a Sagnac interferometer (see Figure 4.4), a PBS splits a laser beam in two beams of opposite polarity. The beam with polarization normal to the plane is reflected by the two PBS. It passes first in the Sagnac loop and it is then redirected towards the DUT where it is reflected. The polarity of the beam is then shifted to a parallel polarization by two passes in a quarter-wave plate. Therefore, it is re-

fracted by the two polarized beam splitters. The second beam with an initial parallel polarization takes the opposite path; it is first refracted by the beam splitters and after the reflection, it takes the Sagnac loop. As a consequence, a time delay ΔT proportional to the Sagnac loop length is generated between the two beams probing the DUT, see Figure 4.4. The interference signal intensity is consequently (see developments in Appendix E.5):

$$I_{12} = I_1 + I_2 + \frac{4\pi\sqrt{I_1 I_2}U_{vib}}{\Lambda}(sin(2\pi f_{vib}t + \pi f_{vib}\Delta T + \phi_{vib})\, sin(\pi f_{vib}\Delta T)) \qquad 4.11$$

In this equation, the first sinusoidal signal depicts the mechanical wave vibration, and the second sine is a constant term that only depends on the delay ΔT generated by the Sagnac loop. To ensure maximum sensitivity, the latter must be close to 1:

$$sin(\pi f_{vib}\Delta T) = 1 \rightarrow \Delta T = \frac{1}{2f_{vib}} \rightarrow \frac{2(\delta_S - \delta_R)}{c} = \frac{1}{2f_{vib}} \qquad 4.12$$

For instance, to achieve a maximum sensitivity at 5 GHz, the delay generated by the Sagnac loop should be of 0.1 ns; this means that the path difference between $\delta_S - \delta_R$ is 6 cm. The sensitivity of such an interferometer optimized for 5 GHz is presented in Figure 4.4 (right). On this graph, we see that the sensitivity decreases rapidly when f_{vib} moves away from 5 GHz.

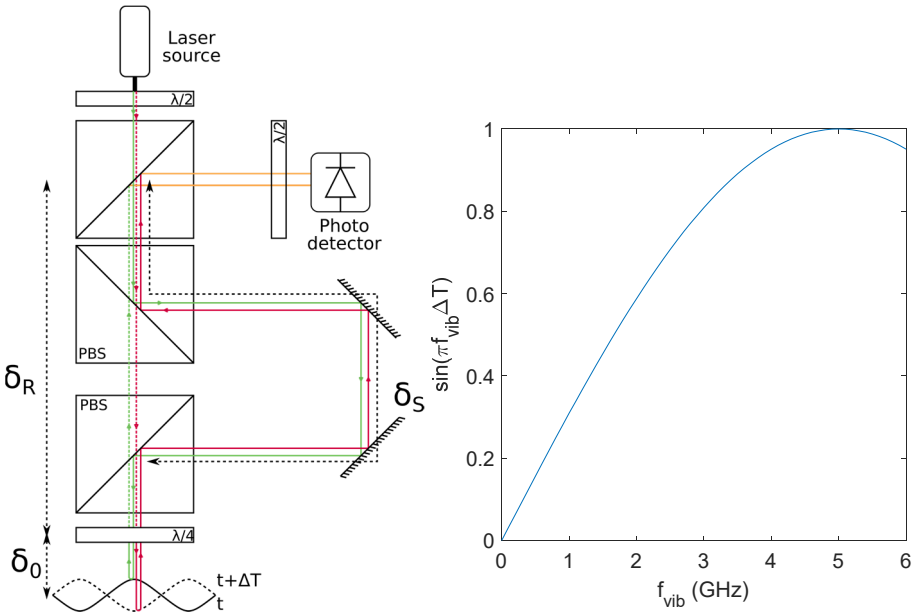

Figure 4.4 Schematic of a Sagnac interferometer. The beam in green has a shorter distance to travel before hitting the DUT. It will consequently probe the DUT at a time t. The beam in red has a longer distance to travel, it will hit the DUT at a time $t + \Delta T$. Since the distance to the photodiode is the same for both beams, the final delay is ΔT. The delay introduced by the Sagnac loop can be adjusted by moving the two mirrors on the right side. (Right) Sensitivity of the interferometer versus frequency, the delay in a Sagnac interferometer is optimized for a given frequency (here 5 GHz).

Because the two beams have the same path length, this interferometer is less sensitive to path variation due to external perturbations (temperature change, undesirable vibrations...). Such an interferometer has been built by Hashimoto *et al.* [146], [147] to observe mechanical vibration on SAW devices until 5 GHz (Aluminium Nitride on diamond structure). They used continuous scanning method to make the measurement faster and developed a miniaturized wafer prober to power their DUT.

The time differential interferometry (see Figure 4.5) relies on the same principle, except that in this configuration the beam is divided after its reflection on the DUT. One of the beams is then delayed (by a delay ΔT) using an optical delay-line (multiple reflections on mirrors, optical fibre, Fabry Perot Cavity). The other beam is directly directed toward the photodiode. The two beams are recombined using a beam splitter to generate interferences.

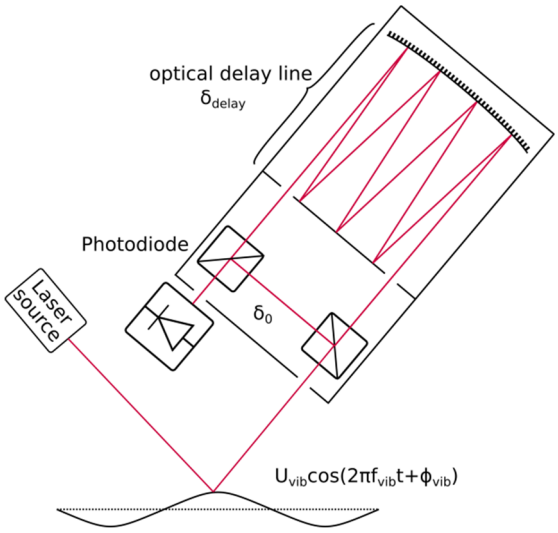

Figure 4.5 Schematic of a time differential interferometer. The large number of reflections on the two mirrors creates an important delay.

In this type of interferometers, the resulting interference intensity is given by the following equation (see developments in Appendix E.6):

$$I_{12} = I_1 + I_2 + \sqrt{I_1 I_2}\frac{4\pi}{\lambda}\big(u(t) - u(t + \Delta T)\big) \qquad 4.13$$

If the delay ΔT is long compared to the signal duration, the intensity is proportional to the normal displacement. On the contrary, if the delay is short compared to the duration of the signal the intensity is proportional to the normal velocity [130].

4.2 Literature review summary/Performance comparison:

In Table 4.1, we summarize the performance of the optical setups that were mentioned above.

Optical method	Reference	Min. disp. detected	Max. freq. (working freq.)	Spot size (wave length detected)	Points per second	Remark
Knife Edge	2006 Kamizuma [134]		1.2 GHz	1.4 µm	2500 pt/s	Continuous stage displacement
Homodyne interferometry	2000 Knuuttila [135],[136]	1.1 pm	GHz	1 µm	14 pt/s	
	2002 Miyamoto [148]		(850 MHz)			Homodyne + Polarization shift induced by shear waves
	2014 Lipiäinen [137], [138]	30 pm	(12 MHz)		780 kpt/s	full field, stroboscopic effect with pulsed laser
Heterodyne interferometry	1986 Royer [139]	40 pm	50 MHz			Compact setup (probe 8x5x3 cm^3)
	2008-2014 Kokkonen [140], [141]	0.3 pm	(2 GHz)	820 nm	75 pt/s	
	2013 Teyssieux [142]		4.5 GHz (392 MHz)	(8 µm)		Double-pass in AOM
	2013 Leirset [149]	7.1 fm	1.3 GHz (220 MHz)	1 µm	0.44 pt/s	Multiple AOM used
	2000-2003 Telschow [143], [144]	0.01 pm	(880 MHz)	(4 µm)	275 kpt/s	EOM, Photorefractive crystal
Sagnac	2010-2014 Hashimoto [146], [147]		6 GHz (5 GHz)	(2 µm)	1000 pt/s	Continuous stage displacement
Doppler vibrometer	Polythech	1 pm	2.45 GHz	<1 µm		Commercial tool
Numerical holography	Lyncée Tec	[5 pm-50 µm]	25 MHz			Full field Commercial tool
Sagnac effect	Neoark		3 Ghz	1 µm		Commercial tool

Table 4.1 Comparison of the different existing optical setups

As expected, the two full-field techniques [137], [138] and [143], [144] are the fastest (in terms of the number of points acquired per second). These methods exceed 100 kpt/s in both cases; this scanning rate is two to three orders of magnitude faster compared to the single point measurement techniques. Unfortunately, the lateral range visible using a full-field detection technique is limited by the objective used to focus the light on the sample. The objective is selected in a trade-off between the field of view and the lateral resolution (which is given by the image size of a CCD pixel through the objective lens). Therefore, these techniques are less suitable for the observation of long devices such as delay-line sensors (unless stitching is applied on multiple images during post-processing). In addition, the full-field techniques are both more complex setups and are limited by the use of more expensive parts. The stroboscopic homodyne interferometer requires an expensive short-pulsed laser. On the other hand, the holographic heterodyne interferometer needs a tuneable electro optic modulator and a photorefractive crystal. Finally, these methods are less documented than the single point counterparts and none of them has

been demonstrated at high frequency (1 GHz). For these reasons, the full-field techniques were not selected in our case.

Among the single-point techniques, the knife-edge is not suitable for probing the BAW, since the main component of the displacement may not generate a tilt of the surface (see [146]). The homodyne solution requires a complex reference mirror controlled by a feedback loop to ensure that the interferometer is in quarter wavelength configuration. The loop must compensate for small path variations due to external perturbations (for instance, thermal expansion, misalignment of the DUT). Finally, the heterodyne solution is well documented. The setups reported in the literature show great performances relative to lateral resolution and maximum frequency detectable. Therefore, we chose to implement a heterodyne probe featuring discrete scanning method and capable to detect vibration up to 6 GHz.

4.3 Heterodyne interferometry implementation

In this sub-section we discuss deals with the practical implementation of the heterodyne interferometer. The following section is divided into three parts in which we tackle respectively, the optical, the electronic and the software implementations.

4.3.1 Optical implementation

In this section we describe the implementation of the present optical setup (see Figure 4.6). More details about the early stage of the optical implementation can be found in [150].

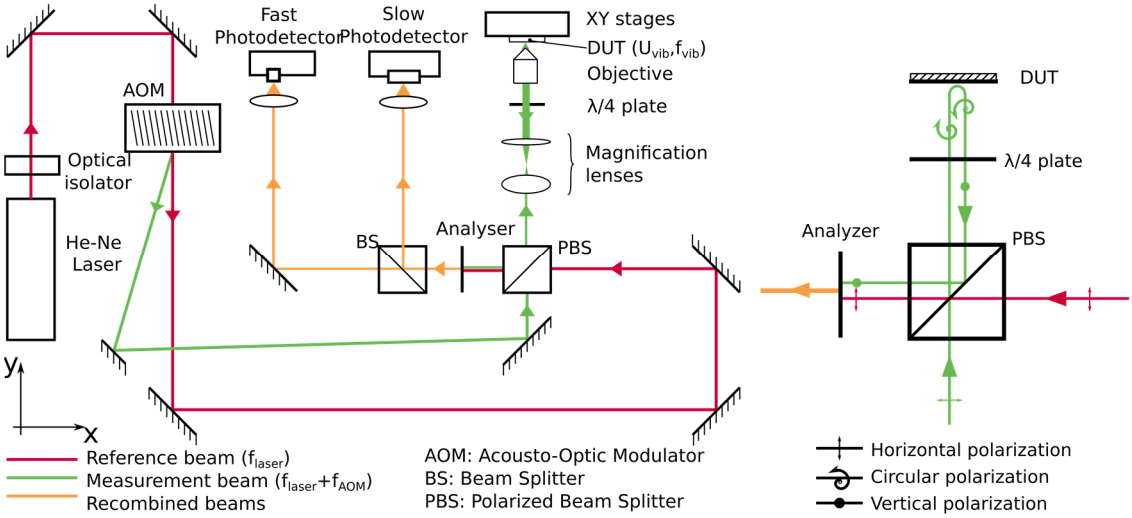

Figure 4.6 Schematic of the optical setup. The interferometer is shown unwrapped. Practically, the measurement arm (after the PBS) has two bends in the z direction (in a periscope like configuration). (Right) Simplified schematic showing the polarization state and the main polarizing components in the setup.

Beam splitting and beam polarization

The optical setup (see Figure 4.6) is based on a stabilized and polarized 5 mW HeNe Laser (Spectra Physic model 117A) with a wavelength Λ=633 nm. The beam is divided into a measurement beam and a reference beam by means of an AOM (Crystal Technology Inc. model 3080-125) operating at 80 MHz (Isomet model 532-C-4). The optical frequency of the measurement beam is shifted by 80 MHz while the reference beam remains at the same frequency. The two incident beams are horizontally polarized before entering the PBS. The latter is built so that the horizontal polarization is refracted, and the perpendicular one is reflected. Therefore, the measurement beam goes through the PBS and enters the measurement arm where it probes the DUT and its phase is modulated by the latter. The reference beam is refracted and goes directly thought the PBS.

Measurement arm and recombination

The measurement arm consists of a set of two achromatic lenses in a confocal configuration, a quarter-wave plate and a microscope objective. The measurement arm is mounted in a periscope configuration, which enables to scan the surface in the horizontal plane, see Figure 4.7. The set of lenses magnifies the laser beam before it passes through the objective. The lenses and the microscope objective are selected together to achieve a given spot size diameter on the DUT. The quarter wave plate changes the polarity of the incident measurement beam. After two passages in the quarter-wave plate the polarization becomes vertical. Consequently, the beam is reflected by the PBS on its way back (see Figure 4.6 (Right)). After the polarized beam splitter, the two beams are recombined using an analyser (polarizer rotated at 45 degree). The resulting interference intensity is observed using a fast photodiode (FPD) (Alphalas UPD-50-SP). Since the sensitive area of the FPD is small (the diameter of the sensitive area is 100 µm) compared to the diameter of the beam, a lens (f'=50 mm) is used to collect and focus the recombined beams on the FPD.

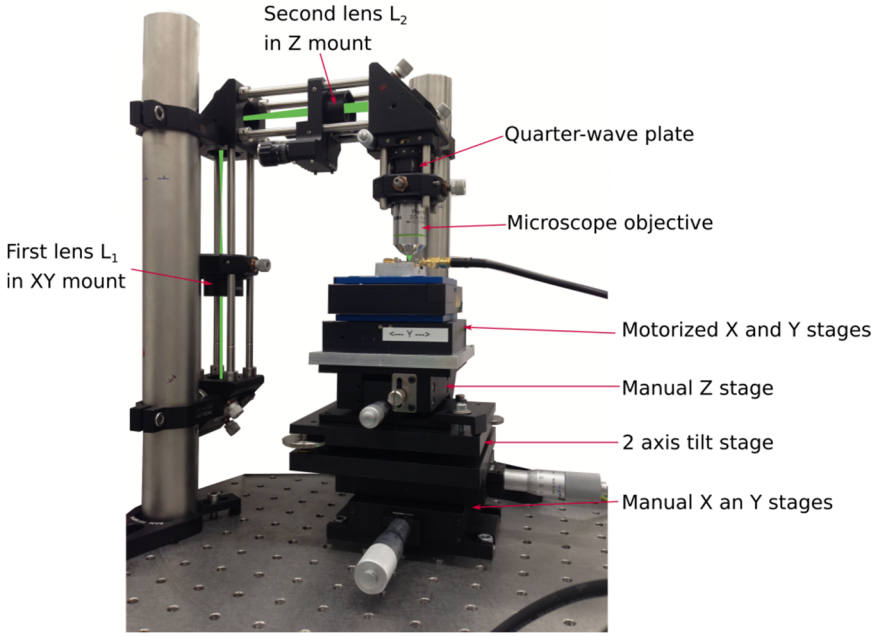

Figure 4.7 Picture of the measurement arm in a periscope configuration.

Scanning the DUT

Two solutions can be considered in order to scan the surface of the DUT. On one hand, we can either move the DUT using translation stages under a stationary laser. On the other hand, we can move the probing beam on a stationary DUT. The practical implementation of this second solution uses two mirror galvanometers. This configuration has less mass to move, since only lightweight mirrors are rotated. Therefore, it is probably a faster method to scan the DUT. In addition, the DUT does not move during the measurement making possible to connect the latter using a conventional wafer prober for instance. However, similarly to the full-field techniques, the system is limited by the field of view of the microscope objective used to focus the light on the DUT. This objective lens, that is used to collimate the light on the DUT, is chosen in a trade-off between the field of view and the minimum lateral resolution, see Appendix E.7.

Despite the advantages of the beam steering method, we chose to move the DUT using translation stages, a more straightforward solution. The DUT is connected to a first high frequency and tuneable frequency synthesizer (Analog Device model ADF4355) providing the excitation frequency f_{vib} required to generate SAW or BAW.

The DUT is placed on two automatic translation stages (Physik Instrumente PI model v-524) that are stacked. These are actuated using direct magnetic field [151]. Therefore, they are not adapted for a use in the vertical plane since they cannot sustain high load for a long period of time. They enable to scan large horizontal surface (1×1 cm^2) with high resolution incremental motion (20×20 nm^2), at a maximum velocity of 250 mm/s (when not loaded). We adopt a simple scanning

strategy consisting in a meander pattern. First, we use one stage to scan the DUT along a line; then, using the second stage, we switch to the next line and we repeat these steps until the complete surface is scanned, see Figure 4.8 (Right). With this technique, the stage scanning the line is much more used than the second one.

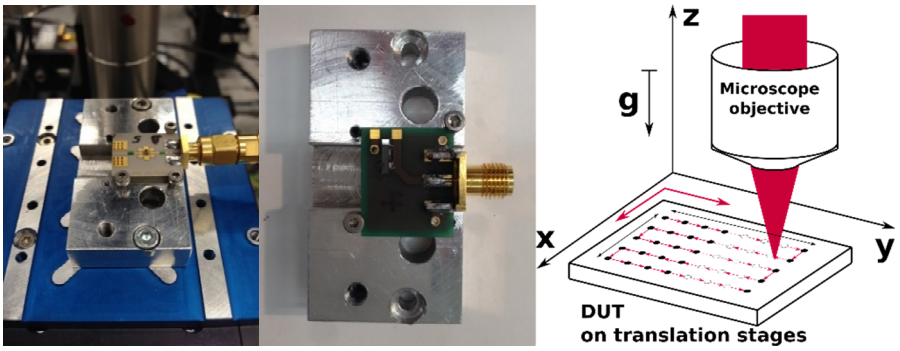

Figure 4.8 Pictures of the devices being measured and schematic of the scanning strategy. (Left and middle) Filter mounted on a RF360 PCB and delay-line sensor mounted on a standard CTR PCB. In both cases, the DUT is glued and wire-bonded on a PCB providing a SMA connector plugged to the frequency synthesizer. The PCB is mounted on an Aluminium part fastened on the translation stages. (Right) Schematic of the scanning strategy.

In addition, the two automatic stages are mounted on a two-axis tilt manual stage and two manual axis translation stages, see Figure 4.7. The two axes of the tilt stage are manually adjusted to compensate the small deviations in the flatness of the DUT mounted on the PCB. Otherwise these deviations could cause the surface DUT to be out of focus during the scan. The two manual translation stages are used to roughly position the DUT before a scan.

Spot size diameter and resolution

Before being reflected by the surface of the DUT, the measurement beam passes through an objective lens. The latter focuses the beam in a small spot on the DUT. The size of this spot in the focal plane defines the lateral resolution of our setup. It must be approximately twice smaller than the wavelength of the mode (propagative as well as standing) that we want to characterize. Theoretically, the minimum achievable spot size diameter (S) with a given objective is given by its diffraction limit. The following classical formula [152] [153] gives the diameter of the first Airy disk, which is considered as the diameter of the spot (Table 4.2 gives some numerical values):

$$S = 1.22 \cdot \frac{\Lambda}{NA} \qquad 4.14$$

where NA is the numerical aperture of the objective.

NA	0.1	0.2	0.3	0.4	0.5	0.6	0.7	0.8	0.9
Spot (nm)	7722	3860	2574	1930	1544	1287	1103	965	858

Table 4.2 Diameter of the spot versus numerical aperture (NA)

The formula (4.14) assumes a uniform illumination of the objective aperture. To come close to this condition, the incoming measurement beam is magnified using two lenses in a confocal configuration so that it covers the aperture of the objective. The two lenses are mounted in the periscope.

Typically, the higher is the magnification of the objective, the higher is its numerical aperture and the shorter is its focal depth. Consequently, for an objective having high numerical aperture (needed to have a small spot size), it is more difficult to keep the DUT surface in the focal plan during the scan. Therefore, in a given application, the objective is selected in a trade-off between the minimum achievable spot size and the ease to keep the DUT in focus.

The main objectives used for the characterizations are the 10× Olympus Plan Achromat Objective, 0.25 NA, the 20× Olympus Plan Achromat Objective, 0.40 NA, and the 20× Olympus Long Working Distance (LWD) Plan Achromat Objective, 0.40 NA.

Opto-mechanical mount

All the mirrors are mounted on two-axes manual rotation mounts. At least two mirrors are placed before entering the AOM, the polarized beam splitter, and the device under test. This method ensures that we can steer the beam correctly through the component and facilitate the optical alignment.

The two beam splitters are mounted on two-axes rotation mounts. The AOM is mounted on a manual rotation stage (rotation around the z axis). The latter is rotated such that we obtain two beams of balanced intensity at the output of the AOM. To make the alignment easier, we added a manual translation stage that makes possible to translate the AOM in the x-direction. The fast photo-detector is mounted on a three-axes manual stage. The latter enables to position the photodetector in the path of the recombined beams.

The periscope uses optical-cage mounts. The mirrors inside are oriented at 45° and the mechanical mounts offer the possibility to finely tune this angle. The first lens has a short focal and is mounted on an XY manual stage. The second lens is mounted on a Z manual stage which enables to precisely ensure the confocality between the two lenses. The quarter wavelength plate is mounted on a rotation stage and the microscope objective is mounted on an XY manual stage (see Figure 4.7).

Setup stability

As recommended by the laser datasheet, we added an optical isolator (Thorlabs IO-2D-633-VLP) to avoid back reflections in the laser source. The entire optical setup is mounted on an actively damped table to avoid any external vibration. The lengths of the two measurement arms are similar in order to stay within the coherent length of the laser.

4.3.2 Electronic implementation

In this section, we introduce and describe the present implementation of the selected detection method. More details about the steps during the implementation and intermediate development stages can be found in [154].

Expected signal levels and challenges

The amplitude of the interference signals generated by the fast photodiode are represented in Figure 4.9. In the frequency domain, we see three peaks. The first one, at low frequency, is referred as the reference-peak. In our case, its frequency is fixed at 80 MHz by the AOM and its amplitude, which depends on the surface reflectivity of the DUT and the quality of the alignment, is expected to be -40 dBm (6.3 mVpp). The two remaining peaks are referred as the signal-peaks. They have a higher frequency and their amplitude is proportional to that of the mechanical vibration.

Because of the high amplitude and frequency difference between the reference and signal peaks, it is difficult to detect the reference and signal-peaks using the same detection electronics. A possible solution to this issue consists in splitting the signal directly after the fast photodiode by using a RF-power splitter and acquiring the 80 MHz signal using a different detection system [149]. However, it is difficult to find a low-loss RF-splitter that has a flat response across the whole frequency range (80 MHz to 5 GHz). To overcome this issue, we split the recombined interference beam optically using a beam splitter and we use a second photodetector (Thorlabs PDA10A-EC) dedicated to the detection of the reference signal. Therefore, the electronics we developed is aimed at the detection of the high-frequency, low amplitude signal-peak. The lower frequency, higher amplitude reference-peak is detected with a commercial oscilloscope.

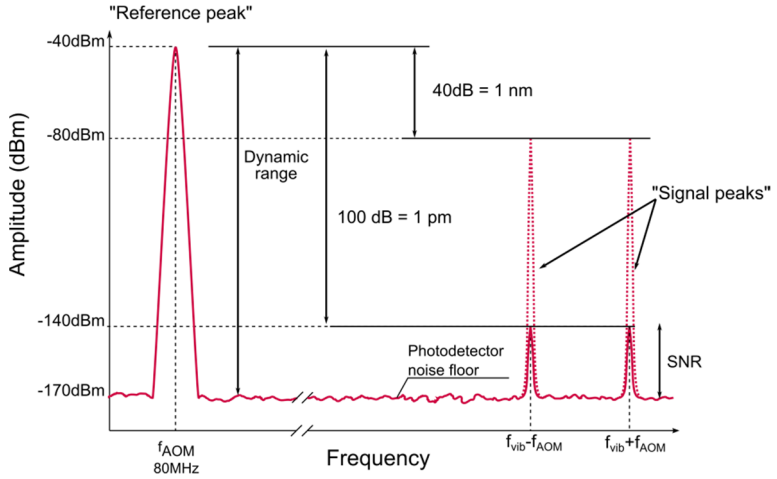

Figure 4.9 Expected signal coming from the fast photodiode in the frequency domain. The detection limit of the photodiode (noise floor) is defined by the thermal noise. In this case, for a resistance of 50 Ω, a bandwidth of 1 Hz and a temperature of 295 K, the noise floor is around -170 dBm. The dashed line represents the highest signal obtained for a detected displacement of 1 nm. The plain line represents the signal obtained for the smallest displacement of 1 pm.

The design of the electronics to detect these high-frequency, low amplitude signals is a challenging task:

- We must pay attention to the **dynamic range** of the electronics. Indeed, to ensure a minimum detected displacement of 1 pm, (*i.e.* 100 dB difference with the reference) and a maximum detected displacement of 1 nm (*i.e.* 40 dB difference with the reference) the system must have a 60 dB dynamic range (see equation 4.10 and Figure 4.9).
- In addition, we must look out for the **sensitivity** of the system. Considering a -40 dBm amplitude for the reference peak, the amplitude of the smallest signal to detect (1 pm) is only -140 dBm (63 nVpp). Therefore, a high gain, in the range of 60 to 100 dB, is required so that the signal comes in a range where it can be processed. We must pay attention to the additional noise that such a high amplification induces. We would like to keep a minimum Signal to Noise Ratio (SNR) of more than 5 dB after the amplification so that at the end of the chain we ensure a proper detection.
- We must ensure that the detection is **selective** enough. Indeed, the two signal-peaks oscillate at high frequency (from 500 MHz to 5 GHz) and are relatively close to each other (there is only a 160 MHz difference between the two signals). In addition, the reference peak at 80 MHz has a high amplitude compared to the other signals and it can interfere with the high frequency measurement.
- The **operational speed** of the detection should be fast enough so that the measuring time needed for a single point satisfies the requirements.

Detection methods

Different methods can be considered to detect the signal peaks. The first approach that comes to mind is to directly oversample the signal coming from the fast photodetector. With this method the sampling frequency should be at least twice the bandwidth of the analogue signal (Shannon's information theorem). This method would require an Analog to Digital Converter (ADC) having a very high sampling rate (>10 GS/s) and a fast computer to deal with the huge amount of data. The method has become popular in the last years because of the development of high-performance ADC. Nevertheless, such an ADC remains expensive. To avoid the expense of a high-performance ADC, one could consider under-sampling (see [155]). Indeed, when the Shannon theorem is not satisfied, a phenomenon called aliasing occurs which folds higher frequency signal in the passband of the ADC. This phenomenon can be used advantageously to sample signals with a lower frequency than their bandwidth. However, the method requires high design effort and advanced signal processing to eliminate spectral issues and recover the original signal. In addition, most of the ADCs are not designed to be used in under-sampling conditions [156].

The second approach consists in down-converting the signal to a lower Intermediate Frequency (IF) signal using frequency mixing. A basic architecture of such

a receiver is presented in Figure 4.10. Note that this architecture is similar that present in mobile phones, see Figure 1.10.

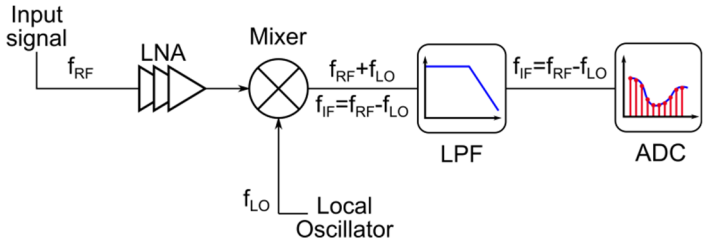

Figure 4.10 Basic architecture of a demodulator receiver. In the latter, the input signal at the frequency f_{RF} is first amplified using Low Noise Amplifiers (LNA) and then mixed with a Local Oscillator (LO) having a frequency f_{LO}. The product of the mixing is a signal containing two sine waves which frequencies are the sum and difference between f_{RF} and f_{LO}. The low frequency signal at $f_{RF} - f_{LO}$ is called Intermediate Frequency (IF) signal and its amplitude is proportional to the amplitude of initial RF signal. After the mixing, a Low Pass Filter (LPF) is placed to keep only the low frequency signal which is afterward sampled to compute its amplitude.

In a homodyne receiver (also called zero-IF receiver), the frequency of the Local Oscillator (LO) is chosen such that $f_{LO} = f_{RF}$. This architecture requires less hardware compared to other possible architectures. However, we observed practically a DC offset at the output of the mixer making the DC output biased with this unpredictable offset value. To address this issue the solution is to use non-zero IF architecture. More details about receiver architectures are given in [13].

Figure 4.11 shows a schematic of the receiver that we implemented. It is designed to enable fast acquisition and processing of the high frequency ($f_{vib} + f_{AOM}$) and low amplitude (-140 dBm) interference signal generated by the fast photodetector; it is described in the section below.

50 Ohms load and LNAs

The fast photodiode gives output in the form of current. It is needed to place a resistive load to convert it into voltage. This load must have a 50 Ω impedance over the whole frequency range. For this purpose, we selected a 1 dB SMA attenuator (Minicircuit FW-1+). Then, the signal passes through a series of three Low Noise Amplifiers (LNAs) (Minicircuits ZX60-83LN12+) that provide 60 dB of amplification. The LNAs provide a linear gain over the whole frequency range of interest while keeping the noise low. The gain flatness is better than 0.5 dB and the noise figure is less than 2 dB over the whole range. On the other hand, the gain is less than 15 dB at 80 MHz; thus, the undesired reference is filtered out.

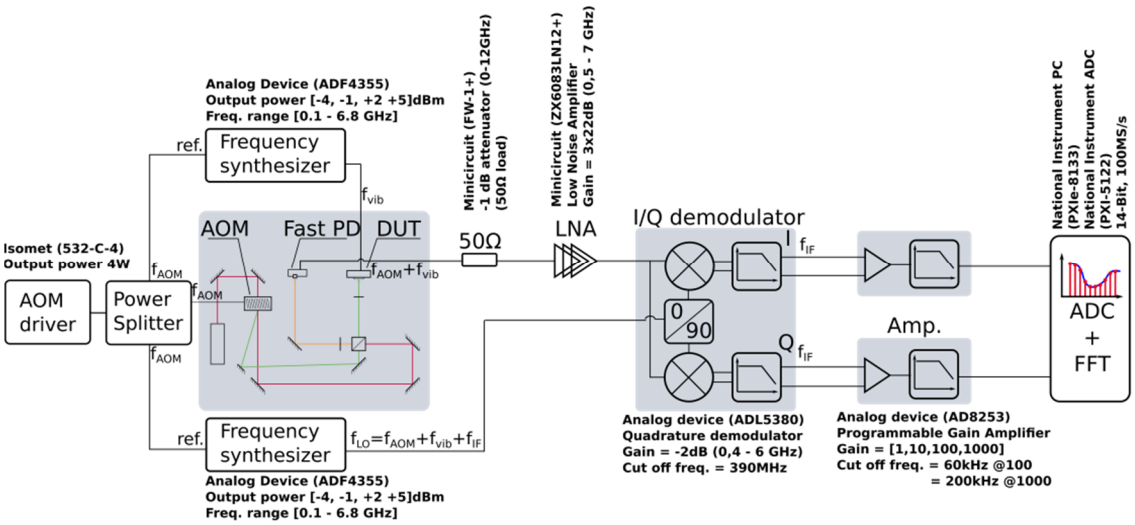

Figure 4.11 Schematic of the detection setup. The schematic features the values of the cut-off frequency and bandwidth of the different components. It is possible to see that the LNAs limit the lower frequency detectable to 500 MHz (their gain becomes non linear under this frequency). The I/Q demodulator limits the upper frequency detectable to 6GHz.

I/Q demodulator

The I/Q demodulator is a key component of the receiver chain. It mixes the local oscillator with the RF signal and converts down the signal of interest at the frequency $f_{vib} + f_{AOM}$ to a low intermediate frequency. The selected I/Q demodulator (Analog device model ADL5380) has a large bandwidth (from 0.4 to 6GHz) and a wide acceptable RF input range from -80 dBm (63 µVpp) to 10dBm (2 Vpp). Hence, the LNAs amplification is carefully chosen to yield a signal in this range. The demodulator features a low-pass filter with a 400 MHz cut-off frequency to reject all the high frequency products. We use the differential-ended output capabilities of the chip that is especially helpful for very low amplitude signals. The chip also supports common mode voltage on the differential output, which is also beneficial for low amplitude signals.

The demodulator is driven by a local oscillator signal, generated by a second tuneable frequency synthesizer identical to that providing the excitation signal (at f_{vib}) to the DUT. The LO generates a frequency $f_{LO} = f_{vib} + f_{AOM} + f_{IF}$, where f_{IF} is to be chosen in the frequency range from 1 to 30 kHz. The selected IF is 17015 Hz. The resulting signal coming out of the I/Q demodulator are (see Appendix E.8 for details):

$$v_I \propto 2\sqrt{I_1 I_2}\frac{\pi U_{vib}}{\Lambda} cos\left(2\pi f_{IF} t + \phi_{vib} + \frac{2\pi}{\Lambda}(\delta_{ref} - \delta_{DUT}) - \phi_{LO}\right) \quad 4.15$$

$$v_Q \propto 2\sqrt{I_1 I_2}\frac{\pi U_{vib}}{\Lambda} cos\left(2\pi f_{IF} t + \phi_{vib} + \frac{2\pi}{\Lambda}(\delta_{ref} - \delta_{DUT}) - \phi_{LO} - \frac{\pi}{2}\right) \quad 4.16$$

The I/Q demodulator comes in the form of an evaluation board. It is configured from the factory to provide single-ended I and Q output signals. It is

necessary in the present application to modify this configuration in order to have differential channels.

Instrument amplifiers (Automatic Gain Controller)

The I and Q intermediate frequency signals are too low in amplitude to be read by the ADC. Consequently, two Automatic Gain Control (AGC) boards (Analog Devices AD8253) provide additional gains. These chips come in the form of evaluation boards. They have the advantage of having built-in capability to convert common mode differential inputs in a single output, which is necessary in this application because of the single ended ADC input and differential output of the I/Q demodulator. They offer gains of 1, 10, 100 or 1000, selectable via two digital Input/Output (I/O). The gains are continuously adjusted during the measurement so that the output signal of the amplifiers best fit the range of the ADC. Four signals are required in total to control the two AGCs. These are generated using a digital I/O (PXI-6534). In the upcoming discussion of the ADC characteristics, we will see that the ADC has a range of ±10 V. For this reason, the amplifiers are powered with ±12 V in order to restrict to maximum outputs so that they stay within the range of the ADC.

The value of the adopted intermediate frequency must be within the bandwidth of the amplifiers. These amplifiers have a cut-off frequency of only 60 kHz for a 1000 gain. This leads to the selected IF frequency of 17015 Hz.

Analogue to Digital Converter (ADC)

A high-resolution ADC (National Instrument PXI5122) converts the IF analogic signals coming from the I and Q channels to digital data. As mentioned previously, the ADC range is ±10 V. It has a 14 bits resolution. If we consider 13 bits as the effective number of bits, the minimum voltage which can be measured by the ADC is $20/2^{13}$=±2.44 mV. This is equivalent to a dynamic range of 72 dB. The ADC can capture up to 100 MS/s. This ADC is part of an integrated system which also comprises a computer supporting LabView and a Digital I/O board.

Frequency synthesizers

To provide the high frequency signals (LO and DUT excitations) required by our detection setup, we use two identical phase lock loop frequency synthesizers (Analog Devices ADF4355). The chips come in the form of evaluation boards controllable via SPI protocol via a USB connection. To improve the frequency and phase stability of the whole electronics, the two frequency synthesizers share the same reference clock, which is that of the AOM driver at 80 MHz. The two evaluation boards come from the factory configured to use the internal reference clock. Therefore, we made the necessary modifications, so that the boards accept the external reference.

Expected signals levels

In Figure 4.12 we represented the signals levels at different locations within the receiver chain. The computation takes simply into account the gain and noise figures of each module present in the receiver chain. Thanks to this representation, we make sure that the signals are within the range of the I/Q demodulator and ADC while the noise floor amplitude remains below the lowest signal to detect.

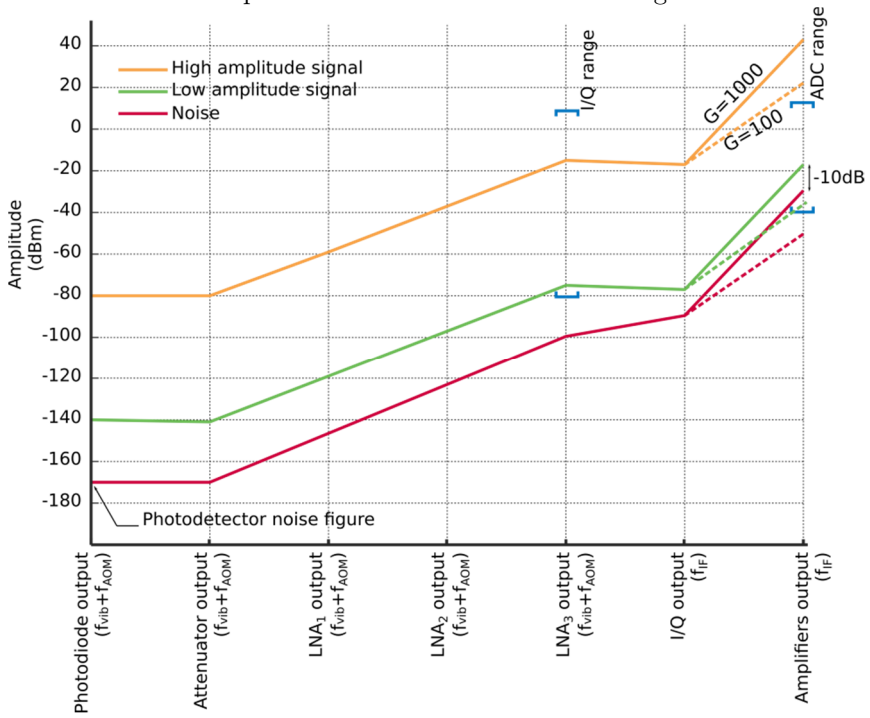

Figure 4.12 Representation of the expected lowest, highest and noise signals levels along the receiver chain. The signals levels are represented at the output of the different modules. In bracket are represented the input dynamic range of the I/Q demodulator and ADC. The role of the LNAs is to bring up the signals into the range of the I/Q demodulator. The AGC must amplify the IF signals so that they reach the ADC range. The graph highlights the need for controlled gain (G) amplifiers (with several gain values) so that the high amplitude signals remain in the ADC range.

Power unit

None of the modules discussed here comes with a power supply. Consequently, a complete power supply has been designed to provide all the necessary power inputs. Due to the presence of RF components in the system, it is required to have stable power supplies. Therefore, the supplies of the RF components have been designed using very stable low drop-out regulators that provide ripple free and stable supplies. In addition, each supply has its own switch to individually switch on the component and facilitate debugging. Figure 4.13 is a summary of the power supplies needed in the setup. A more detailed diagram of the power unit is given in Appendix E.9. The latter features the components names and wiring.

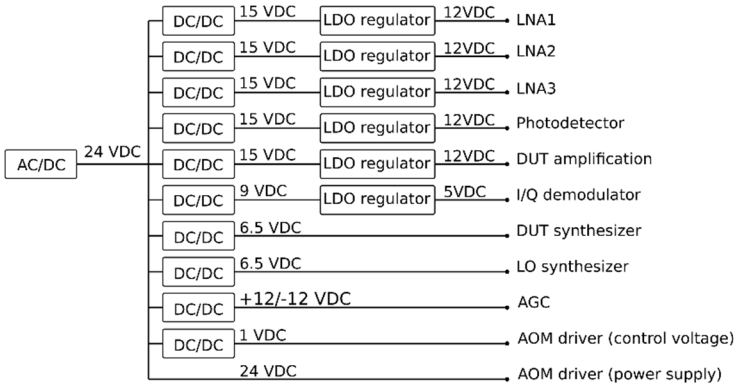

Figure 4.13 Diagram of the power unit. The latter converts the AC input from the building into all the necessary DC supplies. A first AD/DC converter generates a 24 V signal, from which the lower voltages are generated using DC/DC converters and Low DropOut (LDO) regulators when needed.

4.3.3 Software implementation

In this section we describe the software implementation; more details about this subject (in particular, the method to control the frequency synthesizers required in the setup) can be found in [157]. The LabVIEW software controls the entire setup (see Figure 4.14), it was chosen because most of the hardware (ADC, digital I/O, translation stage, oscilloscope) have built-in library function in LabVIEW. In addition, CTR has expertise with this software. The computer running the software is a National Instrument (NI PXIe 8133) that is mounted in a chassis (NI PXIe-1062Q) which also integrates the ADC (used to sample the IF signal) and the digital I/O (to control the AGC) discussed previously. The communication with the translation stage driver and frequency synthesizers is done via USB. The oscilloscope is connected via an Ethernet cable.

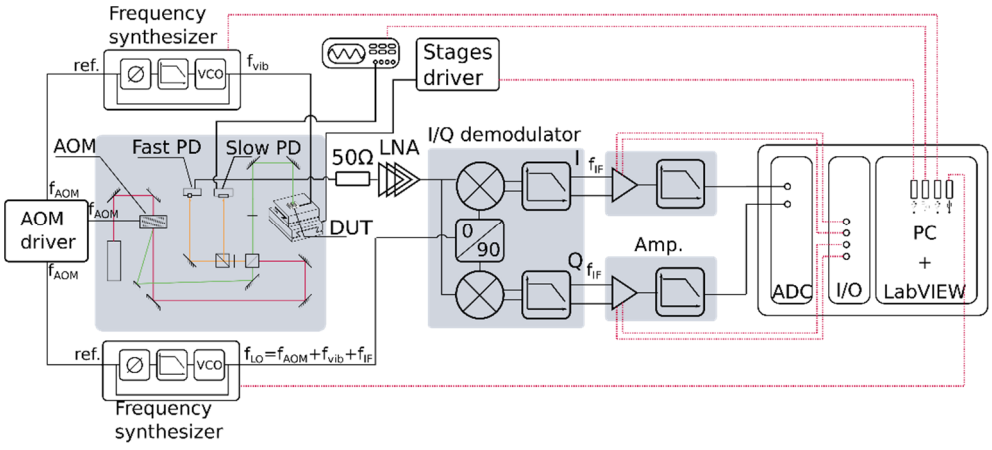

Figure 4.14 Schematic showing the connection between the computer, ADC and digital I/O with the rest of the hardware.

Two different strategies can be considered to scan the surface of the DUT and acquire the vibration amplitude topology at different frequencies:

- The first strategy consists in scanning all the desired frequencies first at a single point, and then the operation is repeated for each spatial point of the surface. This technique benefits from the fast sweeping capability of the frequency synthesizers.
- The second strategy consists in scanning the entire surface, and then the operation is repeated for all the desired frequencies. This technique offers the possibility to scan the surface extremely fast using continuous displacement method.

Motivated by the ease and rapidity of integration, we chose to implement the first technique. During the development of the system, the continuous displacement scanning method was not considered because it requires additional efforts on the signal processing to extract the useful information (amplitude of the vibration). When not considering continuous displacement, the first strategy is expected to be faster than the second, since it is faster to discretely switch between frequencies than it is to switch between positions.

Following this choice, the state diagram of the LabVIEW program is presented in Figure 4.15. After the initialization of the hardware instruments, the software goes in the idle case. The idle case enables real time recognition of a change in input parameters. After setting its experiment, the user can either start a surface scan or a single point measurement. The single point measurement is a continuous measurement (until stopped by the user) of the sample at a given point and a given frequency. This function is mainly used to tune the setup before a complete surface scan. During a surface scan, the program will scan the surface point per point, and for each point sweeps the frequency.

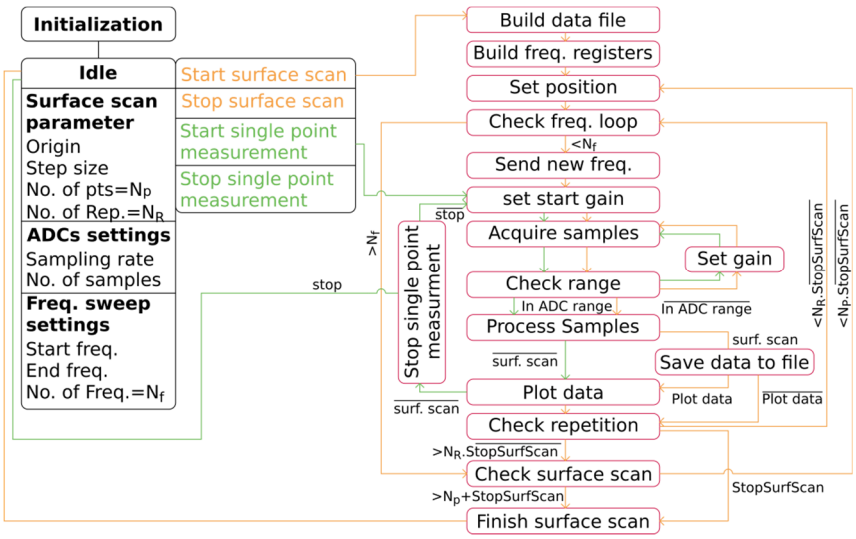

Figure 4.15 State diagram of the LabVIEW program. The program uses sub functions (red boxes) to realize the two main measurement types. The transition between the sub functions is done when the state condition is fulfilled. For the surface scan measurement, in addition to the real time visualisation of the vibration, the software stores the raw data in a text file. Because the "plot data" step slows down the measurement, the user has the possibility to activate it only when desired.

The implementation of the translation stage in LabVIEW is straight forward using the built-in library. They are controlled in close loop operation. The stages integrated sensors give a minimum resolution of 10 nm. The two stages are stacked on each other, resulting in different dynamic properties. The bottom stage has more mass to move (the mass of the stage on top, plus the mass of the DUT); consequently, its dynamic characteristics (PID controller) have been changed so that it is more stable but also slower. For this reason, the top stage, which moves faster, is used to scan lines over the device and the bottom stage is used to switch between lines (see the scanning method in Figure 4.8).

As mentioned previously, the two AGCs adjust the amplitude of the IF signals so that they take advantage of the entire ADC resolution. To select the suitable gain, the software starts by applying the higher gain value possible (×1000). If the signals are not within the range of the ADC, the AGC gains are reduced iteratively. If the signals are in the range, the samples are processed in the next step.

The samples are then digitally processed. A built-in LabVIEW function called "Single tone extraction" is used. The latter applies the Fast Fourier Transform (FFT) to the signals (I and Q channels) and extract the main amplitude in a range around a centre frequency. Both the range and the centre frequency are specified by the user. Typically, the specified frequency is f_{IF}. The detected signal amplitude is then reworked to determine its amplitude as it is at the output of the photodiode. Basically, all the gains we added in the detection chain are divided to retrieve the original signal. Finally, the absolute amplitude of the mechanical vibration is computed from this original signal and the amplitude of the reference peak detected by the slow photodetector connected to an oscilloscope. The relation used is described by equation 4.10. More details are given in the diagram of Figure 4.16.

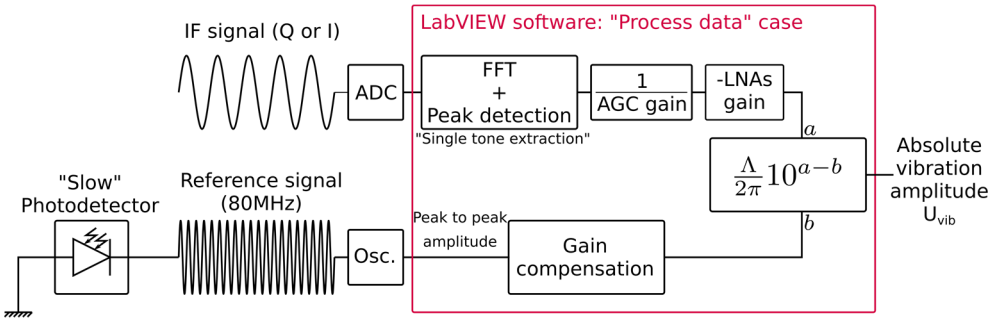

Figure 4.16 Diagram explaining the functioning of the data processing in LabVIEW to obtain the absolute amplitude of the mechanical vibration.

Controlling the frequency synthesizer using LabVIEW is a more tedious task. The frequency synthesizers are controlled by thirteen registers, each of them has 32 bits. They are sent via a SPD-S control board connected to the evaluation board of the ADF4355. These registers contain the information about the frequency to be generated (for instance its amplitude) as well as internal information about the ADF4355 such as the values for the dividers in the phase-lock loop synthesiser or the used reference frequency. The bits needed to code the frequency, its amplitude

(power in dBm) and its activation are contained in only four of the thirteen registers (numbered 0 to 12). The remaining nine registers contain information that does not vary for our application. These registers will be constant regardless of the frequency to be fed.

During the global initialization, the two frequency synthesizers are also initialized. A configuration file is sent to each of the frequency synthesizer containing, their address, the frequency and trigger type (rising or falling edge) of the clock. Then the program builds the registers for all the frequencies that will be sent during the scan. In reality, a total of seventeen registers are sent to set a unique frequency. Indeed, there are four additional registers that are sub-steps, corresponding to registers 0, 1, 2 and 4 bits, programmed for a halved reference frequency.

4.4 Results and performance

The first part of this section is dedicated to the performance evaluation of the individual aspects of the setup (optic signal level, lateral resolution...). Indeed, during its development, the setup was characterized regularly to find out its current capabilities and weaknesses. These intermediate results are presented here to highlight design choices that we made during the developments. The second part of this section focuses on the global performance of the setup and the characterizations that are possible to make with this tool.

4.4.1 Optical results

Observed interference level

The level of the interference signal at 80 MHz was observed at the output of the fast photodiode and slow photodiode for different optical configurations of the measurement arm and DUT surface reflectivity. The former was modified iteratively by adding/removing the magnification system and objective, while the latter was either a high reflective optical mirror or a lower reflective $LiNbO_3$ crystal. In order to have comparable data, it is necessary to realign the mirrors for each configuration. Attention was paid to this alignment so that the data are as reliable as possible. This study is useful in several ways. First, it enables to compare the different configurations in term of light intensity loss. When we add an optical element, the interference signal should not lose too much intensity. Secondly, it provides the optical power received by the two photodiodes. The optical power levels should be comparable, meaning that we can optically measure the reference peak using the slow photodiode and still have reliable signal comparison with the high frequency signal. The obtained results are summarized in Table 4.3. Finally, the latter also gives reference values for the observation of future devices. If the detected reference signal is too low, compared to these reference values, then one should consider checking the alignment or the surface reflectivity of the sample.

Magnification type	DUT type	Level on slow photodetector PDA10-EC		Level on fast photodetector	
		Osc. reading (mV)	**Opt. power (mW)**	**S.A reading (dbm)**	**Opt. power (mW)**
No Magnification	Mirror	960	0.240	-43.80	0.256
Magnification		1100	0.275	-42.70	0.291
Obj. X10		950	0.238	-43.80	0.256
X2magnification +Obj. X10		890	0.223	-44.67	0.232
Obj. X20		950	0.238	-43.00	0.281
X2 magnification + Obj. X20		920	0.230	-44.80	0.228
Obj. X20b		980	0.245	-43.50	0.265
X2 magnification + Obj. X20b		990	0.248	-44.00	0.251
Obj. X10	$LiNbO_3$	430	0.108	-51.50	0.106
X2magnification + Obj. X10		410	0.103	-51.80	0.102
Obj. X20		430	0.108	-51.80	0.102
X2 magnification + Obj. X20		420	0.105	-51.70	0.103
Obj. X20b		441	0.110	-50.80	0.115
X2 magnification + Obj. X20b		405	0.101	-52.50	0.094

Table 4.3 Level of the interference signal at 80 MHz in different optical configurations. The signal coming from the slow photodetector is observed thanks to an oscilloscope whereas the signal coming from the fast photodetector is observed using a Spectrum Analyser (SA). One can see that there is no significant optical power loss when adding/switching an optical component (magnification and objectives). On the contrary, there is an important loss (>50%) when using the $LiNbO_3$ surface compared to the mirror. Finally, the power measured by the two photodiodes are comparable.

Characterization of the spot size (diameter)

The size and shape of the spot reflected on the DUT was characterized using the knife-edge technique. The method consists in observing the amount of light reflected by a reflecting blade as it passes under the laser beam, see Figure 4.17. The edge of this reflecting blade must be very well defined; that is why we used a resolution test chart (USAF target) as a translating edge. Since the laser beam intensity can be approximated by a Gaussian distribution after the objective, the result of the knife edge scan is a Gaussian error function which standard deviation is a direct measurement of the spot diameter. The resulting light intensity (I) is given as:

$$I(x) = -\frac{1}{2}a\left(1 + erf\left(\frac{x-\mu}{\sqrt{2}\sigma}\right)\right) + b \qquad 4.17$$

Where, a and b are the scale factors and the offset. x is the position of the knife-edge. $erf(x)$ is the error function. σ and μ are respectively, the variance and average value of the Gaussian distribution.

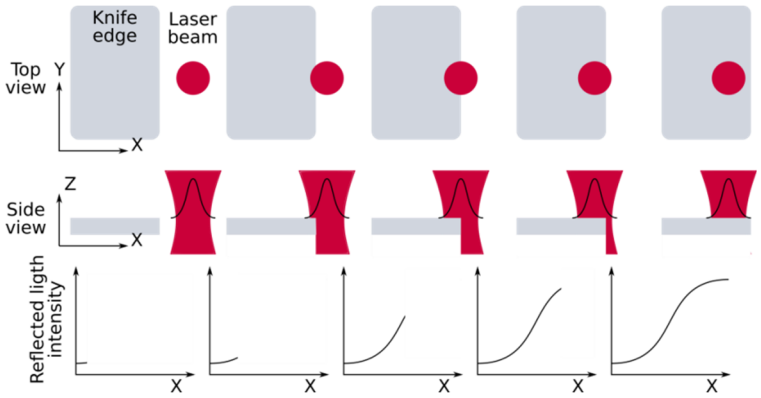

Figure 4.17 Illustration of the knife edge method to evaluate the spot diameter.

Experimentally, the focal plane of the objective (where the spot size should be measured) is found using the heterodyne interferences maximum intensity. The beam diameter was characterized in two perpendicular directions in order to have an evaluation of the spot deformation. The high-resolution translation stages were used to move the target, and the amplified photodetector, connected to an oscilloscope, measures the slow amplitude variations of the reflected light. A program in LabVIEW was built to facilitate the control of the stages and photodetector output amplitude acquisition (see in Appendix E.10 the state diagram of the LabVIEW program). The software also processes the data; it fits the theoretical error function and returns the fitted variance and average value. Figure 4.18 shows examples of characterization results.

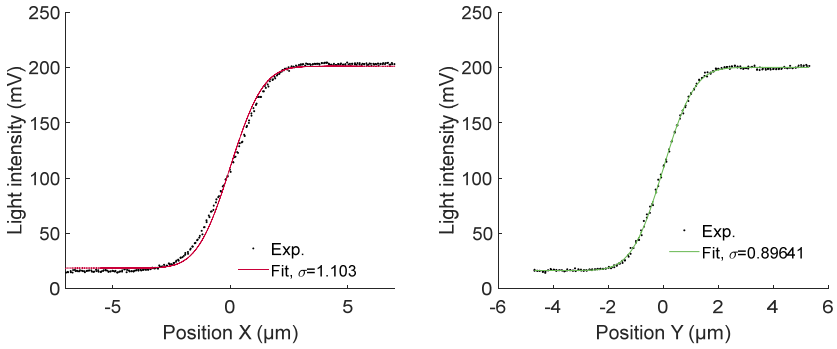

Figure 4.18 Reflected light intensity versus position of the knife edge. The objective tested in this case is the Olympus 20X plan achromat objective. The method is applied in X direction (left) and Y direction (right) in order to have an idea about the shape of the spot.

As mentioned in subsection 4.3.1, the two lenses constituting a beam expander are placed before the objective lens. Their function is to magnify the laser beam so that it approaches a uniform illumination of the objective aperture. However, the magnification should not cause the beam to lose intensity on the edge of the objective.

The three main objectives used for the actual device characterizations were characterized. For these objectives, we found that the best magnification is $\times 2$. It

was achieved by using a first lens having a focal length f=75 mm and a second lens having a focal length f=150 mm. For comparison purposes, the spots obtained with both objectives have been characterized with and without the ×2 magnification. The spot sizes were only observed in the X and Y directions. Figure 4.19 summarizes the results and compares them to the best theoretical spot achievable. In this figure, the ellipses semi-major and semi-minor axes are simply the experimentally determined standard deviations in the X and Y directions. The obtained results show that the laser spot obtained with the two objectives is slightly elliptical.

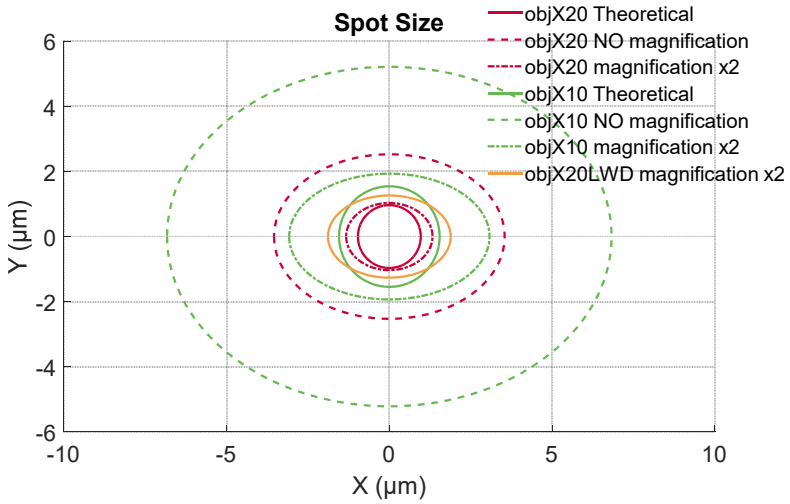

Figure 4.19 Representation of the spot size in the different configurations. The scales of the two axes are the same in order to better reflect the elliptical shape of the spots. The plain circles represent the theoretical size of the spot as given by the first zero in the Airy function. The dashed ellipses represent the measured spot. The abbreviation LWD stands for Long Working Distance.

4.4.2 Electronic/Software results

The smallest mechanical amplitude that can be measured with our system is directly proportional to the minimum achievable noise floor. The measurement noise was evaluated at the digital signal processing output. As expected, the noise level is reduced, when more samples are measured (see Figure 4.20, blue and orange curves). On the other hand, the acquisition of more samples requires more time. The noise level therefore depends on the measurement time (see Figure 4.20, yellow curve). As an example, the measurement time was 50 ms with a noise level of -145 dBm, for a sampling rate of 1 MS/s, 25600 samples and f_{IF}=25 kHz.

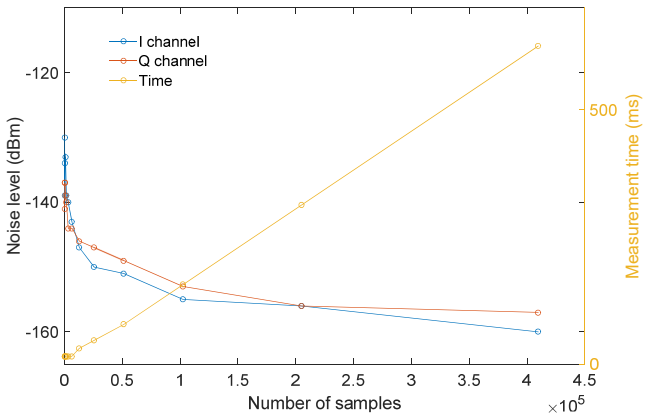

Figure 4.20 Graph showing the relation between the measurement time, the noise level and the number of samples taken. One can notice that the measurement time increases linearly with the number of samples.

4.4.3 Vibration isolation

As mentioned in subsection 4.3.1, the isolation of the setup from the external vibrations is critical. The frequencies of these external vibrations are typically far from the frequency range of interest. Nevertheless, they may have enough amplitude to influence the reference signal at 80 MHz and therefore disrupt the high frequency signal readings. The isolation of the setup was improved step by step. First the setup was moved far from a flow-box table that is present in the room. Indeed, the vibration coming from the flow-box ventilation affected the measurement see Figure 4.21 (left). Then the setup was re-built on an air-damped table. One can see the benefit of using such a table in Figure 4.21 (right). Finally, the mechanical mount enabling to move the DUT in the z-direction has been changed for a more stable one.

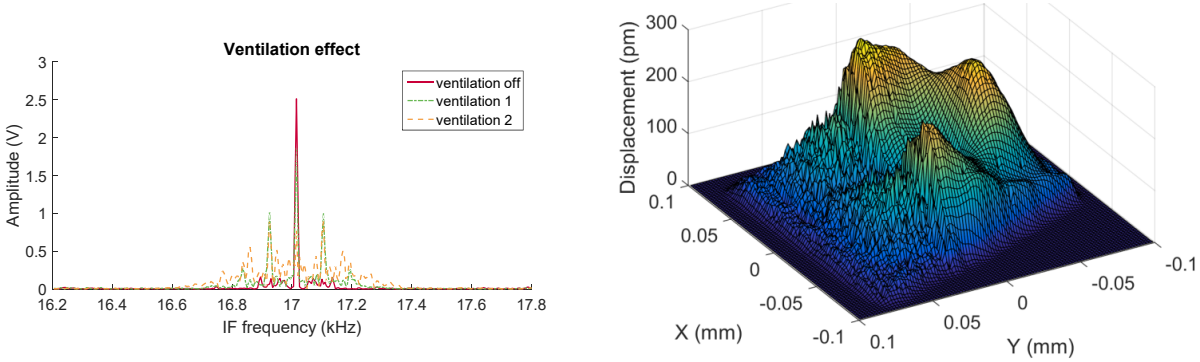

Figure 4.21 Influence of external vibration on the setup. (Left) Graph showing the effect of the ventilation on the IF. The graph shows the Fourier Transform of the IF signal from which the amplitude of the vibration is computed. The ventilation of the flow box has two settings for high and low aspiration. When the ventilation is turned off, the IF peak at 17015 Hz appears clearly. When the ventilation is activated on the first setting, noise starts to appear around the IF peak and weakens it. These effects are even more significant on the second setting of the ventilation. (Right) Picture showing the influence of the table isolation. The picture was obtained by turning off the air pressure supply by mistake during a scan. After it is turned off, the table takes several minutes to release all the air it contains. After that, the damping is completely inefficient and external vibration disturbs the measurement.

4.4.4 Laser stability

The first laser originally planned for the setup was more powerful (Thorlabs HNL210L, having 21 mW output power). With a laser of such power, the interference intensity is higher which improves the signal to noise ratio. Nevertheless, this laser exhibits a non-stable behaviour leading to the detection of undesirable displacement on the surface of the DUT, see Figure 4.22.

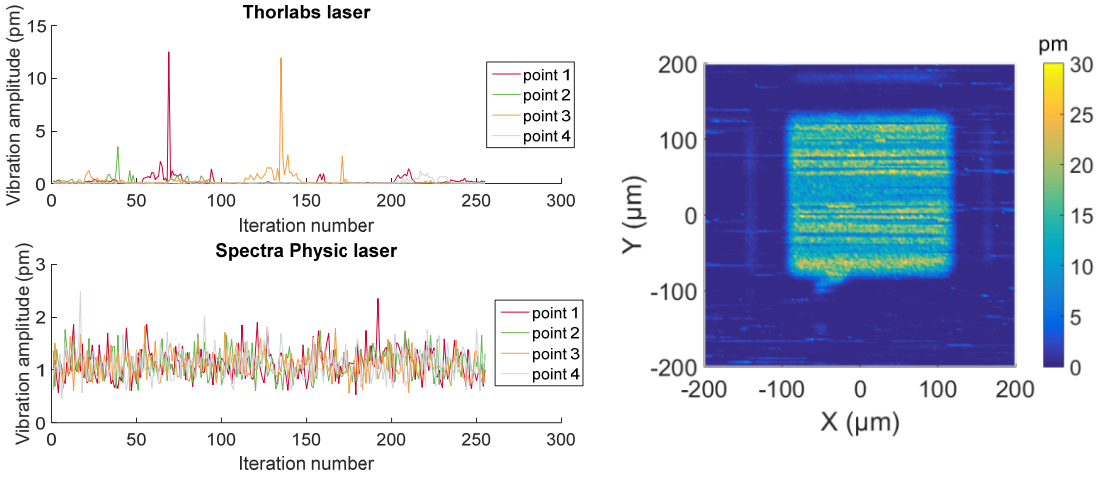

Figure 4.22 Graphs and picture showing the instability of the laser. To obtain these graphs we made 250 measurements of the vibration amplitude on four different points of a DUT (not excited). The results show that the Thorlabs laser (Top left) although having a really low minimum detectable displacement, exhibits unwanted peaks due to its instability. The Spectra physic laser (Top bottom), on the other hand, has a higher minimum detectable displacement around 1pm, but it is much more stable. Note that these measurements were performed without using an optical isolator. (Right) measurement of the vibration on top of a BAW device made with the Thorlabs laser. The laser instability produces "lines" of higher detected vibrations oriented along the main scanning direction.

After finding out this problem the laser was replaced by a more stable one (Spectra-Physics 117A) and an optical isolator was placed in front to avoid back reflection.

4.4.5 Device characterisation

In this subsection we discuss the characterization of micro-acoustic devices either BAW or SAW.

Thermally compensated SAW filter at 900 MHz

We characterized the RF Filter which electrical characteristics are presented in Figure 4.23 and a microscope picture is shown in Figure 4.24. This is a ladder-type filter, composed of two SAW resonators, one in series and one in parallel. The substrate is made of Lithium Niobate 128YX, the electrodes are made of a Copper-based material. The pitch of the long resonator (series resonator) is 1.978 µm and the metallization ratio is 0.5. The shorter resonator (parallel resonator) has a pitch of 2.047 µm and a metallization ratio of 0.5. The IDTs and reflectors are covered

by a planarized SiO_2 layer which thickness is approximately 1500 nm, followed by a Silicon Nitride layer of approximately 80 nm in thickness. The purpose of these layers is to reduce the TCF of the stack. This technology is called TC-SAW (for Temperature Compensated SAW).

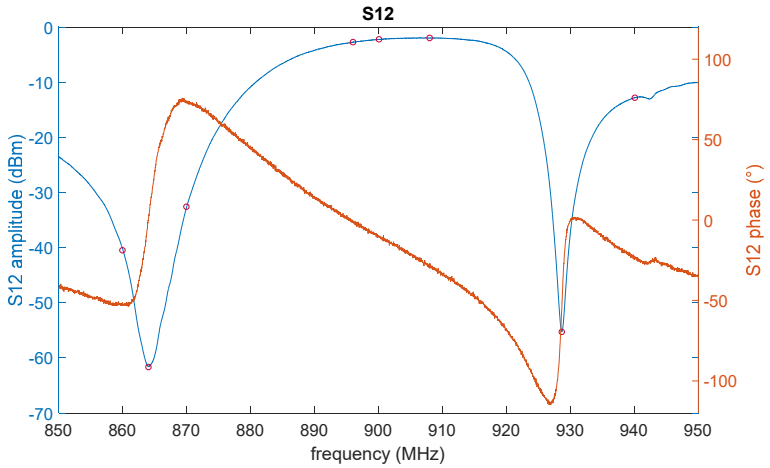

Figure 4.23 Electrical S_{12} parameter of the filter. The latter has a central frequency of 896 MHz. The red circles represent the frequencies at which the filter was optically characterized.

During the characterization, the filter was driven with sinusoidal signals at different frequencies. The input frequencies were chosen at the beginning, in the middle and at the end of the passband (see Figure 4.23). The input power was +15 dBm. The output of the filter was connected to a spectrum analyser allowing to check the input signal in frequency and amplitude.

The second slow photodetector was used to measure the reference signal. The mapping of the latter is presented in Figure 4.24. It is used to correct the detected amplitude vibration following the equation (4.8). We recall that the amplitude of the reference signal is influenced by the surface reflectivity and the relative position of the surface to the focal plane of the microscope objective. If the DUT surface is tilted, the translation of the stages can cause the surface to be out of focus. When comparing the microscope image (Figure 4.24 left) to the mapping of the reference signal (Figure 4.24 right) one notices that both show the same defects (dust particles, scratches…). In addition, we clearly see the difference in surface reflectivity between the different components (resonators, connector pads, raw substrate). The reference signal mapping also shows that it is stronger in the middle than on the left and right sides. This attests a tilt of the DUT around the Y axis that causes the right and left sides to be slightly out of focus.

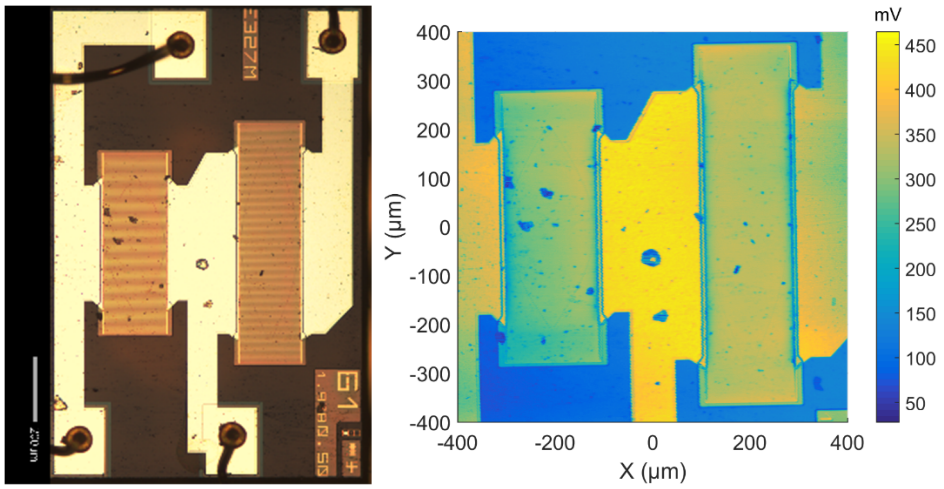

Figure 4.24 (Left) Microscope image of the filter. (Right) Mapping of the reference signal amplitude over the surface.

Figure 4.25 shows large field-of-view vibration characterizations of the filter. The device was characterized at eight different frequencies (pictured by red circles on the S12 characteristic Figure 4.23). For these measurements, the number of points is 320000, with 400 points in the x-direction spaced by 2 µm and 800 points in the y-direction spaced by 1 µm. The scan of the entire surface took 15 hours (one frequency), which is approximately 6 points/s. For the first three frequencies (860, 864, 870 MHz), we see energy leaking out of the short resonator; this is expected since the driving frequency is far from its resonance. The three following frequencies (896, 900, 908 MHz) lay in the middle of the passband where the long resonator is at its resonant frequency and the short resonator is at its anti-resonance. We see that, at these frequencies the acoustic energy is trapped in the two resonators. The wave patterns take the form of the IDT apodization. Some small leakages are visible at both ends of the IDTs. The last two frequencies are localized at the end of the passband. At 928 MHz, we observe the anti-resonance of the long resonator; thus, no electrical power goes to the short resonator. That is the reason why the latter appears completely switched off.

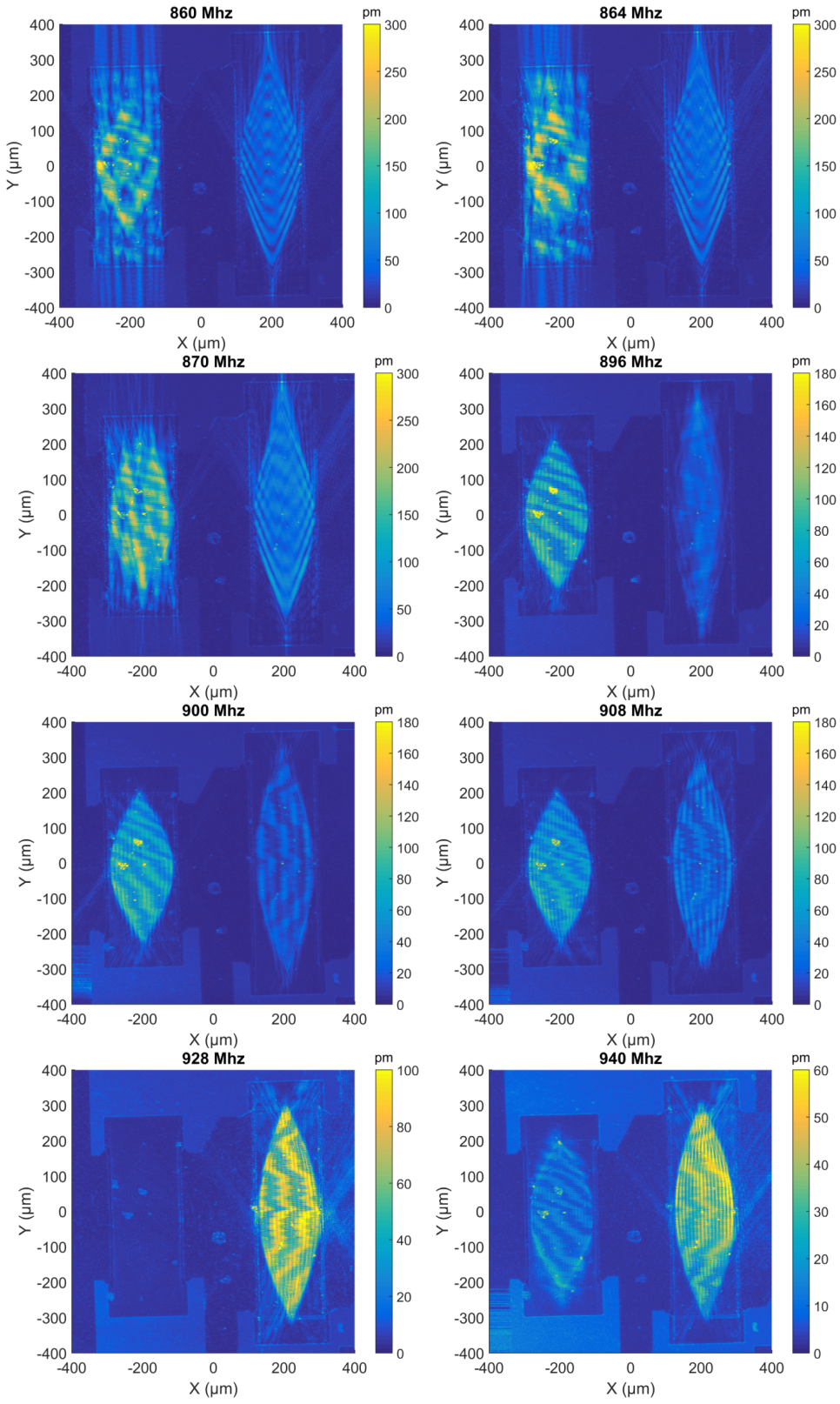

Figure 4.25 Filter surface vibration characterization at different frequencies

A detailed characterization of a small section of the short resonator (λ=2.047 µm) was also performed, see Figure 4.26. For this measurement, we acquired and computed the vibration amplitude and reference signal thirty times successively in order to compute a standard deviation on these values. The total image is composed of 900 points (30×30) with step sizes of 500 nm in the x-direction and 250 nm in the y-direction. From these results, we can see that the spot size diameter is small enough to resolve the wavelength of the acoustic waves (Figure 4.26 top-left). From the computed standard deviation, we observe that the uncertainty in the amplitude measurement is less than 3 pm.

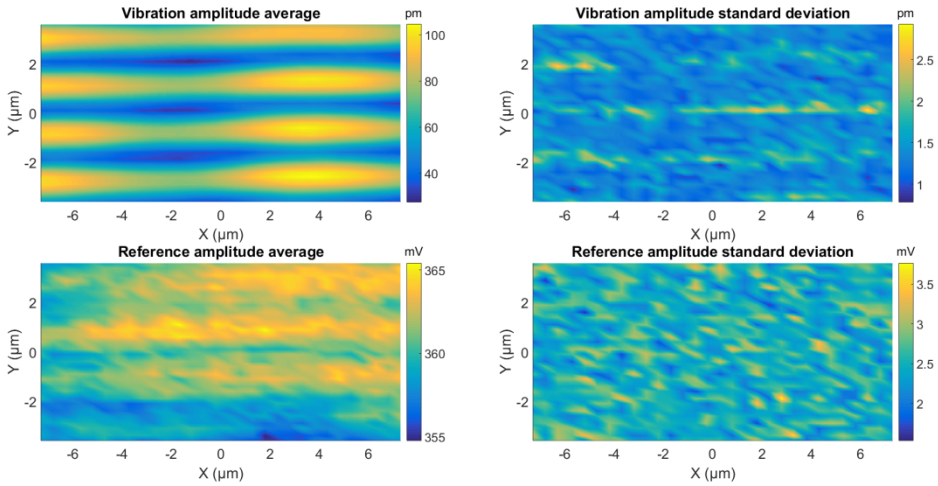

Figure 4.26 High-resolution scans of a small section of the short SAW resonator. For each spatial point, the amplitude measurement is repeated 30 times in order to compute the average and the standard deviation. (Top) Average and standard deviation of the vibration amplitude. (Bottom) Average and standard deviation of the reference signal.

Resonator at 1.820 GHz

Next, we characterized the SAW resonator which electrical characteristics and microscope picture are presented in Figure 4.27. The structure is similar to the bandpass filter. The substrate is made of Lithium Niobate. The electrodes are made of a Copper-based material having a pitch of 1 µm and a metallization ratio of 0.5. The IDTs and reflectors are covered by a planarized SiO_2 layer followed by a Silicon Nitride layer to reduce the TCF of the stack (TC-SAW technology).

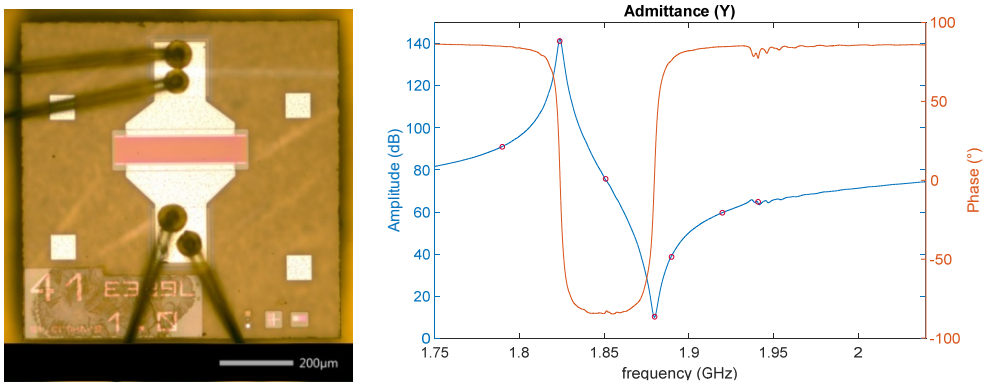

Figure 4.27 (Left) Microscope image of the resonator. (Rigth) Electrical characterization of the resonator (admittance curves: amplitude and phase).

For this study, we measured 160000 points, with 100 points in the y-direction spaced by 1 µm and 1600 points in the x-direction spaced by 250 nm. 10 hours were required to scan the entire surface at a single frequency, which corresponds to approximately 4.4 points/s. The mapping of the reference signal (Figure 4.28, bottom right) enables to see the apodization of the IDT. One can also see that there is a slight tilt around the y-direction that causes a difference in surface reflectivity from left to right. The resonator was characterized at different frequencies (marked by the red dot in the impedance characteristics in Figure 4.27). The vibration patterns (Figure 4.28) show that with the increasing frequency, higher lateral modes are visible (lines parallel to the x-direction). The vibration patterns also exhibit acoustic energy leaking out of the IDT, especially at the resonant frequency (1823.8 MHz) and anti-resonance frequency (1879.8MHz) although the acoustic energy should be perfectly confined within the IDT.

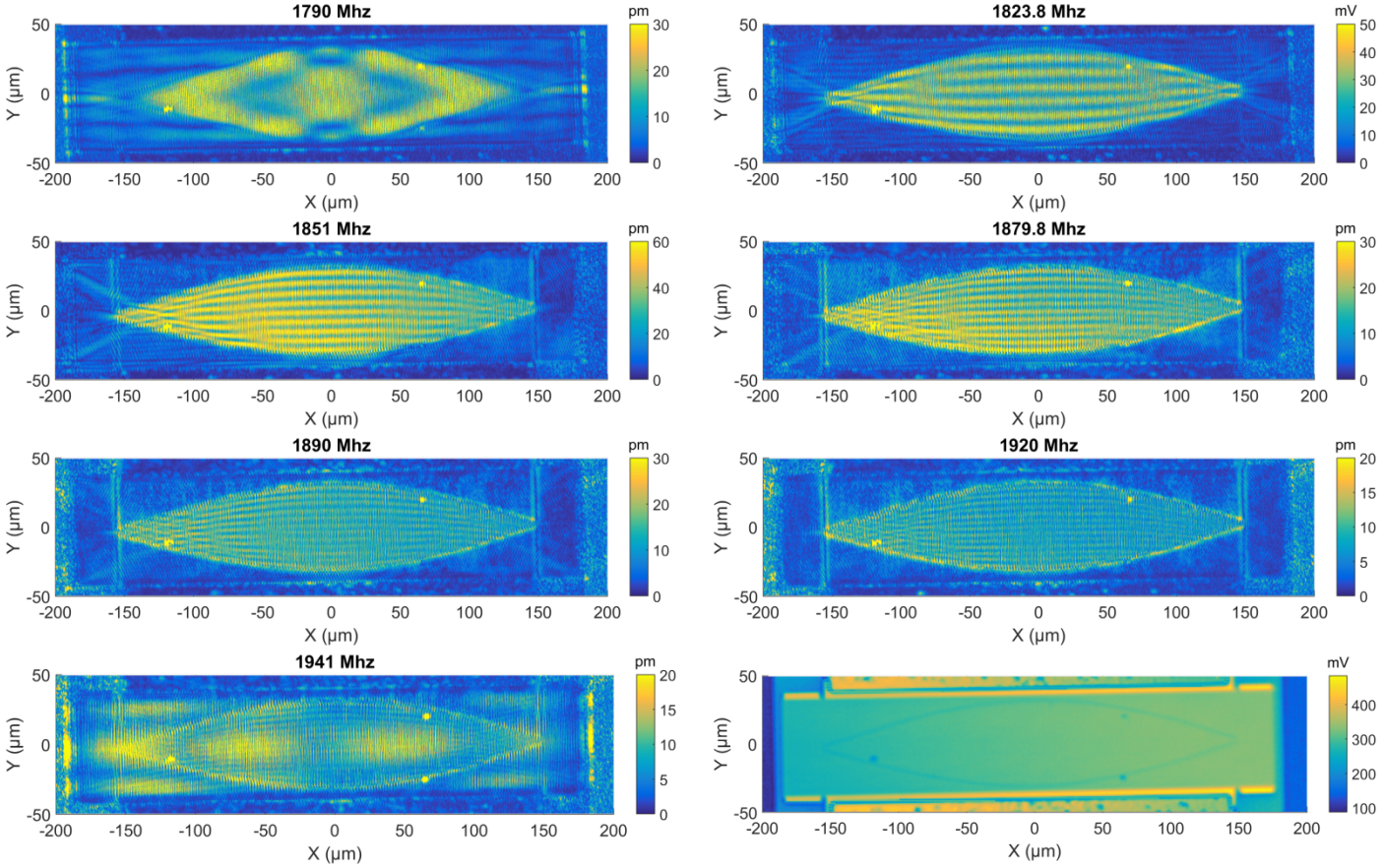

Figure 4.28 Vibration characterization of the SAW resonator at different frequencies. (Bottom right) Mapping of the reference signal amplitude.

Delay-line sensor working at 2.45 GHz

Figure 4.29 shows the characterization of a 2.45GHz, 5mm long reflective delay-line. The delay-line is made of Lithium Niobate Y-Z with Aluminium IDTs and 3 reflectors. The IDT consists of two parallel acoustic ports with a bus-bar in the middle. The structure width of the IDT is 0.346 µm. The first characterization (Figure 4.29 top) shows the whole device. For the latter, 150000 points were acquired, 3000 in the x-direction spaced by 2 µm and 50 in the y-direction, spaced by 4 µm. The characterization took 11 hours (3.8 pt/s). This large view characterization enables to see the 3 reflectors positioned along the acoustic path of the delay-line. In addition, we can see that a lot of energy is leaking out of the acoustic path due to the diffraction caused by the finite aperture of the IDT.

The second picture (Figure 4.29 bottom) shows a detailed characterisation of the same device around the IDT (marked by a red rectangle in the top-figure). For this characterization, 300000 points were taken, 3000 in the x-direction, spaced by 100 nm and 100 in the y-direction, spaced by 1 µm. The characterization took 24 hours (3.5 pt/s). The wave propagates towards the left and right from the IDT. The image shows the part of the wave that is not used in the sensor delay-line but sent to a sink structure built out of tilted reflectors with a wider finger structure.

The sink is applied to prevent reflections on the edges of the chip. It partly converts the Rayleigh waves to bulk waves and partly reflects them in a tilted direction. The characterization of this device was challenging because of three factors; the small acoustic wavelength requires a small laser spot diameter, the low surface reflectivity of the $LiNbO_3$ reduces the interferences intensity and lastly the large dimension of the device makes the alignment of the latter difficult.

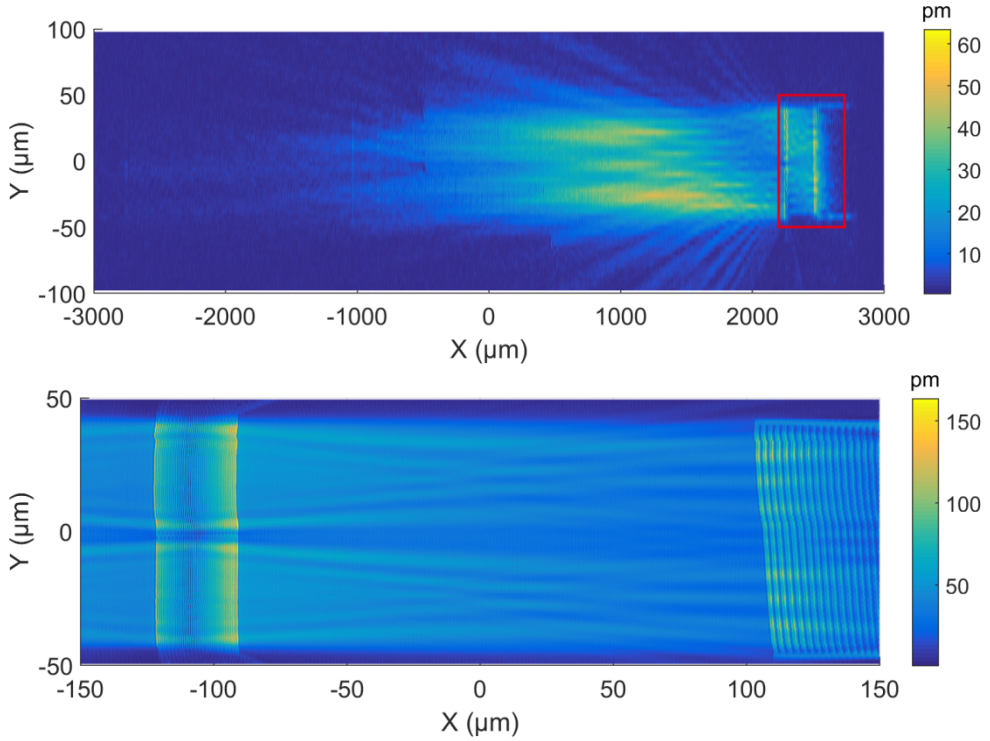

Figure 4.29 Characterization of a delay-line sensor. (Top) Characterization of the whole delay-line acoustic path driven at 2.45 GHz. (Bottom) Detailed characterization. The image shows the interference pattern of the waves between IDT and sink.

BAW resonators characterization

Along the development of the interferometer, we characterized BAW-SMR devices having increasingly higher resonant frequency. The first BAW resonator presented (Figure 4.30 left) has a resonance frequency around 2 GHz. Its top electrode has a trapezoidal shape that is designed to reduce the spurious modes by breaking the symmetry of the device. During the experiment, the resonator was driven at 1993 MHz with 15 dBm of power. The device was characterized on 40000 points (200×200 points with a 2×2 µm² resolution). The characterization took 13 hours (1pt/s). The measurement rate for this study is particularly low due to software issues in the early stage of the development. The image shows ripples on the device that correspond to lateral modes.

The second BAW resonator we characterized has a resonant frequency at 3.128GHz. The resonance frequency was first identified, using a vector network analyser. During the experiment, the device was driven at its resonant frequency and the injected power was again 15dBm. The obtained results are shown in Figure

4.30 (right). The acquisition time was 13 hours for 350×350=122500 points with a resolution of 1×1 µm². The minimum detectable displacement was 0.5 pm (small ripples detected close to the scan edges).

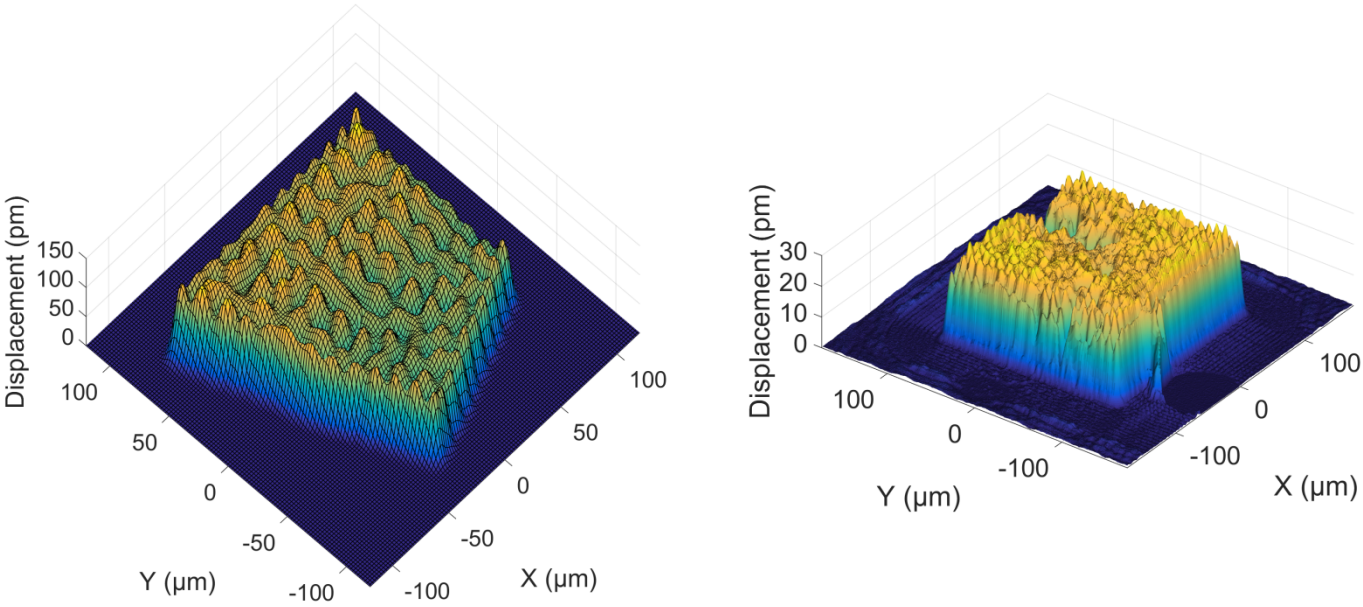

Figure 4.30 Characterization of BAW resonators. (Left) BAW resonator characterized at 1993MHz. The figure is cut for the sake of visual rendering (Right) BAW resonator characterized at 3128 MHz. The figure was shaded to highlight the small ripples.

The third test BAW resonator characterized has a resonance frequency of 5950 MHz. The acquisition time was 9 hours for 240×240=48000 points (1.5pt/s) with a resolution of 500×500 nm². Since the surface displacements are small, the number of samples is increased to have a lower detection limit. The non-linearity in the detection electronics that is likely present at high frequencies may cause the signal to appear lower than it is in reality.

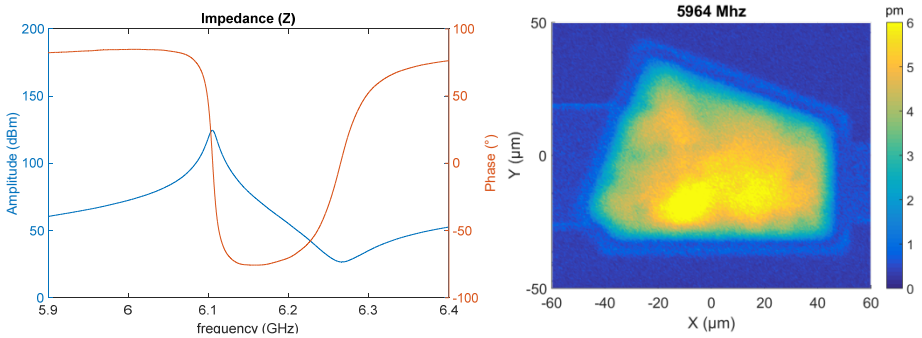

Figure 4.31 Electrical characterization of a high-frequency BAW resonator (~6 GHz)

Frequency scanning capability

We built a programme so that the two frequency synthesizers are controllable using LabVIEW. Thanks to this feature, the setup can be used to scan a device in fre-

quency (in addition to the spatial scan). Figure 4.32 shows an example of such a frequency scan. This scan was realized with a low spatial resolution. The setup showed bad performances for this kind of characterization due to the instability of the frequency synthesizers.

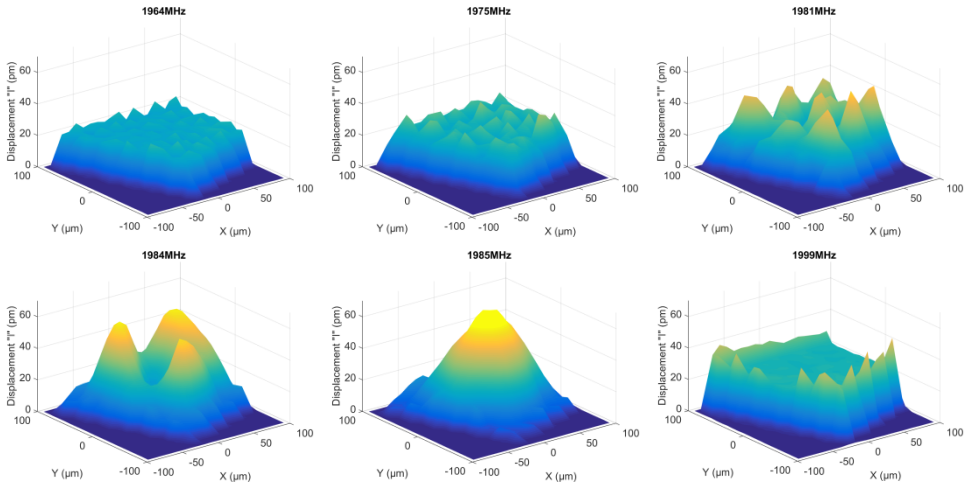

Figure 4.32 Selected images form a frequency scan. The BAW test device was characterized from 1950 MHz to 2010 MHz with 1 MHz step size. The selected pictures exhibit how the topology of the surface changes with the excitation frequency.

4.5 Setup limitations and future developments

This section discusses a non-exhaustive list of the present limitations and problems of the setup and the possible improvements. Further optical and electronic characterizations are required to highlight thoroughly the weaknesses of the actual setup.

Acquisition of the reference signal at 80MHz

The setup is using a non-polarized beam splitter to separate the recombined beams in two beams of equal intensity. One beam is oriented towards the fast photodiode used to compute the high frequency interference signal. The second beam is used to detect the reference signal at 80 MHz via a photodetector connected to an oscilloscope (Tektronix 3054B). The latter sends the measurement data through an Ethernet cable to the computer. Unfortunately, the data transfer rate of this communication system is limited and slows down the entire measurement setup. In addition, the oscilloscope was identified to be not reliable for long characterization. Therefore, the oscilloscope constitutes a weak point in the current setup and it should be replaced.

Alternatively, instead of splitting the recombined signal optically, one could also consider splitting the interference signal electronically. This can be done by using an electrical power splitter after the fast photodiode. One half of the signal is then directed towards the existing receiver, the second half would be used to detect the reference signal at 80 MHz. The difficulty of this implementation is to find a power splitter with a flat frequency response and a sufficiently large bandwidth.

The latter should be able to split both the reference signal and the vibration signal (with a frequency up to 6 GHz).

Calibration of the measurement

In order to have an absolute and precise measurement of the mechanical vibration amplitudes, the setup must be calibrated. The actual setup can be calibrated in two steps. First, we compare the reference signal amplitude at the output of the slow and fast photodetectors. Since the reference signal is determined using the slow photodetector, the signal processing should account for the level difference between the two detection methods. Secondly, we should characterize the receiver gain across the entire frequency range so that the non-flat response of the different components can be compensated numerically. The components of the receiver chain have been chosen for their gain flatness over the entire bandwidth of interest (0.5 to 6 GHz). Nevertheless, nonlinearities persist, and the digital signal processing should compensate for them.

Improving the spot size diameter

The diameter of the spot size could be theoretically reduced using higher aperture objectives. Nevertheless, it is expected that the laser beam needs to be "cleaned" before entering the objective. Indeed, the laser is multimodal, meaning that its wave front is not perfectly flat but instead it has some speckles. After passing through the objective, these different modes do not meet coherently in the focal plane resulting in a spot size larger than the theoretical. A well-known solution to obtain a clean beam is to use a spatial filter. But this is made at the expense of some intensity which is fundamental in order to keep a high enough SNR.

Gain of the receiver chain (LNAs and AGC)

The design of the receiver chain assumed a reference peak around -40 dBm and minimum detectable vibration amplitude of 1 pm, resulting in a minimum peak amplitude to detect around -140 dBm. However, experimentally, the reference peak is often below -40 dBm, resulting in a signal peak below -140 dBm (for a 1 pm amplitude vibration) thus below the I/Q demodulator range despite of the LNAs amplification. A solution to this problem is to add more amplification before the I/Q demodulator. Doing so, has the advantage to bring up the signal into the dynamic range of the I/Q demodulator. The signal will lay further from lowest amplitude detectable by the I/Q.

During the design of the setup we overestimated the total dynamic range of the receiver chain. It was designed for maximum vibration amplitude around 1 nm and minimum amplitude of 1 pm, which is equivalent to a 60 dB dynamic range (see Figure 4.9). However, the dynamic range is much lower in reality. During the characterization, it was noticed that the amplitude of the waves rarely exceeds a few hundreds of picometers when providing 30 mW (15 dBm) to the DUT. Consequently, it is not necessary to adjust the gain of the AGC to ensure that the IF

signal is within the range of the ADC. The controllable gain feature of the AGC is not necessary; in fact, simpler fixed gain amplifiers would suffice.

Phase detection

Detecting the mechanical phase enables to determine if the observed vibration is in-phase or in quadrature compared to the excitation signal. The intermediate frequency signal (output of the I/Q demodulator, see Appendix E.8) carries the information about the phase of the vibration ϕ_{vib} in addition to the phase of the local oscillator ϕ_{LO} and a phase related to the difference in optic path between the two interferometer arms $2\pi/\Lambda\left(\delta_{ref} - \delta_{DUT}\right)$. The latter should remain constant during the experiment. The present setup is not able to detect the phase of the mechanical vibration because the time when the acquisition starts is arbitrary. Therefore, ϕ_{LO} has a random value at each new measurement and it is not possible to distinguish the phase ϕ_{LO} from ϕ_{vib}. This explains why we observe the rectified amplitude of the waves. A possible solution to detect the phase would be to set the phase of the local oscillator (see Figure 4.33). To do so, it is possible to trigger the sample acquisition using the local oscillator so that the sampling always starts on a determined phase of the LO. Since the trigger input of the ADC is slow compared to the LO signal, it would be necessary to divide the frequency of the LO before using it as a trigger.

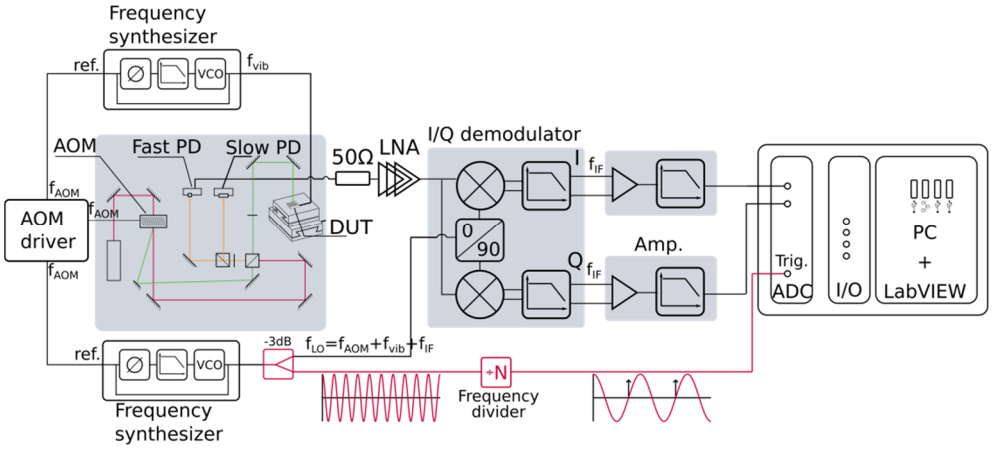

Figure 4.33 Receiver chain with the detection of the phase implemented. The detection of the phase requires to remove the phase of the local oscillator. To do so, the ADC is triggered on the LO signal, for instance on the zero crossing.

Detection rate

The detection rate of the current setup is limited to 6 points/s in the best case. Even though this rate suffices to fulfil the initial requirement, it is lower than the rate reported in the literature. We can consider several strategies to improve the velocity of a scan.

In the present setup, the detection rate is limited by the frequency of the intermediate frequency signal. Indeed, to determine the mechanical amplitude vibration, we average and compute the amplitude of the IF signal. A certain num-

ber of periods of the IF signal are required for the averaging. The more periods we average, the lower is the noise but the longer is the sampling time. Typically, in the setup, we observe thousands of periods and the IF signal is in the kHz range. Therefore, the sampling time cannot be less than a fraction of a second. Increasing the frequency of the intermediate frequency (f_{IF}) signal would enable to sample as many periods in less time while keeping the noise low. To do so, one could consider changing the two automatic gain controllers as their bandwidth (60 kHz cut-off frequency for a 1000 gain) limits the intermediate frequency (f_{IF}) to a low value. Typically, we choose f_{IF}<30 kHz. In addition, as discussed earlier, the multiple gain selection feature of the AGC is not needed because of the low amplitude of the observed wave in general. Consequently, swapping the AGCs by fixed gain amplifiers enables to increase the intermediate frequency. The maximum sampling rate possible with the ADC is 100 MS/s thus allowing an f_{IF} in the megahertz range before the ADC becomes a bottleneck. On the other hand, the cut-off frequency of the I/Q demodulator (390 MHz cut-off frequency) is not a liming factor.

A second method to improve the scanning speed is to consider software improvements. On one hand, it is possible to continuously scan the device in one direction at a constant velocity and repeat this operation until scanning the entire surface. This technique is used in [134], [146], [147]. Figure 4.34 illustrates the expected intermediate frequency signal for such a continuous scan. The resulting IF signal is modulated in amplitude by the mechanical vibration. With this method, samples are taken all along the scanned line. This results in a large number of samples produced which could saturate the memory of the ADC. In addition, attention must be paid on the start and the end of the line where the scan velocity is not constant. Nevertheless, the continuous scanning method benefits from a smoother operation compared to the discrete method which generates more jolts. On the other hand, one could improve the frequency scan capability of the setup. Instead of a discrete frequency scan, as it is done presently, one could consider sending a continuously varying frequency chirp. The resulting IF signal would also be a signal modulated by the frequency response at a spatial given point.

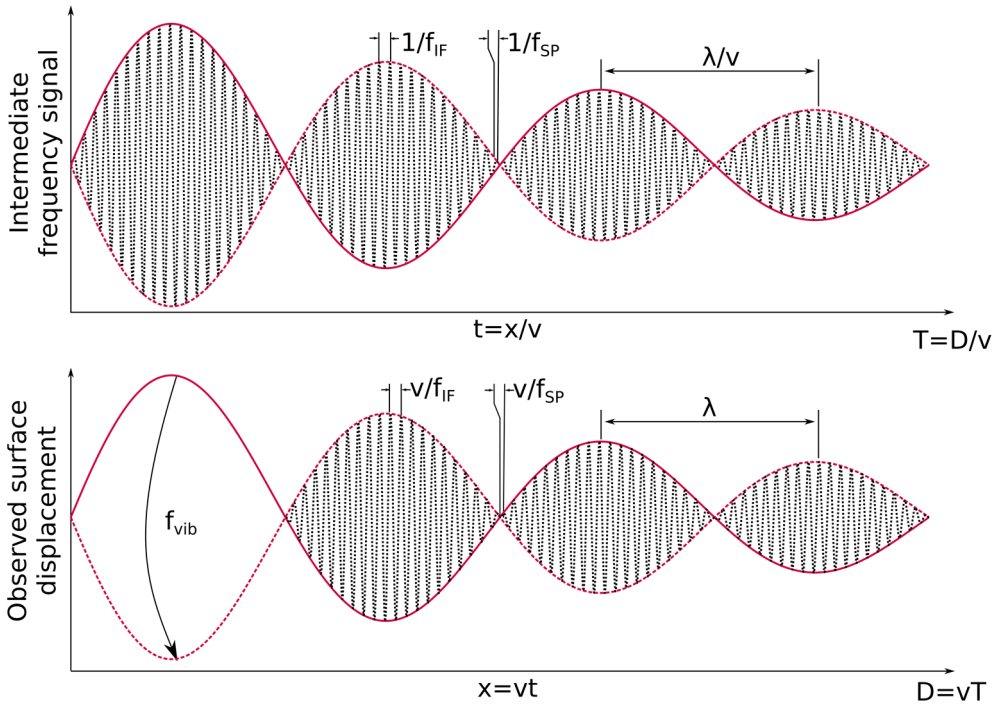

Figure 4.34 Expected signal from a continuous scan at velocity v. The red line represents the displacement on the surface generated by the acoustic wave (λ is its wavelength). The dashed line in black represents the intermediate frequency signal. The samples are taken at a sampling rate f_{SP}. The amplitude of the IF signal follows the amplitude of the detected displacement. One can read the result as an amplitude modulated signal; the carrier frequency is the frequency of the intermediate frequency signal f_{IF} and the signal is the vibration at the surface of the DUT.

Chapter 5 Summary and Conclusion

In recent years, the proliferation of mobile telecommunication systems has increased the demand for high-performance Surface Acoustic Wave (SAW) filters. Filters with higher frequencies, wider bandwidth and lower cost are now expected to meet the requirements of the new generation of communicating devices (5G), with dedicated characterization tool. In parallel, more efficient SAW sensors have been developed for niche applications. Because of their robustness, simplicity, and ability to be wirelessly interrogated, they are used as sensors in harsh environments. However, the cost of the sensors remains a blocking point for most applications. This could be overcome by reducing the time needed for their development and by finding innovative packaging solutions. Recently, multilayer structures have been developed to meet these challenges.

In Chapter 1, we discussed the method that we implemented and applied to quickly simulate the electrical response of multi-layered SAW devices. First, single-cell FEM models are used to extract four phenomenological COM-parameters (i.e. SAW velocity, reflection coefficient, transduction coefficient and capacitance). The latter are then used in P-Matrix algorithms, to compute the electrical response.

In Chapter 2, we focused on SAW sensor applications. First, we improved the unit-cell model to account for the change in SAW velocity due to an external perturbation. We compared the simulation results to reference results found in the literature, and to experimental ones. The simulation procedure made it possible to accurately predict the sensitivity of the sensor. Nevertheless, it is limited by the availability and reliability of the material constants used in the model.

The simulation tool was then used to better understand the experimental behaviour of an innovative bi-layered pressure sensor. In addition to accurately predicting the observed sensitivity of the device, the model could also predict some of its failure modes. Especially, we showed that the remaining sensitivity to temperature comes from an incorrect positioning of the reflectors along the reflective delay-line. Besides, the non-linearity in the thermal response was identified as the consequence of a buckling of the membrane. Furthermore, the FE model was able to accurately predict the buckling temperature and the post-buckling sensor response.

Finally, the tool helped us in designing an innovative, multi-layered packageless sensor for which we optimized the stack thicknesses in order to improve the device ElectroMechanical Coupling Factor (EMCF). Additionally, we computed its sensitivity to temperature as well as its expected electric response. The study also highlighted some limitations of the sensors design, especially at high temperatures.

As a first step towards 5G applications, we participated in the development of solidly mounted Lamb wave resonators based on highly doped Aluminium Nitride films. Our contribution is reported in Chapter 3. The devices were implemented on two different Bragg mirrors (W/SiO_2 and AlN/SiO_2). Using the FEM tool we de-

veloped, the layers thicknesses within the structure were devised to improve the performances of the resonators. The device on the W/SiO_2 mirror exhibited an EMCF of k^2=5.03% and a quality factor of Q=768, resulting in a figure-of-merit (FoM) of 38.6, while the device on the SiO_2/AlN mirror exhibited an EMCF of k^2=4.5% and a quality factor Q=862, resulting in a FoM of 38.7. To our knowledge, these FoMs are the largest reported in the literature. In addition, a good agreement was found between the simulation and experimental results, which supports the good accuracy of the material parameters determined by our partner.

In Chapter 4, we reported the design and implementation of a heterodyne interferometer that is devoted to the characterization of high frequency vibrations on the surface of micro-acoustic devices. We built this tool from scratch. During its implementation, a particular care was devoted to the reduction of the size of the Laser spot. We eventually achieved a spot size smaller than 1.4 µm, which was good enough to observe the vibration patterns of SAW devices, with a wavelength smaller than 2 µm. In addition, we identified and removed set-up instabilities. To detect the high frequency interferometric signals, a custom-built electronic was also developed, based on I/Q demodulation. In order to reduce the phase noise in the setup, all the generated frequencies are derived from a unique source. With the current setup, we characterized BAW and SAW devices with an amplitude resolution in the picometer range, up to 6 GHz.

The whole set of results presented in this work demonstrate the high potential of multi-layered structures, for the improvement of existing SAW devices. They might even be the only possible solution, to develop SAW filters that meet the 5G-requirements. Concerning the sensors, they open new interesting perspectives, as they make it possible to combine materials with complementary properties. In some cases, it becomes even possible to build package-less SAW sensors, which might be advantageously integrated in smart materials for monitoring structural parts, in the near future.

Appendix A TFBAR (Thin Film Bulk Acoustic Resonator)

A.1 Principle

A Thin Film Bulk Acoustic Resonator (TFBAR) exploits the Bulk Acoustic Wave (BAW) that propagates through the bulk of the piezoelectric material. Three different acoustic modes may be used: the vertical shear mode, the horizontal shear mode and the longitudinal mode. The mechanical deformation generated by the shear mode is perpendicular to the propagation of the wave, while the deformation generated by the longitudinal mode is in the direction of the propagation. When propagating, these acoustic modes involve different material constants, which are responsible for the specific velocity and electromechanical coupling coefficient of the mode.

In its simplest form, a TFBAR consists in a piezoelectric layer sandwiched between two metallic electrodes (see Figure A.1). The thickness of the piezoelectric layer is directly related to the device frequency. In the case of infinitely thin electrodes, the resonant frequency is given by the following equation [115]:

$$f_R = \frac{v \cdot N}{2t} \tag{A.1}$$

Where, v is the velocity of the considered mode, t is the thickness of the piezoelectric layer and N is an odd integer number which defines the harmonic of the mode being used.

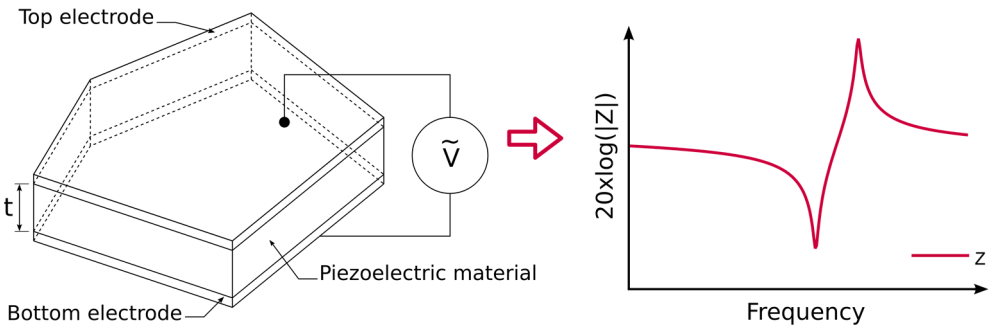

Figure A.1 Schematic of a simplified TFBAR and its impedance characteristics. The BAW resonator has a frequency response which is similar to that of a SAW resonator. The electrodes of the FBAR may be shaped (apodized) to avoid the generation of unwanted spurious modes.

In order to generate a resonant cavity and ensure minimum loss of the acoustic energy in the surroundings (substrate), the piezoelectric layer must be mechanically isolated. Two techniques exist to do so [158], [159]. The latter are illustrated in Figure A.2 and Figure A.3. The first method consists in creating a free-standing (suspended) piezoelectric layer. In this case, a sacrificial layer is primarily used to grow a piezoelectric film. The latter is etched away at the end of the fabrication to obtain a suspended structure.

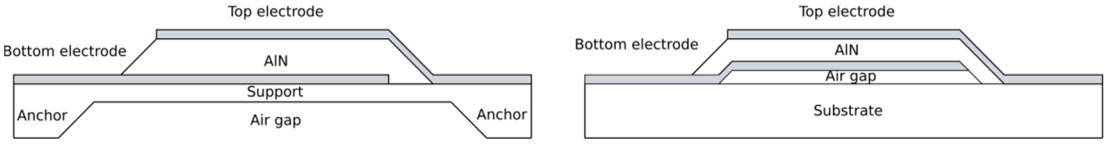

Figure A.2 The two methods to obtain a free-standing FBAR. (Left) The FBAR is fabricated by backside etching of the wafer [160]. (Right) The arched FBAR is fabricated by depositing the device on top of a sacrificial layer which is later removed to leave an air gap [161].

The second solution consists in building the resonator on top of an acoustic Bragg mirror. The latter is made of alternated layers of low and high acoustic impedances to reflect the acoustic waves. This solution is called BAW-SMR (SMR stands for Solidly Mounted Resonator). The resulting structure has the advantage to be more robust than its suspended counterpart.

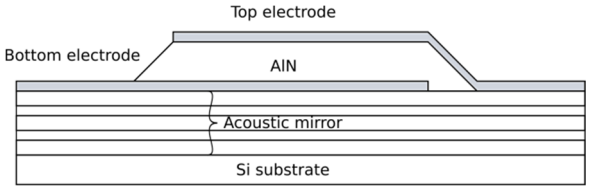

Figure A.3 Illustration of the method that uses an acoustic Bragg mirror made of different layers to reflect the acoustic wave [119], [162].

A comparison between these technologies can be found in [163]. To summarize, the free-standing structure has typically a higher effective coupling and higher quality factor, whereas the resonators on Bragg mirror have less temperature drift (due to a lower TCF) and less residual stress. The manufacturing is comparable in both cases in terms of complexity.

A.2 Material

Today, most of the commercially available TFBAR devices use Aluminium Nitride (AlN) as piezoelectric material because of its compatibility with the CMOS technology (unlike Zinc Oxide (ZnO)). AlN also benefits from a relatively high velocity, a low temperature drift (≈25 ppm/K) and a high thermal conductivity. AlN has an hexagonal wurtzite lattice structure, see Figure A.4. It is a piezoelectric material with spontaneous polarization along the c-axis of the unit cell. The growth of a c-textured or an epitaxial layer is needed to have a piezoelectric effect. A polycrystalline AlN does not exhibit piezoelectric properties.

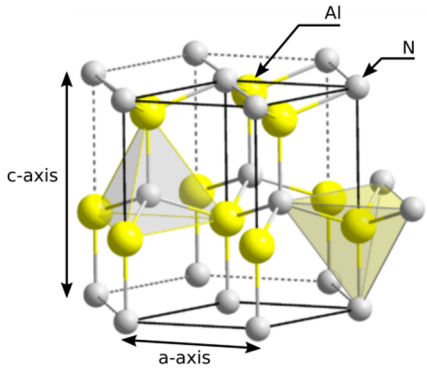

Figure A.4 Hexagonal wurzite crystal structure of Aluminium Nitride

A.3 Fabrication

The metallic electrodes and piezoelectric layers are deposited using vacuum technologies. The thickness of the piezoelectric layer is typically in the micrometre range which leads to devices operating in the gigahertz frequency range. The prevailing method to deposit piezoelectric AlN is magnetron sputtering of a pure Aluminium target in a Nitrogen (N_2) and Argon (Ar) mixture [115].

Appendix B Material parameters

B.1 Piezoelectric materials ($LiNbO_3$, ZnO, AlN)

Mainly three piezoelectric materials are used in this document; that is, Lithium Niobate ($LiNbO_3$) Zinc Oxide (ZnO) and Aluminium Nitride (AlN). The general forms of the tensors describing their piezoelectric behaviours are given below.

Short-circuit stiffness (in GPa)

$$C = \begin{bmatrix} C_{11} & C_{12} & C_{13} & C_{14} & 0 & 0 \\ C_{12} & C_{11} & C_{13} & -C_{14} & 0 & 0 \\ C_{13} & C_{13} & C_{33} & 0 & 0 & 0 \\ C_{14} & -C_{14} & 0 & C_{44} & 0 & 0 \\ 0 & 0 & 0 & 0 & C_{44} & C_{14} \\ 0 & 0 & 0 & 0 & C_{14} & (C_{11} - C_{12})/2 \end{bmatrix} \quad \text{B.1}$$

Stress piezoelectric matrix (in C/m^2)

$$e = \begin{bmatrix} 0 & 0 & 0 & 0 & e_{15} & e_{22} \\ -e_{22} & e_{22} & 0 & e_{15} & 0 & 0 \\ e_{31} & e_{31} & e_{33} & 0 & 0 & 0 \end{bmatrix} \quad \text{B.2}$$

Relative blocked permittivity matrix

$$\epsilon = \begin{bmatrix} \epsilon_{11} & 0 & 0 \\ 0 & \epsilon_{11} & 0 \\ 0 & 0 & \epsilon_{33} \end{bmatrix} \quad \text{B.3}$$

Different sets of constants exist in the literature for these materials. Those used in the document, are highlighted in bold fonts in the following Table B-1 to Table B-5.

	$LiNbO_3$ [164]	$LiNbO_3$ [165]	$LiNbO_3$ [48]	$LiNbO_3$ [166]	ZnO [167]	AlN [168]	AlSc[15]N [108]
Stiffness constants C_{ij} in GPa							
C_{11}	199.5	198.9	**198.4**	203.1	**157**	**345**	**343**
C_{12}	55.3	54.7	**54.7**	53	**89**	**125**	**171**
C_{13}	67.7	68.0	**65.1**	74.2	**83**	**120**	**110**
C_{14}	8.7	7.8	**7.9**	8.5	0	0	**0**
C_{33}	235.2	234.2	**227.9**	241.3	**204**	**395**	**277**
C_{44}	59.5	59.9	**59.7**	64.6	**38**	**118**	**101**
C_{66}	72.1	71.8	**71.8**	75.1	**34**	**110**	**86**
Piezoelectric constants e_{ij} in C/m^2							
e_{15}			**3.69**		**−0.45**	**−0.48**	**−0.40**
e_{22}			**2.42**		**0**	**0**	**0**
e_{31}			**0.30**		**−0.51**	**−0.58**	**−0.63**
e_{33}			**1.77**		**1.22**	**1.5**	**1.88**
Dielectric constants in ε_0 (relative permittivity)							
ϵ_{11}			**45.6**		**6.69**	**8**	**14.2**
ϵ_{33}			**26.3**		**7.9**	**9.5**	**9.7**
Density in kg/m^3							
ρ			**4628**		**5720**	**3260**	**3280**
Isotropic damping coefficient (not reported in the reference)							
						1/5000	**1/5000**

Table B-1 Material constants.

The following Table B-2 gives the temperature dependent coefficients of $LiNbO_3$, ZnO and AlN together with their thermal expansion coefficients.

	$LiNbO_3$ [64]	ZnO [167]	AlN [169]
Change in stiffness constants C_{ij} in ppm/K			
C_{11}^T	-174	-1.12	-0.37
C_{12}^T	-252	-1.44	-0.018
C_{13}^T	-159	-1.61	-0.018
C_{14}^T	-214	0	0
C_{33}^T	-153	1.23	-0.65
C_{44}^T	-204	-0.7	-0.5
C_{66}^T	-143	-0.7	-0.57
Change in piezoelectric constants e_{ij}^T in ppm/K			
e_{15}^T	147	n.a	n.a
e_{22}^T	79	n.a	n.a
e_{31}^T	221	n.a	n.a
e_{33}^T	887	n.a	n.a
Change in dielectric constants ϵ_{ij} in ppm/K			
ϵ_{11}^T	323	n.a	n.a
ϵ_{33}^T	627	n.a	n.a
Expansion coefficients ppm/K			
$\alpha 1$	15.4	4.31	5.27
$\alpha 3$	7.5	2.49	4.15

Table B-2 Temperature-dependent coefficients of $LiNbO_3$, ZnO and AlN (the values marked n.a are not available in the literature).

The following Table B-3 summarizes the 14 third-order coefficients needed to determine the dependency of $LiNbO_3$ to a strain field. The complete set of constants can be calculated using the crystal symmetries; the relations can be found in [170].

C_{ijk}	$LiNbO_3$ [63]	$LiNbO_3$ [171]	C_{ijk}	
C_{111}	$\mathbf{-2120}$	-512	C_{122}	$(C_{111}+C_{112}-C_{222})$
C_{112}	$\mathbf{-530}$	454	C_{156}	$(C_{114}+3C_{124})/2$
C_{113}	$\mathbf{-570}$	728	C_{166}	$(-2C_{111}-C_{112}+3C_{222})/4$
C_{114}	$\mathbf{200}$	-410	C_{223}	C_{113}
C_{123}	$\mathbf{-250}$	79	C_{224}	$(-C_{114}-2C_{124})$
C_{124}	$\mathbf{40}$	55	C_{233}	C_{133}
C_{133}	$\mathbf{-780}$	-34	C_{234}	$-C_{134}$
C_{134}	$\mathbf{-150}$	-1	C_{244}	C_{155}
C_{144}	$\mathbf{-300}$	-37	C_{255}	C_{144}
C_{155}	$\mathbf{-670}$	-599	C_{256}	$(C_{114}-C_{124})/2$
C_{222}	$\mathbf{-2330}$	-599	C_{266}	$(2C_{111}-C_{112}-C_{222})/4$
C_{333}	$\mathbf{-2960}$	-478	C_{355}	C_{344}
C_{344}	$\mathbf{-680}$	-540	C_{356}	C_{134}
C_{444}	$\mathbf{-30}$	-41	C_{366}	$(C_{113}-C_{123})/2$
			C_{455}	$-C_{444}$
			C_{456}	$(C_{115}-C_{144})/2$
			C_{466}	C_{124}

Table B-3 Third-order stiffness coefficients of $LiNbO_3$.

B.2 Silicon (Si)

The silicon is often used as substrate material in the document. Table B-4 summarizes the material parameters that are used in the simulation.

Property	Value	unit
Stiffness (in GPa)	$C_{11} = C_{22} = C_{33} = 166$ $C_{12} = C_{13} = C_{23} = 64$ $C_{44} = C_{55} = C_{66} = 80$	GPa
Density	2329	kg/m^3
Thermal Expansion Coefficient	2.6	$ppm/°C$
Relative Permittivity	12	
Isotropic damping coefficient	1/8000	

Table B-4 Material properties of Silicon

B.3 Isotropic materials

Table B-5 summarizes the parameters of the isotropic materials used in this document. It also features the computed velocities and acoustic impedances for some of these materials.

	Al	Cu	Pt	W	SiO_2
Young modulus E (GPa)	70	120	168	411	70
Poisson's ratio ν	0.35	0.34	0.38	0.28	0.17
Density ρ (kg/m^3)	2700	8960	21450	19350	2200
Longi. Velocity $v_L(m/s)$	6451	4540	3829	5211	5848
Shear velocity $v_S(m/s)$	3099	2235	1685	2880	3687
Imped. longi. $Z_L(N.s/m^3)$ (10^6)	17.42	40.68	82.1	100.8	12.9
Imped. Shear $Z_S(N.s/m^3)$ (10^6)	8.37	20.03	36.13	55.7	8.1
Isotropic damping coefficient	1/1000	1/500	1/1000	1/1000	1/1000

Table B-5 Material properties of some isotropic materials

The longitudinal and shear velocities are computed as follows:

$$v_L = \sqrt{\frac{c_{11}}{\rho}} = \sqrt{\frac{E(1-\nu)}{\rho(1+\nu)(1-2\nu)}} \quad \text{B.4}$$

$$v_S = \sqrt{\frac{c_{44}}{\rho}} = \sqrt{\frac{E}{2*\rho(1+\nu)}} \quad \text{B.5}$$

And the acoustic impedances are:

$$Z_L = \rho V_L \; and \; Z_S = \rho V_S \quad \text{B.6}$$

Appendix C Appendix to chapter 2

C.1 Rotation of a strain tensor.

The below matrix S is that of the strain tensor corresponding to a transverse shearless state for which the axis (Oz) is perpendicular to the plane:

$$S = \begin{bmatrix} S_{xx} & S_{xy} & 0 \\ S_{xy} & S_{yy} & 0 \\ 0 & 0 & S_{zz} \end{bmatrix}_{x,y,z} \quad \text{C.1}$$

A rotation of the matrix is made around the Oz axis using the following transformation matrix:

$$R = \begin{bmatrix} cos\ \alpha & sin\,\alpha & 0 \\ -sin\ \alpha & cos\ \alpha & 0 \\ 0 & 0 & 1 \end{bmatrix}_{x,y,z} \quad \text{C.2}$$

The strain matrix after the rotation is given by:

$$S' = RSR^T \quad \text{C.3}$$

$$S' = \begin{bmatrix} S_{xx}c(\alpha)^2 - S_{yy}s(\alpha)^2 + 2S_{xy}s(\alpha)c(\alpha) & (S_{xx} - S_{yy})c(\alpha)s(\alpha) + S_{xy}(c(\alpha)^2 - s(\alpha)^2) & 0 \\ (S_{xx} - S_{yy})c(\alpha)s(\alpha) + S_{xy}(c(\alpha)^2 - s(\alpha)^2) & S_{xx}c(\alpha)^2 - S_{yy}s(\alpha)^2 - 2S_{xy}s(\alpha)c(\alpha) & 0 \\ 0 & 0 & S_{zz} \end{bmatrix}_{x',y',z'} \quad \text{C.4}$$

Figure C.1 shows the evolution of the strain components S'_{xx}, S'_{yy} and S'_{xy} with the angle α. To plot this graph, we used strains generated by a pure longitudinal stress field (see equation 2.6) with a unitary S_{xx} component and a Poisson's ratio of 0.3. We see that the strain S'_{xx} in the Ox' direction becomes zero at $\alpha = 61.3°$.

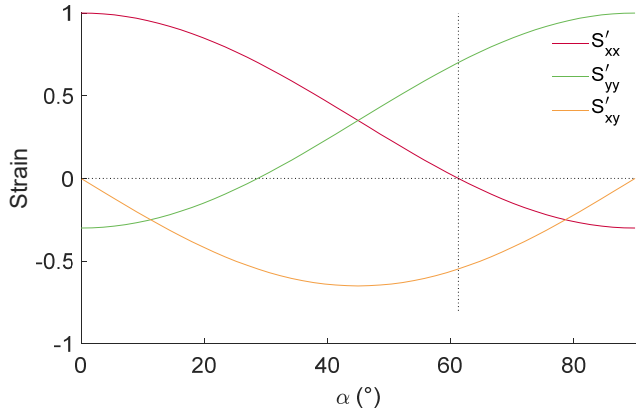

Figure C.1 Evolution of the in-plane strains versus the rotation angle α.

C.2 Circular membrane analytic model:

In this section, we compute the stress and strain fields generated in a thin circular membrane loaded by a homogenous pressure. The parameters of the study are presented in Figure C.2.

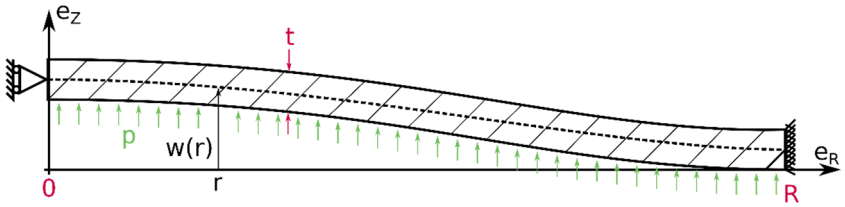

Figure C.2 Schematic of the deformed membrane under a pressure field p. The radius of the membrane is R and its thickness is t.

For a circular membrane, uniformly loaded, the displacement along the out-of-plane direction ($\overrightarrow{e_Z}$) is given by [71]:

$$w(r) = -\frac{pr^4}{64D} + A + Br^2 \quad \text{C.5}$$

Where, $D = \frac{Et^3}{12(1-\nu^2)}$ is the flexural rigidity of the plate and A and B are two constants that we determine using the boundary conditions. At $r = R$, the displacement and its first derivative ($\frac{dw}{dr}(R)$) are zero; consequently:

$$\frac{dw}{dr}(R) = -\frac{pR^3}{16D} + 2BR = 0 \rightarrow B = \frac{pR^2}{32D} = \frac{2pR^2}{64D} \quad \text{C.6}$$

$$w(R) = -\frac{pR^4}{64D} + A + \frac{2pR^4}{64D} = 0 \rightarrow A = -\frac{pR^4}{64D} \quad \text{C.7}$$

$$w(r) = -\frac{pr^4}{64D} - \frac{pR^4}{64D} + \frac{2pR^2}{64D}r^2 = \frac{p}{64D}(R^2 - r^2)^2 \quad \text{C.8}$$

From these expressions, we can compute the strains and stresses in the thickness of the membrane:

$$\epsilon_{rr}(r,z) = \frac{du}{dr} = -z\frac{d^2w}{dr^2} = \frac{Pz}{16D}(R^2 - 3r^2) \quad \text{C.9}$$

$$\epsilon_{\theta\theta} = \frac{u}{r} = -\frac{z}{r}\frac{dw}{dr} = \frac{Pz}{16D}(R^2 - r^2) \quad \text{C.10}$$

$$\epsilon_{r\theta} = 0 \quad \text{C.11}$$

$$\sigma_{rr} = \frac{3}{4}\frac{zP}{t^3}\left(R^2(1+\nu) - r^2(3+\nu)\right) \quad \text{C.12}$$

$$\sigma_{\theta\theta} = \frac{3}{4}\frac{zP}{t^3}\left(R^2(1+\nu) - r^2(1+3\nu)\right) \quad \text{C.13}$$

$$\sigma_{r\theta} = 0 \quad \text{C.14}$$

$$\epsilon_{zz} = -\frac{\nu}{E}(\sigma_{rr} + \sigma_{\theta\theta}) \quad \text{C.15}$$

C.3 Membrane under a homogenous temperature field:

When a circular membrane, fixed at its border, is heated up, the thermal expansion generates a compression. At first, the behaviour of the membrane is linear, and the stresses and strains are purely radial. When the temperature exceeds a threshold value (the critical temperature), the membrane buckles, see Figure C.3

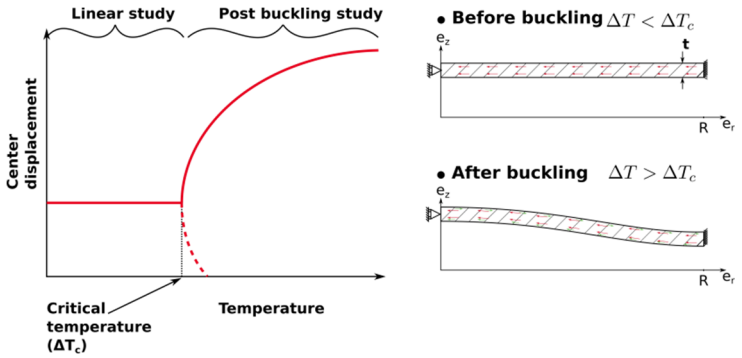

Figure C.3 Schematic of thin homogeneous membrane under buckling

Before the buckling, the relation between the increase in temperature and the generated radial stress can be computed analytically. Figure C.3 introduces the model parameters. The form of the stress matrix is the following:

$$\bar{\sigma} = \begin{bmatrix} \sigma_{rr}(T) & 0 & 0 \\ 0 & \sigma_{\theta\theta}(T) & 0 \\ 0 & 0 & 0 \end{bmatrix}_{\vec{e_r},\vec{e_\theta},\vec{e_z}} \quad \text{C.16}$$

The static equation of the equilibrium $div(\sigma) = 0$ implies that $\sigma_{rr} = \sigma_{\theta\theta} = \sigma$, thus

$$\bar{\sigma} = \begin{bmatrix} \sigma(T) & 0 & 0 \\ 0 & \sigma(T) & 0 \\ 0 & 0 & 0 \end{bmatrix}_{\vec{e_r},\vec{e_\theta},\vec{e_z}} \quad \text{C.17}$$

From the Hook's law in a thermo-elastic medium ($\epsilon_{ij} = \frac{1+\nu}{E}\sigma - \frac{\nu}{E}\sigma_{kk}\delta_{ij} + \alpha\Delta T\delta_{ij}$), we compute the corresponding strain tensor matrix as:

$$\bar{\epsilon} = \begin{bmatrix} \frac{1-\nu}{E}\sigma + \alpha\Delta T & 0 & 0 \\ 0 & \frac{1-\nu}{E}\sigma + \alpha\Delta T & 0 \\ 0 & 0 & \frac{-2\nu}{E}\sigma + \alpha\Delta T \end{bmatrix}_{\vec{e_r},\vec{e_\theta},\vec{e_z}} \quad \text{C.18}$$

From the strains, we can compute the displacements vector as:

$$\vec{u} = \begin{Bmatrix} \frac{1-\nu}{E}\sigma r + \alpha\Delta T r \\ 0 \\ \frac{-2\nu}{E}\sigma z + \alpha\Delta T z \end{Bmatrix}_{\vec{e_r},\vec{e_\theta},\vec{e_z}} \quad \text{C.19}$$

At the outer edge of the membrane, the displacements are fixed; consequently, we can determine the radial displacement as:

$$u_r(R) = \frac{1-\nu}{E}\sigma R + \alpha\Delta T R = 0 \quad \text{C.20}$$

Finally, the radial stress, generated by a temperature elevation of ΔT, is:

$$\sigma(T) = \frac{\alpha\Delta T E}{1-\nu} \quad \text{C.21}$$

In the simple case of a circular membrane, radially loaded on its edges, the critical linear load (Q_c in N/m) that leads to the buckling is [71]:

$$Q_c = 14.682\frac{D}{R^2} \quad \text{C.22}$$

We can formulate the stress previously found as a linear load by integrating the stress (equation C.21) in the thickness of the membrane. Thus, the thermal load is:

$$Q_T = \int_{-\frac{t}{2}}^{\frac{t}{2}} \sigma\,(T)dz = \frac{\alpha \Delta T t E}{1-\nu} \qquad \text{C.23}$$

And the membrane buckles at the critical temperature elevation ΔT_c when the thermal load is equal to the critical load ($Q_T(T_c) = Q_c$); consequently:

$$14.682\frac{D}{R^2} = \frac{\alpha \Delta T_c t E}{1-\nu} \qquad \text{C.24}$$

Thus, the critical temperature elevation is:

$$\Delta T_c = 14.682\frac{t^2}{12\alpha R^2(1+\nu)} \qquad \text{C.25}$$

Numerical application:

α (ppm/°C)	t (µm)	R (µm)	ν	ΔT_c
8	30	2350	0.3	19.17
10	30	2350	0.3	15.34
12	30	2350	0.3	12.78

Table C-1 Computation of the critical temperature elevation for different coefficients of thermal expansion.

Appendix D Analytic SAW velocity

This section is dedicated to the analytic computation of the SAW or Lamb wave velocity V in a piezoelectric medium. The method described here is taken from [2]. The coordinate system used for the study is presented in Figure D.1.

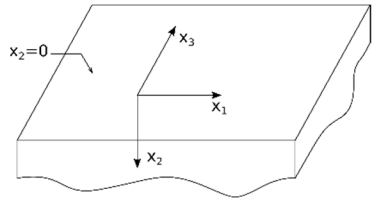

Figure D.1 Coordinate system used in this study

In this problem, the piezoelectric crystal in which the wave propagates is considered semi-infinite or between two parallel planes. The waves are assumed to propagate towards x_1 and the axis perpendicular to the surface is x_2.

When we consider no attenuation in the propagation direction, the displacement u_i and electrical potential ϕ can be written as:

$$u_i = u_i exp\{-\chi k x_2\} exp\{j[\omega t - k x_1]\} \; i = 1,2,3 \tag{D.1}$$

$$\phi = u_4 exp\{j[\omega t - k x_1]\} \tag{D.2}$$

where, $k = \omega/V$ is the wave number and α_i the amplitude of the displacements.

The harmonic piezoelectric equations describing the propagation of a wave in a medium are as follows:

$$\rho \frac{\partial^2 u_i}{\partial t^2} - c^E_{ijkl} \frac{\partial^2 u_k}{\partial x_l \partial x_k} - e_{kil} \frac{\partial^2 \phi}{\partial x_k \partial x_j} = 0 \tag{D.3}$$

$$e_{jkl} \frac{\partial^2 u_k}{\partial x_i \partial x_j} - \epsilon^S_{kj} \frac{\partial^2 \phi}{\partial x_k \partial x_j} \quad i,j,k,l = 1,2,3 \tag{D.4}$$

here c^E_{ijkl} are the stiffness coefficients under constant electric field, e_{ijk} are the stress piezoelectric coefficients, and ϵ^S_{ij} are the dielectric coefficients under constant strain, ρ is the medium mass density.

Neglecting the diffraction in the x_3 direction related to the partial derivative leads to $\frac{\partial}{\partial x_3} = 0$. The other derivatives are: $\frac{\partial}{\partial x_1} = -ik$, $\frac{\partial}{\partial x_2} = -\chi k$. Combining equations D.1 and D.2 into D.3 and D.4, we obtain the Christoffel equation:

$$\begin{bmatrix} \Gamma_{11} - \rho V^2 & \Gamma_{12} & \Gamma_{13} & \gamma_1 \\ \Gamma_{12} & \Gamma_{22} - \rho V^2 & \Gamma_{23} & \gamma_2 \\ \Gamma_{13} & \Gamma_{23} & \Gamma_{33} - \rho V^2 & \gamma_3 \\ \gamma_1 & \gamma_2 & \gamma_3 & -\epsilon \end{bmatrix} \begin{Bmatrix} u_1 \\ u_2 \\ u_3 \\ u_4 \end{Bmatrix} = 0 \tag{D.5}$$

Where:

$$\Gamma_{il} = c^E_{i11l} + c^E_{i22l} \rho (i\chi)^2 - i\left(c^E_{i12l} - c^E_{i21l}\right)(i\chi) = 0 \tag{D.6}$$

$$\gamma_l = e_{11l} + e_{22l}(i\chi) - i(e_{12l} + e_{21l})(i\chi) \tag{D.7}$$

$$\epsilon = \epsilon_{11}^{S} + \epsilon_{22}^{S}(i\chi) - 2i\epsilon_{12}^{S}(i\chi) \quad \text{D.8}$$

In this equation the velocity is the parameter to determine. Solving the determinant of this matrix for a given velocity V results in a degree 8 polynomial equation in χ having four pairs of conjugated solutions $\chi_r(r = 1{:}8)$. For each of these 8 solutions, the matrix D.1 enables to write partial waves (eigenvectors), which displacements are $u_i^{(r)}$ and the electrical potential is $\phi^{(r)} = u_4^{(r)}$. Then the general solution is a combination of these 8 partial waves:

$$u_i = \left(\sum_{r=1}^{8} A_r u_i^{(r)} exp\,(-k\chi_r x_2)\right) exp(i(\omega t - kx_1)) \quad \text{D.9}$$

Then, the coefficients A_r are determined by the mechanical and electrical boundary conditions. The former on a free-surface are:

$$T_{i2} = 0 \qquad i = 1,2,3 \quad \text{D.10}$$

And the so-called free-velocity (V_0) and metallized-velocity (V_∞) are computed by considering the corresponding electric boundary conditions. The metallized-velocity is computed assuming that the potential on top surface is grounded:

$$\phi = 0 \quad \text{D.11}$$

The free-velocity is computed considering the out-of-plane electrical displacement on the surface is zero.

$$-D_2 = \epsilon_{21}\frac{\partial \phi}{\partial x_1} + \epsilon_{22}\frac{\partial \phi}{\partial x_2} = (-ik\epsilon_{21} + \epsilon_{22}\chi)\phi = 0 \quad \text{D.12}$$

In practice, these equations are solved numerically using flowchart:

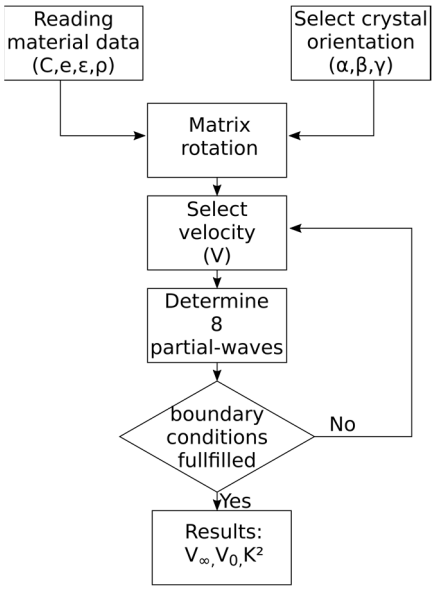

Figure D.2 Flowchart of the analytical method enabling the computation of the metallized and free velocity as well as the coupling factor.

Appendix E Appendix to chapter 4

E.1 Intensity variation by deflection

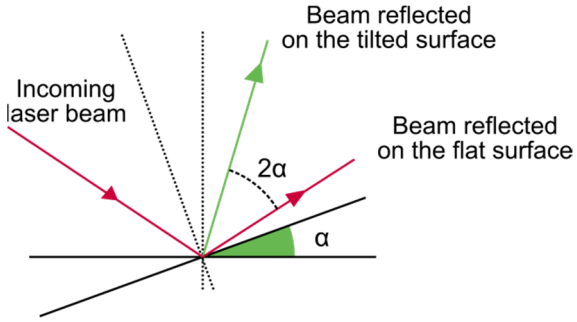

Figure E.1 Schematic of a laser reflection on a tilted surface. The angle between the reflected beam on the flat surface and the beam reflected on the tilted surface is twice the tilting angle.

In this section we detail the computation related to the knife edge (or deflection) technique explained in 4.1.1. We consider an acoustic wave propagating (with a wavelength λ) in the (x,y) horizontal plane propagating in the x-direction. The out-of-plane surface displacement generated by the wave is:

$$U_z = U_{vib}cos(2\pi f_{vib}t + \phi_{vib}) = U_{vib}cos\left(2\pi f_{vib}t + \frac{2\pi}{\lambda}x\right) \quad \text{E.1}$$

Where, U_{vib} and f_{vib} are the amplitude and frequency of the acoustic wave. The acoustic wave tilts the surface with an angle α, which is given by the spatial derivative of the displacement:

$$\alpha = \frac{dU_z}{dx} = -\frac{2\pi U_{vib}}{\lambda} sin\left(2\pi f_{vib}t + \frac{2\pi}{\lambda}x\right) \quad \text{E.2}$$

When a laser beam hits the tilted surface, the reflected beam makes an angle 2α with the original deflection (see Figure E.1 and Figure 4.1). After passing through the second lens (L2) of focal length f_2, the beam is deviated by a quantity δ:

$$\delta = f_2\, tan(2\alpha) = -f_2 tan\left(\frac{4\pi U_{vib}}{\lambda} sin\left(2\pi f_{vib}t + \frac{2\pi}{\lambda}x\right)\right) \quad \text{E.3}$$

Since the amplitude of the acoustic wave is smaller than its wavelength ($U_{vib} \ll \lambda$), the deflection angle is small, and we approximate the displacement δ by:

$$\delta = f_2 2\alpha = -\frac{4\pi f_2 U_{vib}}{\lambda} sin\left(2\pi f_{vib}t + \frac{2\pi}{\lambda}x\right) \quad \text{E.4}$$

Then, the maximum displacement $\delta_{max}\ is:$

$$\delta_{max} = \frac{4\pi f_2 U_{vib}}{\lambda} \quad \text{E.5}$$

And the peak to peak amplitude is:

$$\delta_{pp} = \frac{8\pi f_2 U_{vib}}{\lambda} \quad \text{E.6}$$

From this relation we see that the second lens (L_2) can be used to magnify the tilt angle. Nevertheless, due to spatial constraints, [134] used the same microscope lens to collimate and probe the reflected light.

E.2 Interferences between two optical beams

In this section, we present the general formula giving the intensity of the interference between two light beams. We consider that, $E_1 = E_{01}cos(\omega_1 t + \phi_1)$ and $E_2 = E_{02}cos(\omega_2 t + \phi_2)$ are two electrical fields coming from two different light sources. ω_1 and ω_2 denote their respective optical frequencies and ϕ_1 and ϕ_2 their respective optical phases. These two electrical fields are written as the real parts of the following complex expressions:

$$E_1^* = E_{01}e^{j(\omega_1 t+\phi_1)} \; and \; E_2^* = E_{02}e^{j(\omega_2 t+\phi_2)} \tag{E.7}$$

The resulting electric fields generated by the interference is the sum of the two signals:

$$E_{12} = E_1 + E_2 \tag{E.8}$$

And the resulting interference intensity is given by:

$$I_{12} = E_{12} \times \overline{E_{12}} \tag{E.9}$$

$$I_{12} = (E_1 + E_2) \times \overline{(E_1 + E_2)} \tag{E.10}$$

$$I_{12} = \left(E_{01}e^{j(\omega_1 t+\phi_1)} + E_{02}e^{j(\omega_2 t+\phi_2)}\right) \times \left(E_{01}e^{-j(\omega_1 t+\phi_1)} + E_{02}e^{-j(\omega_2 t+\phi_2)}\right) \tag{E.11}$$

$$I_{12} = E_{01}^2 + E_{02}^2 + E_{01}E_{02}\left(e^{j((\omega_1-\omega_2)t+\phi_1-\phi_2)} + e^{-j((\omega_1-\omega_2)t+\phi_1-\phi_2)}\right) \tag{E.12}$$

By applying the Moivre formula and replacing $E_{01}^2 = I_1$and $E_{02}^2 = I_2$ we obtain:

$$I_{12} = I_1 + I_2 + 2\sqrt{I_1 I_2}cos\left((\omega_1 - \omega_2)t + \phi_1 - \phi_2\right) \tag{E.13}$$

In the case where the two beams are polarized with opposite polarizations, we must add an additional $\pi/2$-phase, therefore:

$$I_{12} = \left(E_{01}e^{j(\omega_1 t+\phi_1)} + E_{02}e^{j(\omega_2 t+\phi_2+\pi/2)}\right) \times \left(E_{01}e^{-j(\omega_1 t+\phi_1)} + E_{02}e^{-j(\omega_2 t+\phi_2+\pi/2)}\right) \tag{E.14}$$

$$I_{12} = E_{01}^2 + E_{02}^2 + E_{01}E_{02}\left(e^{j((\omega_1-\omega_2)t+\phi_1-\phi_2+\pi/2)} + e^{-j((\omega_1-\omega_2)t+\phi_1-\phi_2+\pi/2)}\right) \tag{E.15}$$

$$I_{12} = I_1 + I_2 + 2\sqrt{I_1 I_2}cos\left((\omega_1 - \omega_2)t + \phi_1 - \phi_2 + \frac{\pi}{2}\right) \tag{E.16}$$

$$\boxed{I_{12} = I_1 + I_2 + 2\sqrt{I_1 I_2}sin\left((\omega_1 - \omega_2)t + \phi_1 - \phi_2\right)} \tag{E.17}$$

E.3 Interference in a homodyne interferometer

In this section, we detail the computation of the intensity of interference in a homodyne interferometer. In a homodyne interferometer, a beam splitter splits a single light source (having a wavelength Λ) in two. Therefore, the two obtained electrical fields have the same light frequency ($\omega_1 = \omega_2$). After recombination, the resulting interference intensity is given by the following equation.

$$I_{12} = I_1 + I_2 + 2\sqrt{I_1 I_2}cos(\phi_1 - \phi_2) \quad \text{E.18}$$

And the phase difference between the two paths is:

$$\phi_1 - \phi_2 = \frac{2\pi}{\Lambda}\left(\delta_{ref} - \delta_{DUT} - U_{vib}cos(2\pi f_{vib}t)\right) \quad \text{E.19}$$

Where, δ_{ref} and δ_{DUT} are described in Figure 4.2. Finally, the resulting interference is:

$$I_{12} = I_1 + I_2 + 2\sqrt{I_1 I_2}cos\left(2\pi\frac{\delta_{ref} - \delta_{DUT}}{\Lambda} - 2\pi\frac{U_{vib}}{\Lambda}cos(2\pi f_{vib}t)\right) \quad \text{E.20}$$

Since the vibration amplitude is small compared to the wavelength of the light source ($2\pi\, U_{vib}/\Lambda \ll 1$), the left term ($2\pi\left(\delta_{ref} - \delta_{DUT}\right)/\Lambda$) in the cosine is a constant. Its value must ensure a maximum sensitivity U_{vib} (*i.e.* $U_{vib}/\Lambda\cos\left(2\pi f_{vib}t\right)$ must generate the highest interference amplitude), which happens when:

$$\frac{d^2 I_{12}}{d\left(\delta_{ref} - \delta_{DUT}\right)^2} = 0 \quad \text{E.21}$$

$$\frac{d^2 I_{12}}{d\left(\delta_{ref} - \delta_{DUT}\right)^2} = -\frac{8\pi^2}{\Lambda^2}\sqrt{I_1 I_2}cos\left(2\pi\frac{\delta_{ref} - \delta_{DUT}}{\Lambda}\right) = 0 \quad \text{E.22}$$

$$\delta_{ref} - \delta_{DUT} = \left(n + \frac{1}{4}\right)\lambda \quad (n \in N) \quad \text{E.23}$$

Therefore, the "constant" path difference $\delta_{ref} - \delta_{DUT}$ should be adjusted such that $\delta_{ref} - \delta_{DUT} = (n + 1/4)\lambda$. This is called the $\lambda/4$-condition. Therefore, the reference mirror (or the DUT) is mounted on a piezoelectric translation stage which displacement is constantly monitored using the continuous part of the interference signal in order to ensure the $\lambda/4$-condition. Then the intensity becomes:

$$I_{12} = I_1 + I_2 + 2\sqrt{I_1 I_2}cos\left(\frac{\pi}{2} - 2\pi\frac{U_{vib}}{\Lambda}cos(2\pi f_{vib}t)\right) \quad \text{E.24}$$

$$I_{12} = I_1 + I_2 + 2\sqrt{I_1 I_2}sin\left(2\pi\frac{U_{vib}}{\Lambda}cos(2\pi f_{vib}t)\right) \quad \text{E.25}$$

And since $U_{vib}/\lambda \ll 1$, we finally have*:

* The error made by linearizing the sine is less than 0.2% for a 10 nm displacement.

$$I_{12} = I_1 + I_2 + 4\pi\sqrt{I_1 I_2}\frac{U_{vib}}{\Lambda}cos(2\pi f_{vib}t) \quad \text{E.26}$$

The homodyne interferometer principle generates a constant signal ($I_1 + I_2$), which amplitude depends on the surface reflectivity of the scanned surface, and an alternative signal which amplitude and frequency are related to the observed mechanical vibration ($4\pi\sqrt{I_1 I_2}\frac{U_{vib}}{\Lambda}cos(2\pi f_{vib}t)$).

E.4 Interference in a heterodyne interferometer

In this section, we detail the computation of the intensity of interference in a heterodyne interferometer. In the latter, an Acousto-Optic Modulator (AOM) driven at a frequency f_{AOM}, splits a unique laser beam in two beams (at least). One beam is called the zero-order beam and its optical circular frequency is identical to that of the laser $\omega_1 = 2\pi \times f_{laser}$. The second beam is called first order beam, which optical frequency is shifted by that of the AOM $\omega_2 = 2\pi \times (f_{laser} + f_{AOM})$. So, in this case, the resulting interference signal is given by:

$$I_{12} = I_1 + I_2 + 2\sqrt{I_1 I_2}cos\big((\omega_1 - \omega_2)t + \phi_1 - \phi_2\big) \quad \text{E.27}$$

$$I_{12} = I_1 + I_2 + 2\sqrt{I_1 I_2}cos(2\pi f_{AOM}t + \phi_1 - \phi_2) \quad \text{E.28}$$

The path length gives, $\phi_1 = 2\pi\frac{\delta_{ref}}{\Lambda}$ and $\phi_2 = 2\pi\frac{\delta_{DUT} + U_{vib}cos(2\pi f_{vib}t + \phi_{vib})}{\Lambda}$, thus:

$$I_{12} = I_1 + I_2 + 2\sqrt{I_1 I_2}cos\left(2\pi f_{AOM}t + \frac{2\pi}{\Lambda}(\delta_{ref} - \delta_{DUT}) - \frac{2\pi U_{vib}}{\Lambda}cos(2\pi f_{vib}t + \phi_{vib})\right) \quad \text{E.29}$$

Using the trigonometric relation, $cos(a+b) = cos(a)cos(b) - sin(a)sin(b)$, we have:

$$\begin{aligned} I_{12} = I_1 + I_2 + 2\sqrt{I_1 I_2}\Bigg(&cos\left(2\pi f_{AOM}t + \frac{2\pi}{\Lambda}(\delta_{ref} - \delta_{DUT})\right)cos\left(-\frac{2\pi U_{vib}}{\Lambda}cos(2\pi f_{vib}t + \phi_{vib})\right) \\ &- sin\left(2\pi f_{AOM}t + \frac{2\pi}{\Lambda}(\delta_{ref} - \delta_{DUT})\right)sin\left(-\frac{2\pi U_{vib}}{\Lambda}cos(2\pi f_{vib}t + \phi_{vib})\right)\Bigg) \end{aligned} \quad \text{E.30}$$

Since $U_{vib}/\lambda \ll 1$, we can make the following approximations:

$$cos\left(-\frac{2\pi U_{vib}}{\Lambda}cos(2\pi f_{vib} + \phi_{vib})\right) \approx 1 \quad \text{E.31}$$

$$sin\left(-\frac{2\pi U_{vib}}{\Lambda}cos(2\pi f_{vib}t + \phi_{vib})\right) \approx -\frac{2\pi U_{vib}}{\Lambda}cos(2\pi f_{vib}t + \phi_{vib}) \quad \text{E.32}$$

Thus, the interference signal becomes:

$$I_{12} = I_1 + I_2 + 2\sqrt{I_1 I_2}\left(cos\left(2\pi f_{AOM} t + \frac{2\pi}{\Lambda}(\delta_{ref} - \delta_{DUT})\right)\right. \\ + sin\left(2\pi f_{AOM} t + \frac{2\pi}{\Lambda}(\delta_{ref} - \delta_{DUT})\right)\frac{2\pi U_{vib}}{\Lambda} cos(2\pi f_{vib} t \\ \left. + \phi_{vib})\right) \tag{E.33}$$

Using the trigonometric relation $cos(a)sin(b) = \frac{1}{2}(sin(a+b) + sin(a-b))$, we get:

$$I_{12} = I_1 + I_2 + 2\sqrt{I_1 I_2}\left(cos\left(2\pi f_{AOM} t + \frac{2\pi}{\Lambda}(\delta_{ref} - \delta_{DUT})\right)\right. \\ + \frac{2\pi U_{vib}}{\Lambda}\left(sin\left(2\pi f_{AOM} t + \frac{2\pi}{\Lambda}(\delta_{ref} - \delta_{DUT}) + 2\pi f_{vib} t + \phi_{vib}\right)\right. \\ \left.\left. + sin\left(-2\pi f_{AOM} t - \frac{2\pi}{\Lambda}(\delta_{ref} - \delta_{DUT}) + 2\pi f_{vib} t + \phi_{vib}\right)\right)\right) \tag{E.34}$$

$$I_{12} = I_1 + I_2 + 2\sqrt{I_1 I_2}\left(cos\left(2\pi f_{AOM} t + \frac{2\pi}{\Lambda}(\delta_{ref} - \delta_{DUT})\right)\right. \\ + \frac{2\pi U_{vib}}{\Lambda}\left(sin\left(2\pi(f_{vib} + f_{AOM})t + \phi_{vib} + \frac{2\pi}{\Lambda}(\delta_{ref} - \delta_{DUT})\right)\right. \\ \left.\left.\left. + sin\left(2\pi(f_{vib} - f_{AOM})t + \phi_{vib} - \frac{2\pi}{\Lambda}(\delta_{ref} - \delta_{DUT})\right)\right)\right) \tag{E.35}$$

Finally, the interference signal is composed of a reference cosine oscillating at f_{AOM} which amplitude depends only on the product $I_1 I_2$; therefore, it is influenced by the reflectivity of the observed surface and the quality of the alignment. The second part of the equation consists of two sinusoidal signals which amplitude and frequency depend on those of the observed vibration.

Note that if the assumption $U_{vib}/\lambda \ll 1$ is not observed, harmonic frequencies will appear in addition to the signal at $f_{vib} - f_{AOM}$ and $f_{vib} + f_{AOM}$.

E.5 Interference in a Sagnac interferometer

The principle of the Sagnac interferometer is explained in section 4.1. This kind of interferometer uses a beam splitter to separate the light coming from a single source. Consequently, the two generated beams have the same optical frequency $\omega_1 = \omega_2$. The two phases can be written as (see Figure 4.4):

$$\phi_1 = \frac{2\pi}{\Lambda}(\delta_R + \delta_0 + U_{vib}\, cos(2\pi f_{vib} t + \phi_{vib}) + \delta_S) \tag{E.36}$$

$$\phi_2 = \frac{2\pi}{\Lambda}(\delta_S + \delta_0 + U_{vib}\, cos(2\pi f_{vib}(t + \Delta t) + \phi_{vib}) + \delta_R) \tag{E.37}$$

A quarter wave-plate placed before the photodiode introduces an additional $\pi/2$ phase shift between the two paths, resulting in this interference signal:

$$I_{12} = I_1 + I_2 + 2\sqrt{I_1 I_2} sin\left(\frac{2\pi}{\Lambda}(\delta_R + \delta_0 + U_{vib}\, cos(2\pi f_{vib} t + \phi_{vib}) + \delta_S - (\delta_S + \delta_0 + U_{vib}\, cos(2\pi f_{vib}(t + \Delta t) + \phi_{vib}) + \delta_R))\right) \quad \text{E.38}$$

Here, we see the advantage of the technique; the two paths are perfectly compensated. Only the path difference, due to the mechanical vibration, remains. Hence, we have:

$$I_{12} = I_1 + I_2 + 2\sqrt{I_1 I_2} sin\left(\frac{2\pi}{\Lambda} U_{vib}(cos(2\pi f_{vib} t + \phi_{vib}) - cos(2\pi f_{vib}(t + \Delta T) + \phi_{vib}))\right) \quad \text{E.39}$$

Using the trigonometric formula, $2 \times sin(a)sin(b) = cos(a - b) - cos(a + b)$, with $a = 2\pi f_{vib} t + \pi f_{vib} \Delta T + \phi_{vib}$ and $b = \pi f_{vib} \Delta T$, we have:

$$I_{12} = I_1 + I_2 + 2\sqrt{I_1 I_2} sin\left(\frac{\pi}{\Lambda} U_{vib}\, sin(2\pi f_{vib} t + \pi f_{vib} \Delta T + \phi_{vib})\, sin(\pi f_{vib} \Delta T)\right) \quad \text{E.40}$$

Since $U_{vib}/\lambda \ll 1$, we get:

$$I_{12} = I_1 + I_2 + \frac{2\pi\sqrt{I_1 I_2} U_{vib}}{\Lambda}(sin(2\pi f_{vib} t + \pi f_{vib} \Delta T + \phi_{vib})\, sin(\pi f_{vib} \Delta T)) \quad \text{E.41}$$

Thus, the interference signal of the Sagnac interferometer is composed of a constant signal and a sinusoidal signal which amplitude and frequency are characteristic of the mechanical vibration. The latter is multiplied by a constant term $sin(\pi f_{vib} \Delta T)$ which depends on the time temporal delay generated in the Sagnac loop.

E.6 Interferences in a time-differential interferometer

In a time-differential interferometer a single light source is separated using a beam splitter; thus, the two generated beams have the same optical circular frequency ($\omega_1 = \omega_2$). The respective phases of the two beams are:

$$\phi_1 = \frac{2\pi}{\Lambda}(u(t) + \delta_0) \; and \; \phi_2 = \frac{2\pi}{\Lambda}\left(u(t + \Delta T) + \delta_{delay}\right) \quad \text{E.42}$$

According to equation (C.20), the intensity resulting from the interference between the two beams is:

$$I_{12} = I_1 + I_2 + 2\sqrt{I_1 I_2} cos\left(2\pi \frac{u(t) - u(t + \Delta T)}{\Lambda} + 2\pi \frac{\delta_0 - \delta_{delay}}{\Lambda}\right) \quad \text{E.43}$$

In addition, the phase difference $\delta_0 - \delta_{delay}$ is tuned so that the interferometer works in a quadrature wavelength mode:

$$2\pi \frac{\delta_0 - \delta_{delay}}{\Lambda} = \mp \frac{\pi}{2}[2\pi] \quad \text{E.44}$$

Consequently, the interference intensity becomes:

$$I_{12} = I_1 + I_2 + 2\sqrt{I_1 I_2} cos\left(2\pi \frac{u(t) - u(t + \Delta T)}{\Lambda} \mp \frac{\pi}{2}\right) \quad \text{E.45}$$

$$I_{12} = I_1 + I_2 + 2\sqrt{I_1 I_2} sin\left(\frac{2\pi}{\Lambda}\big(u(t) - u(t + \Delta T)\big)\right) \quad \text{E.46}$$

Since U_{vib} is typically small compared to the optical wavelength $U_{vib}/\lambda \ll 1$, we can linearize the sine and have:

$$I_{12} = I_1 + I_2 + \sqrt{I_1 I_2}\frac{4\pi}{\lambda}\big(u(t) - u(t + \Delta T)\big) \quad \text{E.47}$$

Here, we can notice that, if the delay is long compared to the signal duration, the intensity is proportional to the normal displacement. On the contrary, if the delay is short compared to the duration of the signal, the intensity is proportional to the normal velocity [130].

E.7 Scanning system

An optical system combining the beam expansion and steering is presented in Figure E.2. The system is designed to scan the surface of a fixed DUT with a laser spot of a given diameter. It features two galvo-mirrors that steer the beam in the plane with an angle (α) but also out of the plane (not represented). The maximum scanning angles are typically around $\mp 15°$. Then, two lenses (L_1, focal f_1' and L_2, focal f_2') magnify the beam and reduce its incoming angle before entering the objective (L_3). The objective lens focuses the laser beam in a small spot on the DUT. The first lens is specific, called "scan lens"; it is designed specifically to accept wide incoming angles.

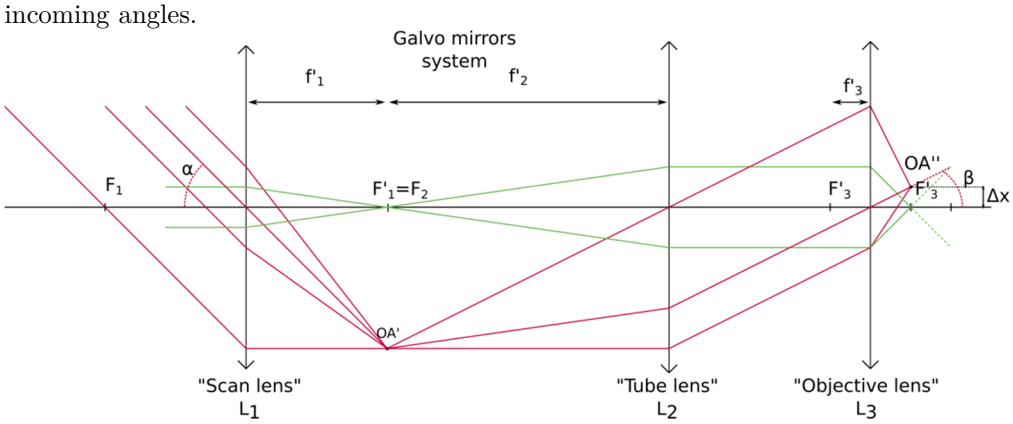

Figure E.2 Schematic of a beam scanning solution. The two first lenses (L_1 and L_2) are in a confocal configuration. They expand the beam and decrease the input angle α by a factor f_2'/f_1' before entering the objective lens.

The resulting displacement of the spot (Δx) on the DUT is given by the relation:

$$\Delta x = \frac{tan(\alpha) \cdot f'1 \cdot f'3}{f'2} \quad \text{E.48}$$

This formula highlights a nonlinear relation between the input angle α and the output displacement Δx. The focal lengths f_1' and f_2' are fixed by the magnification we want to achieve. The maximum displacement is obtained when α is the biggest.

The spot size diameter (S) is given by the diffraction limit through the objective [152] [153]:

$$S = 1.22 \cdot \frac{\Lambda}{2 \cdot NA} \tag{E.49}$$

Where, NA is the numerical aperture of the objective. These relations show that the objective lens must be selected in a trade-off between a long focal length (to ensure a sufficient scanning area on the DUT) and a large numerical aperture (to ensure a small enough spot diameter). Unfortunately, these two characteristics do not come together.

E.8 I/Q demodulation

A general schematic of an I/Q demodulator is presented in Figure E.3. In the former, a quadrature phase splitter divides the local oscillator (LO) in two parts, one in-phase, and another is delayed by $\pi/2$. Then, these two signals are mixed with the RF input. Assuming that the RF and LO signals are:

$$v_{RF} = A_{RF}\, cos(2\pi f_{RF} t + \phi_{RF}) \;\; and \;\; v_{LO} = cos(2\pi f_{LO} t + \phi_{LO}) \tag{E.50}$$

The resulting signals are, on the I channel:

$$\begin{aligned} v_I = \frac{A_{RF}}{2} cos(2\pi(f_{RF} - f_{LO})t + \phi_{RF} - \phi_{LO}) \\ + \frac{A_{RF}}{2} cos(2\pi(f_{RF} + f_{LO})t + \phi_{RF} + \phi_{LO}) \end{aligned} \tag{E.51}$$

And on the Q channel:

$$\begin{aligned} v_Q = \frac{A_{RF}}{2} cos\left(2\pi(f_{RF} - f_{LO})t + \phi_{RF} - \phi_{LO} - \frac{\pi}{2}\right) \\ + \frac{A_{RF}}{2} cos\left(2\pi(f_{RF} + f_{LO})t + \phi_{RF} + \phi_{LO} - \frac{\pi}{2}\right) \end{aligned} \tag{E.52}$$

Since Low Pass Filters (LPF) are present after the mixers, the high frequencies are filtered out, resulting in these signals:

$$v_I = \frac{A_{RF}}{2} cos(2\pi(f_{RF} - f_{LO})t + \phi_{RF} - \phi_{LO}) \tag{E.53}$$

$$v_Q = \frac{A_{RF}}{2} cos\left(2\pi(f_{RF} - f_{LO})t + \phi_{RF} - \phi_{LO} - \frac{\pi}{2}\right) \tag{E.54}$$

When the LO and RF frequencies are the same, the I and Q output signals are continuous. Their Euclidian norm is the amplitude of the RF signal, and their ratio gives the phase difference between the two input signals (see Figure E.3).

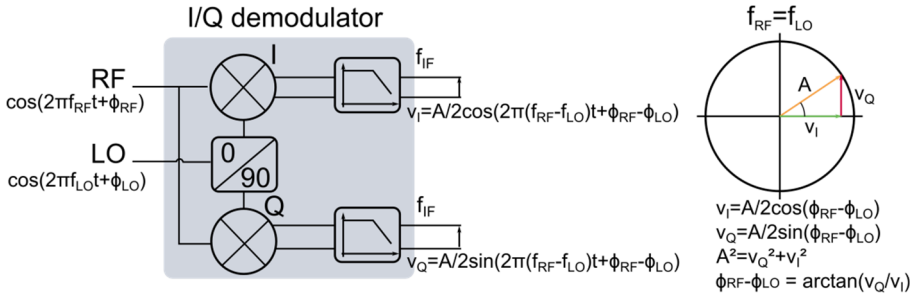

Figure E.3 Schematic of a I/Q demodulator. (Left) the I (In-phase) channel results directly from the multiplication of the RF signal with the Local Oscillator (LO). The Q (Quadrature) channel is the product of the RF input signal and a $\pi/2$ delayed LO. (Right) Schematic showing the I/Q outputs when the RF and LO frequencies are the same.

In our case the input RF signal has the following form:

$$v_{RF} = A_{RF}\, cos\left(2\pi(f_{vib} + f_{AOM})t + \phi_{vib} + \frac{2\pi}{\Lambda}(\delta_{ref} - \delta_{DUT})\right) \quad \text{E.55}$$

Where, A_{RF} is proportional to the observed amplitude of the mechanical vibration. And the LO signal is:

$$v_{LO} = cos(2\pi(f_{vib} + f_{AOM} + f_{IF})t + \phi_{LO}) \quad \text{E.56}$$

Therefore, the signals on the I and Q channels are:

$$v_I = \frac{A_{RF}}{2} cos\left(2\pi f_{IF} t + \phi_{vib} + \frac{2\pi}{\Lambda}(\delta_{ref} - \delta_{DUT}) - \phi_{LO}\right) \quad \text{E.57}$$

$$v_Q = \frac{A_{RF}}{2} cos\left(2\pi f_{IF} t + \phi_{vib} + \frac{2\pi}{\Lambda}(\delta_{ref} - \delta_{DUT}) - \phi_{LO} - \frac{\pi}{2}\right) \quad \text{E.58}$$

Thus, the I/Q demodulator outputs two signals at low frequency (intermediate frequency) which carry the amplitude and phase information of the original RF signal.

E.9 Power unit

The power supplies, for each module of the receiver chain, are provided by a single power unit containing all the necessary electronics to generate and regulate the voltages (see Figure E.4).

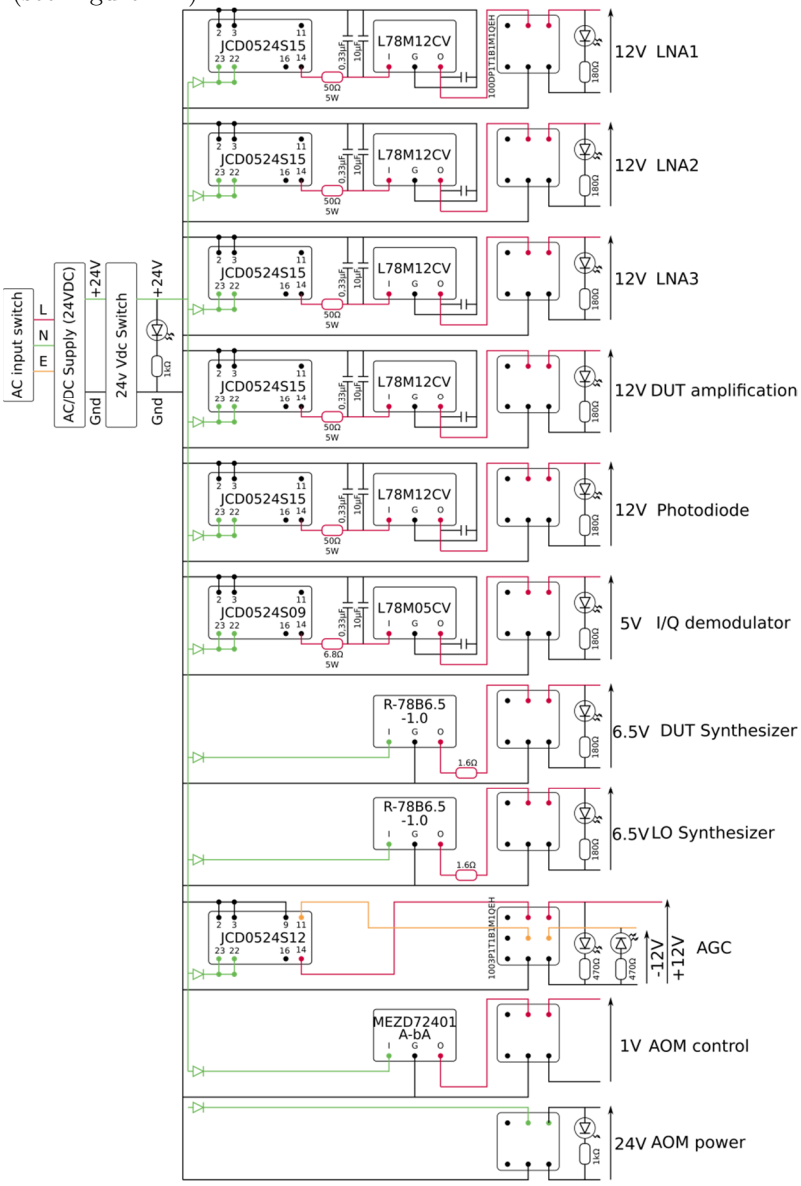

Figure E.4 Detailed schematic of the power unit. Each voltage supply has at its output a LED to warn the user about failure. The electronic components are mounted on a perf board. The entire circuitry is embedded in a box.

E.10 State diagram of the spot size program

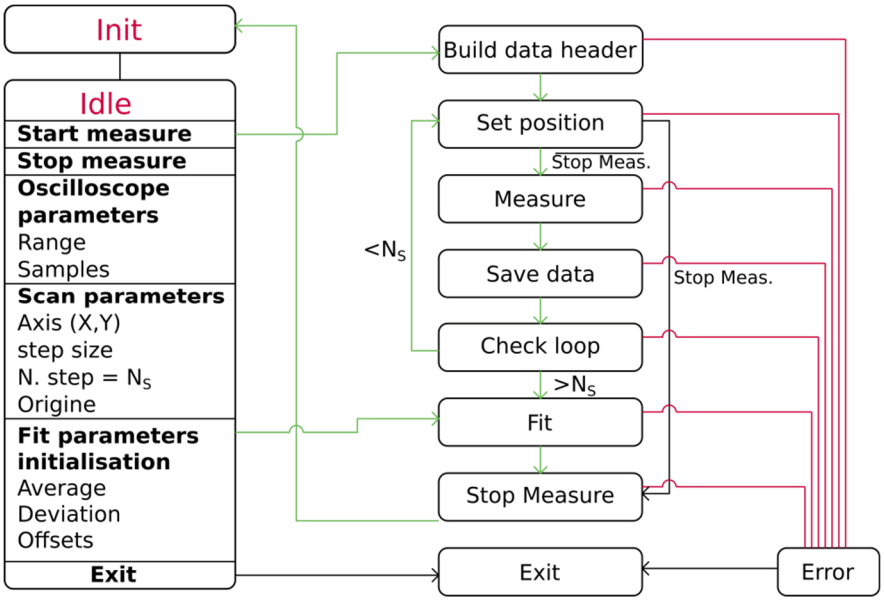

Figure E.5 State diagram of the LabVIEW program enabling to determine the spot size. After the initialization of the hardware (stages, oscilloscope), the program let the user setting his experiment. The program offers the possibility to define an origin position. The latter should be the position of the edge that is found experimentally. For a given axis, the program will scan around the origin point in both directions. After the scan, the program uses the "guess parameter" to fit a theoretical error function to the experimental data and returns the fitted parameters.

Bibliography

[1] Lord Rayleigh, "On waves propagated along the plane surface of an elastic solid," *Proc. Lond. Math. Soc.*, vol. s1-17, no. 1, pp. 4–11, 1885.

[2] D. Royer and E. Dieulesaint, *Elastic waves in solids I: free and guided propagation*. Berlin Heidelberg: Springer-Verlag, 2000.

[3] G. Bu, D. Ciplys, M. Shur, L. J. Schowalter, S. Schujman, and R. Gaska, "Surface acoustic wave velocity in single-crystal AlN substrates," *IEEE Trans Ultras Ferroelec Freq Contr*, vol. 53, no. 1, pp. 251–254, 2006.

[4] J. Curie and P. Curie, "Développement par compression de l'électricité polaire dans les cristaux hémièdres à faces inclinées," *Bull. Minéralogie*, vol. 3, no. 4, pp. 90–93, 1880.

[5] J. G. Gualtieri, J. A. Kosinski, and A. Ballato, "Piezoelectric materials for SAW applications," in *IEEE Int. Ultras. Symp.*, 1992, vol. 1, pp. 403–412.

[6] R. M. White and F. W. Voltmer, "Direct piezoelectric coupling to surface elastic waves," *Appl. Phys. Lett.*, vol. 7, no. 12, pp. 314–316, 1965.

[7] D. Morgan and E. G. S. Paige, "1 - Basic survey," in *Surface Acoustic Wave filters*, D. Morgan and E. G. S. Paige, Eds. Oxford: Academic Press, 2007, pp. 1–37.

[8] P. Nicolay, "Les capteurs à ondes élastiques de surface : applications pour la mesure des basses pressions et des hautes températures," PhD dissertation, Nancy 1, 2007.

[9] D. Morgan, "Preface," in *Surface Acoustic Wave Filters (Second edition)*, D. Morgan and E. G. S. Paige, Eds. Oxford: Academic Press, 2007, pp. xi–xiv.

[10] R. Weigel *et al.*, "Microwave acoustic materials, devices, and applications," *IEEE Trans. Microw. Theory Tech.*, vol. 50, no. 3, pp. 738–749, 2002.

[11] M. Chatras *et al.*, "Modeling and design of BAW resonators and filters for integration in a UMTS transmitter," *Model. Meas. Methods Acoust. Waves Acoust. Microdevices*, 2013.

[12] C. C. W. Ruppel, "Acoustic wave filter technology–A review," *IEEE Trans Ultras Ferroelec Freq Contr*, vol. 64, no. 9, pp. 1390–1400, 2017.

[13] S. Bronckers, A. Roc'h, and B. Smolders, "Wireless receiver architectures towards 5G: Where are we?," *IEEE Circuits Syst. Mag.*, vol. 17, no. 3, pp. 6–16, 2017.

[14] Y. Hori, H. Kobayashi, K. Tohyama, Y. Iwasaki, and K. Suzuki, "A hybrid substrate for a temperature-compensated surface acoustic wave filter," in *IEEE Int. Ultras. Symp.*, 2009, pp. 2631–2634.

[15] O. Elmazria, A. Bartasyte, E. Blampain, M. Gonzalez, and L. Bouvot, "$LiTaO_3$ single crystals treated by vapour transport equilibration for temperature-compensated SAW devices," in *IEEE Int. Ultras. Symp.*, 2012, pp. 1252–1255.

[16] M. Miura *et al.*, "Temperature compensated $LiTaO_3$ sapphire bonded SAW substrate with low loss and high coupling factor suitable for US-PCS application," in *IEEE Int. Ultras. Symp.*, 2004, vol. 2, pp. 1322–1325.

[17] K. Higaki *et al.*, "High frequency SAW filter on diamond," in *IEEE MTT-S Int. Microwave Symp. Dig.*, 1997, vol. 2, pp. 829–832.

[18] L. Reindl, G. Scholl, T. Ostertag, H. Scherr, U. Wolff, and F. Schmidt, "Theory and application of passive SAW radio transponders as sensors," *IEEE Trans Ultras Ferroelec Freq Contr*, vol. 45, no. 5, pp. 1281–1292, 1998.

[19] V. Ferrari and R. Lucklum, "Overview of acoustic-wave microsensors," in *Piezoelectric Transducers and Applications*, A. A. Vives, Ed. Berlin, Heidelberg: Springer Berlin Heidelberg, 2008, pp. 39–62.

[20] A. Pohl, "A review of wireless SAW sensors," *IEEE Trans Ultras Ferroelec Freq Contr*, vol. 47, no. 2, pp. 317–332, 2000.

[21] F. Lurz, T. Ostertag, B. Scheiner, R. Weigel, and A. Koelpin, "Reader architectures for wireless surface acoustic wave sensors," *Sensors*, vol. 18, no. 6, p. 1734, 2018.

[22] G. Bruckner and R. Fachberger, "SAW ID tag for industrial application with large data capacity and anticollision capability," in *IEEE Int. Ultras. Symp.*, 2008, pp. 300–303.

[23] R. Fachberger, A. Binder, and A. Erlacher, "SAW-RFID and temperature monitoring of slide gate plates," in *IEEE Sens. J.*, 2009, pp. 1514–1517.

[24] A. Binder and R. Fachberger, "Wireless SAW temperature sensor system for high-speed high-voltage motors," *IEEE Sens J*, vol. 11, no. 4, pp. 966–970, 2011.

[25] C. Bernauer *et al.*, "Temperature measurement on overhead transmission lines (OHTL) utilizing surface acoustic wave (SAW) sensors," in *CIRED*, 2007, pp. 788–791.

[26] P. Nicolay and T. Aubert, "A numerical method to derive accurate temperature coefficients of material constants from high-temperature SAW measurements: application to langasite," *IEEE Trans Ultras Ferroelec Freq Contr*, vol. 60, no. 10, pp. 2137–2141, 2013.

[27] W. Buff, S. Klett, M. Rusko, J. Ehrenpfordt, and M. Goroli, "Passive remote sensing for temperature and pressure using SAW resonator devices," *IEEE Trans Ultras Ferroelec Freq Contr*, vol. 45, no. 5, pp. 1388–1392, 1998.

[28] A. Binder, G. Bruckner, N. Schobernig, and D. Schmitt, "Wireless surface acoustic wave pressure and temperature sensor with unique identification based on $LiNbO_3$," *IEEE Sens J*, vol. 13, no. 5, pp. 1801–1805, 2013.

[29] A. Pohl, R. Steindl, and L. Reindl, "The 'intelligent tire' utilizing passive SAW sensors measurement of tire friction," *IEEE Trans. Instrum. Meas.*, vol. 48, no. 6, pp. 1041–1046, 1999.

[30] J. Beckley, V. Kalinin, M. Lee, and K. Voliansky, "Non-contact torque sensors based on SAW resonators," in *IEEE Int. Freq. Contr. Symp.*, 2002, pp. 202–213.

[31] W. C. Wilson *et al.*, "Orthogonal frequency coded SAW sensors for aerospace SHM applications," *IEEE Sens J*, vol. 9, no. 11, pp. 1546–1556, 2009.

[32] W. C. Wilson, M. D. Rogge, B. H. Fisher, D. C. Malocha, and G. M. Atkinson, "Fastener failure detection using a surface acoustic wave strain sensor," *IEEE Sens J*, vol. 12, no. 6, pp. 1993–2000, 2012.

[33] W. C. Wilson and P. D. Juarez, "Emerging needs for pervasive passive wireless sensor networks on aerospace vehicles," *Procedia Comput. Sci.*, vol. 37, pp. 101–108, 2014.

[34] M. Perry, I. McKeeman, M. Saafi, and P. Niewczas, "Wireless surface acoustic wave sensors for displacement and crack monitoring in concrete structures," *Smart Mater. Struct.*, vol. 25, no. 3, p. 035035, 2016.

[35] H.-M. Lee, D.-Y. Han, and H. Ahn, "Design and fabrication of SAW gas sensor with resonator structure," in *5th Int. Conf. Prop. Appl. Dielectric Mater.*, 1997, vol. 2, pp. 1058–1061.

[36] W. Wang *et al.*, "Development of a room temperature SAW methane gas sensor incorporating a supramolecular Cryptophane A coating," *Sensors*, vol. 16, no. 1, p. 73, 2016.

[37] J. Du, G. L. Harding, J. A. Ogilvy, P. R. Dencher, and M. Lake, "A study of Love-wave acoustic sensors," *Sens Actuat Phys*, vol. 56, no. 3, pp. 211–219, 1996.

[38] G. Kovacs, M. J. Vellekoop, R. Haueis, G. W. Lubking, and A. Venema, "A Love wave sensor for (bio)chemical sensing in liquids," *Sens. Actuators Phys.*, vol. 43, no. 1, pp. 38–43, 1994.

[39] C. Caliendo, E. Verona, and A. D'Amico, "Surface Acoustic Wave (SAW) gas sensors," in *Gas Sensors: Principles, Operation and Developments*, G. Sberveglieri, Ed. Dordrecht: Springer Netherlands, 1992, pp. 281–306.

[40] A. Hagelauer, T. Ussmueller, and R. Weigel, "SAW and CMOS RFID transponder-based wireless systems and their applications," in *IEEE Int. Freq. Contr. Symp.*, 2012, pp. 1–6.

[41] V. P. Plessky and L. M. Reindl, "Review on SAW RFID tags," *IEEE Trans Ultras Ferroelec Freq Contr*, vol. 57, no. 3, pp. 654–668, 2010.

[42] X. Ding *et al.*, "Surface acoustic wave microfluidics," *Lab. Chip*, vol. 13, no. 18, pp. 3626–3649, 2013.

[43] C. C. W. Ruppel, W. Ruile, G. Scholl, K. C. Wagner, and O. Manner, "Review of models for low-loss filter design and applications," in *IEEE Int. Ultras. Symp.*, 1994, vol. 1, pp. 313–324.

[44] K. Shaposhnikov, "Finite Element simulation of piezoelectric surface acoustic wave sensors," PhD dissertation, TU Wien, 2015.

[45] J. Koskela, V. P. Plessky, and M. M. Salomaa, "SAW/LSAW COM parameter extraction from computer experiments with harmonic admittance of a periodic array of electrodes," *IEEE Trans Ultras Ferroelec Freq Contr*, vol. 46, no. 4, pp. 806–816, 1999.

[46] K. Hashimoto, *Surface acoustic wave devices in telecommunications*. Berlin, Heidelberg: Springer, 2000.

[47] K. Shaposhnikov, M. Kaltenbacher, and P. Nicolay, "Fast full-FEM computation of COM parameters. Application to multilayered SAW structures," in *IEEE Int. Ultras. Symp.*, 2014, pp. 1501–1504.

[48] G. Kovacs, M. Anhorn, H. E. Engan, G. Visintini, and C. C. W. Ruppel, "Improved material constants for $LiNbO_3$ and $LiTaO_3$," in *IEEE Int. Ultras. Symp.*, 1990, pp. 435–438.

[49] W. Wang, K. Lee, S. Yang, J. Hwang, and G. Kim, "Optimized surface acoustic wave-based pressure sensor using equivalent circuit model," in *1st IEEE Int. Conf. Nano/Micro Eng. Molecular Syst.*, 2006, pp. 1092–1096.

[50] W. Wang, K. Lee, T. Kim, I. Park, and S. Yang, "Modeling and performance evaluation of 2.4GHz SAW-based pressure sensor," in *IEEE Sensors*, 2006, pp. 1031–1034.

[51] B. Zhang, H. Hu, A. Ye, and F. Cao, "A surface acoustic wave resonator type sensor for measuring temperature," in *Int. Conf. Comput. Sci. Mech. Automation*, 2015, pp. 162–165.

[52] W. Hao, J. Liu, M. Liu, Y. Liang, and S. He, "Mass sensitivity optimization of a surface acoustic wave sensor incorporating a resonator configuration," *Sensors*, vol. 16, no. 4, 2016.

[53] "Surface acoustic wave gas sensor." [Online]. Available: https://www.comsol.fr/model/surface-acoustic-wave-gas-sensor-2129. [Accessed: 15-Dec-2018].

[54] Q. Fu, W. Luo, Y. Wang, J. Wang, and D. Zhou, "Simulation of wireless passive SAW sensors based on FEM/BEM model," in *IEEE Int. Ultras. Symp.*, 2008, pp. 1861–1864.

[55] X. Zhang, Y. Xu, M. Pan, Y. Fan, and H. Zhang, "Modeling and simulation of wireless passive sensors based on surface acoustic wave delay lines," in *Int. Conf. Com. Tech.*, 2006, pp. 1–4.

[56] X. Zhang, Y. Xu, M. Zhao, M. Pan, Y. Fan, and Z. Zhang, "Modeling and simulation of wireless passive pressure sensors based on surface acoustic wave resonators," in *8th int. Conf. Signal Processing*, 2006, vol. 4.

[57] B. K. Sinha and H. F. Tiersten, "On the influence of uniaxial biasing stresses on the velocity of piezoelectric surface waves," in *IEEE Int. Ultras. Symp.*, 1976, pp. 475–479.

[58] B. K. Sinha and S. Locke, "Acceleration and vibration sensitivity of SAW devices," *IEEE Trans. Ultrason. Ferroelectr. Freq. Control*, vol. 34, no. 1, pp. 29–38, 1987.

[59] D. Hauden, M. Planat, and J. J. Gagnepain, "Nonlinear properties of surface acoustic waves: applications to oscillators and sensors," *IEEE Trans. Sonics Ultrason.*, vol. 28, no. 5, pp. 342–348, 1981.

[60] B. M. Cormack, D. Geraghty, and M. O'Mahony, "Modeling of surface acoustic wave strain sensors using coupling-of-modes analysis," *IEEE Trans. Ultrason. Ferroelectr. Freq. Control*, vol. 58, no. 11, pp. 2461–2468, 2011.

[61] V. V. Bolotin, *Non conservative problems of the theory of elastic stability.* Macmillan, 1963.

[62] A. L. Nalamwar and M. Epstein, "Surface acoustic waves in strained media," *J. Appl. Phys.*, vol. 47, no. 1, pp. 43–48, 1976.

[63] Y. Cho and K. Yamanouchi, "Nonlinear, elastic, piezoelectric, electrostrictive, and dielectric constants of Lithium Niobate," *J. Appl. Phys.*, vol. 61, no. 3, pp. 875–887, 1987.

[64] R. T. Smith and F. S. Welsh, "Temperature dependence of the elastic, piezoelectric, and dielectric constants of Lithium Tantalate and Lithium Niobate," *J. Appl. Phys.*, vol. 42, no. 6, pp. 2219–2230, 1971.

[65] B. Maier, "Design of a test procedure and characterization of the correlation between strain and SAW propagation time in single crystals," Fachhochschule Kärnten, Villach Austria, Carinthian Tech Research AG, Villach, Austria, Master thesis, 2011.

[66] G. Bruckner, J. Schicker, N. Schobernig, V. Stojanov, and P. Schlumpf, "Design study of a wireless pressure sensor for medical application," *Proc. Sens.*, pp. 192–197, 2013.

[67] P. Nicolay *et al.*, "A LN/Si-Based SAW Pressure Sensor," *Sensors*, vol. 18, no. 10, 2018.

[68] J. C. Baumhauer and H. F. Tiersten, "Nonlinear electroelastic equations for small fields superposed on a bias," *J. Acoust. Soc. Am.*, vol. 54, no. 4, pp. 1017–1034, 1973.

[69] J. J. Gagnepain, "Nonlinear constants and their significance," in *IEEE Int. Freq. Contr. Symp.*, 1987, pp. 266–276.

[70] "IEEE standard on piezoelectricity," *ANSIIEEE Std 176-1987*, pp. 0_1-, 1988.

[71] J. Courbon, "Calcul des structures, plaques minces élastiques," *Ref: TIP052WEB - "Mathématiques,"* 1980. [Online]. Available: https://www.techniques-ingenieur.fr/base-documentaire/archives-th12/archives-mathematiques-pour-l-ingenieur-tiafm/archive-1/calcul-des-structures-plaques-minces-elastiques-a310/. [Accessed: 12-Dec-2018].

[72] O. Elmazria, S. Zhgoon, L. L. Brizoual, F. Sarry, D. Tsimbal, and M. A. Djouadi, "AlN/ZnO/diamond structure combining isolated and surface acoustic waves," *Appl. Phys. Lett.*, vol. 95, no. 23, p. 233503, 2009.

[73] C. Floer *et al.*, "AlN/ZnO/$LiNbO_3$ packageless structure as a low-profile sensor for potential on-body applications," *IEEE Trans. Ultrason. Ferroelectr. Freq. Control*, vol. 65, no. 10, pp. 1925–1932, 2018.

[74] C. W. Ong, D. G. Zong, M. Aravind, C. L. Choy, and D. R. Lu, "Tensile strength of Zinc Oxide films measured by a microbridge method," *J. Mater. Res.*, vol. 18, no. 10, pp. 2464–2472, 2003.

[75] D. G. Zong *et al.*, "Tensile strength of Aluminium Nitride films," *Philos. Mag.*, vol. 84, no. 31, pp. 3353–3373, 2004.

[76] T. Aubert, P. Nicolay, and F. Sarry, "Thermoelastic effects in Pt IDTs. Impact on the behavior of high-temperature LGS-based SAW devices," in *IEEE Int. Ultras. Symp.*, 2013, pp. 259–262.

[77] V. Plessky and J. Koskela, "Coupling-of-modes analysis of saw devices," *Int. J. High Speed Electron. Syst.*, vol. 10, no. 04, pp. 867–947, 2000.

[78] J. Bjurström, I. Katardjiev, and V. Yantchev, "Lateral-field-excited thin-film Lamb wave resonator," *Appl. Phys. Lett.*, vol. 86, no. 15, p. 154103, 2005.

[79] J. Bjurström, V. Yantchev, and I. Katardjiev, "Thin film Lamb wave resonant structures – The first approach," *Solid-State Electron.*, vol. 50, no. 3, pp. 322–326, 2006.

[80] C.-M. Lin, Y.-J. Lai, J.-C. Hsu, Y.-Y. Chen, D. G. Senesky, and A. P. Pisano, "High-Q Aluminum Nitride Lamb wave resonators with biconvex edges," *Appl. Phys. Lett.*, vol. 99, no. 14, p. 143501, 2011.

[81] C. Lin, V. Yantchev, J. Zou, Y. Chen, and A. P. Pisano, "Micromachined one-port Aluminum Nitride Lamb wave resonators utilizing the lowest-order symmetric mode," *J. Microelectromechanical Syst.*, vol. 23, no. 1, pp. 78–91, 2014.

[82] C. Lin, V. Yantchev, Y. Chen, V. V. Felmetsger, and A. P. Pisano, "Characteristics of AlN Lamb wave resonators with various bottom electrode configurations," in *Joint Conference of the IEEE International Frequency Control and the European Frequency and Time Forum (FCS) Proceedings*, 2011, pp. 1–5.

[83] M. Rinaldi, C. Zuniga, C. Zuo, and G. Piazza, "Super-high-frequency two-port AlN contour-mode resonators for RF applications," *IEEE Trans. Ultrason. Ferroelectr. Freq. Control*, vol. 57, no. 1, pp. 38–45, 2010.

[84] P. J. Stephanou and A. P. Pisano, "PS-4 GHZ contour extensional mode Aluminum Nitride MEMS resonators," in *IEEE Int. Ultras. Symp.*, 2006, pp. 2401–2404.

[85] A. Volatier, G. Caruyer, D. P. Tanon, P. Ancey, E. Defay, and B. Dubus, "UHF/VHF resonators using lamb waves co-integrated with bulk acoustic wave resonators," in *IEEE Int. Ultras. Symp.*, 2005, vol. 2, pp. 902–905.

[86] C. Zuo, N. Sinha, M. B. Pisani, C. R. Perez, R. Mahameed, and G. Piazza, "12E-3 channel-select RF MEMS filters based on self-coupled AlN contour-mode piezoelectric resonators," in *IEEE Int. Ultras. Symp.*, 2007, pp. 1156–1159.

[87] G. Piazza, P. J. Stephanou, and A. P. Pisano, "One and two port piezoelectric higher order contour-mode MEMS resonators for mechanical signal processing," *Solid-State Electron.*, vol. 51, no. 11, pp. 1596–1608, 2007.

[88] V. Yantchev and I. Katardjiev, "Thin film Lamb wave resonators in frequency control and sensing applications: a review," *J. Micromechanics Microengineering*, vol. 23, no. 4, p. 043001, 2013.

[89] I. Kone *et al.*, "Electrode sizing for guided wave resonator above a Bragg mirror," in *IEEE Int. Freq. Contr. Symp.*, 2009, pp. 904–907.

[90] I. Kone *et al.*, "Resonator using guided waves in a piezoelectric layer above a Bragg mirror," in *IEEE Int. Freq. Contr. Symp.*, 2008, pp. 581–585.

[91] I. Koné *et al.*, "Guided acoustic wave resonators using an acoustic Bragg mirror," *Appl. Phys. Lett.*, vol. 96, no. 22, p. 223504, 2010.

[92] V. Yantchev and I. Katardjiev, "Micromachined thin film plate acoustic resonators utilizing the lowest order symmetric Lamb wave mode," *IEEE Trans. Ultrason. Ferroelectr. Freq. Control*, vol. 54, no. 1, pp. 87–95, 2007.

[93] A. Konno *et al.*, "ScAlN Lamb wave resonator in GHz range released by XeF_2 etching," in *IEEE Int. Ultras. Symp.*, 2013, pp. 1378–1381.

[94] J. T. Luo, B. Fan, F. Zeng, and F. Pan, "Influence of Cr-doping on microstructure and piezoelectric response of AlN films," *J. Phys. Appl. Phys.*, vol. 42, no. 23, p. 235406, 2009.

[95] A. Kabulski, V. R. Pagán, and D. Korakakis, "Erbium alloyed Aluminum Nitride films for piezoelectric applications," *MRS Online Proc. Libr. Arch.*, vol. 1129, 2008.

[96] H. Liu, F. Zeng, G. Tang, and F. Pan, "Enhancement of piezoelectric response of diluted Ta doped AlN," *Appl. Surf. Sci.*, vol. 270, pp. 225–230, 2013.

[97] M. Akiyama, T. Kamohara, K. Kano, A. Teshigahara, Y. Takeuchi, and N. Kawahara, "Enhancement of piezoelectric response in Scandium Aluminum Nitride alloy thin films prepared by dual reactive cosputtering," *Adv. Mater.*, vol. 21, no. 5, pp. 593–596, 2009.

[98] M. Akiyama, K. Kano, and A. Teshigahara, "Influence of growth temperature and scandium concentration on piezoelectric response of Scandium Aluminum Nitride alloy thin films," *Appl. Phys. Lett.*, vol. 95, no. 16, p. 162107, 2009.

[99] R. Matloub, A. Artieda, C. Sandu, E. Milyutin, and P. Muralt, "Electromechanical properties of $Al_{0.9}Sc_{0.1}N$ thin films evaluated at 2.5 GHz film bulk acoustic resonators," *Appl. Phys. Lett.*, vol. 99, no. 9, p. 092903, 2011.

[100] R. Matloub *et al.*, "Piezoelectric $Al_{1-x}Sc_xN$ thin films: A semiconductor compatible solution for mechanical energy harvesting and sensors," *Appl. Phys. Lett.*, vol. 102, no. 15, p. 152903, 2013.

[101] M. A. Caro *et al.*, "Piezoelectric coefficients and spontaneous polarization of ScAlN," *J. Phys. Condens. Matter*, vol. 27, no. 24, p. 245901, 2015.

[102] F. Tasnádi *et al.*, "Origin of the anomalous piezoelectric response in wurtzite $Sc_xAl_{1-x}N$ alloys," *Phys. Rev. Lett.*, vol. 104, no. 13, p. 137601, 2010.

[103] F. Parsapour, "Growth, integration, and functional characterization of AlScN thin films for RF MEMS devices," PhD dissertation, EPFL, Lausanne, Switzerland, 2019.

[104] N. Kurz, "Untersuchung der piezoelektrischen und pyroelektrischen Eigenschaften von Aluminium-Scandium-Nitrid für mikroakustische Hochfrequenzfilter," PhD dissertation, University of Freiburg, IMTEK, 2019.

[105] "Rayleigh and Lamb waves - physical theory and applications | I. A. Viktorov | Springer." [Online]. Available: https://www.springer.com/gp/book/9781489956835. [Accessed: 21-Jan-2019].

[106] J. J. Campbell and W. R. Jones, "Propagation of surface waves at the boundary between a piezoelectric crystal and a fluid medium," *IEEE Trans. Sonics Ultrason.*, vol. 17, no. 2, pp. 71–76, 1970.

[107] N. Kurz *et al.*, "Experimental determination of the electro-acoustic properties of thin film AlScN using surface acoustic wave resonators," *J. Appl. Phys.*, vol. Under revision.

[108] N. Kurz *et al.*, "Determination of elastic and piezoelectric properties of $Al_{0.84}Sc_{0.16}N$ thin films," in *IEEE Int. Ultras. Symp.*, 2018, pp. 1–5.

[109] G. F. Iriarte, J. G. Rodríguez, and F. Calle, "Synthesis of c-axis oriented AlN thin films on different substrates: A review," *Mater. Res. Bull.*, vol. 45, no. 9, pp. 1039–1045, 2010.

[110] M. Akiyama, K. Nagao, N. Ueno, H. Tateyama, and T. Yamada, "Influence of metal electrodes on crystal orientation of Aluminum Nitride thin films," *Vacuum*, vol. 74, no. 3, pp. 699–703, 2004.

[111] S. Zhang, W. Y. Fu, D. Holec, C. J. Humphreys, and M. A. Moram, "Elastic constants and critical thicknesses of ScGaN and ScAlN," *J. Appl. Phys.*, vol. 114, no. 24, p. 243516, 2013.

[112] K. Umeda, H. Kawai, A. Honda, M. Akiyama, T. Kato, and T. Fukura, "Piezoelectric properties of ScAlN thin films for piezo-MEMS devices," in *IEEE 26th International Conference on Micro Electro Mechanical Systems (MEMS)*, 2013, pp. 733–736.

[113] F. Parsapour, V. Pashchenko, P. Nicolay, and P. Muralt, "Material constants extraction for AlScN thin films using a dual mode BAW resonator," in *IEEE Micro Electro Mechanical Systems (MEMS)*, 2018, pp. 763–766.

[114] F. Parsapour *et al.*, "Ex-situ AlN seed layer for (0001)-textured $Al_{0.84}Sc_{0.16}N$ thin films grown on SiO_2 substrates," in *IEEE Int. Ultras. Symp.*, 2017, pp. 1–4.

[115] H. Bhugra and G. Piazza, Eds., *Piezoelectric MEMS Resonators*. Springer International Publishing, 2017.

[116] J. Segovia-Fernandez, M. Cremonesi, C. Cassella, A. Frangi, and G. Piazza, "Anchor Losses in AlN Contour Mode Resonators," *J. Microelectromechanical Syst.*, vol. 24, no. 2, pp. 265–275, 2015.

[117] J. Zou, C.-M. Lin, C. S. Lam, and A. P. Pisano, "Transducer design for AlN Lamb wave resonators," *J. Appl. Phys.*, vol. 121, no. 15, p. 154502, 2017.

[118] F. Parsapour *et al.*, "Material parameter extraction for complex AlScN thin film using dual mode resonators in combination with advanced microstructural analysis and finite element modeling," *Adv. Electron. Mater.*, vol. 5, no. 5, p. 1800776, 2019.

[119] W. E. Newell, "Face-mounted piezoelectric resonators," *Proc. IEEE*, vol. 53, no. 6, pp. 575–581, Jun. 1965.

[120] E. W. Weisstein, "Lorentzian Function." [Online]. Available: http://mathworld.wolfram.com/LorentzianFunction.html. [Accessed: 30-May-2019].

[121] R. Veith, G. Eberharter, H. P. Feuerbaum, and U. Knauer, "Visualization of SAW propagation with the scanning electron microscope," in *IEEE Int. Ultras. Symp.*, 1980, pp. 348–351.

[122] D. V. Roshchupkin, "Visualization of acoustic radiation fields in piezoelectric crystals by scanning electron microscopy method," in *Proceedings of the X Session of the Russian Acoustical Society: Wave diffraction and propagation,* 2000.

[123] D. V. Roshchupkin, M. Brunel, and L. Tucoulou, "Visualization of surface acoustic waves by scanning electron microscopy," *J. Phys. IV*, vol. 04, no. C5, pp. C5-1229-C5-1232, 1994.

[124] A. Godet *et al.*, "Mapping acoustic field distributions of VHF to SHF SAW transducers using a Scanning Electron Microscope," in *Europ. Freq. Time Forum*, 2016, pp. 1–4.

[125] T. Hesjedal and G. Behme, "High-resolution imaging of a single circular surface acoustic wave source: Effects of crystal anisotropy," *Appl. Phys. Lett.*, vol. 79, no. 7, pp. 1054–1056, 2001.

[126] T. Hesjedal and G. Behme, "High-resolution imaging of surface acoustic wave scattering," *Appl. Phys. Lett.*, vol. 78, no. 13, pp. 1948–1950, 2001.

[127] S. Ryder, K. B. Lee, X. Meng, and L. Lin, "Characterization of out-of-plane high frequency microresonators by AFM," in *TRANSDUCERS '03. 12th International Conference on Solid-State Sensors, Actuators and Microsystems. Digest of Technical Papers (Cat. No.03TH8664)*, 2003, vol. 1, pp. 424–427.

[128] A. A. Kolomenskii and A. A. Maznev, "Visualization of laser-generated SAW beams by shake-off of fine particles," in *IEEE Int. Ultras. Symp.*, 1994, vol. 1, pp. 351–354.

[129] M. K. Tan, J. R. Friend, and L. Y. Yeo, "Direct visualization of surface acoustic waves along substrates using smoke particles," *Appl. Phys. Lett.*, vol. 91, no. 22, p. 224101, 2007.

[130] D. Royer, "Génération et détection optiques d'ondes élastiques," *Tech. Ing. CND Méthodes Glob. Vol.*, vol. base documentaire : TIB585DUO., no. ref. article : e4415, 1996.

[131] D. Royer and E. Dieulesaint, *Elastic waves in solids II: generation, acousto-optic interaction, applications*. Berlin Heidelberg: Springer-Verlag, 2000.

[132] J.- Monchalin, "Optical detection of ultrasound," *IEEE Trans. Ultrason. Ferroelectr. Freq. Control*, vol. 33, no. 5, pp. 485–499, 1986.

[133] "Fundamentals of Picoscience," *CRC Press*. [Online]. Available: https://www.crcpress.com/Fundamentals-of-Picoscience/Sattler/p/book/9781466505094. [Accessed: 05-Dec-2018].

[134] H. Kamizuma, T. Omori, K. Hamishoto, and M. Yamaguchi, "Development of fast-scanning laser probe system based on knife-edge method for

diagnosis of RF surface acoustic wave devices," *IEEE Trans. Ultrason. Ferroelectr. Freq. Control*, vol. 53, no. 6, pp. 1186–1191, 2006.

[135] J. V. Knuuttila, P. T. Tikka, and M. M. Salomaa, "Scanning Michelson interferometer for imaging surface acoustic wave fields," *Opt. Lett.*, vol. 25, no. 9, pp. 613–615, 2000.

[136] J. Knuuttila, *Laser-interferometric analysis of surface acoustic wave resonators*, vol. PhD dissertation. Helsinki University of Technology, 2005.

[137] L. Lipiäinen, K. Kokkonen, S. Novotny, I. Shavrin, H. Ludvigsen, and M. Kaivola, "Full-field characterization of surface vibrations in microacoustic components by supercontinuum laser stroboscopic white-light interferometry," in *IEEE Int. Ultras. Symp.*, 2014, pp. 158–161.

[138] L. Lipiäinen, K. Kokkonen, and M. Kaivola, "Stabilized stroboscopic full-field interferometer for characterization of subnanometer surface vibrations," *J. Microelectromechanical Syst.*, vol. 24, no. 5, pp. 1642–1646, 2015.

[139] D. Royer and E. Dieulesaint, "Optical detection of sub-Angstrom transient mechanical displacements," in *IEEE Int. Ultras. Symp.*, 1986, pp. 527–530.

[140] K. Kokkonen and M. Kaivola, "Scanning heterodyne laser interferometer for phase-sensitive absolute-amplitude measurements of surface vibrations," *Appl. Phys. Lett.*, vol. 92, no. 6, p. 063502, 2008.

[141] K. Kokkonen, *Imaging of surface vibrations using heterodyne interferometry*, vol. PhD dissertation. Aalto University, 2014.

[142] D. Teyssieux, T. Baron, J. Friedt, G. Martin, and P. Vairac, "Absolute phase and amplitude mapping of surface acoustic wave fields," in *Europ. Freq. Time Forum*, 2013, pp. 73–76.

[143] K. L. Telschow, V. A. Deason, D. L. Cottle, and J. D. Larson, "Full-field imaging of gigahertz film bulk acoustic resonator motion," *IEEE Trans. Ultrason. Ferroelectr. Freq. Control*, vol. 50, no. 10, pp. 1279–1285, 2003.

[144] K. L. Telschow, V. A. Deason, D. L. Cottle, and J. D. Larson, "UHF acoustic microscopic imaging of resonator motion," in *IEEE Int. Ultras. Symp.*, 2000, vol. 1, pp. 631–634.

[145] J. D. Larson, R. C. Ruby, and K. L. Telschow, "Observation of flexural modes in FBAR resonators at MHz frequencies," in *IEEE Int. Ultras. Symp.*, 2003, vol. 1, pp. 88–91.

[146] K. Hashimoto *et al.*, "A laser probe based on a sagnac interferometer with fast mechanical scan for RF surface and bulk acoustic wave devices," *IEEE Trans. Ultrason. Ferroelectr. Freq. Control*, vol. 58, no. 1, pp. 187–194, 2011.

[147] K. Hashimoto and T. Omori, "Phase-sensitive and fast-scanning laser probe system for radio frequency surface/bulk acoustic wave devices," in *Europ. Freq. Time Forum*, 2014, pp. 56–59.

[148] A. Miyamoto, S. I. Wakana, and A. Ito, "Novel optical observation technique for shear horizontal wave in SAW resonators on 42°YX-cut lithium tantalate," in *IEEE Int. Ultras. Symp.*, 2002, vol. 1, pp. 89–92.

[149] E. Leirset, H. E. Engan, and A. Aksnes, "Heterodyne interferometer for absolute amplitude vibration measurements with femtometer sensitivity," *Opt. Express*, vol. 21, no. 17, p. 19900, 2013.

[150] C. Humbert, "Acoustic losses visualization in high-frequency SAW RF-filters," Supméca, Paris, France, Carinthian Tech Research AG, Villach, Austria, Master thesis, 2016.

[151] P. I. (PI) G. & C. KG, "PIMag® Magnetic Direct Drives." [Online]. Available: https://www.physikinstrumente.com/en/technology/electromagnetic-drives/pimag-magnetic-direct-drives/. [Accessed: 14-Oct-2018].

[152] M. W. Davidson, "Resolution," *Nikon's MicroscopyU*. [Online]. Available: https://www.microscopyu.com/microscopy-basics/resolution. [Accessed: 30-May-2019].

[153] "Pupil Diameter and Beam Spot Diameter of Objective Lens | Olympus IMS." [Online]. Available: https://www.olympus-ims.com/en/microscope/terms/luminous_flux/. [Accessed: 30-May-2019].

[154] A. Amin Awan, "Detection of high frequency mechanical vibrations of SAW devices using a low IF receiver architecture," Fachhochschule Kärnten, villach Austria, Carinthian Tech Research AG, Villach, Austria, Master Thesis, 2017.

[155] A. D. I. Engineeri and A. D. inc, *Mixed-signal and DSP Design Techniques*. Newnes, 2003.

[156] W. Kester, "Undersampling applications," 2008. [Online]. Available: https://www.analog.com/media/en/training-seminars/tutorials/MT-002.pdf.

[157] Q. Chapelier, "Automation and management of an innovative measurement system for the detection of high-frequency, sub-nanometric vibrations.," Université de Lorraine, Nancy, France, Carinthian Tech Research AG, Villach, Austria, Master thesis, 2018.

[158] P. D. Bradley *et al.*, "A 5 mmx5 mmx1.37 mm hermetic FBAR duplexer for PCS handsets with wafer-scale packaging," in *IEEE Ultrasonics Symposium*, 2002, vol. 1, pp. 931–934.

[159] E. Schmidhammer, H. Heinze, M. Schmiedgen, M. Mayer, and A. Link, "4D-2 High Volume Production of a Fully Matched 5050 PCS-CDMA-BAW Duplexer," in *IEEE Ultrasonics Symposium*, 2006, pp. 329–332.

[160] R. Ruby, "Micromachined cellular filters," in *IEEE MTT-S International Microwave Symposium Digest*, 1996, vol. 2, pp. 1149–1152.

[161] H. Satoh, Y. Ebata, H. Suzuki, and C. Narahara, "An Air-Gap Type Piezoelectric Composite Thin Film Resonator," in *39th Annual Symposium on Frequency Control*, 1985, pp. 361–366.

[162] K. M. Lakin, K. T. McCarron, and R. E. Rose, "Solidly mounted resonators and filters," in *IEEE Ultrasonics Symposium. Proceedings. An International Symposium*, 1995, vol. 2, pp. 905–908.

[163] R. Ruby, "11E-2 Review and Comparison of Bulk Acoustic Wave FBAR, SMR Technology," in *IEEE Ultrasonics Symposium Proceedings*, 2007, pp. 1029–1040.

[164] H. Ogi, Y. Kawasaki, M. Hirao, and H. Ledbetter, "Acoustic spectroscopy of Lithium Niobate: elastic and piezoelectric coefficients," *J. Appl. Phys.*, vol. 92, no. 5, pp. 2451–2456, 2002.

[165] J. Kushibiki, I. Takanaga, M. Arakawa, and T. Sannomiya, "Accurate measurements of the acoustical physical constants of $LiNbO_3$ and $LiTaO_3$ single crystals," *IEEE Trans Ultras Ferroelec Freq Contr*, vol. 46, no. 5, pp. 1315–1323, 1999.

[166] R. V. Damie, "Elastic constants of Lithium Niobate," *J. Appl. Phys.*, vol. 25, no. 7, pp. 1091–1095, 1992.

[167] G. Carlotti, G. Socino, A. Petri, and E. Verona, "Acoustic investigation of the elastic properties of ZnO films," *Appl. Phys. Lett.*, vol. 51, no. 23, pp. 1889–1891, 1987.

[168] K. Tsubouchi, K. Sugai, and N. Mikoshiba, "AlN material constants evaluation and SAW properties on AlN/Al_2O_3 and AlN/Si," in *IEEE Int. Ultras. Symp.*, 1981, pp. 375–380.

[169] J. Bjurström, G. Wingqvist, V. Yantchev, and I. Katardjiev, "Temperature compensation of liquid FBAR sensors," *J. Micromechanics Microengineering*, vol. 17, no. 3, pp. 651–658, 2007.

[170] "Nonlinear Mechanics of Crystals | John D. Clayton | Springer." [Online]. Available: https://www.springer.com/us/book/9789400703490. [Accessed: 18-Dec-2018].

[171] Y. Nakagawa, K. Yamanouchi, and K. Shibayama, "Third-order elastic constants of Lithium Niobate," *J. Appl. Phys.*, vol. 44, no. 9, pp. 3969–3974, 1973.